Dynamics of Chemisorption

Age Raukema

PhD thesis
University of Amsterdam
The Netherlands
13 April 1995

second edition
20 June 1996

Dynamics of Chemisorption

Academisch Proefschrift

ter verkrijging van de graad van doctor aan de Universiteit van Amsterdam
op gezag van de Rector Magnificus prof. dr P W M de Meijer,
ten overstaan van een door het college van dekanen ingestelde commissie
in het openbaar te verdedigen in de Aula der Universiteit
op donderdag 13 april 1995 om 10.30 uur

door

Age Raukema

geboren te Halsteren

promotor prof. dr A W Kleyn

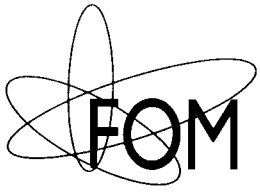

The work in this thesis was performed at the *FOM-Institute for Atomic and Molecular Physics*, Kruislaan 407, 1098 SJ Amsterdam, The Netherlands. It is part of the research program of the *Stichting voor Fundamenteel Onderzoek der Materie* (FOM, Foundation for Fundamental Research on Matter) and was made possible by financial support from the *Nederlandse Organisatie voor Wetenschappelijk Onderzoek* (NWO, Dutch Organisation for Scientific Research).

This thesis is based upon the following papers:

chapter 2
A Raukema, A P de Jongh, H P Alberda, R Boddenberg, F G Giskes, E de Haas, A W Kleyn, H Neerings, R Schaafsma and H Veerman
A 3-Axis Goniometer in an UHV Molecular Beam Experiment
submitted to Measurement Science and Technology

chapter 3
A Raukema, R J Dirksen and A W Kleyn
Probing the (dual) repulsive wall in the interaction of O_2, N_2 and Ar with the Ag(111) surface
Journal of Chemical Physics 103 (1995), pages 6217–6231

chapter 4
A Raukema and A W Kleyn
Transient trapping desorption of molecules at surfaces
Physical Review Letters 74 (1995), pages 4333–4336

A Raukema, D A Butler and A W Kleyn
O_2 transient trapping-desorption at the Ag(111) surface
submitted to Journal of Chemical Physics

chapter 5
A Raukema, D A Butler, F M A Box and A W Kleyn
Dissociative and non-dissociative sticking of O_2 at the Ag(111) surface
Surface Science 347 (1996), pages 151–168

chapter 6
A Raukema, D A Butler and A W Kleyn
The interaction of O_2 with the Ag(110) surface
Journal of Physics: Condensed Matter 8 (1996), pages 2247–2263

Related papers:

D A Butler, A Raukema and A W Kleyn
The growth of oxygen adlayers on Ag(110)
Surface Science 357/358 (1996), pages 619–623

D A Butler, A Raukema and A W Kleyn
Molecular beam studies of the interaction of oxygen with silver surfaces
Journal of the Chemical Society, Faraday Transactions 92 (1996)

A W Kleyn, D A Butler and A Raukema
Dynamics of the interaction of O_2 with silver surfaces
Surface Science (in print)

D A Butler, J Sanders, A Raukema, A W Kleyn and J W M Frenken
Oxygen dissociation on Ag(110): a ruin game
in preparation

Contents

Chapter 1

Dynamics of Chemisorption; an introduction

Abstract *A short overview will be presented on general information about gas-surface interactions to obtain an impression on the different mechanisms which play a role in these interactions. Emphasis is put on the oxygen-silver system, which is mainly studied, with the use of a molecular beam, in this thesis. Some details on the experimant will also be presented and the chapter ends with a brief outline of the thesis.*

1.1 General introduction

The mechanism of chemical reactions taking place at solid surfaces is still not fully understood. In heterogeneous catalysis for instance molecules or their dissociated fragments "somehow" and in "some state" meet at the surface and react to yield a desired product molecule. One material may act as a catalyst for a certain reaction, but another material may not. For the epoxidation reaction of ethene (= ethylene, C_2H_4) a heterogeneous catalyst is used. Ethene can either react with oxygen to form the epoxide (C_2H_4O) or burn to yield CO_2 and H_2O, which is the common combustion process in the gas phase. Silver has been shown to catalyse the epoxidation reaction, although not with 100% selectivity [1]. Heterogeneous catalysis is one example of chemical reactions at surfaces. Corrosion and etching, for instance in semi-conductor processing, are other examples.

This thesis deals with the dynamics of chemisorption. Chemisorption often is the first step in a surface reaction [2]. Chemisorption is the adsorption of a particle at the surface with the formation of a chemical bond with one or more surface atoms. Probing the dynamics of the interaction means probing of the process on an atomic (sub-picosecond) time scale. The system studied in particular is the interaction of oxygen with a silver surface. At first sight it seems a very simple reaction. It is studied to gain more insight in the fundamental processes governing molecule-surface interactions. The results obtained may also help in providing a better understanding of the epoxidation reaction.

Different processes can occur when the molecule approaches the surface [3,4]. The molecule can either reflect or adsorb at the surface and the adsorption can either be as a molecule or as atoms in the case of molecular dissociation. Dissociation can occur either

directly upon hitting the surface or proceed after molecular adsorption. In the last case the molecular adsorption acts as a precursor to dissociation. Once the molecule has (dissociatively) adsorbed it may desorb again if the energy supplied by the thermal bath as represented by the solid is sufficient for escaping from the surface into the gas phase. So far the possible fates of the molecule are either described as a direct or as a thermalised process. It is very well possible that a continuous range of processes exists beween the two extremes. What at first sight appears as a simple interaction proves to be a rather complicated process.

A gas particle hitting a surface will exchange energy with the surface and internal degrees of freedom may be excited in the case of a molecule [3,4]. For light particles, such as helium and hydrogen, the interaction with single phonons at the surface can be observed. Since helium and hydrogen of thermal velocity have also a wavelength in the order of the distance scale of surface structure they can also be used to determine this structure by measuring their diffraction patterns. Rotational excitation may also occur for hydrogen scattering and discrete rotational state transitions have been observed in time-of-flight experiments. Helium and hydrogen are also very sensitive to adsorbates and defects present at the surface. The scattering cross sections are very large due to the long range of the attractive part in the Van-der-Waals interaction [5]. For Ar scattering from H/W(100) diffraction has also been observed at low surface temperature [6], but in general multi-phonon processes are involved in the scattering of heavier atoms and molecules and obscure the discrete nature of the phonon interaction. The results are rather broad angular scattering distributions.

The angular energy and intensity distributions of scattered particles will depend on the way the incident particle "feels" the surface. For low incident energies the individual surface atoms may not or hardly be visible to the incident particle and the surface will appear rather flat, although the motion of the surface atoms due to the finite temperature of the sample will be felt. An interaction in this range can be approximated by representing the surface by moving cubes, to which energy can transfered or from which energy can be gained by the incident particle [7,8]. The hard cube can be made soft by connecting a Lennard-Jones type of potential to the cube. Caps can also be put on the cubes to represent the corrugation by the individual surface atoms [9,10].

For increasing incident translational energies the incident particle will reflect from a point higher on the repulsive wall of the interaction potential, which will be closer to the surface atoms. The individual surface atoms will become better visible for the incident particle, resulting in an increasing corrugation in the interaction potential. The increase in corrugation should be reflected in the angular energy and intensity of the scattered particles.

Not only the translational energy but also the rotational and vibrational energy of the scattered particle will in general be a function of the scattering angle. Restricting to simple molecules, rotational excitation has been shown to occur for several gas-surface systems such as N_2-Ag(111) [11,12], NO-Ag(111) [13], NO-Pt(111) [14] and CO-Ag(111) [15]. Alignment of $\vec{J}$-vectors has been seen to occur in scattering and also rotational rainbows are observed. A rainbow is a considerable increase in intensity as function of some variable, which is the rotational quantum number for a rotational rainbow, at a distinct value after which the intensity drops sharply. Vibrational excitation of these simple molecules has been measured for NO-Ag(111) [16,17] and electron-hole pair formation was inferred to account for the observation. Due to electron capture by the incident molecule, its bond is

suddenly weakened resulting in vibrational excitation. A hole is created in the solid since an electron is captured by the molecule. The internal state excitation of the molecules mentioned is measured with techniques like resonance enhanced multi-photon ionisation (REMPI) or laser-induced fluorescence (LiF). Detection is possible due to the well known excitation spectroscopy of these molecules and their large excitation cross section. These two arguments do not hold for, for instance, the oxygen molecule.

The interaction of NO with a surface has been shown to be anisotropic [18–23], meaning that both ends of the molecule experience a different interaction with the surface. The anisotropy can be governed by the repulsive or the attractive part of the interaction or even by both.

For adsorption (sticking or trapping) to occur also several mechanisms can be involved. I will refer to trapping when the residence time of the particle at the surface is short as compared to the time scale of the experiment. A trapped particle will thus desorb again at the surface temperature of the experiment and a particle that has stuck will remain at the surface. Adsorption may be activated or not. If it is activated an energy barrier exists between the gas phase particle and the adsorbed state. This barrier may be along different degrees of freedom describing the particle-surface interaction, such as the particle-surface distance and/or the internuclear distance, and adsorption will occur if the incident particle can overcome this barrier. Crossing the barrier to adsorption may be enhanced by the thermal motion of the surface atoms [24]. Tunneling through a barrier is another possibility for entering an adsorption state [25]. For a state that can be accessed directly from the gas phase the probability of adsorption in this state is given by the probability that the incident particle can loose enough of its incident energy. A part of the incident translational energy, increased by the well depth of the adsorption state, will be transferred to the sample or to internal degrees of freedom of the particle. If the loss is large enough that it cannot escape from the well it will reside in the adsorption state.

The processes described give some idea on the phenomena occuring in gas-surface collisions. In this thesis the system of study is the oxygen-silver interaction. It is a relatively simple system having different adsorption states and dissociation of the oxygen molecule can occur. A molecular beam is used in the experiments described to probe the interaction.

1.2 The oxygen-silver interaction

Over the years an extensive number of studies have already dealt with the oxygen-silver interaction [26–109]. Comparing the number of publications the Ag(110) surface plane is the most favoured followed by the Ag(111) surface plane. A limited number of studies concerns the Ag(100) surface plane. The studies reveal the existence of dissociated oxygen at the surface for surface temperatures above at least $T_s = 150$ K and recombinative desorption at about $T_s = 600$ K. A subsurface oxygen state has also been observed and desorbs at a higher surface temperature. At low surface temperature oxygen is adsorbed as a molecule, either in a physisorbed state desorbing at about $T_s = 40$ K, or in a molecularly chemisorbed state desorbing at about $T_s = 200$ K.

A potential energy surface of the O_2-Ag(111) interaction as derived from reviewing available spectroscopic data is shown in figure 1.1 [60]. The hypersurface of the O_2-Ag(110)

system as derived from ab-initio calculations [71] is quite similar. The figure shows the potential energy surface as a topographic plot. Only two variables are assumed to be important for the interaction potential: the molecule-surface distance and the internuclear separation within the molecule. In the entrance channel first the physisorption interaction, denoted as O_2, is seen. The molecule is only weakly perturbed with respect to the gas phase in this state. Some charge transfer to the molecule will lead to molecular chemisorption, denoted as O_2^-, and the molecular bond will weaken and stretch somewhat. In the exit channel the internuclear distance increases and the molecule dissociates. The atoms are separately bonded to the surface, denoted as $O^- + O^-$. However, this description implies dissociation as a sequence of steps, which may not be necessary. A certain state might be accessed directly. A subsurface state of oxygen desorbing above $T_s = 700$ K is also possible, but not taken into account for the potential energy surface of figure 1.1.

Most studies use an ambient gas for oxygen adsorption and only a very limited number of studies employ a molecular beam to probe the interaction. This thesis deals the interaction of O_2 with two surface planes of silver, namely Ag(111) and Ag(110) as probed with a molecular oxygen beam. The Ag(111) surface is a very smooth [110] hexagonal close packed surface and the Ag(110) surface is a more open surface showing a reconstruction with throughs along the $<1\bar{1}0>$ direction over the surface. Both dissociative and non-dissociative sticking from ambient gas adsorption has been shown to be larger on the Ag(110) surface [46,48]: 10^{-7}–10^{-6} for the Ag(111) surface and 10^{-4}–10^{-3} for Ag(110). Using a molecular beam the sticking on the Ag(110) surface shows an increase with increasing incident energy to approximately 0.5 [103], whereas the Ag(111) surface seems to remain below 10^{-4} [68]. These are very puzzling results in view of the remarkably similar potential energy diagrams for both silver surfaces.

1.3 Experimental technique

A molecular and/or atomic beam is used for the experiments described in this thesis and further referred to simply as a molecular beam. It is generated by the supersonic expansion of a gas at a pressure in the order of bars to vacuum through a small orifice [111]. The expansion is supersonic if the mean free path of the molecule is considerably smaller than the diameter of the opening of the source and the result is that many collisions take place during the expansion as opposed to an effusive beam for which no collisions occur when a molecule is leaving the source. In the supersonic expansion cooling of the gas with respect to a reference frame moving with the flow velocity v_β of the beam takes place, due to the collisions during the expansion. An enthalpy balance exists before and after the expansion, with the enthalpy after the expansion given by the enthalpy in a point in the beam plus a kinetic energy term due to the flow velocity of the beam. Before the expansion the enthalpy of the gas is given by the internal energy of the gas plus the product of pressure and volume. The enthalpy in the gas after expansion in the moving reference frame is given in the same way. Cooling of the gas in the expansion means a decrease of the enthalpy in the moving reference frame in favour of the flow velocity of the beam (which is the flow velocity of the reference frame) and the result is a sharp velocity distribution, and thus a sharp translational energy distribution, of the particles in the beam. The cooling does not

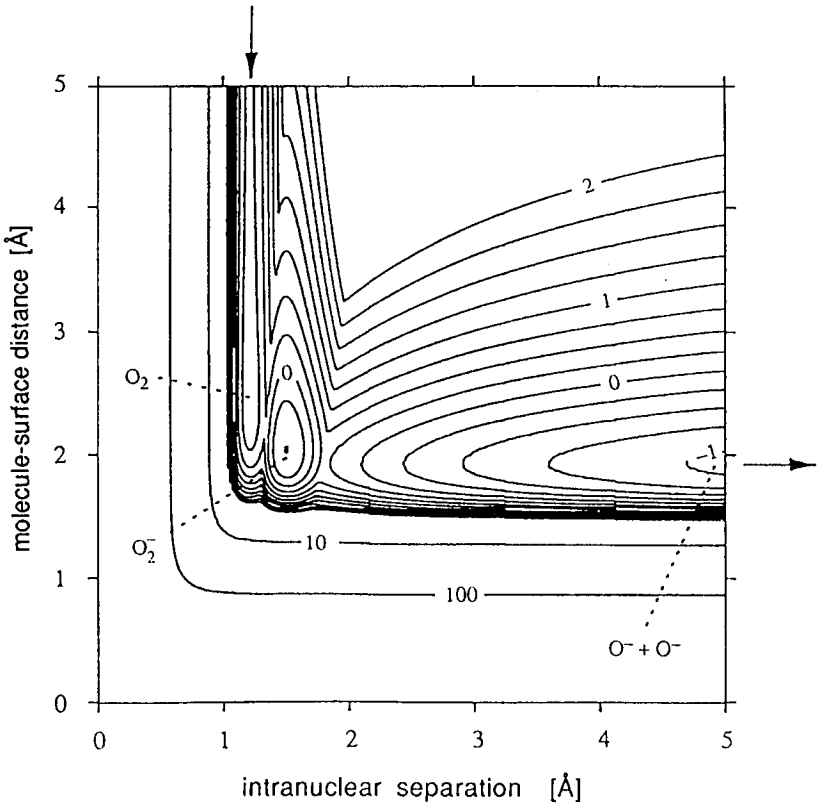

Figure 1.1 *Potential energy diagram for the O_2-Ag(111) interaction as function of molecule-surface distance and internuclear separation. The figure is taken from the PhD thesis of Spruit [60].*

only concern the translational degrees of freedom of the particles in the gas, but also the internal degrees of freedom in the case of molecules. However, not all degrees of freedom are efficiently cooled. Rotation and translation are cooled quite well, but the coupling to the vibrational degree of freedom in the expansion is weak resulting in an inefficient cooling. Generally, it is assumed that the temperature of the vibrational excitation of the molecules in the beam is described very well by the temperature of the orifice [111], mostly referred to as nozzle.

The translational energy of the particles in the beam can be varied in two ways. Since the enthalpy increases with increasing temperature of the gas and the flow velocity of the beam increases with increasing enthalpy before the expansion, the translational energy of the beam particles can be increased by increasing the temperature of the nozzle. An other way to increase the translational energy is to make use of a gas mixture. Since all the particles have equal velocity after the supersonic expansion, disregarding slip effects, and the kinetic energy term after the expansion is given by the average mass in the beam, the kinetic energy of gas particles can be increased by mixing with a lighter, so-called seeding gas. The translational energy of oxygen molecules for instance can be increased by mixing with helium. By using both seeding and nozzle heating a large translational energy range of a gas particle can be covered.

The divergent, but forwardly peaked, supersonic beam is collimated using apertures to

acquire a beam with low divergence in the experiment. Two differential pumping stages in the beam line separate the source chamber from the UHV chamber, containing the sample, to reduce the effusive gas load from the source chamber. The intensity of the continuous beam is in the order of 10^{14} particles s^{-1}, dependent on the exact flow and nozzle conditions. At the sample surface the flux of the beam is in the order of 10^{18} particles m^{-2} s^{-1}, which means approximately one particle hitting a surface atom per second. This arrival rate is equal to the arrival rate of an ambient oxygen gas of 300 K with a pressure in the order of 10^{-6} mbar. The pressure is in this case taken as a measure of density and not as a force per unit area. Taking the pressure as a force per unit area for a molecular oxygen beam of 1 eV translational energy (approximately 2455 m s^{-1}) the beam pressure is in the order of 10^{-3} Pa $= 0.1$ mbar, based on momentum transfer of the molecule to the surface and assuming elastic collisions. If an oxygen molecule is able to cause a reaction, such as (dissociative) sticking, at the surface if it has a translational energy of 1 eV or higher (an activation energy of 1 eV) the equivalent pressure of an ambient oxygen gas should be in the order of a million bar to yield an equal reaction rate as the 1 eV molecular oxygen beam with an intensity as stated above. In this case the pressure is again related to the arrival rate. The angular arrival distribution of the ambient gas is neglected in the comparisons of the molecular beam with an ambient gas.

The demand on the quality of the surface is high since the experiments deal with the fundamental properties of the particle-surface interaction, wich can be influenced by contaminants present on the surface or defects. To obtain a high quality surface of the sample, the samples were cut by spark erosion from a single crystal rod of very high purity ($99.999\% = 5$N) and polished to within $0.1°$ from a principle surface plane as can be checked using Laue diffraction. The sample is kept in ultra high vacuum (UHV) to prevent a build up of contamination from the background gas on the sample surface in the course of the experiments. Once in vacuum the sample surface received a treatment of sputtering with Ar^+ ions and annealing to obtain a smooth surface.

Both scattering and sticking experiments are described in this thesis. For the scattering experiments the continuous beam is chopped into pulses of short duration (approximately 15 μs) and reflected from the surface. Scattered particles are detected as a function of time using a rotatable differentially pumped quadrupole mass spectrometer. The short pulses allow for a good resolution in time of the recorded flight times of the particles from the chopper to the detector. A trigger generated by the chopper sets the zero of the time axis and the flight times are in the order of 100 μs. Once the time-of-flight spectra are recorded they are analysed to yield an angular flux and translational energy distribution of the scattered particles.

Sticking probabilities are measured by monitoring the partial pressure in the system. The ratio of the pressure drop in the system when the beam is allowed to hit the sample surface and the partial pressure increase due to the beam entering the system is a measure for the sticking probability. This so-called King&Wells-technique works only for sticking probabilities exceeding a few percent. Another technique employed to derive the sticking probability is to measure the amount of particles adsorbed after exposing the sample surface to the molecular beam. For the work described in this thesis the amount adsorbed has been measured by linearly increasing the surface temperature and monitoring the partial pressure of the desorbing particles. Differentiating the uptake versus exposure curve yields

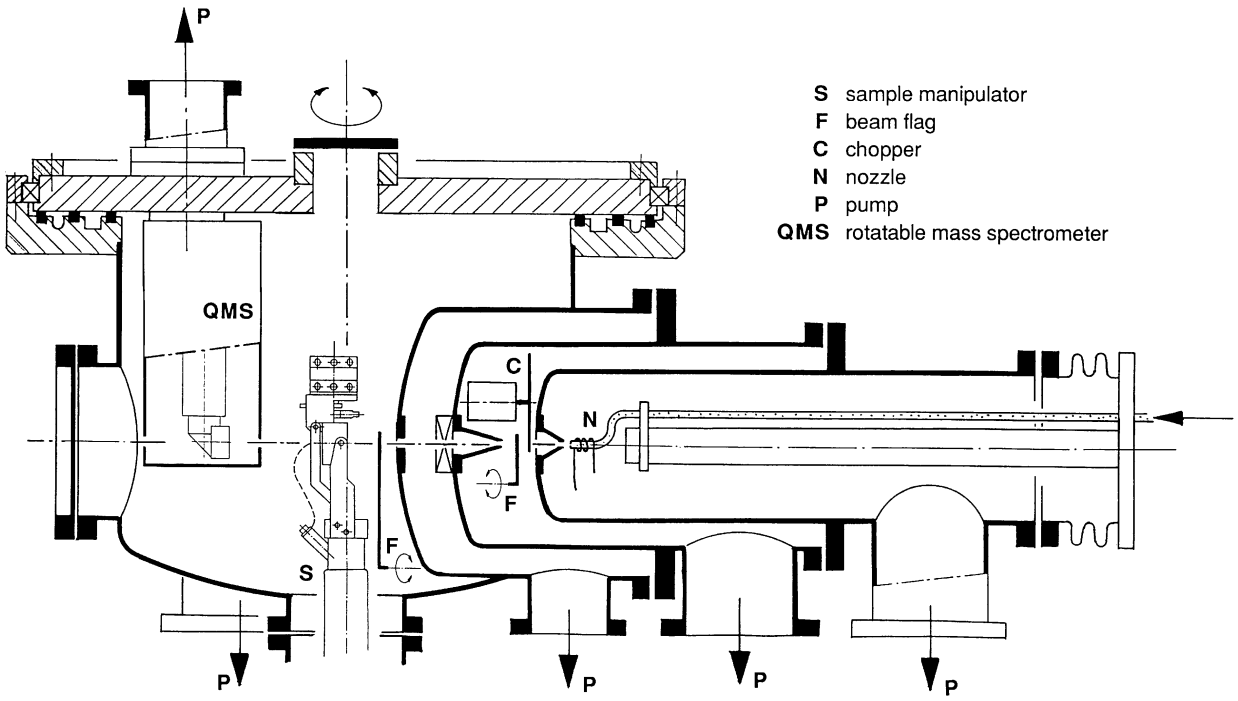

Figure 1.2 *Overview of the experimental setup. It shows the molecular beam line, consisting of three pumping stages, entering a UHV chamber in which the sample is mounted on a sample manipulator. The cover of the UHV chamber can be rotated.*

the sticking probability.

Scattering and sticking is studied as a function of several accessible experimental parameters, such as the energy and the angle of the incident particles as well as the surface temperature. The incident angle is defined with respect to the surface normal and with respect to some crystallographic direction over the surface.

1.4 This thesis

For the experiments described in this thesis a new sample manipulator was developed and is described in **chapter 2**. It enables positioning of the sample over all six degrees of freedom. In combination with the rotatable detector we have now control over both scattering in and out of the plane of incidence, which is defined through the surface normal and the molecular beam. The new manipulator also allows for cooling with ℓN_2 and both heating of the sample by radiatione and electron beam bombardment.

Scattering experiments of O_2, N_2 and Ar are presented in **chapter 3**. Those experiments will probe the repulsive wall in the interaction potential for directly scattered molecules and may show the influence of potential energy wells sampled by the scattered particles. O_2 is chemically reactive (adsorption) at this surface, but N_2 and Ar are not. The last two particles are used as a comparison with the O_2 scattering. Most experiments are done at a surface temperature of $T_s = 600$ K, for which the residence times in both the molecular

and dissociated O_2 state are small compared to the time scale of the experiment. Some experiments are done at a surface with a surface temperature $T_s = 150$ K.

In **chapter 4** the scattering of O_2 from the Ag(111) surface at the low surface temperature is examined in more detail. The existence of a yet unknown state of oxygen at the Ag(111) surface is revealed in these experiments. Trapping in the physisorption state is also seen to occur at low incident energies.

Both molecular and dissociative sticking are described in **chapter 5**. For the whole range of experimental parameters accessible in our experimental setup the sticking remains extremely low (approximately 10^{-3}). A correlation with the scattering experiments presented in the previous chapters is observed. Temperature programmed desorption experiments have also been carried out.

Finally, **chapter 6** is concerned with the O_2-Ag(110) interaction. Results on scattering, dissociative sticking, dissociative oxygen uptake and recombinative desorption experiments are presented.

Chapter 2

An Ultra High Vacuum Compatible 3-Axis Goniometer in a Molecular Beam Scattering Apparatus

Abstract *A sample manipulator with six degrees of freedom is described, which is part of a molecular beam scattering apparatus used to study gas-surface interactions. The incident and final angles of particles before and after scattering can be set, under computer control, by a combination of the movement of the manipulator and the detector. The sample can also be cooled to ℓN_2 temperatures and heated to at least 800 K. A relation is derived between the position of the manipulator and the detector and the required incident and final angles of incident and scattered particles.*

2.1 Introduction

One of the ways to study molecule-surface interactions is to aim a beam of molecules at a surface and to analyse the scattered particles or measure the fraction of the incident molecules that adsorb at the surface. Several experimental parameters can be varied to gain information on the interaction such as the energy (translational and/or internal) of the incident molecules, the surface temperature, the orientation of the molecules with respect to the surface, the incident angle of the molecules, the crystallographic direction along which the molecules approach the sample surface and the exit angle of the scattered molecules with respect to the surface normal and to the plane of incidence.

The molecules leaving the surface can be analysed using a time-of-flight (TOF) technique to yield their translational energy distribution and in some cases their residence time at the surface. Detection of the molecules can be done with a (differentially pumped) mass spectrometer or an internal state sensitive detection technique such as resonance enhanced multiphoton ionisation (REMPI).

Sticking probabilities can be measured by monitoring the residual gas pressure while exposing the surface to the molecular beam or by monitoring the specular He reflectivity while dosing. Desorbing (associatively) the adsorbed molecules by ramping the surface temperature (temperature programmed desorption (TPD) or thermal desorption spectroscopy (TDS)) after exposing the surface to the molecular beam can also be used to determine the

sticking probability and to discriminate between different adsorption states. A more detailed analysis of these TPD spectra, optionally at different linear ramp rates of the sample temperature, can also give more information on desorption energies and pre-exponential factors in the desorption rates.

The above certainly does not give a full list of the capabilities of a molecular beam system but gives an overview of the possibilities of our system in which the sample manipulator plays a vital role. Changing the conditions of the incident particles will give information on the dynamics of the interaction and the structure of the surface.

2.2 Experimental setup

The experimental setup consists of two molecular beam lines connected to a UHV chamber in which a sample is mounted. In the beam line a molecular or atomic beam is generated by the supersonic expansion of a gas from a nozzle. One of the beam lines enters the UHV chamber to keep the distance between the nozzle and the sample as short as possible for a maximum particle flux at the sample. The other beam line is used for experiments with oriented nitric oxide (NO) molecules. Both beam lines are differentially pumped.

The sample is mounted on a manipulator in the center of the UHV chamber. A differentially pumped quadrupole mass spectrometer (QMS) and a REMPI detector can rotate in a horizontal plane around the sample. Both detectors are connected to the cover of the UHV chamber, which is rotatable. UHV is maintained while rotating the cover by doubly differentially pumping the seal between the cover and rest of the chamber. The seal consists of three spring loaded teflon seals and two pumping stages.

The existing 2-axis sample manipulator poses limitations on the possible experiments and will be replaced by the 3-axis manipulator described. Since no commercial manipulator that satisfied our demands was available we developed one ourselves.

2.3 Design criteria

The most obvious demand on a sample manipulator is the positioning of the sample and in our case UHV compatibility. It should be possible to face the sample towards the molecular beam, but also towards the surface analytical tools LEED and AES, an ion sputter gun and a sample exchange chamber which are positioned in an almost full circle around the sample. When doing a surface scattering or sticking experiment we like to have control over the angle of incidence, measured with respect to the surface normal, but also over the azimuthal angle (see figure 2.4). The azimuthal angle is defined as the angle between a chosen crystallographic direction over the surface and the plane of incidence of the particle, which is the plane through the surface normal and the incident trajectory of the particle. We also want to have control over the angles, both in and out of the plane of incidence, under which scattered particles are detected. Since our detector can only rotate in one plane it should be possible to rotate (tilt) the sample such that also control of out-of-plane scattering is obtained. It is obvious that the incident and final angles of the particles as referenced to a frame connected to the sample will not be the same as the angles describing the sample and the detector position as referenced to a frame connected to the experimental

setup. The manipulator should be retractable from of the beam path to be able to measure the particles in the beam. Sample positioning should be computer controlled and the desired accuracy in the positioning of the sample is only moderate. These considerations did lead to the following design criteria:

- UHV compatibility,
- 360° polar rotation (θ_{P}) of the sample manipulator around a vertical axis of the experimental setup,
- tilt rotation (θ_{T}) of the sample with respect to the (horizontal) detector plane (90° tilt backwards and 20° forwards),
- 360° spin rotation (θ_{S}) of the sample with respect to the surface normal,
- $\pm$15 mm X-, Y- and Z-translation of the sample manipulator with respect to the center of the experiment,
- rotational accuracy of $\pm$0.1°,
- translational accuracy of $\pm$0.1 mm,
- motor driven positioning and
- computer readout and control of the positioning.

The sample temperature should be controlable. To obtain a large sample temperature range it must be coolable to about ℓN_2 temperature and heatable to about 1200 K. Both radiative heating and heating by electron bombardment of the sample should be possible. The last method gives the opportunity of fast heating rates of the sample. To avoid a large heat load on the sample surroundings it should be thermally isolated at elevated temperatures, but not during cooling of the sample. The sample should also be electrically isolated from its surroundings. In this way it is possible to connect it to ground potential or to positively or negatively bias it. Listing these demands:

- readout of the sample temperature with a K-type thermocouple,
- ℓN_2-cooling of the sample,
- radiative and e-beam bombardment heating of the sample,
- thermal insulation of the sample at elevated temperatures and
- electrical insulation of the sample from its surroundings.

Samples should be easily exchanged and preferably without breaking the vacuum, but using the sample exchange chamber. It should also be possible to do experiments with oriented NO. To do so a strong electrical field is employed in which the molecules orient due to the stark effect of the NO molecules. An orientation electrode in front of the (earthed) sample should therefore be provided for. The electrode must be movable in order to be able to put into a position where it does not interfere with certain experiments or during sample exchange. Adding these demands to the list:

- easy sample exchange without breaking UHV and
- provision of an orientation electrode, which can be moved into a neutral position.

The manipulator should be mounted on an 8 inch O.D. flange in the bottom of the experimental setup. The space available in the experiment is limited. Between one of the beam lines and the center of the UHV chamber only 65 mm is available. Since the demand on the polar rotation is a full 360°, the top of the manipulator should not occupy more space than fits in a cylinder with 65 mm radius. Positioning of a beam flag between the sample and the in the UHV chamber entering beam line should be possible. In the vertical direction no limitations of this order are imposed. The detector used for REMPI experiments is very close to the sample in these kind of experiments in order not to loose intensity and this should not be obstructed by the manipulator. Incident and scattered/desorbing particles should also not be obstructed by parts of the manipulator (except the orientation electrode). Ending the list of demands:

- vertical upward mounting on an 8 inch O.D. flange,
- restricting the size of the top of the manipulator within a radius of 65 mm,
- no obstructions for incident and scattered/desorbing particles and
- no obstructions in front of the sample for the REMPI detector and an UHV beam flag.

In the following sections a description of the manipulator will be given and the relation between manipulator position and incident and final angles of incident and scattered particles will be derived.

2.4 Implementation and Performance

The newly designed sample manipulator is based on a Fisons Omniax MXY25 and MXZ100 high precision XY-translation and Z-translation stage. It consists, as is shown in figure 2.1, of a wide bore bellows XY-stage on which a 100 mm bellows for the Z-movement is mounted. The XY-stage will be connected to the flange of the UHV system and thus be on top of the Z-stage. The Z-movement bellows ends in another flange on which a Fisons DPRF55 differentially pumped rotational feedthrough is mounted. Through this rotational feedthrough and through the Z-bellows a 50 mm diameter column is put. One end of this column is a 4.5 inch flange, which is connected to the rotational feedthrough. On the other side of this flange a piece is put with several ports allowing for the connection of ℓN_2-tubing and several electrical feedthroughs. At the bottom a Fisons SLMD100 linear translation stage is mounted closing this end of the manipulator. The column allows for the polar rotation (θ_P) and Z-translation of the manipulator and moves at the top of the XY-stage through a bearing allowing for both polar rotation and Z-translation.

On top of the column the mechanism allowing for the tilt (θ_T) and spin rotation (θ_S) is put and a push rod connected to the linear translation stage moves, through the column, the tilt rotation of the sample. This part is shown enlarged in figure 2.1 and photos are

shown in figure 2.2. A housing is mounted via two small ball bearings and in between two arms on the column. The push rod is connected via two rotation centers to the housing and allows, by moving up or down, for the tilt rotation of the housing. In the housing the sample holder is put in a slide bearing allowing for spinning the sample holder and thus the sample. Spin rotation of the holder is done by the model B23.1 UHV compatible stepper motor from Arun Microelectronics Limited (AML). The stepper motor is mounted on top of the housing. A 10:1 gear connection reduces the sample holder rotation speed with respect to the stepper motor rotation speed. The sample holder can be removed from the housing via a sample exchange rod to transport it to the sample exchange chamber. In the back of the housing, in an alumina plate, five connectors are placed in which five pins of the sample holder are pushed. These allow for electrical connections: 2 for the filament for heating the sample, 1 for electrical connection to the sample and 2 for a K-type thermocouple. A drawing of the sample holder is shown in figure 2.3. All the electrical wiring for the manipulator in UHV is also put through the column and ends in a alumina plate with connectors. Wiring for the sample holder from this plate is taken long enough to also allow for the tilt and spin rotation.

On the alumina plate in the housing also a CuCr-piece is mounted. In this piece a Mo-plate mounted at the back of the sample holder fits loosely. On the other side of the CuCr-piece a set of Cu-braids is clamped and the Cu-braids are connected to a heat exchanger. CuCr has a larger expansion coefficient than Mo, so upon cooling the CuCr-piece shrinks faster than the Mo-plate of the sample holder and will make mechanical and thus thermal contact when cold enough. In this way a cooling connection is made to the sample. For good thermal heat contact the Cu-braids are e-beam welded into two Cu-blocks. One is clamped on the CuCr-piece and the other one on the ℓN_2 heat exchanger (not exactly shown in figure 2.1). Flexible Cu-braids are used to allow for the tilt and spin rotation of the sample. A temperature of $T_s = 120$ K can be reached at the sample after cooling for about one hour. Cooling of the sample is in the order of minutes after flashing it from a low temperature to a temperature of about 800 K. Much larger temperatures can be reached and are limited by the applied materials in the vicinity of the sample.

In the sample holder the sample is clamped on a CuCr block with sapphire insulation in between. The sapphire acts as an electrical insulation for the sample, but also as a heat diode. At low temperatures it has a large heat conductivity and at high temperatures a low one. In this way the sample is thermally insulated at high temperatures and it can be cooled via the copper block. A tungsten filament for heating is mounted behind the sample. When applying e-beam bombardment heating, all the electrons should hit the sample in order not to heat the surroundings. Therefore the heat screen behind the filament is at the same potential as the filament and a +25 V bias is applied to the sample.

The orientation electrode is mounted on the block in between the sample holder housing and the stepper motor. It can be moved in and out of position with the aid of the sample exchange rod.

The motors for all except the spin rotation are mounted outside the vacuum. They are all DC-motors and their positions are given by Hewlett-Packard HEDS-5010/6010 optical increment encoders mounted on the back of the motors. In the controllers for these motors the position in encoder steps with respect to a reference position is kept track of. If the position is somehow lost the reference position can be found back easily again by optical

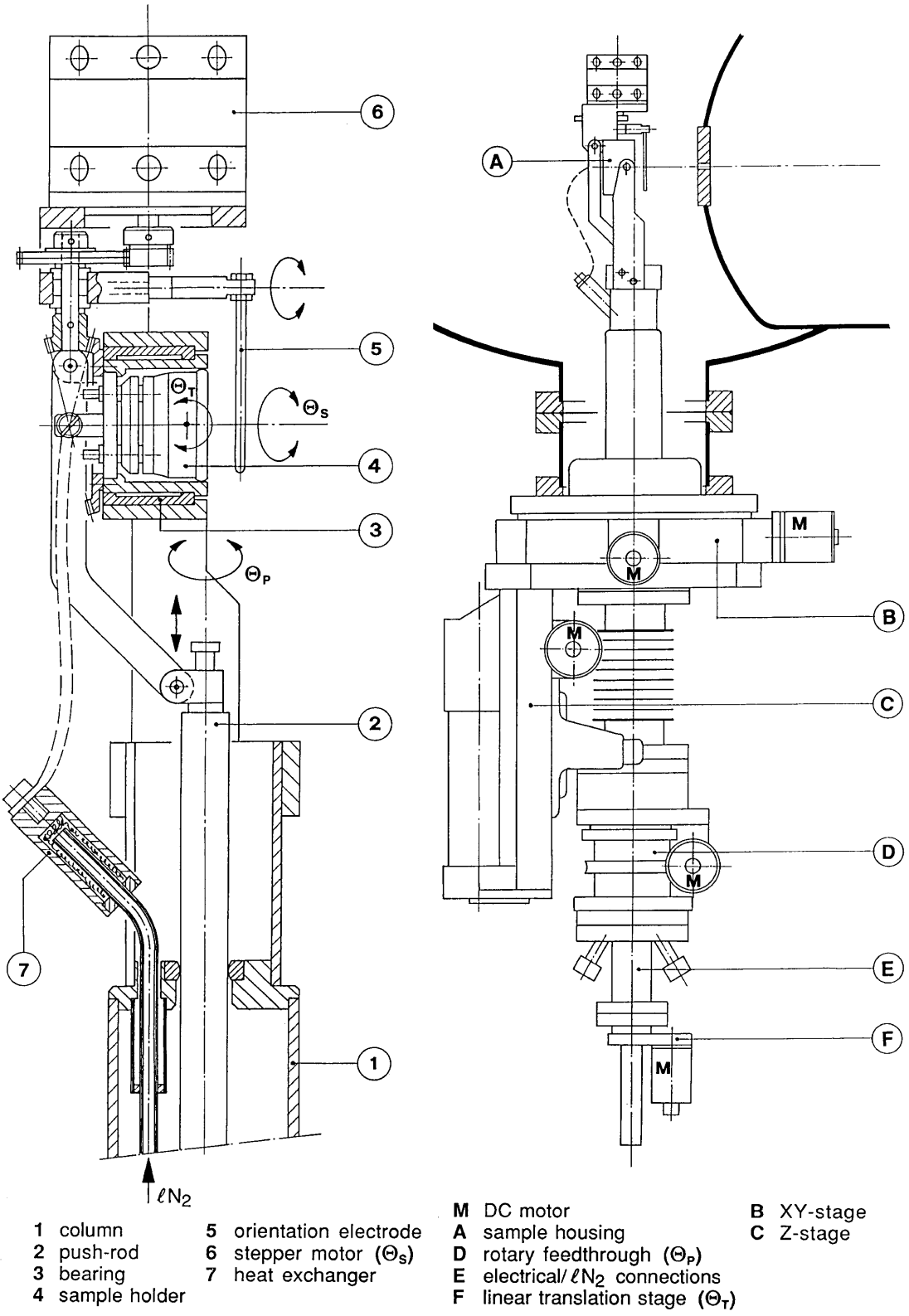

Figure 2.1 *A drawing of the sample manipulator as it is mounted in the experimental setup is shown on the right. The top of the manipulator allowing for the tilt and spin rotation is shown enlarged on the left.*

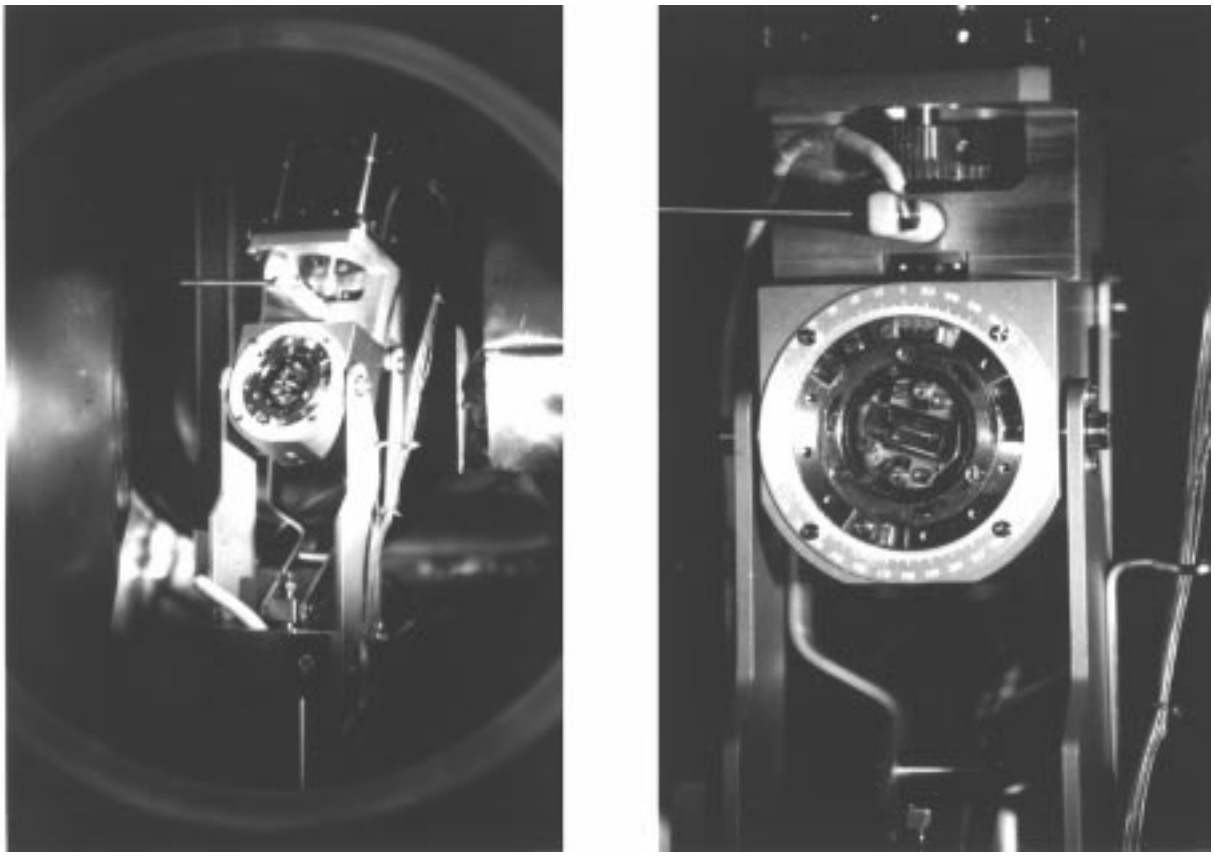

Figure 2.2 *The left photograph shows the top of the manipulator slightly tilted and the right photograph a close-up of the housing for the sample holder with the sample holder in. A sample is not mounted, which makes the heating filament visible.*

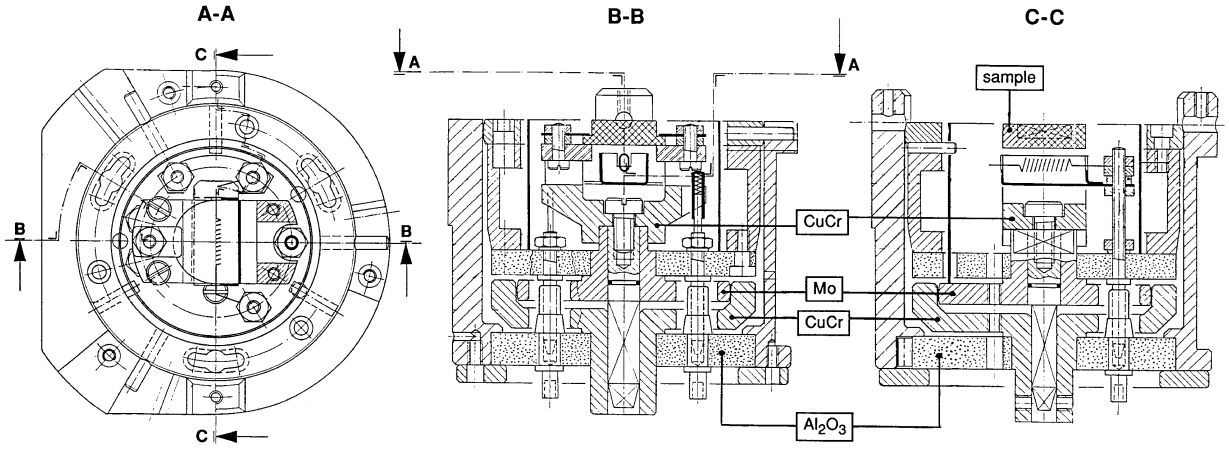

Figure 2.3 *The sample holder for easy sample exchange drawn in the housing of another sample manipulator than the one described in the text.*

marks which can be traced with the aid of Hewlett-Packerd HBCS-1100 optical sensors. The resolution of the encoders in combination with the gear boxes used and the reproducibility of the Fisons components is far better than the accuracy required and will not further be evaluated. For the spin rotation the accuracy in the position is given by the steps of the stepper motor and the reduction and backlash in the gears. Since the steps of the stepper motor are 1.8° and the reduction 10:1, the accuracy of the position, disregarding the backlash, will be ±0.1°. The backlash is estimated to be also 0.1°, giving an accuracy in the spin rotation position of ±0.2°, slightly worse than was set in the design criteria. No encoder is used for the stepper motor. The spin position would be in error if steps were lost in spinning the sample. Loss of steps is not expected since the torque of the stepper motor is rather large. The spin position in steps with respect to a reference is kept track of in the controller supplied with the stepper motor. The reference can be read by human eye from a precision scale mounted on front of the housing of the sample holder.

The three rotational axes of the sample manipulator are positioned such that the θ_{P}-axis is perpendicular to the XY-plane of the manipulator, the θ_{T}-axis is perpendicular to the θ_{P}-axis and the θ_{S}-axis perpendicular to the θ_{T}-axis. Both the θ_{P}-axis and the θ_{S}-axis are designed to go through the center of the sample surface. The θ_{S}-axis is designed to be perpendicular to the sample surface. If the thickness of the sample is larger or smaller than required or when the back and front surface of the sample are not parallel this will no longer hold and when moving the manipulator it should be corrected for. When the XY-plane of the manipulator is not parallel with the XY-plane of the experiment (the plane of the detector), which is the case by approximately 2° in our experiment, it should also be corrected for when positioning the sample. The θ_{T}-axis is designed to ly behind the sample surface. The sample surface will thus move out of the center of the experiment when tilting the sample and this means a coupling of the tilt of the sample to the XYZ-co-ordinates of the manipulator. A linear translation drives the θ_{T}-rotation and a relation is derived between the translation and the angle θ_{T}. This is easily done with the dimensions of the different parts employed in the tilt movement.

The cover to which the detectors are attached is moved by a large torque DC-motor and its position is read via a Sony PL-20 magnetic ruler and readout unit. The resolution is far better than the error of 0.1° in finding the maximum intensity of the direct He-atom beam, which is a reference for the alignment.

Calibrations of the different degrees of freedom has been carried out by moving the manipulator positions over a certain distance or angle and reading the number of increments of the encoders or the steps of the stepper motor. These calibrations are set in the computer program controlling the manipulator and also the zero position can be set. In this way the sample manipulator is easily positioned. Finding the zero positions is done with the aid of a HeNe-laser directed through the molecular beam and (specularly) reflecting from the surface and with the aid of specular helium atom reflectivity. It is estimated that the zero position can be found in this way with about 0.2° and 0.5 mm accuracy for the different degrees of freedom. The fact that the XY-plane of manipulator and of the detector and the XY-plane of the back and of the front plane of the sample are not parallel can also be traced using these reflections.

2.5 Moving the manipulator and detector

The angles describing the particles incident on and the particles scattered from the surface ($\theta_{\rm i}$, $\phi_{\rm i}$, $\theta_{\rm f}$ and $\phi_{\rm f}$) are not the same as the angles describing the position of the sample and detector ($\theta_{\rm P}$, $\theta_{\rm T}$, $\theta_{\rm S}$ and $\theta_{\rm D}$). To be able to position the sample and detector for a specified scattering geometry, a relation between both sets of angles must be derived. Before we can do so, both sets of angles have to be defined.

Both the incident and exit vector of the incident and scattered particle, respectively, are described by two angles. The incident vector is defined as pointing in the direction of the nozzle, so opposite to the direction of the moving particles. The exit vector is defined as pointing in the direction to where the particles are scattered, so in the direction of the detector. The angle between a vector and the surface normal is referred to as θ, and the angle between the projection of a vector on the surface and some reference direction on the surface is referred to as ϕ. Figure 2.4 shows a drawing of these vectors and angles. The reference on the surface for the incident particles is a high symmetry direction, indicated by the vector $\vec{p}$ in figure 2.4. For the scattered particles the reference is the plane of incidence, defined through the surface normal $\vec{n}$ and the incident vector $\vec{\imath}$. The vector $\vec{q}$ is defined such that the vector set ($\vec{n}$,$\vec{p}$,$\vec{q}$) makes up a right handed basis set that is connected to the sample surface. $\theta_{\rm i}$ and $\phi_{\rm i}$ are the angles for the incident particles and $\theta_{\rm f}$ and $\phi_{\rm f}$ for the scattered particles. With these angles the incident vector $\vec{\imath}$ and exit vector $\vec{u}$ can be described in coordinates refering to the basis set ($\vec{n}$,$\vec{p}$,$\vec{q}$):

$$\vec{\imath} = \begin{pmatrix} \cos\theta_{\rm i} \\ -\sin\theta_{\rm i}\cos\phi_{\rm i} \\ -\sin\theta_{\rm i}\sin\phi_{\rm i} \end{pmatrix}_{(\vec{n},\vec{p},\vec{q})} \quad \text{and} \quad \vec{u} = \begin{pmatrix} \cos\theta_{\rm f} \\ \sin\theta_{\rm f}\cos(\phi_{\rm f}+\phi_{\rm i}) \\ \sin\theta_{\rm f}\sin(\phi_{\rm f}+\phi_{\rm i}) \end{pmatrix}_{(\vec{n},\vec{p},\vec{q})} . \tag{2.1}$$

The four angles are defined to be in the ranges

$$0 \le \theta_{\rm i}, \theta_{\rm f} < 90^\circ \quad \text{and} \quad -180^\circ < \phi_{\rm i}, \phi_{\rm f} \le 180^\circ . \tag{2.2}$$

Particles that have trapped at the surface and desorb again in a scattering experiment are described by characteristics (energy, temperature and intensity) that are only dependent on $\theta_{\rm f}$ and not on $\phi_{\rm f}$. Defining those two angles in another way leads to less obvious description of these characteristics in terms of scattering angles.

The position of the sample is described with three angles: the polar rotation angle $\theta_{\rm P}$, the tilt rotation angle $\theta_{\rm T}$ and the spin rotation angle $\theta_{\rm S}$. Together with the rotation angle $\theta_{\rm D}$ of the detector this gives another four angles describing the position of the sample and the detector. Both the angles $\theta_{\rm P}$ and $\theta_{\rm D}$ are described with respect to a coordinate system connected to our scattering apparatus as is also depicted in figure 2.4. The basis set ($\vec{x}_0$,$\vec{y}_0$,$\vec{z}_0$) is choosen in such a way that the vector $\vec{x}_0$ points in the direction of the nozzle source and is thus identical to the incident vector $\vec{\imath}$. Both the vector $\vec{x}_0$ and $\vec{y}_0$ are in the detection plane, so the plane in which our detector rotates, and $\vec{y}_0$ points in such a direction that $\theta_{\rm D}$ is positive for attainable detector positions. The vector $\vec{z}_0$ is choosen to make again a right handed basis set ($\vec{x}_0$,$\vec{y}_0$,$\vec{z}_0$) and is pointing down for our setup. Incident and exit

vector of incident and scattered particles, respectively, are in this basis set described as

$$\vec{\imath} = \begin{pmatrix} 1 \\ 0 \\ 0 \end{pmatrix}_{(\vec{x}_0,\vec{y}_0,\vec{z}_0)} \quad \text{and} \quad \vec{u} = \begin{pmatrix} \cos\theta_{\mathrm{D}} \\ \sin\theta_{\mathrm{D}} \\ 0 \end{pmatrix}_{(\vec{x}_0,\vec{y}_0,\vec{z}_0)} , \tag{2.3}$$

with the detector angle θ_{D} measured with respect to the vector $\vec{x}_0$. In a scattering experiment will in general hold

$$0 \leq \theta_{\mathrm{D}} \leq 180^\circ \ , \tag{2.4}$$

but in practice the interval will be smaller as the detector cannot reach all positions. For our experimental setup holds $58^\circ \leq \theta_{\mathrm{D}} \leq 180^\circ$. In the case of $\theta_{\mathrm{D}} = 180^\circ$ to hold both $\theta_{\mathrm{i}} = 90^\circ$ and $\theta_{\mathrm{f}} = 90^\circ$, which will also not be the case in a scattering experiment.

The polar rotation angle θ_{P} is the rotation of the manipulator around the vector $\vec{z}_{m0}$, of a basis set $(\vec{x}_{m0},\vec{y}_{m0},\vec{z}_{m0})$ connected to the sample manipulator. With this rotation we define the transformation $\mathcal{R}_{\vec{z}_{m0}}(\theta_{\mathrm{P}})$ to another basis set $(\vec{x}_{m1},\vec{y}_{m1},\vec{z}_{m1})$, with $\vec{z}_{m0}$ of course identical to $\vec{z}_{m1}$. These rotations are shown in figure 2.5. The tilt axis of the manipulator is through the vector $\vec{y}_{m1}$ after the transformation $\mathcal{R}_{\vec{z}_{m0}}(\theta_{\mathrm{P}})$. Performing a tilt rotation of the sample defines another rotation transformation $\mathcal{R}_{\vec{y}_{m1}}(\theta_{\mathrm{T}})$ to the basis set $(\vec{x}_{m2},\vec{y}_{m2},\vec{z}_{m2})$, with $\vec{y}_{m1}$ identical to $\vec{y}_{m2}$. A spin rotation leads to the rotation transformation $\mathcal{R}_{\vec{x}_{m2}}(\theta_{\mathrm{S}})$ to the basis set $(\vec{x}_{m3},\vec{y}_{m3},\vec{z}_{m3})$. If the sample is mounted in the manipulator in such a way that the surface normal $\vec{n}$ coincides with the spin rotation axis, thus if $\vec{n} = \vec{x}_{m3} = \vec{x}_{m2}$ and the set $(\vec{x}_{m0},\vec{y}_{m0},\vec{z}_{m0})$ connected to the manipulator coincides with the set $(\vec{x}_0,\vec{y}_0,\vec{z}_0)$ connected to the scattering chamber, then we have defined the transformation

$$\mathcal{R} = \mathcal{R}_{\vec{x}_{m2}(=\vec{n})}(\theta_{\mathrm{S}})\ \mathcal{R}_{\vec{y}_{m1}}(\theta_{\mathrm{T}})\ \mathcal{R}_{\vec{z}_{m0}(=\vec{z}_0)}(\theta_{\mathrm{P}}) \tag{2.5}$$

from the basis set $(\vec{x}_0,\vec{y}_0,\vec{z}_0)$ to the basis set $(\vec{n},\vec{p},\vec{q}\,)$ with these three rotations. The rotation transformations can be expressed in the well known rotation matrices:

$$\mathcal{R}_{\vec{z}_{m0}}(\theta_{\mathrm{P}}) = \begin{pmatrix} \cos\theta_{\mathrm{P}} & \sin\theta_{\mathrm{P}} & 0 \\ -\sin\theta_{\mathrm{P}} & \cos\theta_{\mathrm{P}} & 0 \\ 0 & 0 & 1 \end{pmatrix} \quad , \quad \mathcal{R}_{\vec{y}_{m1}}(\theta_{\mathrm{T}}) = \begin{pmatrix} \cos\theta_{\mathrm{T}} & 0 & -\sin\theta_{\mathrm{T}} \\ 0 & 1 & 0 \\ \sin\theta_{\mathrm{T}} & 0 & \cos\theta_{\mathrm{T}} \end{pmatrix}$$

$$\text{and} \quad \mathcal{R}_{\vec{x}_{m2}}(\theta_{\mathrm{S}}) = \begin{pmatrix} 1 & 0 & 0 \\ 0 & \cos\theta_{\mathrm{S}} & \sin\theta_{\mathrm{S}} \\ 0 & -\sin\theta_{\mathrm{S}} & \cos\theta_{\mathrm{S}} \end{pmatrix} . \tag{2.6}$$

With the aid of the transformation $\mathcal{R}$, the expression for the incident vector $\vec{\imath}$ and exit vector $\vec{u}$ in the basis set $(\vec{x}_0,\vec{y}_0,\vec{z}_0)$ can be transformed to the expression in the basis set $(\vec{n},\vec{p},\vec{q}\,)$. By doing so a relation is derived between the angles θ_{P}, θ_{T}, θ_{S} and θ_{D} on one hand and the angles θ_{i}, ϕ_{i}, θ_{f} and ϕ_{f} on the other. It turned out to be easier to work with the inverse transformation:

$$\mathcal{R}^{-1} \begin{pmatrix} \cos\theta_{\mathrm{i}} \\ -\sin\theta_{\mathrm{i}}\cos\phi_{\mathrm{i}} \\ -\sin\theta_{\mathrm{i}}\sin\phi_{\mathrm{i}} \end{pmatrix}_{(\vec{n},\vec{p},\vec{q}\,)} = \begin{pmatrix} 1 \\ 0 \\ 0 \end{pmatrix}_{(\vec{x}_0,\vec{y}_0,\vec{z}_0)} \tag{2.7}$$

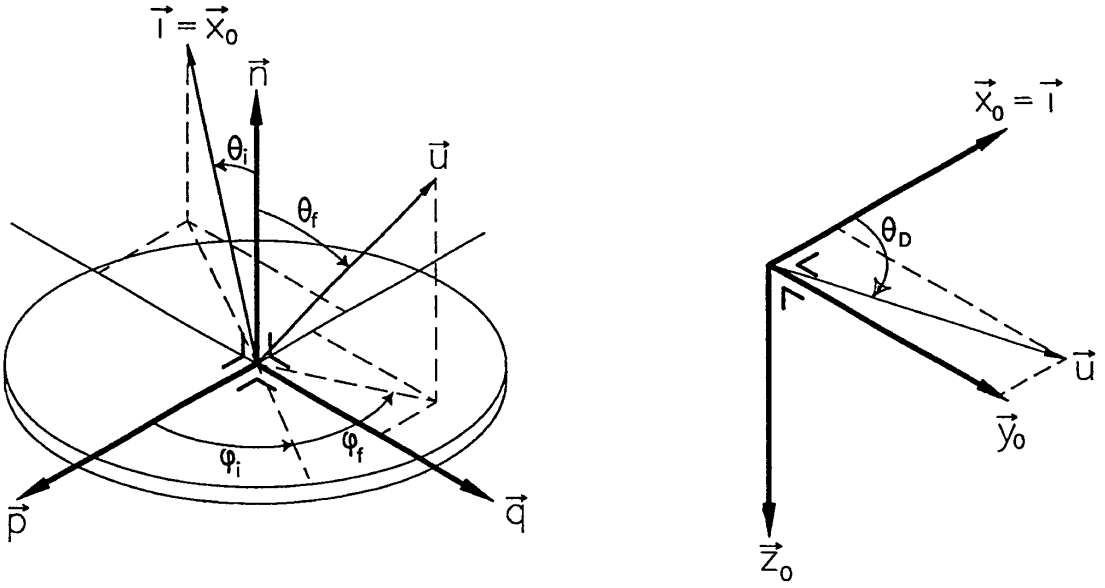

Figure 2.4 *Incident and exit vector describing the incident and scattered particles in terms of the angles θ_i, ϕ_i, θ_f and ϕ_f in the basis set $(\vec{n},\vec{p},\vec{q})$ and as function of θ_D in the basis set $(\vec{x}_0,\vec{y}_0,\vec{z}_0)$. The vector $\vec{p}$ is defined to be along a high symmetry line on the surface, $\vec{n}$ is the surface normal. The vector $\vec{x}_0$ points in the direction of the molecular beam and the vector $\vec{z}_0$ points downwards and is perpendicular to the detector plane.*

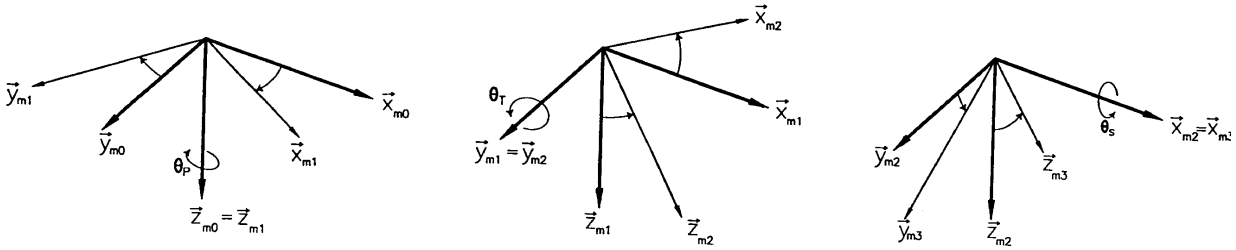

Figure 2.5 *Successive rotations of the sample manipulator.*

$$\mathcal{R}^{-1} \begin{pmatrix} \sin\theta_f \\ \sin\theta_f \cos(\phi_f + \phi_i) \\ \sin\theta_f \sin(\phi_f + \phi_i) \end{pmatrix}_{(\vec{n},\vec{p},\vec{q})} = \begin{pmatrix} \cos\theta_D \\ \sin\theta_D \\ 0 \end{pmatrix}_{(\vec{x}_0,\vec{y}_0,\vec{z}_0)} . \tag{2.8}$$

Since the transformation $\mathcal{R}$ is made up of multiple rotation transformations which are orthogonal, $\mathcal{R}$ is also orthogonal. The inverse matrix of the transformation is than easily found because it is equal to the transpose matrix $\mathcal{R}^{-1}=\mathcal{R}^{T}$. The easiest way to the solution is now to take the equations resulting from the 2nd and 3rd component of equation 2.7 and the 3rd component of equation 2.8 (right-hand sides = 0) and solving these together with the identity of the expression for the vector inproduct of $\vec{i}$ and $\vec{u}$ in both basis sets $(\vec{n},\vec{p},\vec{q})$ and $(\vec{x}_0,\vec{y}_0,\vec{z}_0)$

$$(\vec{i}\cdot\vec{u})_{(\vec{n},\vec{p},\vec{q})} \equiv (\vec{i}\cdot\vec{u})_{(\vec{x}_0,\vec{y}_0,\vec{z}_0)} . \tag{2.9}$$

The latter leads to the expression for the detector angle

$$\theta_D = \arccos(\cos\theta_f \cos\theta_i - \sin\theta_i \sin\theta_f \cos\phi_f) . \tag{2.10}$$

Under the constraint of detecting particles out of the plane of incidence with a constant angle between incident and scattered particles, so with a constant detector angle $\theta_{\rm D}$, both the angle $\theta_{\rm f}$ and $\phi_{\rm f}$ have to be varied. Their relation is given by

$$\theta_{\rm f} = 2\arctan\left(\frac{-\sin\theta_{\rm i}\cos\phi_{\rm f}+\sqrt{\sin^2\theta_{\rm i}\cos^2\phi_{\rm f}-\cos^2\theta_{\rm D}+\cos^2\theta_{\rm i}}}{\cos\theta_{\rm D}+\cos\theta_{\rm i}}\right) \tag{2.11}$$

$$\phi_{\rm f} = \pm\left[\pi-\arccos\left(\frac{\cos\theta_{\rm D}-\cos\theta_{\rm f}\cos\theta_{\rm i}}{\sin\theta_{\rm i}\sin\theta_{\rm f}}\right)\right] \quad . \tag{2.12}$$

In the analysis as described it is assumed that the surface normal $\vec{n}$ coincides with the vector $\vec{x}_{m3}$, but also that the polar rotation axis of the manipulator coincides with the vector $\vec{z}_0$ (perpendicular to the scattering plane). If both assumptions are not true another four rotations have to be introduced. The assumptions do not hold if the XY-plane of the experiment (detector) does not coincide with the XY-plane of the manipulator and if the front and the back plane of the sample are not parallel. First the vector coordinates expressed in the set ($\vec{x}_0$,$\vec{y}_0$,$\vec{z}_0$) have to be transformed to a basis set for which the vector $\vec{z}$ coincides with the polar rotation axis of the manipulator $\vec{z}_{m0}$, which can be done with two rotations α and β. Then the three manipulator rotation transformations can be performed followed by two rotations γ and δ to make the vector $\vec{x}_{m3}$ coincide with the surface normal. The transformation $\mathcal{R}$ is now written as

$$\mathcal{R} = \mathcal{R}_{\vec{z}_6}(\delta)\,\mathcal{R}_{\vec{y}_{m3}}(\gamma)\,\mathcal{R}_{\vec{x}_{m2}}(\theta_S)\,\mathcal{R}_{\vec{y}_{m1}}(\theta_T)\,\mathcal{R}_{\vec{z}_{m0}}(\theta_P)\,\mathcal{R}_{\vec{x}_1}(\beta)\,\mathcal{R}_{\vec{y}_0}(\alpha) \tag{2.13}$$

and it should be noted that the equations 2.7 and 2.8 are still valid for the last expression for $\mathcal{R}$.

Evaluating the 2$^{\rm nd}$ and 3$^{\rm rd}$ component of equation 2.7 and the 3$^{\rm rd}$ component of equation 2.8 (right-hand sides = 0) leads to the expressions

$$\cos\theta_{\rm T}\tan\theta_{\rm P}-\tan\theta_{\rm i}\sin\theta_{\rm T}\tan\theta_{\rm P}\sin(\theta_{\rm S}+\phi_{\rm i})-\tan\theta_{\rm i}\cos(\theta_{\rm S}+\phi_{\rm i}) = A(\alpha,\beta,\gamma,\delta,\theta_{\rm P},\theta_{\rm T},\theta_{\rm S},\theta_{\rm i},\phi_{\rm i},\theta_{\rm f},\phi_{\rm f}) \tag{2.14}$$

$$\tan\theta_{\rm i}\sin(\theta_{\rm S}+\phi_{\rm i})-\tan\theta_{\rm T} = B(\alpha,\beta,\gamma,\delta,\theta_{\rm P},\theta_{\rm T},\theta_{\rm S},\theta_{\rm i},\phi_{\rm i},\theta_{\rm f},\phi_{\rm f}) \tag{2.15}$$

$$\tan\theta_{\rm T}-\tan\theta_{\rm f}\sin\phi_{\rm f}\cos(\theta_{\rm S}+\phi_{\rm i})-\tan\theta_{\rm f}\cos\phi_{\rm f}\sin(\theta_{\rm S}+\phi_{\rm i}) = C(\alpha,\beta,\gamma,\delta,\theta_{\rm P},\theta_{\rm T},\theta_{\rm S},\theta_{\rm i},\phi_{\rm i},\theta_{\rm f},\phi_{\rm f}) \quad . \tag{2.16}$$

Solving these equations gives the solution for the sample manipulator angles

$$\theta_{\rm S} = -\phi_{\rm i}+\arctan\left(\frac{\tan\theta_{\rm f}\sin\phi_{\rm f}+B(\cdots)+C(\cdots)}{\tan\theta_{\rm i}-\tan\theta_{\rm f}\cos\phi_{\rm f}}\right) \tag{2.17}$$

$$\theta_{\rm T} = \arctan\left(\tan\theta_{\rm i}\sin(\theta_{\rm S}+\phi_{\rm i})-B(\cdots)\right) \tag{2.18}$$

$$\theta_{\rm P} = \arctan\left(\frac{\tan\theta_{\rm i}\cos(\theta_{\rm S}+\phi_{\rm i})+A(\cdots)}{\cos\theta_{\rm T}-\tan\theta_{\rm i}\sin\theta_{\rm T}\sin(\theta_{\rm S}+\phi_{\rm i})}\right) \quad . \tag{2.19}$$

Finding the solutions is straightforward, but all the mathematics involved is extremely tedious. We used a formula manipulation software package (Waterloo Maple Software, University of Waterloo) to solve the problem. In the case of $\phi_f = 0$, so measuring in the plane of incidence, and $A = B = C = 0$ ($\alpha = \beta = \gamma = \delta = 0°$) it is seen that the different equations reduce to $\theta_S = -\phi_i$, $\theta_T = 0$, $\theta_P = \theta_i$ and $\theta_D = \theta_i + \theta_f$.

In the case of the angles $\alpha = \beta = \gamma = \delta = 0°$ ($A = B = C = 0$) the equations 2.14, 2.15 and 2.16 are identical to the ones found by solving equation 2.7 and 2.8 with the transformation as defined by equation 2.5. However, the expressions 2.14, 2.15 and 2.16 are not exact as they could only be obtained under the assumptions $\sin\alpha \approx \alpha$, $\cos\alpha \approx 1$, $\sin\beta \approx \beta$, ... and $\cos\delta \approx 1$ (α, β, γ and δ expressed in radians). This assumption is only valid for small angles α, β, γ and δ as will be fulfilled in practice. The values of A, B and C will also be small under these circumstances.

Since A, B and C are also expressed in the angles, θ_P, θ_T and θ_S, to be calculated we use an iterative process to find the value for these sample manipulator angles for a given scattering geometry (θ_i, ϕ_i, θ_f and ϕ_f) and known angles α, β, γ and δ. We start by taking $A = B = C = 0$ and calculating θ_P, θ_T and θ_S. Then we can calculate A, B and C after which we can calculate a new value for θ_P, θ_T and θ_S. These last two steps are repeated until values for θ_P, θ_T and θ_S are found within a required accuracy. It should be pointed out that this iterative process only works for small values of A, B and C and thus small angles α, β, γ and δ.

Since the tilt rotation axis is behind the sample it will move the center of the sample surface out of the center of the UHV chamber when tilting the sample. Keeping the center of the sample surface in place when tilting implies a coupling to the XYZ-degrees of freedom of the manipulator. If the thickness of the sample is different than required it must also be corrected for by XYZ-movements. The couplings of the different rotations to XYZ are given by

$$X = (a+d)(1-\cos\theta_T)\cos\theta_P - d\cos\theta_P = [a-(a+d)\cos\theta_T]\cos\theta_P \quad (2.20)$$

$$Y = (a+d)(1-\cos\theta_T)\sin\theta_P - d\sin\theta_P = [a-(a+d)\cos\theta_T]\sin\theta_P \quad (2.21)$$

$$Z = (a+d)\sin\theta_T = (a+d)\sin\theta_T \ , \quad (2.22)$$

with a the distance between the tilt rotation axis and the sample surface reference plane and d the distance of the sample surface from this reference plane ($d > 0$ for a thicker sample than required).

2.6 Conclusions

We have given a description of sample manipulator with three translational and three rotational degrees of freedom. The X- and Y- movement is about ± 15 mm, the Z-movement about -10 mm and $+90$ mm, the polar rotation continuous and limited by the electrical wiring and ℓN_2 tubing outside the vacuum, the tilt rotation $-20°$ and $+90°$ and the spin rotation continuous and limited by electrical wiring and the cooling connection. At first

cooling is rather slow, but once cooled it takes in the order of minutes to cool down from flash heating. By a combination of the movement of the manipulator and the detector the experimental angles can be set and a relation between the manipulator position and these angles has been derived. The resolution of the different degrees of freedom is more than sufficient with respect to the larger error made in the alignment of the zero position.

Chapter 3

Probing the (Dual) Repulsive Wall in the Interaction of Oxygen, Nitrogen and Argon with the Ag(111) Surface

Abstract *We have performed molecular beam scattering experiments of O_2, N_2 and Ar from the Ag(111) surface in the translational energy regime from 0.2 eV to 2.6 eV and at a surface temperature of 600 K and 150 K. The experiments were carried out to probe the repulsive part in the particle-surface interaction potential. It is shown that the scattering dynamics of the systems N_2-Ag(111) and Ar-Ag(111) is characteristic of physisorption systems. The scattering data for the system O_2-Ag(111) shows that both the physisorption and chemisorption part of the interaction potential are probed in the experiment. For "normal incident energies" exceeding a threshold energy the barrier to the chemisorption part of the interaction potential can be crossed. An upper limit for this threshold is 0.3 eV. Although the chemisorption part is probed, the (dissociative and non-dissociative) chemisorption probability is still negligible.*

3.1 Introduction

The interaction dynamics of an atom or a molecule approaching a surface will be governed by the potential energy hypersurface in phase space on which the atom or molecule is moving and by the energy transfer from particle to sample surface or vice versa [112–114]. The energy transfer is not only governed by the lattice dynamics of the sample and the masses of both the impinging particles and atoms in the sample, but also by the potential energy hypersurface of the interaction. Knowledge of this interaction potential is thus of key importance in understanding gas-surface dynamics.

For the case of oxygen-silver the interaction potential is thought to be described by four different states as recently reviewed by Besenbacher and Nørskov [115]: a physisorption state, a molecular chemisorption state, an atomic chemisorption one and a subsurface state. The physisorption represents the weakest and the atomic chemisorption the strongest interaction. This information has mostly been derived from temperature programmed des-

orption measurements [48]. It shows the adsorption wells in the minimum energy path along a non-specified reaction coordinate, which will be a function of the phase space parameters, such as molecule-surface separation, internuclear distance, surface site and molecular orientation. Deviations from the minimum energy path will show larger barriers and less deep wells. Larger deviations might not even show barriers or wells but only a repulsive wall and, in general, not all parts of the interaction potential will be directly accessible to the impinging molecule. In the case of chemisorption, holes can be present in the repulsive wall [116,117]. When more states are present in the interaction potential the incident particle might scatter from different repulsive walls for different sets of incident parameters. In gas phase scattering this is equivalent to recrossing trajectories [118–121].

In this study we will focus on those particles that scatter from the surface. Analysing the characteristics (flux and energy distribution) will yield information on the interaction potential. The shape of the repulsive wall is probed by the direct-inelastically scattered molecules. For a repulsive wall far away from the surface atoms the surface will seem rather flat to the incident molecule, but for a repulsive wall close to the atoms, the surface will appear very corrugated. The scattering behaviour should reflect the shape of the repulsive wall.

In general, desorption of trapped molecules can also be observed in scattering experiments. It gives information on the incident parameters which will lead to trapping and on the desorption path followed by the desorbed molecules. In the case of O_2-Ag(111) part of the incident oxygen flux will trap at the surface and lead to a fast desorbing species. In the $T_s = 600$ K oxygen scattering experiments presented it is not resolved, but it is clearly present in the low surface temperature scattering. A study of the trapping-desorption of oxygen at the Ag(111) surface is the subject of another study [122,123, chapter 4].

Of the systems studied here sticking of molecules at the surface will occur only for O_2-Ag(111), but is negligable for the experimental conditions employed in this study. The probability for the sticking of oxygen on the Ag(111) surface is the topic of another study [124, chapter 5] giving complementary information on the interaction potential. It remains below 2×10^{-3} [68,124]. This low sticking probability is in contrast with results on the other silver surfaces, Ag(100) and Ag(110), showing larger sticking coefficients. For the Ag(110) surface a probability of approximately 0.5 can be reached by increasing the translational energy of the incident oxygen molecule [103]. These results show that the details of the interaction potential for oxygen-silver are quite different for the different surface planes.

This study has been undertaken to derive a more detailed understanding of the interaction potential for O_2-Ag(111) in addition to the scattering results already in the literature [65,67]. The angular and energy range have been extended and measurements out of the plane of incidence and at a cold surface were carried out. The scattered fluxes for all incident parameters will also be linked to each other. Loss or gain of scattered flux in specific directions with changing incident parameters can thus be traced. Invoking a dual repulsive wall, arising from the physisorption and chemisorption part of the interaction potential, explains the scattering results. A simplified one-dimensional view of such scattering events is shown in figure 3.1. In the discussion we will restrict ourselves to two states. For simplicity we will not make a distinction between the molecular and atomic chemisorption state. Scattering of N_2 and Ar from the same surface has been carried out and added for comparison.For these two particles only a physisorption interaction is known, indicating a

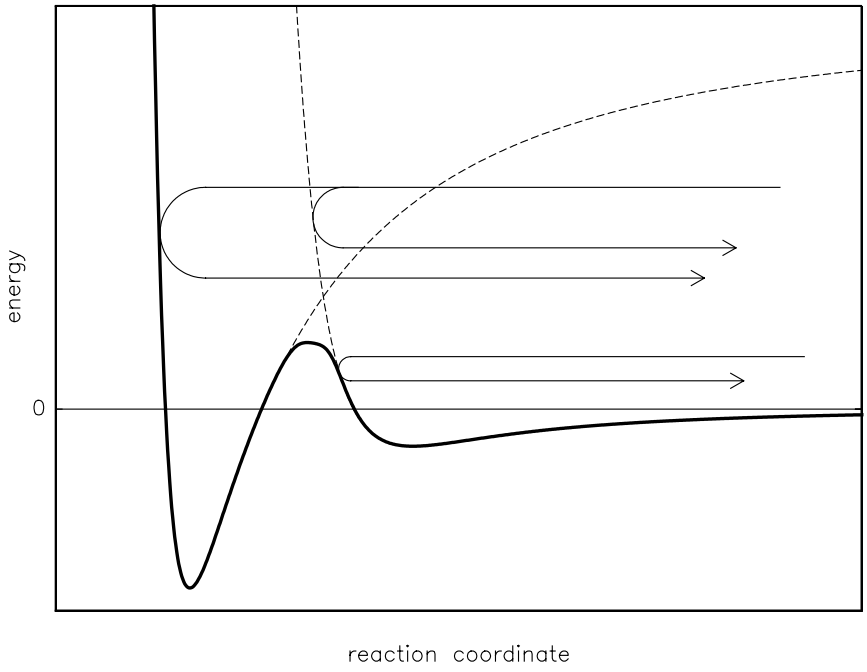

Figure 3.1 *Simplified potential energy diagram of a molecule-surface interaction potential along a non-specified reaction coordinate. Two potentials are shown, the one with the deep well representing chemisorption and the other one physisorption. The drawn trajectories show reflection from the repulsive walls connected to either state.*

rather shallow well and a repulsive wall relatively far out the surface. Nitrogen is, just as oxygen, a homonuclear molecule with comparable mass for which internal state excitation might also occur in the scattering event. Argon is the rare gas atom closest in mass to oxygen for which effects of rotation and vibration can be ruled out.

3.2 Experimental

The oxygen scattering experiments reported here have been carried out in a molecular beam apparatus which has been first described by Spruit et al. [56] and consists of a three stage differentially pumped molecular beam line connected to a UHV scattering chamber. The oxygen and argon scattering experiments at $T_s = 600$ K were carried out in the experimental setup as described in the reference above. Nitrogen and low T_s oxygen scattering were performed in a modified setup. We will give a full description of the modified setup, which is shown schematically in figure 1.2, here.

The UHV scattering chamber, pumped by a 500 $\ell\ s^{-1}$ turbomolecular pump (Balzers TPU510) which is backed by a 7.5 $\ell\ s^{-1}$ molecular drag pump (Alcatel MDP5010) and a titanium sublimation pump supplied with an (optionally) ℓN_2 cooled cold trap, has a diameter of 60 cm. A quadrupole mass spectrometer (QMS, Extranuclear) can be rotated in a horizontal plane around the sample, placed in the middle of the chamber. A 180 $\ell\ s^{-1}$ turbomolecular drag pump (Balzers TPU180H) differentially pumps this QMS, which is

placed in a box with a $\phi = 3$ mm diaphragm in the scattering chamber. Rotation of the QMS is allowed through rotation of the cover of the scattering chamber to which this detector is connected. UHV is maintained while rotating the cover by doubly differentially pumping the seal between the cover and the rest of the chamber. The seal consists of three spring loaded teflon rings, a first stage is pumped by a 15 $m^3\ h^{-1}$ ($=4.2\ \ell\ s^{-1}$) rotary pump (Alcatel Pascal 2015) and the second stage by a 18 $\ell\ s^{-1}$ molecular drag pump (Balzers TPD020). Both molecular drag pumps and the turbomolecular drag pump of the QMS drain to the rotary pump; the last through the first pumping ring of the cover seal.

The molecular beam is generated by the supersonic expansion of a gas from a 80 μm CW quartz nozzle, which can be heated to about 1100 K by passing a DC current through a $\phi = 0.2$ mm tungsten wire wrapped around the nozzle tip over a length of approximately 3 cm. To prevent the tungsten wire from burning in an oxygen environment, present during the generation of an oxygen beam, the wire was covered with a ceramic cement. For the first experiments a mixture of 2% oxygen in helium was used. Later, electronically controlled flow controllers (Bronkhorst Hi-Tec EL-flow) were added to the nozzle gas supply so the ratio of oxygen, nitrogen or argon and one or two carrier gasses could be changed on-line by changing the flow of the constituents through their separate flow controllers. Flows of about 1.2 $m\ell_n\ s^{-1}$ ($1\ m\ell_n\ s^{-1} = 60\ m\ell_n\ min^{-1} = 60$ sccm, the volume is taken at the standard conditions of 1 atmosphere and 0° C) are the maximum in our set-up, determined by the pumping speed in the nozzle chamber. Beam energies can be varied by changing the seeding ratio and/or changing the nozzle temperature. A translational energy of 1.8 eV for oxygen seeded in helium can be reached. Seeding in the lighter hydrogen did not lead to larger oxygen energies as the oxygen/hydrogen mixture reacted to form water at nozzle temperatures above 800 K. Seeding in hydrogen has been employed for the argon scattering experiments. The width (FWHM) of the energy distribution of the particles in the beam is approximately 10% for the lower energies, increasing to 20% for 1.0 eV oxygen and 30% for 1.7 eV oxygen.

After the supersonic expansion in the first stage of the beamline, which is pumped by a 3100 $\ell\ s^{-1}$ unbaffled diffusion pump (Balzers DIF250), the beam enters the second stage through a skimmer with a $\phi = 1$ mm opening. This skimmer was replaced later by a $\phi = 0.5$ mm one to reduce the pressure rise in the second stage due to effusion from the first stage. The second stage is pumped by a 1250 $\ell\ s^{-1}$ baffled (water cooled) diffusion pump (Balzers DIF200) and contained only the chopper motor for the chopper blade used for the time-of- flight (TOF) experiments. The beam then entered the third stage through a $\phi = 1$ mm skimmer shaped diaphragm, which limits the divergence of the beam to approximately 0.6°. This last stage, pumped by a 330 $\ell\ s^{-1}$ turbomolecular pump, contained the chopper blade. Chopper blade and motor were connected through a hole in the wall between the second and third chamber. A valve was placed between the last stage and the UHV scattering chamber to enable venting of the beam line without venting the whole system.

To further increase the differential pumping capacity of the beam line the chopper assembly was put completely in the second stage, so the open connection between the second and third stage of the beam line for the connection between chopper blade and motor in the old setup could be closed. For this new assembly a chopper blade was made with under 45° tapered slit edges, such that the influence of the finite chopper thickness can be neglected in the TOF analysis (see appendix). A beam flag, for switching the beam

on and off, was also added in this pumping stage and the valve between the third stage and the scattering chamber was placed between the second and third stage. The third stage now acts as a buffer stage and its turbomolecular pump drains to the same molecular drag pump as the turbomolecular pump of the scattering chamber. Pressures of 1×10^{-6} mbar and 1×10^{-8} mbar could be reached in the second and last stage, respectively, with no supersonic expansion present. With an expansion of 1.2 m$\ell_{\rm n}$ s^{-1} pure nitrogen the pressure rise is approximately 1×10^{-3} mbar, 1×10^{-5} mbar and 2×10^{-8} mbar in the respective stages. The pressure rise in the main chamber was about 3×10^{-10} mbar and in the differentially pumped QMS it could not be measured.

First the sample was mounted on a 2-axis goniometer allowing for manual control of the incident angle of the molecular beam on the sample. Sample heating was achieved by radiatively heating the molybdenum cup in which the sample was placed and the temperature was measured with a K-type thermocouple (chromel/alumel) placed between the cup and the sample. The 2-axis sample manipulator was later replaced by a 3-axis manipulator [125, chapter 2]. In combination with the rotatable QMS we can now change accurately, and under computer control, the incident angle measured with respect to the surface normal $\theta_{\rm i}$, the azimuthal angle measured with respect to a high symmetry direction on the surface $\phi_{\rm i}$, the outgoing angle with respect to the surface normal $\theta_{\rm f}$ and the outgoing angle measured with respect to the plane of incidence $\phi_{\rm f}$ (see figure 2.4). The sample can be cooled to about 120 K by liquid nitrogen and heated by radiation or electron bombardment from a tungsten filament behind the sample. A 0.5 mm diameter thermocoax K-type thermocouple, placed in a hole in the side of the sample, is used to measure the temperature, which is controlled by a commercial controller (Eurotherm 900 EPC series). When heating the sample by electron bombardment the filament is negatively and the sample about 25 V positively biased, in order to attract all the electrons towards the sample (thus not heating the surroundings) and not to damage the thermocouple input of the controller.

The system is equipped with Auger electron spectroscopy (AES, Riber cylindrical mirror analyser) and low energy electron diffraction (LEED, Omicron 4-grid rear view) for surface characterisation, a residual gas analyser (RGA, Balzers QMG420) for monitoring the background gas and an ion sputter gun (Riber CI-10) for cleaning the sample.

Experiments were performed on two different samples, cut by spark erosion from a 5N purity single crystal rod to within 0.1° of the (111) face and polished by standard polishing techniques. Once in vacuum the sample surfaces were prepared by sputtering and annealing. First sputtering for several hours at room temperature and then several cycles of sputtering for a few hours at 600 K and annealing for several minutes at 800 K. A silver surface anneals in the order of minutes at this temperature [126]. Subsequently, we sputtered the sample at 750 K. Annealing then took place during sputtering. For sputtering 500 eV Ar^+ ions were used with a target current of about 0.3 μA. This rather low value is due to a large distance between the sputter gun and our sample.

Sputtering and annealing were pursued until the angular flux distribution of scattered He was identical to the angular distribution of a scan of the rotatable QMS through the direct He beam, having a FWHM of approximately 2°. Width and shape of this distribution are a result of a convolution of the cross-section of the beam over the detector opening. After this procedure a sharp LEED pattern was observed, especially at lower surface temperatures.

For the experiments reported we recorded the time-of-flight (TOF, or time-of-arrival)

distributions of the particles under study at our rotatable differentially pumped mass spectrometer (QMS) by a home built multichannel scaler in 2 μs bins. By analysing these distributions we can deduce the energy distribution of the particles detected and give a measure of their flux. First the TOF distributions were recorded for particles entering the QMS with an undisturbed flight path, so without scattering from the surface. In this way the characteristics of a particle beam under certain nozzle conditions (temperature and flows) are derived. After characterisation of the direct beam the sample is placed in the beam path and the TOF distributions of scattered particles are recorded. For further details on the TOF measurements and their analysis we refer to the appendix of this chapter. Identical TOF results were obtained with the modified and previous setup.

The scattering results will be discussed in terms of a measure for the scattered flux corrected for the incident flux, the mean energy per particle $<E>$ and E_α or T_α, both a measure for the width of the energy distribution of the detected particles. The scattered flux intensities cannot only be compared when changing the scattering angle θ_f, but also when changing the surface temperature or when changing the incident energy as long as the ionisation and detection efficiency of the QMS are not changed. For a choosen set of experimental parameters the scattered flux intensity will be normalised.

3.3 Results

The scattering results obtained for O_2, N_2 and Ar will be described separately in the above order. Most experiments were carried out at a surface temperature of $T_s = 600$ K, the desorption temperature of dissociated oxygen on the surface, so the surface remained clean during the oxygen scattering experiment and are done on particles scattered in the plane through the incident beam and the surface normal (plane of incidence, $\phi_f = 0°$). Some measurements are done for oxygen scattering away from this plane at a low surface temperature. Adsorption of N_2 and Ar will also not occur at $T_s = 600$ K. Both the angle of incidence and the incident energy were varied. For one angle of incidence and one incident energy of Ar the surface temperature also has been varied. Our results compare very well with scattering results obtained previously at the same conditions [65,67].

3.3.1 Oxygen scattering

Let us first focus on the results obtained for oxygen scattering as displayed in figures 3.2, 3.3 and 3.4. For the four different angles of incidence the angular resolved ratio of the mean final translational energy $<E_f>$ over the mean incident energy $<E_i>$ and the flux of the scattered particles are shown in the lower and upper panels, respectively. In the rest of the text we will denote the mean energy per particle as E and not as $<E>$. The scattered flux is normalised to the maximum in the angular flux distribution of $E_i = 0.46$ eV for $\theta_i = 40°$. All the measured flux for oxygen scattering relates to this normalisation. The lines through the data points are just a guide to the eye and the thick line in the panels showing the angular resolved translational energy distributions E_f/E_i holds for a situation in which the

parallel momentum of scattered particles is conserved:

$$mv_{\rm f}\,\sin\theta_{\rm f} = mv_{\rm i}\,\sin\theta_{\rm i} \iff \frac{\frac{1}{2}mv_{\rm f}^2}{\frac{1}{2}mv_{\rm i}^2} = \frac{E_{\rm f}}{E_{\rm i}} = \frac{\sin^2\theta_{\rm i}}{\sin^2\theta_{\rm f}}\,. \tag{3.1}$$

Looking at the results for $\theta_{\rm i} = 70°$ (figure 3.3) one sees that the energy ratio curves for the different incident energies are rather close together and close to parallel momentum conservation for most of the scattered flux. Only for a small fraction of the scattered flux the energy loss does increase for scattering angles towards the surface normal. Increasing the incident energy results in a larger fractional energy loss in this region. A steady increase in the maximum of the scattered flux distributions and a decrease in the width of the distributions (FWHM) is also observed when increasing the incident energy. These results are also displayed in figure 3.4; the upper panels show the width and the lower panels the peak intensity in the flux distributions of figure 3.2 and 3.3. In the left panels the results are shown as function of incident energy and in the right panels as function of "normal incident energy" ($E_{\rm i}\cos^2\theta_{\rm i}$). The full lines through the data points are again a guide to the eye only; the dashed and dashed-dotted lines are results for nitrogen and argon scattering, respectively, and will be discussed later.

Going to the $\theta_{\rm i}=60°$ results (figure 3.3) we observe larger deviations from parallel momentum conservation for smaller angles $\theta_{\rm f}$ and more of the flux deviates from this line. Although the width of the flux distributions monotonically decreases with increasing incident energy, the peak intensity of the flux distributions as a function of incident energy shows a maximum (figure 3.4). For $E_{\rm i} = 1.04$ eV and 1.33 eV the flux distributions can hardly be distinguished around their peak maximum. At the larger angles $\theta_{\rm f}$ the distribution of $E_{\rm i}=1.33$ eV is below the one for 1.04 eV, but at angles $\theta_{\rm f}<50°$ this is reversed. This effect is even stronger for $E_{\rm i} = 1.62$ eV, which also shows a lower peak intensity as compared to $E_{\rm i}=1.04$ eV. So a broadening of the flux distributions towards the surface normal with increasing incident energy occurs at the expense of flux in the rest of the distribution. Because the broadening starts in the foot of the flux distributions it does not (yet) show in the FWHM as function of incident energy, but is observed in the peak intensities of the flux distributions. For this reason we monitored the peak intensities, to have a quantity that is a sensitive measure of changes occuring in the shape of the flux distributions.

The results for $\theta_{\rm i}=50°$ (figure 3.2) show the same behaviour, starting at a lower incident energy. A slight broadening of the flux distributions towards the surface normal is already observed for $E_{\rm i}=0.75$ eV where the maximum in the peak intensity of the flux distribution as function of incident energy also occurs. A similar result is seen for $\theta_{\rm i} = 40°$, but a somewhat larger broadening towards the surface normal leads to a decrease in the peak flux. Again it is seen that the peak flux is sensitive to the broadening towards the surface normal. This broadening appears already below the incident energy for which the maximum in the peak flux is observed.

For $\theta_{\rm i}=50°$ and $40°$ the broadening also shows in the plot of the FWHM against incident energy (figure 3.4), but the onset of the increase in the FWHM is at a higher incident energy than the value for which a decrease in peak flux and an onset in broadening towards the surface normal in the foot of the flux distributions is seen. A decrease in FWHM and increase in peak intensity with increasing incident energy can be rationalised by a decrease of the influence of the velocities of the surface atoms due to the higher incident velocities of

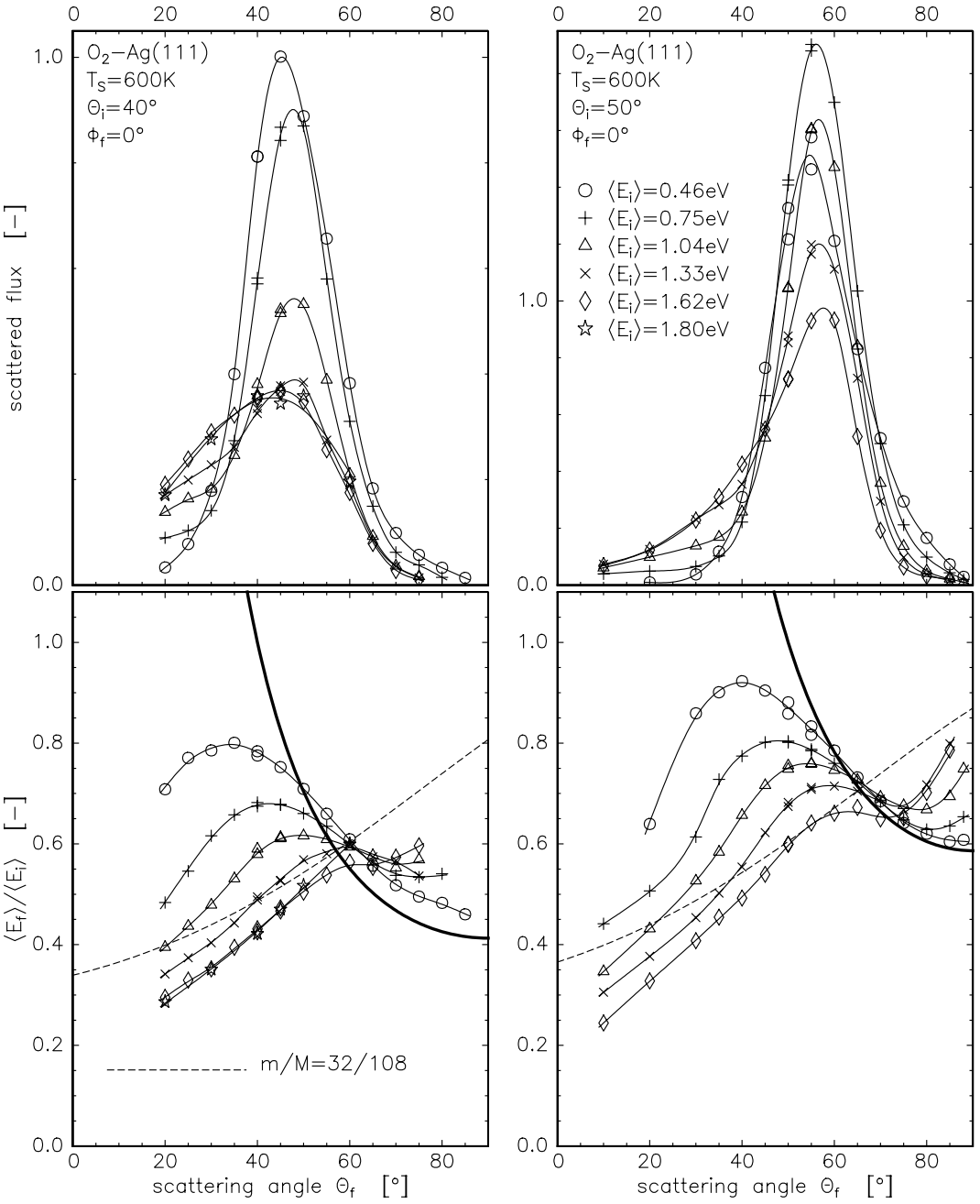

Figure 3.2 *Angularly resolved energy and flux distributions of O_2 molecules scattered from a Ag(111) surface for $\theta_i = 40°$ and 50°. Lines through the data points are to guide the eye only. The thick lines in the lower panels hold for parallel momentum conservation and the dashed line for hard sphere scattering.*

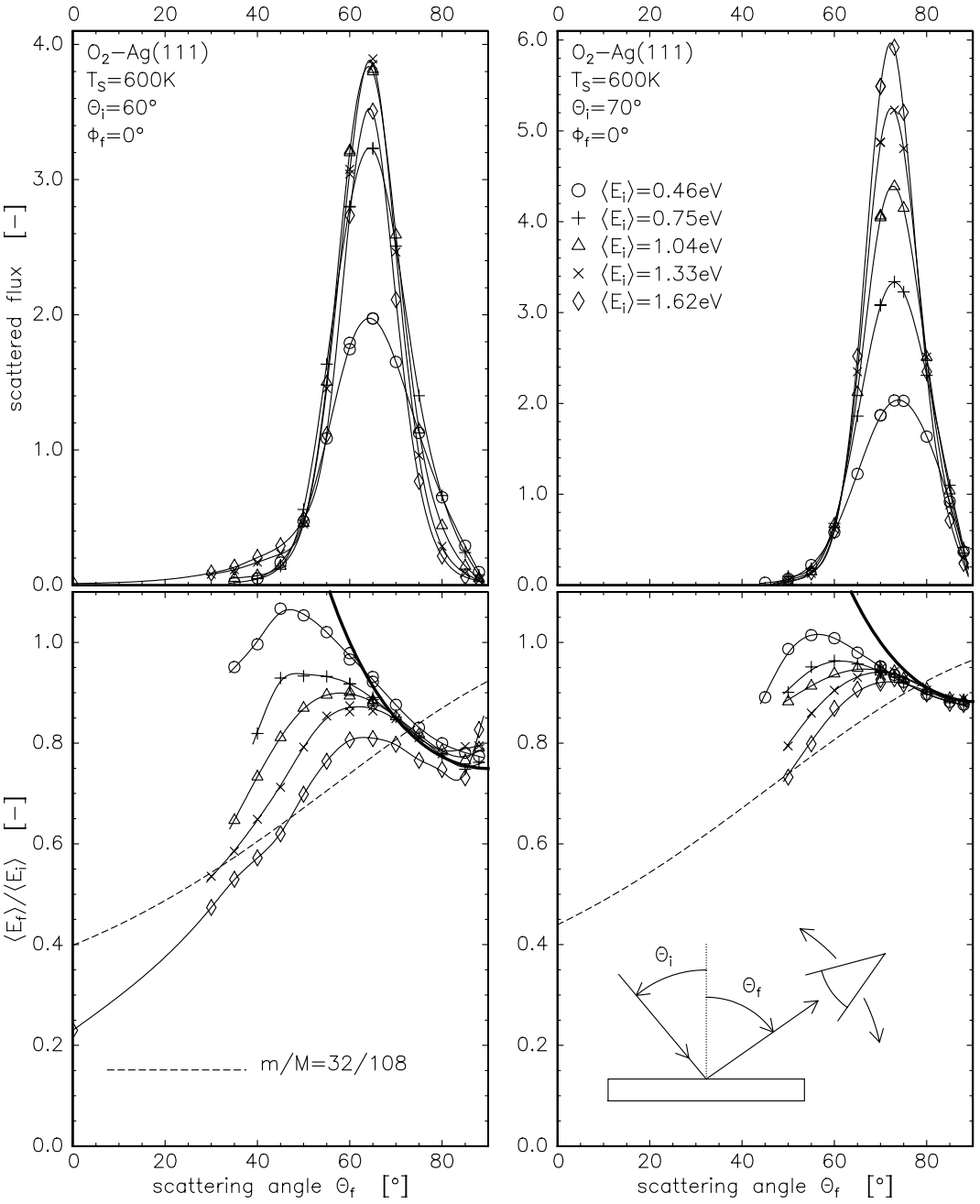

Figure 3.3 *Angularly resolved energy and flux distributions of O_2 molecules scattered from a Ag(111) surface for $\theta_i = 60°$ and 70°. Lines through the data points are to guide the eye only. The thick lines in the lower panels hold for parallel momentum conservation and the dashed line for hard sphere scattering.*

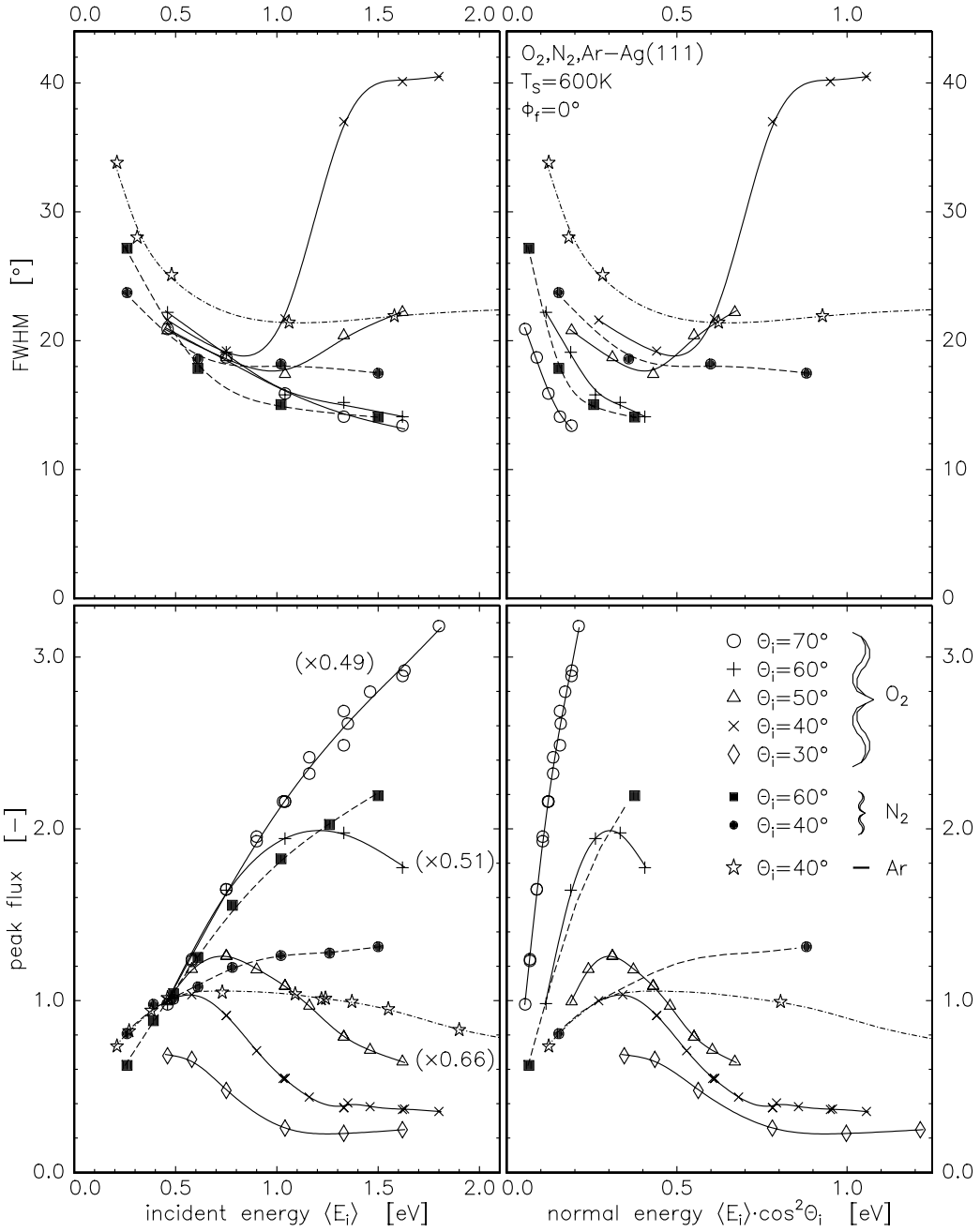

Figure 3.4 *The peak intensity in the scattered flux distributions of O_2 and N_2 from Ag(111) and the full width at half maximum (FWHM) of these flux distributions as a function of incident energy and normal incident energy. Full lines are to guide the eye for the O_2 results, the dashed ones for the N_2 results and the dashed-dotted ones for the Ar results. The peak flux curves for O_2 for $\theta_i = 50°$, 60° and 70° are scaled by the indicated factors. The peak flux curves for N_2 and Ar are scaled to yield an interpolated value 1.0 for $E_i = 0.46$ eV. Only 2 data points are shown for each incident angle for N_2 and Ar in the lower right panel. The highest energy points for Ar scattering fall outside the energy axes.*

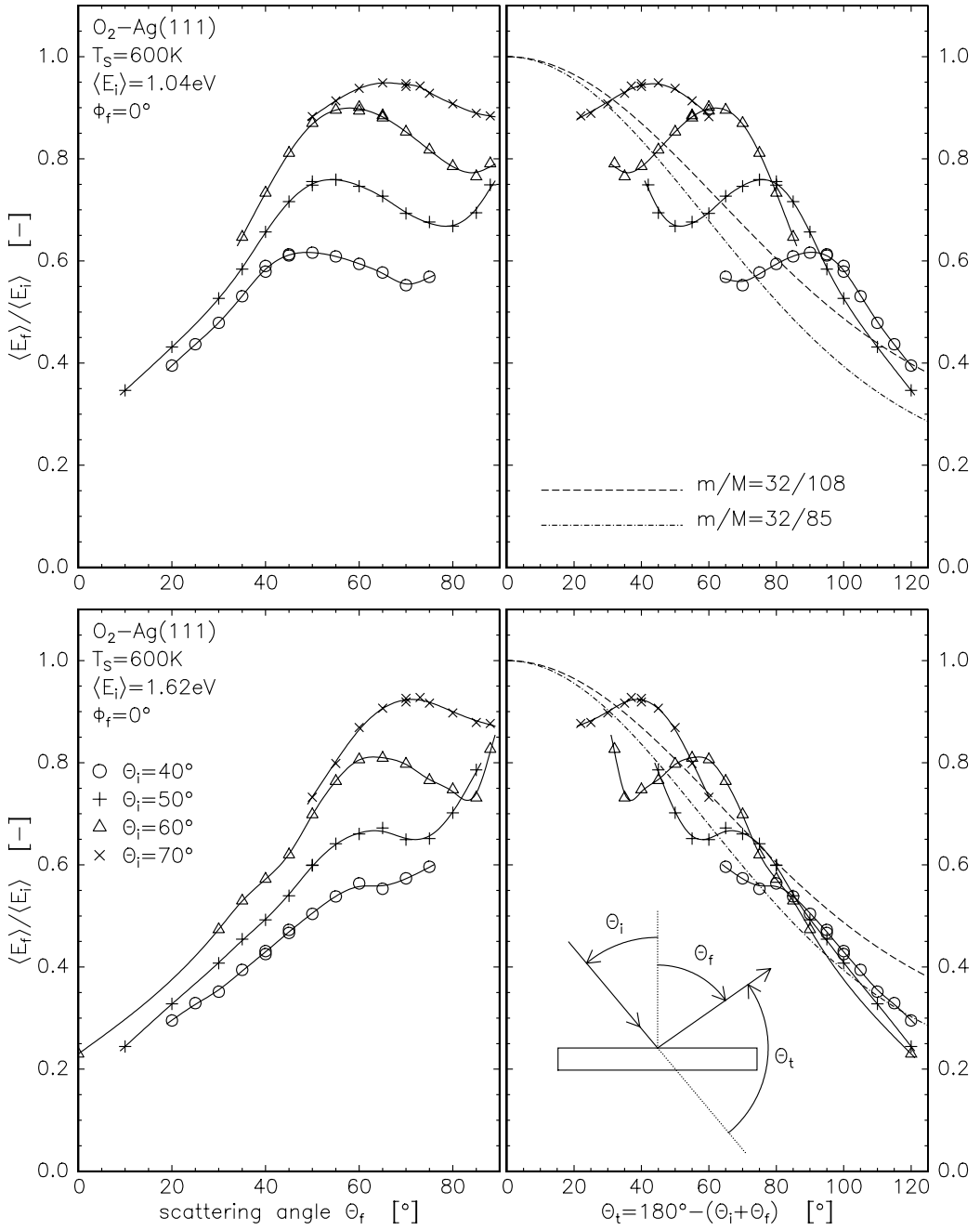

Figure 3.5 *Angularly resolved energy ratios for $E_i = 1.04$ eV and 1.62 eV incident O_2 and various angles of incidence as a function of scattering angle measured with respect to the surface normal in the left panels and as function of total scattering angle in the right panels. Full lines through the data points are to guide the eye only, the dashed and dashed-dotted ones a result of the hard sphere scattering formula.*

the impinging molecules; a decrease of thermal broadening with increasing incident energy [127]. An increase in the width with increasing incident energy is explained by an increase in surface corrugation (structure scattering). It is observed that the increase in the width saturates for $\theta_i = 40°$.

The peak flux for $\theta_i = 40°$ and 30° and the FWHM for $\theta_i = 40°$ show a levelling off at the higher incident energies, although the saturation point for the FWHM is larger than the one for the peak flux. The $\theta_i = 50°$ peak flux curve seems also to level off at the highest incident energies.

Looking at the peak flux as a function of normal incident energy in the right panels in figure 3.4, one sees that the maxima in the peak flux curves appear at approximately equal normal incident energy of 0.3 eV. Remembering that the broadening towards the surface normal appears just before the maximum in the peak flux is reached, 0.3 eV normal energy is an upper limit for marking the onset in broadening of the flux distributions. At a value of 0.7 eV for the normal energy the peak flux curves level off.

For $\theta_i = 40°$ and 50° deviations from parallel momentum conservation become still larger with increasing incident energy. It is seen in figure 3.2 that the energy ratio curves not only deviate downwards from the parallel momentum conservation line for angles θ_f towards the surface normal, but also start moving upwards from this line for angles θ_f above specular. For these angles and the higher incident energies hardly any flux scatters according to parallel momentum conservation, contrary to the results for $\theta_i = 70°$. So a completely different scattering mechanism seems to be at work here.

Figure 3.5 shows the energy ratio curves again for $E_i = 1.04$ eV and 1.62 eV in the top and lower panels, respectively. Results for all four angles of incidence are shown as a function of scattering angle θ_f in the left panels and as function of total scattering angle $\theta_t = 180° - (\theta_i + \theta_f)$ in the right panels. For $E_i = 1.62$ eV the energy ratio curves start to overlap. A decrease in translational energy after scattering with increasing total scattering angle θ_t is in accord with a binary collision model. When no energy is allowed to go into the internal degrees of freedom (rotation and/or vibration) the energy ratio E_f/E_i can be written as

$$\frac{E_f}{E_i} = \left[\frac{\sqrt{1 - \left(\frac{m}{M}\right)^2 \sin^2\theta_t} + \frac{m}{M}\cos\theta_t}{1 + \frac{m}{M}} \right]^2 , \qquad (3.2)$$

which can be derived from energy and momentum conservation for a two body collision. A limiting and visually appealing case of a two body collision is the scattering of two hard spheres and we will refer to equation 3.2 as the "hard sphere scattering formula". The right panels of figure 3.5 also show the results of applying this formula for two different mass ratios. One which holds for the mass ratio $m/M = 32/108$ (also shown in figures 3.2 and 3.3), appropriate for an oxygen molecule and a silver atom, and the other which describes the result for the larger total scattering angles at 1.62 eV incident energy rather well. In the latter case a smaller value for the mass of the silver atom is taken, $m/M = 32/85$.

It is clear that the energy ratios for $E_i = 1.62$ eV follow the hard sphere scattering behaviour quite well. For scattering angles θ_f around specular a variation around the hard sphere scattering line is seen. For the larger scattering angles θ_f, so for the smaller total scattering angles θ_t, the energy ratio curves again approach the hard sphere scattering

line. The energy ratios converging to a line below the hard sphere scattering line for $m/M = 32/108$ suggests internal degrees of freedom of the oxygen molecule to be excited in the scattering process or a larger energy transfer to the surface due to an accelleration of the molecule over a well of a molecular state present in the molecule-surface interaction. However, if this well is connected to the molecular chemisorption state it is rather deep (approximately 0.5 eV) and a large sticking into this state is expected. But a large molecular or dissociative sticking is not observed [124, chapter 5]. Later we will show a fast trapping-desorption from a transient oxygen state, but this will hardly affect the energy ratio curves observed here. The physisorption well is present for low incident energies and its influence will only decrease for increasing incident energies. If no internal excitation or extra energy loss due to accelleration over a well occurs the hard sphere scattering line should represent a lower limit in this energy range. Since a silver atom "connected" to other silver atoms at the surface is expected to have a larger effective mass, less energy transfer should occur. For incident energies exceeding a few eV the energy ratio is expected to decrease due to energy transfer to more than one surface atom [128].

Both the $E_i = 1.04$ eV and the 1.62 eV results seem to converge to a hard sphere scattering line, but the modulation around this behaviour is larger in the $E_i = 1.04$ eV case. It seems that the results are made up of a part scattered from a very corrugated surface ("hard sphere scattering"), with a broad angular intensity distribution, and a part scattered from a smooth surface ("parallel momentum conservation"), with an angular intensity distribution peaked around the specular. The combination of the two scattering regimes is responsible for the modulation around the hard sphere scattering line. With increasing incident energy more of the incoming flux will "see" the very corrugated surface and the modulation becomes smaller.

Low surface temperature and out-of-plane oxygen scattering

Lowering the surface temperature to $T_s = 150$ K and studying the time-of-flight spectra taken in the plane of incidence ($\phi_f = 0°$) for $\theta_i = 40°$ and $\theta_f = 20°$, as is shown in figure 3.6, one sees that two contributions can be distinguished. Here it will only be noted that the fast contribution is direct-inelastic scattering and the slower one is a fast trapping-desorption contribution sharply peaked around the surface normal. For scattering angles θ_f larger than 30° this contribution is negligable with respect to the direct-inelastic scattered intensity. For the $T_s = 600$ K results presented it will be neglected and those will only be discussed in terms of direct-inelastic scattering. The conclusions are not affected by this trapping-desorption contribution. Elsewhere a more detailed study on this contribution will be reported [122,123, chapter 4].

The upper left panel of figure 3.7 shows the results for in-plane scattering for both surface temperatures $T_s = 150$ K and 600 K, an incident energy of $E_i \approx 0.75$ eV and $\theta_i = 40°$. The lower surface temperature shows a smaller angular width of the scattered flux. It also shows a peak shift towards the surface for the higher surface temperature. Part of this shift is probably caused by a slight misalignment ($< 1°$) of the sample for the higher surface temperature. The measurement for this temperature was done with the 2-axis manipulator for which aligning was more difficult; the low temperature measurement was done on another sample mounted on the 3-axis manipulator. To relate the scattered

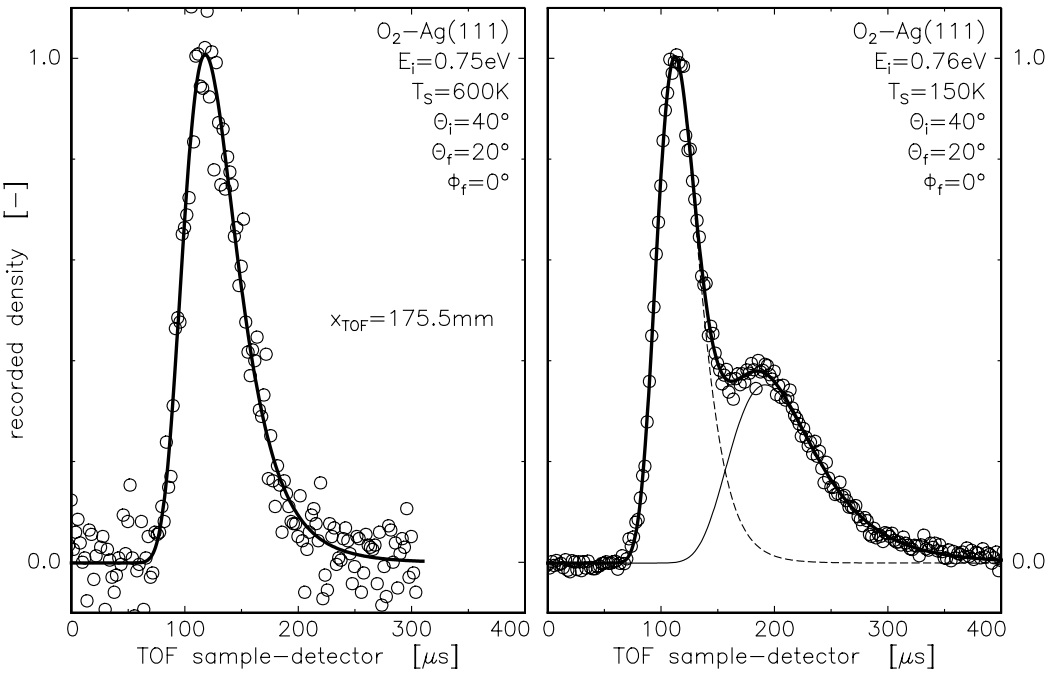

Figure 3.6 *Time-of-flight spectra for $E_i \approx 0.75$ eV incident O_2 scattered from a $T_s = 150$ K Ag(111) surface for $\theta_i = 40°$, $\theta_f = 20°$ and $\phi_f = 0°$. The time axes is the measured flight time corrected for the trigger delay, flight time through the detector and the flight time from the chopper to the sample according to the flow velocity of the incident molecules.*

intensities, the intensity distributions were measured for both surface temperatures using a 50% duty cycle chopper. This measurement showed a peak shift for $T_s = 600$ K of about 1.5° relative to the $T_s = 150$ K measurement, thus about half the shift shown in figure 3.7.

The energy ratio curves overlap for $\theta_f \leq 60°$, but for larger angles θ_f the $T_s = 150$ K results follows the hard sphere scattering scattering line for the mass ratio of an oxygen molecule and a silver atom ($m/M = 32/108$). Lowering the surface temperature thus allows probing a relatively larger fraction of the scattered molecules which probe a large surface corrugation for large angles θ_f, due to a decrease in the angular width of the molecules which probe the smoother surface. Observing a larger fraction of molecules probing the corrugated surface results in an energy ratio line closer to the hard sphere scattering line. It is seen that the intensity for these large scattering angles hardly, if at all, decreases with increasing surface temperature, whereas the intensity in the peak does decrease.

The other three panels of figure 3.7 show the results for measuring the TOF spectra out of the plane of incidence. We chose three scattering geometries so as to keep the angle between incident and scattered particles constant, meaning that both the angle ϕ_f and the angle θ_f had to be varied [125, chapter 2]. In our setup this means keeping the detector in a fixed position and thus a fixed detector angle θ_D. It also means a constant total scattering angle θ_t and the energy ratio curves should be flat in the case of hard sphere scattering.

The measurements for $\theta_D = 87.5°$, which is close to the maximum in the flux distribution measured in the plane of incidence, show a rapid decrease in intensity with increasing angle

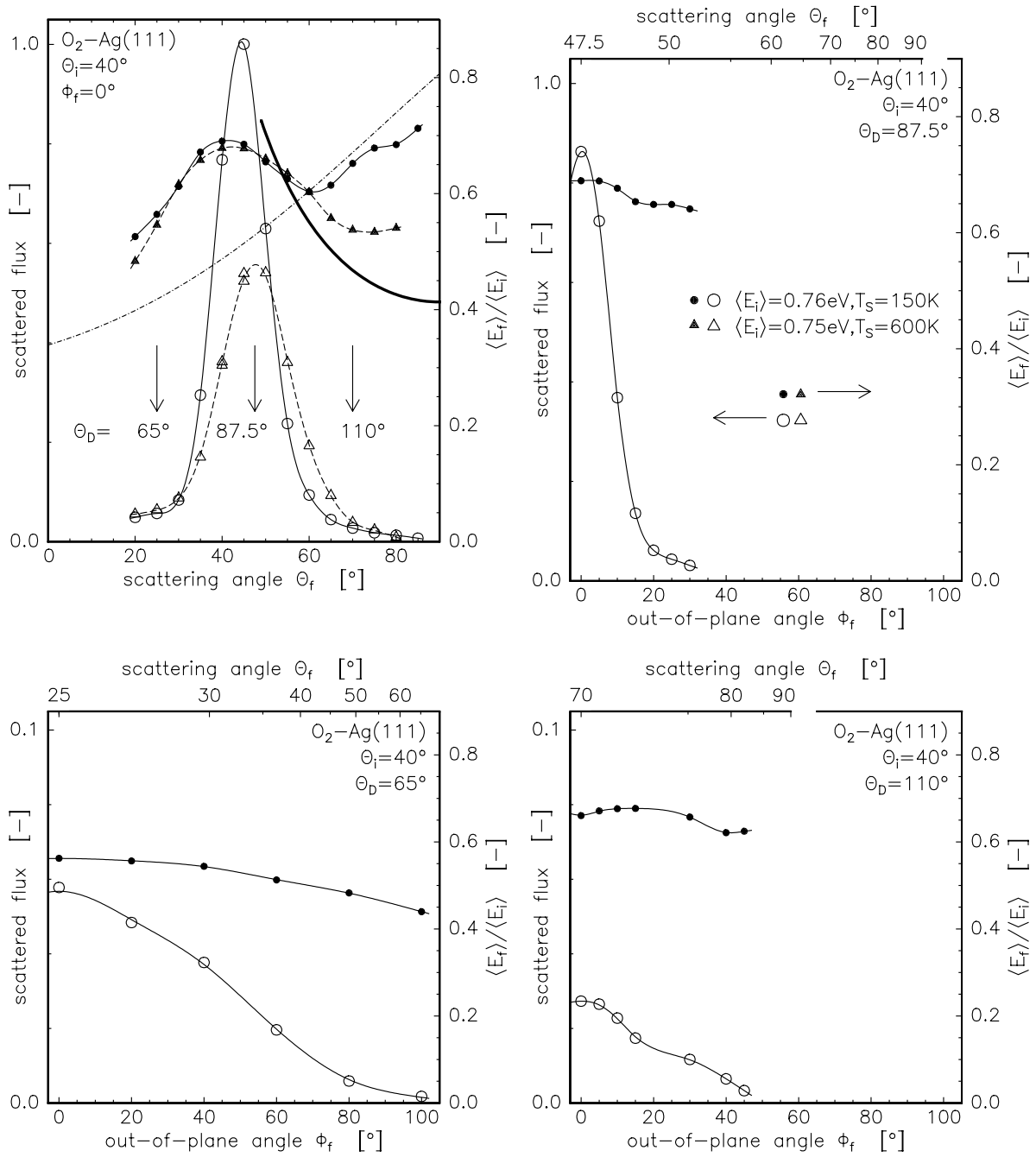

Figure 3.7 *In-plane and out-of-plane scattering of $E_i \approx 0.75$ eV incident O_2 from a $T_s = 150$ K Ag(111) surface. Both scattered flux and energy ratio are shown in one panel. The upper left panel shows scattering in the plane of incidence and also the scattering results for a $T_s = 600$ K surface. The thick line holds for parallel momentum conservation and the dashed line for hard sphere scattering ($m/M = 32/108$). In the other panels, the results for scattering out of the plane of incidence are shown, keeping the angle between the incident and scattered molecules (θ_D) fixed. Scanning the out-of-plane angle ϕ_f also implies changing the scattering angle θ_f as is shown in the top axes ($\theta_{f,MAX} = 90°$).*

ϕ_f (and θ_f) and a tail. In the energy ratio curve a kink is observed coinciding with the start of the tail in the intensity distribution. This suggests two scattering mechanisms. The particles in the tail have undergone a larger energy transfer, resulting in an energy ratio closer to that of hard sphere scattering, compatible with probing a larger corrugation than the particles scattered close to the plane of incidence. Particles scattered from a corrugated surface are also expected to be scattered further away from the plane of incidence.

For $\theta_D = 110°$ a same type of of intensity distribution is observed, but with a larger tail. The energy ratio curve is now seen to slightly increase with increasing angle ϕ_f and thus coming closer to the hard sphere scattering line. So again the effect of both direct-inelastic scattered contributions (parallel momentum conservation and hard sphere scattering) can be distinguished in the results of scattering out of the plane of incidence. In the case of of $\theta_D = 65°$ no change in the direct-inelastic scattering mechanism can be observed. Probably all scattered flux has probed the corrugated surface resulting in a (back)scattered intensity detected far from the specular direction. Even for a direction perpendicular to the plane of incidence ($\phi_f = 90°$) intensity is detected.

It should be noted that the results for the fast trapping-desorption seen in the TOF spectra of figure 3.6 for $T_s = 150$ K (the slowest peak) are not shown in figure 3.7. Only the direct-inelastic scattering contribution is shown and taken into account in the calculation of the energy ratios. For $T_s = 600$ K the direct-inelastic scattered and fast trapping-desorption contribution cannot be distinguished and the TOF spectra were therefore fitted with only a single Maxwell-Boltzmann distribution. For $T_s = 600$ K the energy of the fast trapping-desorption is expected to be approximately 0.37 eV [122,123, chapter 4]. So, if the fast trapping-desorption is of influence on fitting the TOF spectra, a lower energy should be found when the direct-inelastically scattered molecules have a larger energy than $E_{DI} = 0.37$ eV. This is indeed observed in the upper left panel of figure 3.7.

3.3.2 Nitrogen scattering

Results for nitrogen scattering are shown in figure 3.8 and 3.4 for $\theta_i = 40°$ and 60° and over a similar incident energy range as for oxygen scattering. The peak intensities are normalised to 1.0 for $E_i = 0.46$ eV to be able to compare the results with oxygen scattering; the flux intensities for both angles are not linked. To allow normalisation to a point that has not been measured a spline based smooth curve is drawn through the data points. A value for $E_i = 0.46$ eV could then be extracted and used for the normalisation. Lines to guide the eye shown in all figures (oxygen, nitrogen and argon scattering) are also spline based smooth curves. Values at every point can be extracted and were also used for finding the peak maximum in the flux curves.

Contrary to the oxygen scattering results the peak flux intensities as a function of incident energy for nitrogen scattering from Ag(111) show an increase with increasing incident energy and no sign of a decrease. As is obvious in figure 3.4 the peak flux intensity increase for $\theta_i = 60°$ compares very well with the $\theta_i = 60°$ oxygen scattering results except for the fall off above 0.3 eV normal energy.

Apart from the lowest incident energy of $E_i = 0.26$ eV, for which the motion of the surface atoms will play a significant role, the flux distributions as a function of scattering angle θ_f are very symmetrical and show no sign of broadening. This is also shown in the

top panels of figure 3.4 showing the FWHM of the flux distributions. The width of the flux distributions for nitrogen scattering are below the ones obtained for oxygen scattering at an equal angle of incidence. They do only show a decrease with increasing incident energy and no increase. The leveling off in this case can also be explained by going from the thermal scattering regime into the structural one as shown for instance by Liu [129,130] and Rettner [127]. We explain the increase in FWHM for oxygen scattering also by structure scattering, but it must be of a totally different kind.

Turning our attention to the energy ratios as a function of scattering angle θ_f we also notice a completely different behaviour as compared to the oxygen scattering results. With increasing incident energy and for scattering angles θ_f below specular the energy ratios also deviate from parallel momentum conservation behaviour towards smaller values, but do not show the decrease in E_f/E_i with decreasing angle θ_f as observed for oxygen scattering. Above specular a deviation from parallel momentum behaviour is observed towards larger values for the energy ratios with increasing incident energy. Deviations in this range are larger than those observed for oxygen scattering. For the largest incident energy the energy ratio curves are almost horizontal.

The energy ratio panels also show the results of applying hard sphere scattering for different mass ratios. Here mass ratios are taken representing once, twice and three times the mass of a silver atom. In the region where the energy ratios are below the parallel momentum behaviour line, they are still above the hard sphere scattering line for $m/M = 32/108$. This can be understood by assuming an intermediate process between the two extremes. The region above parallel momentum behaviour also shows energy ratios above hard sphere scattering for $m/M = 32/108$ and the higher incident energies. At $\theta_i = 60°$ and $E_i = 1.50$ eV, the energy ratio seems to converge to a behaviour close to a mass ratio taking two or three times the mass of the silver atom. A more complex mechanism than the two extreme cases mentioned so far must be at work.

3.3.3 Argon scattering

Figure 3.9 shows the results of argon scattering and were taken only for $\theta_i = 40°$. The left panels show results for a surface temperature of 600 K and incident energies up to 2.56 eV, the right panels show the results for $E_i = 1.06$ eV incident energy and various surface temperatures. Again the scattered flux intensities are normalised to the interpolated peak value for $E_i = 0.46$ eV. In the lower right panel the evolution of the width and the peak flux with surface temperature are also shown. As can be seen, an increase in surface temperature results in an increase in the width of the flux distribution and a decrease in peak flux intensity. However, the energy ratio curves are hardly affected by changing the surface temperature. The differences observed are probably within the experimental accuracy. As is also seen, the maximum in the angular intensity does not move when changing the surface temperature. Extrapolating the width to $T_s = 0$ K results in a residual width of approximately 12°.

The FWHM of the flux distributions as a function of incident energy, shown in figure 3.4, is larger than the width measured for oxygen and nitrogen scattering. An increasing width at equal incident energy and incident angle for nitrogen, oxygen and argon, respectively, is readily explained by their increasing mass and lower incident velocity at equal incident

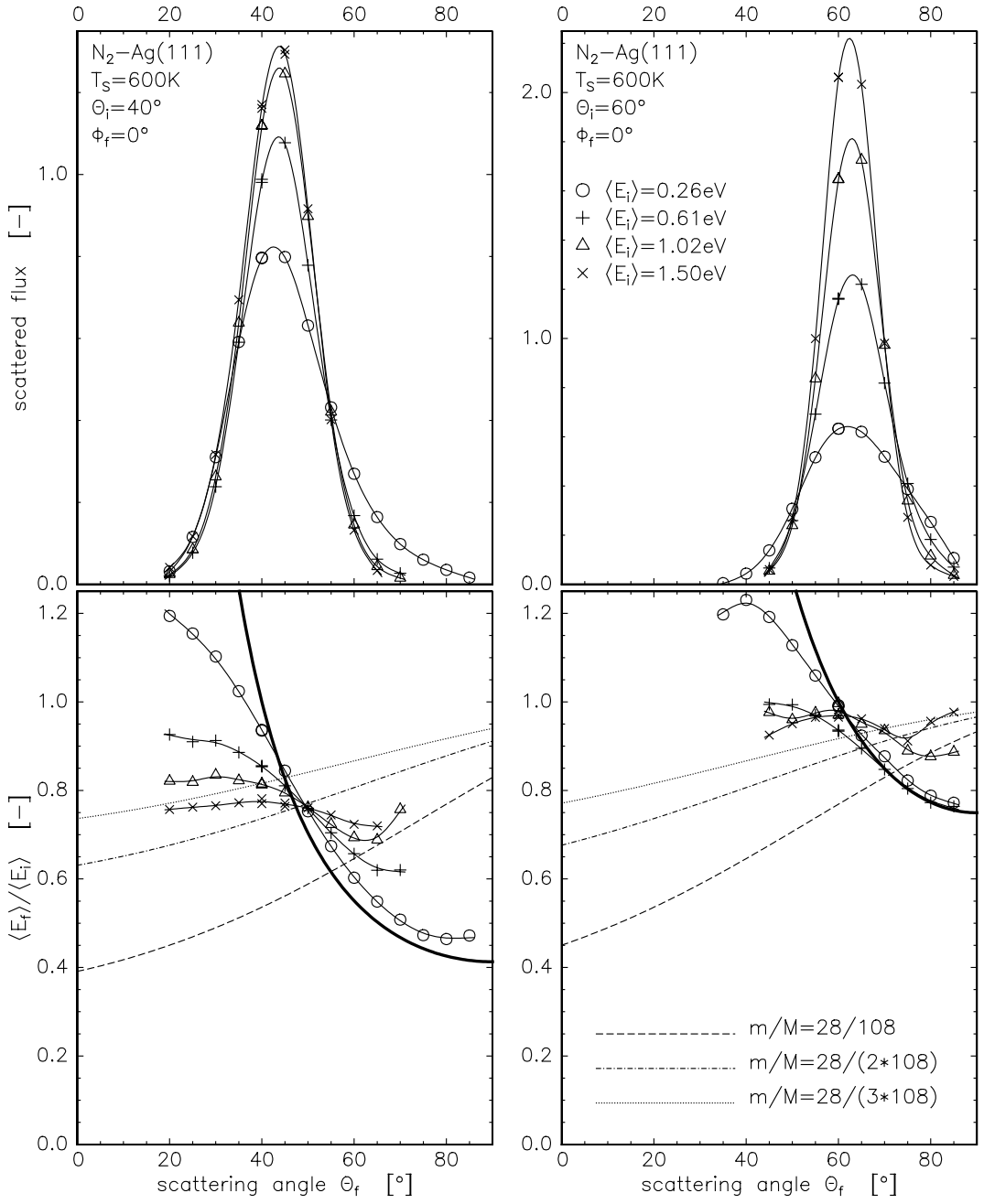

Figure 3.8 *Angularly resolved energy and flux distributions of N_2 molecules scattered from a Ag(111) surface for 40° and 60° angles of incidence. Lines through the data points are to guide the eye only. For an interpolated energy of $E_i = 0.46$ eV the scattered flux is normalised to the peak flux separately for both angles of incidence. The thick lines in the lower panels hold for parallel momentum conservation and the dashed, dashed-dotted and dotted lines are a result of hard sphere scattering.*

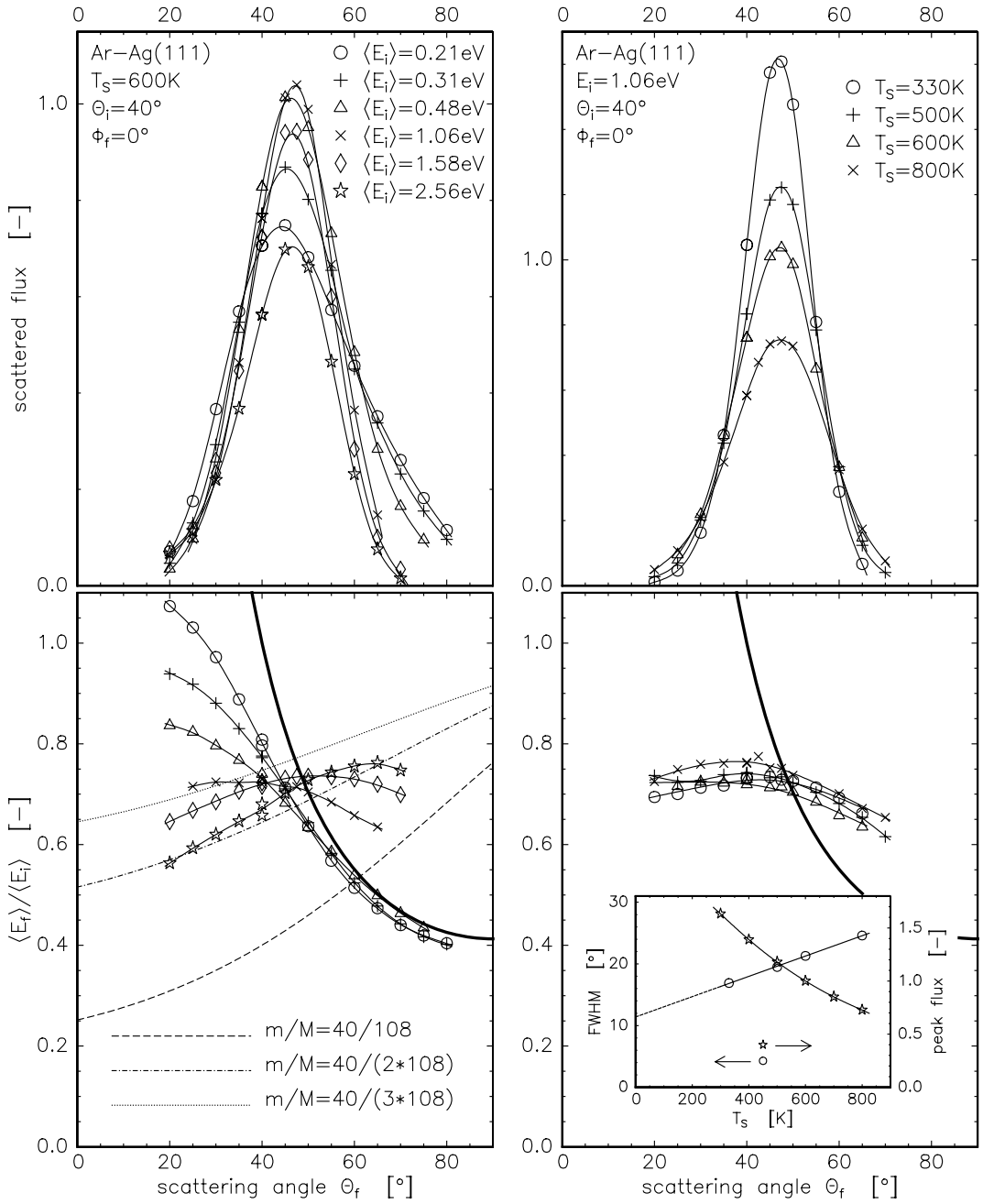

Figure 3.9 *Angularly resolved energy and flux distributions of Ar atoms scattered from a Ag(111) surface for 40° angle of incidence. The left panels are for one surface temperature and different incident energies, the right panels for one incident energy and different surface temperatures. Lines through the data points are to guide the eye only. For an interpolated energy of E_i = 0.46 eV at T_s = 600 K the scattered flux is normalised to the peak flux. The thick lines in the lower panels hold for parallel momentum conservation and the dashed, dashed-dotted and dotted lines hold for hard sphere scattering. The inset in the lower right panel shows the evolution of the width and the peak flux of the scattered angular flux distributions for 1.06 eV incident energy.*

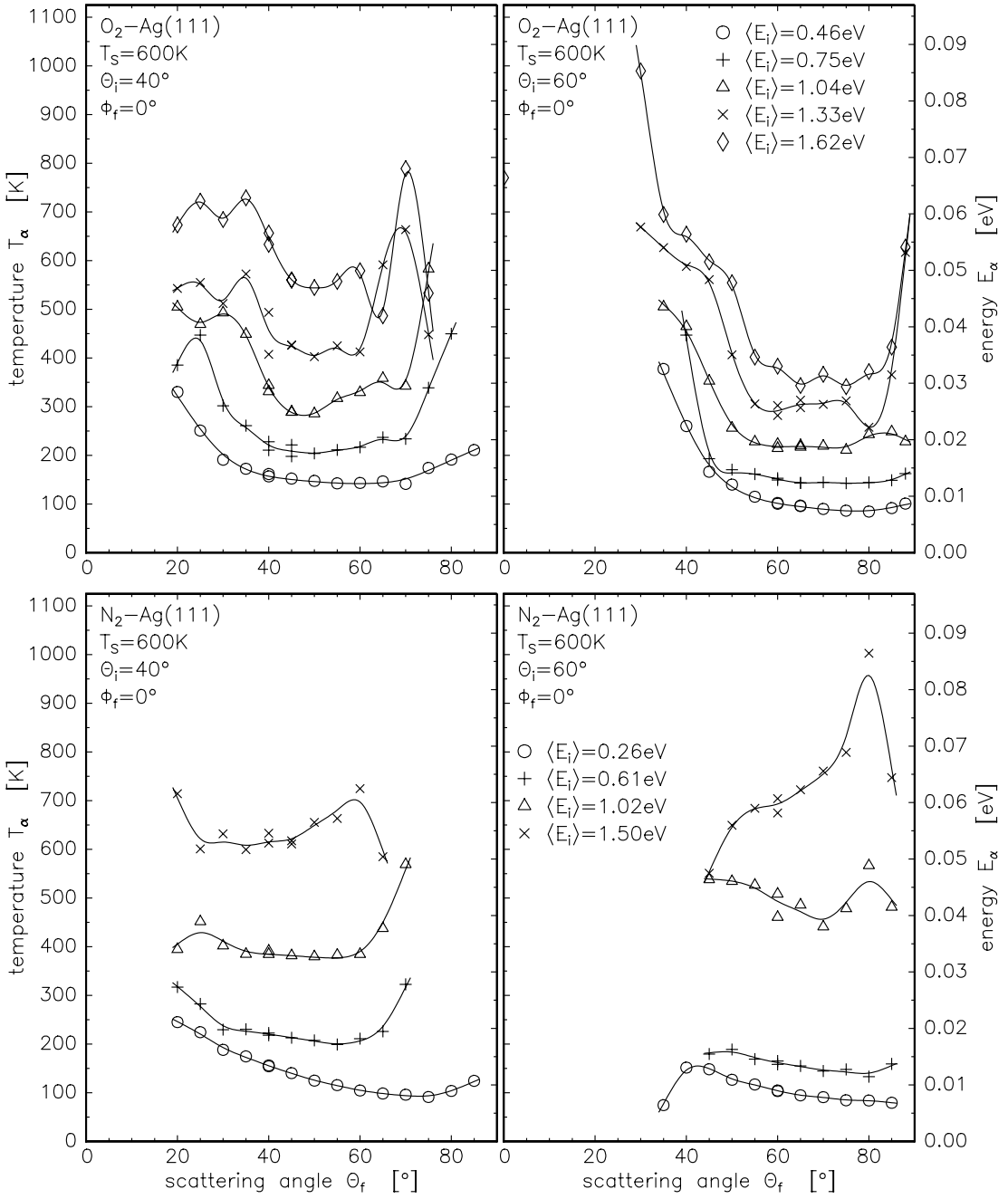

Figure 3.10 *Angularly resolved widths of the energy distribution of O_2 and N_2 scattered from a Ag(111) surface at 40° and 60° angles of incidence and various incident energies. T_α is shown on the left axis and E_α on the right axis of the four panels. Lines through the data points are to guide the eye only.*

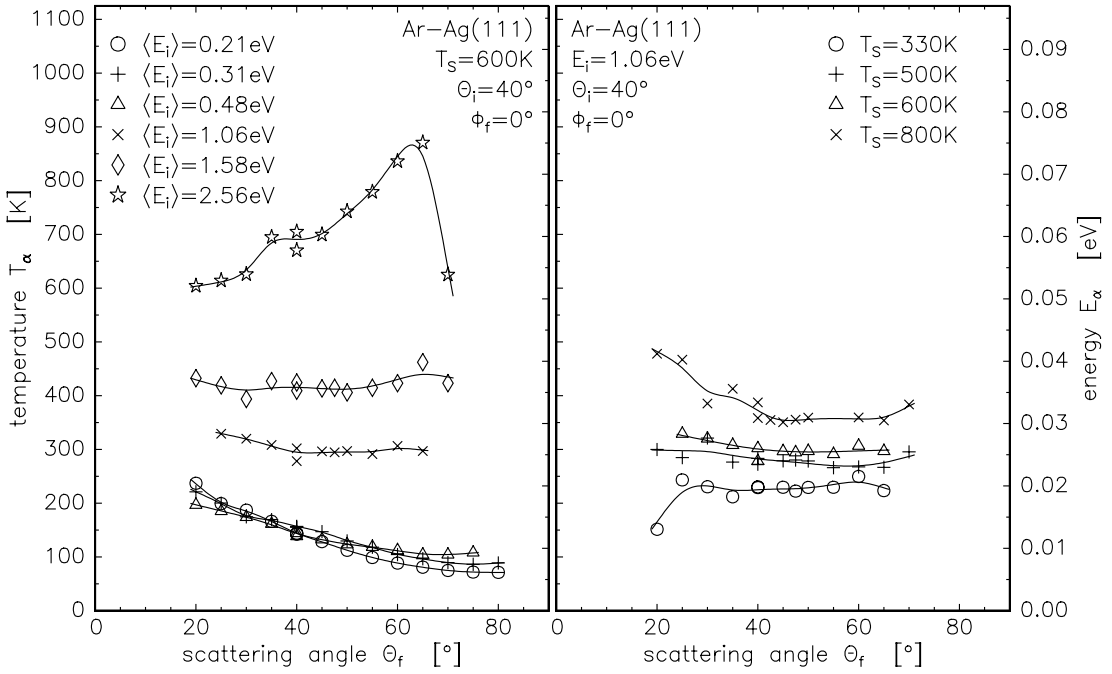

Figure 3.11 *Angular resolved widths of the energy distribution of Ar scattered from a Ag(111) surface at 40° angle of incidence and constant surface temperature in the left panel and constant incident energy in the right panel. T_α is shown on the left axis and E_α on the right axis of the two panels. Lines through the data points are a guide to the eye only.*

energy as can be seen by scattering simulations from flat moving cubes [65]. From figure 3.4 it can also be seen that the width for argon scattering shows a minimum and the peak flux intensity a maximum at about 1 eV incident energy and are thus in accord with each other. The data points for 2.56 eV incident energy fall outside the range of the energy axes of figure 3.4 and are therefore not visible. The width and peak flux curves do show a larger corrugation for argon scattering at the higher incident energies.

Comparing the energy transfer, in the energy ratio curves, for nitrogen and argon scattering we see that the results are quite similar. Although, for argon with a 1.58 eV incident energy, comparable to the highest incident nitrogen energy, a decrease in energy ratio is observed with decreasing angle θ_f, also suggesting a larger corrugation for argon scattering. The energy ratio curves above parallel momentum behaviour are also somewhat higher. For $E_\mathrm{i} = 2.56$ eV it is very close to the result for hard sphere scattering taking a mass of twice the mass of the silver atom into account. Lahaye et al. also observed in their simulations a larger effective mass of the silver surface atom. Possibly, multiple bounces of the particle at the surface should be included for the scattering.

3.3.4 Widths of the energy distributions of the scattered particles

The width of the energy distributions of the scattered particles, expressed as T_α or E_α, are shown in figure 3.10 and 3.11. Looking at the results for $\theta_i = 40°$ we see that argon scattering shows the smallest widths for comparable energies. The widths for oxygen scattering are somewhat smaller than those for nitrogen scattering, which is even more obvious for the $\theta_i = 60°$ measurements. A decreasing angle θ_f shows an increasing width for oxygen scattering at both incident angles. The results for the largest incident energies for nitrogen at $\theta_i = 60°$ and argon at $\theta_i = 40°$ increase with increasing angle θ_f. The widths are fairly small as compared to the mean final energy, indicating direct-inelastic scattering, and for most incident parameters the widths are fairly monochromatic over the scattering angle θ_f. In the right panel of figure 3.11 it can be seen that an increase of the surface temperature causes an increase in the width of the energy distributions.

3.3.5 Azimuthal dependence

The $T_s = 600$ K oxygen scattering experiments presented are taken on one silver sample. Oxygen scattering from another silver sample yielded identical results. For both samples the azimuthal angle was not checked and was most probably different for both samples. The low temperature oxygen scattering was done on a sample mounted on the 3-axis goniometer for which some scattering experiments were done as function of azimuth. No azimuthal dependence was found. Sticking of O_2 at the Ag(111) surface does also not depend on the azimuth as will be presented elsewhere [124, chapter 5]. It can therefore be concluded that no (noticable) azimuthal dependence is present for the O_2-Ag(111) interaction.

3.4 Discussion

3.4.1 Argon scattering

Our argon scattering results do compare with the scattering experiments of xenon from a Pt(111) surface carried out by Rettner et al. [127]. They also observed a transition from thermal to structure scattering with increasing incident energy and found a correspondence between an almost flat energy ratio curve as a function of scattering angle θ_f and the minimum in the angular width of the scattered flux distributions. Both appeared at about the same incident energy. In our case, the almost constant energy ratio also appears at approximately the incident energy for which a minimum in the angular width is observed. Our results, expressed in angular width and shift of the peak flux from specular, are also in accord with the results obtained by Liu [129]. Rettner et al. have extended their measurements to an incident energy of $E_i = 14.3$ eV and observed a quite dramatic decrease in energy ratio with increasing scattering angle θ_f. If one should draw a hard sphere scattering line, for a mass ratio $m/M = 132/195$ representing the mass of a xenon and a platinum atom, in their figures it can be observed that even for the highest incident energy the results lie above this line. So also for these results a larger mass for the surface atom should be taken into account for this extreme model. Their data does not cross the parallel momentum

behaviour line, due to a higher energy loss in a collision with a larger mass ratio of incident and surface atom.

The scattering data of Rettner et al. and other experimental data available for Xe-Pt(111) could be reproduced very well by Barker et al. [131–133]. They performed scattering simulations applying an interaction potential optimised to give a maximum correspondence between simulations and experimental data. A single interaction potential finally turned out sufficient to reproduce a whole set of experimental data. The energy ratios and flux distributions for xenon scattering from a Pt(111) surface are thus, in this respect, very well described.

Tully has performed scattering simulations of argon scattered from different platinum surfaces [134]. He used both a "washboard-model" and 16 moving platinum atoms contained in three layers to describe his surface. For $E_i \approx 2$ eV which he uses in his simulations, he observes a crossing of the energy line corresponding to parallel momentum conservation. Should one draw the hard sphere scattering line, for the appropriate mass ratio of $m/M = 40/195$, in his figures it is seen that the simulation results are above this line. So again an intermediate behaviour between parallel momentum conservation and hard sphere scattering is observed. The more corrugated platinum surfaces do show broader flux distributions and even rainbow scattering [135].

Recently, Lahaye et al. have undertaken scattering simulations of argon from the Ag(111) surface [136]. They have based their interaction potential on an ab-initio calculated potential of argon with a silver cluster as carried out by Kirchner et al. [137]. The trends of the energy ratio curves and the shape of the scattered flux distributions presented here are reproduced very well, although their energy ratio curves are somewhat too high. The energy ratio curves do cross the parallel momentum conservation line and are above the hard sphere scattering line for $m/M = 40/108$. Even for a simulation at 22 eV incident energy the energy ratio curve is above this hard sphere scattering line.

3.4.2 Nitrogen scattering

The nitrogen scattering results are quite similar to the argon scattering results and can be explained basically in the same way. Only the widths of the energy distributions of the scattered nitrogen molecules are larger and increasing for a larger incident angle θ_i. This might be explained by a coupling to the rotation of the molecule in the scattering event. An extreme case for which this has been observed is the scattering of nitric oxide (NO) from a Pt(111) surface [138]. The widths of the energy distributions of the scattered nitric oxide molecules are very large and their rotational excitation after scattering is very high, especially for larger scattering angles θ_f. The rotational excitation takes so much energy from the translational degree of freedom that the (translational) energy ratio curve is seen to lie below the hard sphere scattering line.

3.4.3 Oxygen scattering

Compared to the results for nitrogen and argon scattering the results for oxygen are remarkably different. The first show a more or less gradual tilting of the slopes of the energy ratio curves with increasing incident energy. But for oxygen the hard sphere scattering be-

haviour begins for lower incident energies at the smaller scattering angles θ_f and then works its way to the larger angles θ_f with increasing incident energy. A hard sphere scattering behaviour is observed for much lower incident energies and is much more pronounced.

The energy ratio curves converge (for $\theta_i = 40°$) close to a hard sphere scattering line for a mass ratio $m/M = 32/108$, representing the mass of the incident oxygen molecule and the mass of one silver surface atom. This indicates an interaction of the incident oxygen molecule with primarily one surface atom, in contrast to nitrogen and argon scattering. The energy loss for $\theta_i = 40°$ is larger than expected from hard sphere scattering. Before converging, a modulation is observed around the hard sphere scattering line, at about the specular angle, with a decreasing amplitude for increasing incident energy. Two different direct-inelastic scattering mechanisms explain this behaviour. One is scattering from a very corrugated surface with a broad angular flux intensity distribution, the other scattering from a smooth surface with a narrower angular flux distribution at about the specular angle. Adding the energy ratio curves of both mechanisms will give rise to the observed one. As the contribution of the smooth surface decreases with increasing incident energy the observed modulation will also decrease.

The angular distributions of the scattered flux prove to be a good measure of the amount of incident flux probing the very corrugated surface. It can be observed from the peak flux intensities that the scattering behaviour starts changing dramatically for normal incident energies above a threshold. An upper limit for this threshold is $E_i \cos^2 \theta_i = 0.3$ eV. For normal incident energies above 0.75 eV the maximum corrugation is reached according to the peak flux intensities and angular scattered flux distributions. The FWHM curve for $\theta_i = 40°$ also shows a sudden rise followed by a saturation which clearly indicates a change from one scattering mechanism to another and a saturation in this change. The shape of the angular flux distributions for 40° incident angle and the highest incident energies does show a close resemblance to the flux distributions obtained from scattering (experimental and simulations) of xenon from Pt(111) at 14.3 eV incident energy [127,131–133] and argon scattering from Ag(111) at 22 eV incident energy [136]. At these high incident energies the noble gas atom will reflect from a point high up the repulsive wall of the (physisorption) interaction potential. Probing a higher point on the repulsive wall implies a turning point of the trajectory closer to a surface atom, so a more corrugated surface. For physisorption systems, as Xe-Pt(111) and Ar-Ag(111), a much higher incident energy is required for the incident particle to probe a comparable corrugation as we observe for O_2-Ag(111) at lower incident energies.

Surface structure was also found to decrease the maximum scattered intensity and to broaden the scattering distribution in the hard-spheroid model of Steinbrüchel [9,10]. Broadening is, in this model, asymmetric relative to the direction of maximum scattered intensity in that backscattering towards the surface normal is favored.

We explain the scattering behaviour of oxygen by invoking scattering from a dual repulsive wall. For low incident energies the oxygen molecules will scatter from the repulsive wall of the physisorption part of the interaction potential which will be relatively far away from the surface atoms. Scattering in this regime exhibits the characteristics of a smooth surface. In this energy range we will show elsewhere that also trapping in the physisorption well occurs [122,123, chapter 4]. By increasing the incident energy the repulsive wall of the chemisorption part of the interaction potential will be probed by an increasing number of

trajectories. This repulsive wall will be closer to the surface atoms and thus shows a much larger corrugation than the physisorption wall which is further out the surface. This is supported by an ab-initio calculated potential energy surface of Van den Hoek and Baerends [71] and potential energy surfaces suggested by Spruit [60] and Nakatsuji et al. [75,96,97]. The repulsive wall can be connected to either the molecular or dissociative chemisorption state. In the last case the repulsive force between the O-atoms in the molecule should be small enough not to give dissociation on the time scale of the collision. Scattering in this higher energy regime shows a broad asymmetric angular distribution of the scattered intensity, leading to a loss in specularly reflected flux, and a large translational energy loss. The energy ratio curves are seen to be below the line representing hard sphere scattering from a single silver atom, opposite to the observation for the physisorption systems. This large translational energy loss can be explained by several effects due to the influence of a molecular chemisorption well on the scattering. A deep well will accellerate the particle towards the surface, thus leading to a larger energy transfer to the surface in the collision. The molecule can also make multiple bounces, leading to a larger energy loss than a single collision, and/or transfer translational energy into internal degrees of freedom of the oxygen molecule [11,12,139–143].

The change between the two scattering regimes is gradual. Not all incident flux will sample the molecular chemisorption part of the interaction potential above the threshold energy. Above $E_i \cos^2 \theta_i \approx 0.75$ eV approximately the maximum amount of incident flux probes the chemisorption potential, as is evidenced by the saturation in the peak flux intensities and the width of the angular intensity distribution. The sudden rise followed by a saturation of the FWHM in figure 3.4 for oxygen is a clear indication of the change of one potential to another. For a single potential such a sharp change followed by saturation is very unlikely. In the intermediate energy regime part of the flux will scatter from the repulsive wall of the physisorption potential and part from the repulsive wall of the chemisorption potential. The result is an increase in flux at the small scattering angles θ_f (back scattering) and a decrease in specular flux. The energy ratio curves are also a "sum" of both processes, leading to undulations around a hard sphere scattering line. The amplitude of the undulation decreases with increasing incident energy when more flux crosses the barrier to the molecular chemisorption part of the potential. All the flux for $\theta_i = 40°$ and $E_i = 1.62$ eV seems to have crossed the barrier.

These observations then lead to the conclusion of the existence of a distribution of barrier heights between both parts of the interaction potential. Geometric (different impact sites on the unit cell) and steric effects (orientation of the molecule) will lead to such a distribution of heights. Overcoming the barriers to molecular chemisorption is not a guarantee for sticking into this well or dissociation as the probability for both is still negligibly small [124, chapter 5].

One can wonder if different explanations for the observed behaviour in oxygen scattering are available. The first would be to assume a very different shape of a single O_2-Ag(111) interaction potential, that is not directly influenced by the chemisorption part of the interaction potential. In that case one would expect this potential and thus the scattering patterns to be similar to that of N_2 scattering. This is clearly not the case. Another possibility is that chemisorption does not lead to a second repulsive wall but strongly modifies the physisorption potential. This case has been studied by Karikorpi et al. [116] and Hal-

stead and Holloway [117]. Clearly addition of a site dependent absorbing part, a hole, to the potential modifies the physisorption potential near the hole. One would expect this to be relevant, when all particles hitting the hole will be chemisorbed. For O_2-Ag(111) this is not the case, because the probability of both molecular chemisorption and atomic chemisorption is much smaller than the proportion of the flux that has undergone hard sphere scattering. Therefore, we conclude that indeed a hole is opening up in the physisorption potential, and that most of the flux entering the hole is reflected back into the vacuum (recrossing), after having undergone accelleration in the molecular chemisorption potential and a close collision with essentially a single Ag atom.

3.4.4 Comparison with scattering for other chemisorption systems

Another system for which scattering experiments have been done and which is known to have an interaction potential with a triple well is the O_2-Pt(111) system [144]. For this system it is known that the dissociative sticking probability is above 0.1 for incident energies above $E_i = 0.3$ eV and proceeds through the molecular chemisorption, which is thus acts as a precursor to dissociation [145]. In the case of O_2 scattering from Pt(111) the scattered flux resembles that measured for N_2 scattering from Ag(111) much more. For O_2 at Pt(111) the probability for chemisorption is quite high (>0.2 at $E_i = 0.5$ eV).

Wiskerke and Kleyn have compared the width of the angular distributions for a number of systems where atomic or molecular chemisorption occurs [138]. Comparing our data to the data from their compilation, we observe that the angular broadening for O_2-Ag(111) at high incident energies exceed those measured for all other systems with the exception of NO scattering from Pt(111). This most presumably due to the very deep chemisorption well (1 eV) present for the NO-Pt(111) system.

3.5 Conclusion

The scattering of nitrogen and argon from Ag(111) are characteristic of a physisorption system. Our results compare very well with other available experimental and simulation data. With increasing incident energy it is observed that the surface gradually transforms from being rather smooth, exhibiting scattering close to parallel momentum conservation, to a more corrugated surface, showing scattering more characteristic of hard sphere scattering.

Oxygen scattering from the Ag(111) surface also shows a transition to a corrugated surface, but is much more pronounced, appears at a lower incident energy and the degree of corrugation is much larger. A dual repulsive wall present in the interaction potential explains the observations. Part of the flux will scatter from the repulsive wall of the physisorption interaction and part from the wall of the chemisorption interaction. The ratio changes with incident energy and angle. At low incident energy all the incident flux will scatter from the first wall, at high incident energies and small incident angle from the second repulsive wall. Contrary to the O_2-Pt(111) or the O_2-Ag(110) system all the flux is observed in the scattering of oxygen from the Ag(111) surface because dissociative and non-dissociative sticking are still negligible.

Appendix

In order to be able to do the TOF experiments our continuous beam has to be chopped into short pulses, which is done by the chopper in the beam line. Due to a velocity distribution of the particles in the pulse it will spread in time while travelling over a flight path of known length. Loss of resolution in the pulse will occur when the initial pulse is too broad. Therefore a 0.5% duty cycle chopper, containing two diametrically placed slits, running at approximately 240 Hz was used in the experiments presented. These conditions lead to initial beam pulses of about 15 μs wide (FWHM). As will be described below the measured TOF spectrum still needs to be corrected for the width of this pulse.

The chopper marks the start of the TOF and also supplies a trigger for the instrument recording the TOF spectrum (multichannel scaler). By measuring the reflectivity of a LED from the chopper blade, a trigger is generated when the reflectivity drops when a slit passes. Both the LED and the light sensitive diode measuring the reflected light are contained in one unit (Hewlett Packard HPCB1100). A timing difference between trigger and passing of the particle beam generally occurs because the trigger pick-off and the passing slit are not exactly aligned. This positive or negative delay will be a linear function of the inverse of the chopper speed and is calibrated by measuring and analysing TOF spectra for different chopper rotation speeds. Extrapolation to infinite rotation speed gives the result for zero delay. Another delay occurs because the TTL trigger pulse for the multichannel analyser is generated at a certain chopper reflectivity level. Its length can be derived by watching its trace together with the trace of the reflectivity on an oscilloscope. The measured TOF spectra are corrected by adding or subtracting the proper delay times.

Detection of the particles marks the end of its flight time, which is the sum of the flight time of the neutral particle before ionisation in the QMS and the flight time of the ionised particle through the QMS (consisting of an ioniser, ion optics, 90° ion deflection, a quadrupole and a secondary electron multiplier). The flight time through the QMS is (mainly) dependent on the strength of the electrical fields present in the QMS and must be taken into account in the analysis.

Another effect which might broaden the measured TOF spectrum is the finite length over which the particles are ionised, giving rise to possibly largely different ion flight times for different ionisation positions. Also space charge effects due to a large ionisation current can be of influence and should be avoided.

To study the ion flight time and the effect of ionisation position we simulated our QMS with a software package capable of calculating the electrical fields and ion flight times through these fields for a set of user defined electrodes (SIMION PC/PS2 version 4.0, EG&G Idaho Inc.). These simulations led us to choose the voltages in our ion optics so that the voltage gradient in the ionisation region is small, resulting in a negligible change in velocity of the ion as compared to the neutral particle, and so that the ion flight time is as short as possible to reduce the effect of the velocity of the neutral particle on the ion flight time. The ion optics should still focus the ions well on the quadrupole ensuring a maximum intensity.

Frome these simulations an ion flight time for a given ionisation position, mass m and charge q was derived. For such a particle with translational energy E upon ionisation it holds that its traveling time over a distance l after ionisation through an arbitrary electrical

field $\epsilon(x)$ is given by

$$t_{\rm ion} = \sqrt{m}\int_0^l \frac{dx}{\sqrt{2q\int_0^x \epsilon(\zeta)d\zeta + 2E}} \ . \tag{3.3}$$

Once the ion flight is known for one mass it is known for all other masses with equal charge. We checked the simulation results by measuring the TOF spectra of a $E = 65$ meV Xe beam, with the QMS tuned to the Xe^+, Xe^{2+}, Xe^{3+} and Xe^{4+} ions. The translational energy term in equation 3.3 can be neglected in this case. Results obtained agree very well with the simulations.

In our analysis of the TOF spectra we corrected the time axis for the ion flight time. We chose it to start from a certain position in the ionisation region. The flight path of the netral particle then ends at this position. For all neutral particle energies one ion flight time was taken so that the error made was small.

Having derived the TOF of the neutral particle with the corrected time axis it needs to be analysed to yield the energy distribution of the measured particles and a measure of their flux. For the measured TOF spectrum of the particles in the direct beam one can write

$$F_{\rm direct}(t_n) = \int_{t_n-\frac{1}{2}\Delta t_{\rm MCS}}^{t_n+\frac{1}{2}\Delta t_{\rm MCS}} d\tau_n \int_{t_{\rm open}}^{\tau_n} d\tau_1\, C(\tau_1)\tilde{S}_{\rm i}(\tau_n-\tau_1) \ , \tag{3.4}$$

where $F_{\rm direct}(t_n)$ denotes a discrete density distribution in time and $t_{\rm open}$ the time when the chopper starts passing the beam. The first integral represents integration of detected particles over the dwell time $\Delta t_{\rm MCS} = t_n - t_{n-1}$ of the multichannel scaler and the second one a convolution over the chopper gating function $C(t)$. This gating function is the initial pulse of approximately 15 μs FWHM mentioned before. $\tilde{S}_{\rm i}(t)$ represents the density distribution of the velocities v of the detected particles in the time domain. A flux distribution will be denoted as $S(t)$ and is related to a density distribution by

$$\tilde{S}(v) = \frac{S(v)}{v} \ , \tag{3.5}$$

stated in the velocity domain now. Velocity and time domain are related through

$$S(v)\,dv = S(t)\,dt \ , \qquad v = \frac{x}{t} \tag{3.6}$$

under the integrals, where x denotes the length of the appropriate flight path.

We will write the TOF density distribution of scattered particle as

$$F_{\rm scatter}(t_n) = \int_{t_n-\frac{1}{2}\Delta t_{\rm MCS}}^{t_n+\frac{1}{2}\Delta t_{\rm MCS}} d\tau_n \int_{t_{\rm open}}^{\tau_n} d\tau_2 \int_{t_{\rm open}}^{\tau_2} d\tau_1\, C(\tau_1)S_{\rm i}(\tau_2-\tau_1)\tilde{S}_{\rm DI}(\tau_n-\tau_2) \tag{3.7}$$

$$= \int_{t_n-\frac{1}{2}\Delta t_{\rm MCS}}^{t_n+\frac{1}{2}\Delta t_{\rm MCS}} d\tau_n \int_{t_{\rm open}}^{\tau_n} d\tau_2\, A_{\rm i}(\tau_2)\tilde{S}_{\rm DI}(\tau_n-\tau_2) \ . \tag{3.8}$$

In this case an extra convolution is present because of the spreading of the initial pulse due to its velocity distribution. However, both convolutions can be combined to one representing the flux distribution of particles arriving at the surface $A_{\rm i}(t)$. $\tilde{S}_{\rm DI}(t)$ represents the density distribution of direct-inelastically (DI) scattered particles. Particles might not only scatter

direct-inelastically from the surface, but might also trap at the surface and desorb again (TD) with a characteristic residence time η_{TD}. Taking this contribution into account leads to

$$F_{\mathrm{scatter}}(t_n) = \int_{t_n-\frac{1}{2}\Delta t_{\mathrm{MCS}}}^{t_n+\frac{1}{2}\Delta t_{\mathrm{MCS}}} d\tau_n \left[\int_{t_{\mathrm{open}}}^{\tau_n} d\tau_2\, A_{\mathrm{i}}(\tau_2) \tilde{S}_{\mathrm{DI}}(\tau_n-\tau_2) + \int_{t_{\mathrm{open}}}^{\tau_n} d\tau_3 \int_{t_{\mathrm{open}}}^{\tau_3} d\tau_2\, A_{\mathrm{i}}(\tau_2) \frac{1}{\eta_{\mathrm{TD}}} \exp\left(-\frac{\tau_3-\tau_2}{\eta_{\mathrm{TD}}}\right) \tilde{S}_{\mathrm{TD}}(\tau_n-\tau_3) \right] \quad (3.9)$$

and shows an extra convolution over the surface residence time. Particles that have stuck do obviously not contribute to the scattered intensity, but can change the scattered distributions as compared to the clean surface.

Some remarks should be made on the expression for the scattered intensity $F_{\mathrm{scatter}}(t_n)$, equation 3.8 or 3.9. It assumes all particles hitting the surface will scatter according to the same distribution $S_{\mathrm{DI}}(v)$ disregarding their incoming translational energy distribution. The flight paths to the surface and after scattering from the surface to the detector will also depend on the impact site on the surface. Since the incoming particle beam has a finite diameter, the flight paths will change with angle of incidence and with detection angle. Both effects have been neglected in our analysis.

For the flux distributions $S(v)$ so-called shifted Maxwell-Boltzmann distributions are taken:

$$S(v) = \frac{I}{N(v_\beta, v_\alpha)} v^3 \exp\left(-\left[\frac{v-v_\beta}{v_\alpha}\right]^2\right) . \quad (3.10)$$

They have proved to describe the energy distribution in a supersonic expansion very well and are flexible enough to both describe desorbing and direct-inelastically scattered particles [66,146–149]. Describing direct-inelastic scattering by a shifted gaussian distribution yielded almost identical results as with the shifted Maxwell-Boltzmann distributions. The parameter I gives a measure for the flux, v_β is the flow velocity of the distribution and v_α a measure for the width of the distribution. It should be noted that I of the scattered flux is expressed as a fraction of the incident flux in this formalism. $N(v_\beta, v_\alpha)$ is the appropriate normalisation factor for this flux distribution and is equal to

$$N(v_\beta, v_\alpha) = \frac{v_\alpha^4}{2}\left[\frac{\sqrt{\pi}}{2}\left[2\left(\frac{v_\beta}{v_\alpha}\right)^3 + 3\left(\frac{v_\beta}{v_\alpha}\right)\right]\left[1+\mathrm{erf}\left(\frac{v_\beta}{v_\alpha}\right)\right] + \left[\left(\frac{v_\beta}{v_\alpha}\right)^2 + 1\right]\exp\left(-\left(\frac{v_\beta}{v_\alpha}\right)^2\right)\right] \quad (3.11)$$

$$\approx \begin{cases} \frac{1}{2}v_\alpha^4 & \text{if } v_\beta \ll v_\alpha \\ \frac{v_\alpha^4\sqrt{\pi}}{2}\left[2\left(\frac{v_\beta}{v_\alpha}\right)^3 + 3\left(\frac{v_\beta}{v_\alpha}\right)\right] & \text{if } v_\beta \gg v_\alpha \end{cases} . \quad (3.12)$$

The corresponding density distribution (equation 3.5) is also described with the flux measure I and the normalisation factor for the flux distribution.

The chopper gating function $C(t)$ in equation 3.4, 3.7 and 3.8 is given by the normalised overlap function of a rectangle, the chopper slit, with a circle, the beam intersection. Passing of the slit through the beam results in a changing overlap with time. For a slit with straight

edges the chopper thickness should be taken into account. The effective slitwidth then is smaller for slower particles when the slit is moving. In our new chopper assembly the slit edges are tapered under 45°. The thickness of the chopper blade needs in this way not to be taken into account for beam particles with velocities larger than the slit speed at the beam intersection. $E = 65$ meV xenon is still fast enough for our maximum chopper frequency of 400 Hz.

The equations 3.4 and 3.8 or 3.9 are implemented as Riemann-sums in our computer code (called 'TofFit') and the parameters of the trial function $F(t)$ are varied according to a Levenberg-Marquardt (LM) scheme to minimise χ^2, the sum of the squares of the difference between measured and fitted distribution. In analysing the oxygen scattering results a LM scheme was used based on subroutines as given by Bevington [150]. Later on, in analysing the nitrogen and argon results a LM scheme based on the routines given in Numerical Recipes [151] was used. The latter gave the possibility to fix fitting parameters to a certain value in the fitting process. In this last version of the deconvolution program χ^2 is defined as

$$\chi^2 = \sum_{n=1}^{N} \frac{(F(t_n) - F_{\mathrm{M}}(t_n))^2}{\sigma_n^2} \ , \tag{3.13}$$

with N the number of points in the measured and fitted TOF distribution, F_{M} and F respectively, and σ_n an estimate of the error in the n^{th} point. Because we work in pulse counting mode, the error will be determined by shot noise and is equal to the square root of the number of counts, $\sigma_n = \sqrt{F_{\mathrm{M}}(t_n)}$. With χ^2 defined in this way it should yield the value $N - \nu$, ν being the number of free fitting parameters, after minimisation. In our case $N \gg \nu$, so after minimisation $\chi^2/N \approx 1$ should hold and was also observed after deconvoluting the TOF spectra.

Not only the three parameters I, v_β and v_α of each Maxwell-Boltzmann distribution and the surface residence time η_{TD} act as the fitting parameters, but also a background level I_{BCKG} measured according to

$$F'(t_n) = I_{\mathrm{BCKG}}\, \Delta t_{\mathrm{MCS}} + F(t_n) \ . \tag{3.14}$$

The trial function $F'(t_n)$ is used in the fitting procedure. The partial derivatives to the various fitting parameters, needed in the LM scheme to guess a next value for the fitting parameters in the minimisation process, can be easily derived analytically from equations 3.14, 3.4 or 3.9, 3.10 and 3.11 and implemented in the computer code in the same way as done for the functions $F'(t_n)$. Deriving the partial derivatives numerically by taking a variation of the fitting parameters results in a slower and less reliable computer code.

When converting the (convolution) integrals into Riemann-sums care is taken to take the time steps small enough to not influence the results. The results are also independent on chopper rotation speed and dwell time of the multichannel scaler.

Having found values for v_β and v_α, these can be converted into more appropriate parameters describing the energy distribution of the detected particles. The width of the energy distribution of the detected particles, with mass m, can be expressed as an energy E_α or a temperature T_α according to

$$E_\alpha = k_{\mathrm{B}} T_\alpha = \frac{1}{2} m v_\alpha^2 \ , \tag{3.15}$$

with $k_{\rm B}$ Boltzmann's constant. A mean value for the energy per particle is found through

$$< E > = \frac{\frac{1}{2}m}{I}\int_0^v dv\, v^2 S(v) \tag{3.16}$$

$$= \frac{\frac{1}{2}mv_\alpha^6}{N(v_\beta,v_\alpha)}\left[\frac{\sqrt{\pi}}{8}\left(\frac{v_\beta}{v_\alpha}\right)\left[15+20\left(\frac{v_\beta}{v_\alpha}\right)^2+4\left(\frac{v_\beta}{v_\alpha}\right)^4\right]\left[1+\mathrm{erf}\left(\frac{v_\beta}{v_\alpha}\right)\right]+ \right.$$
$$\left. \frac{1}{4}\left[4+9\left(\frac{v_\beta}{v_\alpha}\right)^2+2\left(\frac{v_\beta}{v_\alpha}\right)^4\right]\exp\left(-\left(\frac{v_\beta}{v_\alpha}\right)^2\right)\right] \tag{3.17}$$

$$\approx \begin{cases} 2E_\alpha = 2k_{\rm B}T_\alpha & \text{if } v_\beta \ll v_\alpha \\ \frac{1}{2}mv_\beta^2 + 5E_\alpha & \text{if } v_\beta \gg v_\alpha \\ \frac{1}{2}mv_\beta^2 = E_\beta & \text{if } v_\beta \gg 10\, v_\alpha \end{cases} . \tag{3.18}$$

For desorbing particles, without a barrier present in the desorption path ($v_\beta = 0$ m s^{-1}), the temperature T_α will be (slightly) below the surface temperature and the mean energy per particle is than twice the energy E_α associated with the temperature T_α [152,153]. The energy per particle is always larger than the energy associated with the flow velocity v_β. For a fast narrow distribution the energy per particle is approximately given by the flow velocity. The value for I is not the absolute flux because the ionisation and detection efficiency are not known. It will be proportional to the flux.

The width of the energy distribution of the particles in the beam after a supersonic expansion from a nozzle, for which holds that v_β is considerably larger than v_α, can be described by

$$\frac{(\Delta E)_{\rm FWHM}}{< E >} \approx 4\sqrt{\ln 2}\sqrt{\frac{E_\alpha}{E_\beta}} \approx 2.77\sqrt{\frac{E_\alpha}{E_\beta}} \qquad \text{if } v_\beta \gg 10\, v_\alpha \ . \tag{3.19}$$

Chapter 4

Transient Trapping-Desorption of Oxygen Molecules at the Ag(111) Surface

Abstract *Molecular beam scattering experiments of O_2 from Ag(111) carried out at a surface temperature $T_s = 150$ K, which is below the desorption temperature for the molecular chemisorption state, shows three different scattering paths: physisorption followed by desorption, direct-inelastic scattering and transient trapping-desorption. These experiments were done for a backscattering geometry. The transient-desorption process is attributed to transient adsorption of the molecule in an $O_2^{\delta-}$ state at the surface without equilibration of the vibrational degree of freedom. The energy of the transient desorption is far above thermal, strongly dependent on the surface temperature and independent of the translational energy and angle of the incident oxygen molecule. A strongly peaked intensity distribution around the surface normal is observed for the desorption. The transient trapping shows a sharp increase above a threshold energy and a subsequent decrease and is accompanied by a strong broadening in the angular direct-inelastically scattered flux distribution.*

4.1 Introduction

Chemical reactions at surfaces play a major role in fields like catalysis and semiconductor processing. Although such reactions have been studied in great detail for a long time, only one reaction mechanism has been firmly established: the Langmuir-Hinshelwood (LH) reaction [154,2]. In this mechanism the reactants adsorb, equilibrate and possibly dissociate at the surface. Subsequently products are formed when the adsorbed reactants at the surface meet and react after which the product may or may not desorb. Recently another mechanism for surface reactions has been unequivocably demonstrated: the Eley-Rideal (ER) reaction [155–157]. In this case the reaction product is formed in a collision between a gas phase particle and an adsorbed particle, without equilibration of the gas phase particle at the surface. Harris and Kasemo [158] have pointed out that there is a continuous transition from the LH to the ER mechanism. An intermediate case would be a reaction in which the reactants only partially accommodate to the surface, for instance by keeping their parallel

momentum. The particle in this case can be considered to be transiently trapped in a metastable state, a metastable intermediate to a chemical reaction. An interesting consequence of the fact that the state is metastable is that it cannot be isolated in a static surface science experiment, for instance carried out at very low surface temperature.

In most considerations of surface chemical reactions the reaction intermediates or precursors are often thought to be states that can be isolated at the surface and independently studied by spectroscopies. Only the transition state, where the reactants are turned into the products, is assumed to escape detection by current surface analytical probes. However, there is a claim that the role of surface transients in surface reactions is demonstrated [159]. In this study we will demonstrate that intermediates at surfaces can be found that are unstable and have not been detected by any other means. The system of study is the interaction of O_2 molecules with the Ag(111) surface.

Oxygen is known to have four binding states with a silver surface: a shallow physisorption state, a molecular chemisorption state with a stronger bonding to the surface, a dissociated state at the surface and a subsurface state of atomic oxygen [36,37,41,44–46,48,54,66,84,102]. Desorption from the physisorption state occurs below $T_s = 50$ K [52], from the molecular chemisorbed state around $T_s = 200$ K [46,48] and from the dissociatively adsorbed state around $T_s = 600$ K [46,48]. Charge transfer to the oxygen molecule is thought to occur in the case of molecular chemisorption, so the formation of an $O_2^{\delta-}$ species at the surface [36,37,45,53,82]. For the Ag(110) surface it seems to be peroxo-like, with the bond order reduced to near unity, and on the Ag(111) surface possibly more superoxo-like, with a larger bond order, but the situation is not fully clear [53,82]. In high energy scattering experiments also formation of free O_2^- has been seen. The electron transfer process leading to negative ion formation is referred to as harpooning [160–164].

For several systems more than one molecularly chemisorbed state has been identified. The system for which this is most clearly demonstrated is the interaction of oxygen with Pd(111): three molecular chemisorption states can be formed as identified with thermal desorption (TPD) and electron energy loss spectroscopy (EELS) [165–168]. One of these states seems to exist or can be isolated only at higher coverages (as is also the case with the physisorption state), but the other two, both peroxo states, are clear phenomena of the clean Pd(111) surface. Dissociation of the oxygen molecule is seen to proceed via the molecular state with the strongest bonding. More than one molecularly chemisorbed state was also seen for O_2-Pt(111) [169–173], although the nature of the different states is not clear and there might be a relation to defects or steps present at the surface. For a Pt(112) surface, so a densily stepped Pt(111) surface, three molecularly chemisorbed states were identified in thermal desorption and two of them were attributed to the steps [174]. More than one molecularly chemisorbed oxygen state due to different binding sites has also been observed on the Pt(110)(1×2) surface [175–177]. On a polycrystalline Ag surface two molecularly chemisorbed oxygen species were identified and characterised as a peroxo and superoxo species [57]. Another molecular chemisorption state, desorbing at $T_s = 380$ K, could be created at special defect sites [45,100]. Desorption experiments of N_2 from W(110) also lead to the conclusion of the presence of more than one molecularly chemisorbed state and more than one adsorption site [178]. A new molecularly chemisorbed species for N_2/W(110) could also be created by electron impact and was electron impact desorption inactive [179].

These are all observations of molecularly chemisorbed states isolated at the surface. In

calculations quasi trapping at surfaces is observed due to vibrational trapping or snarled trajectories in a negative ion state [180–184]. The quasi trapping reported refers to the case that temporarily the molecule switches from the vibrational and electronic ground state to an excited vibronic state. In this state the molecule has insufficient energy to overcome the barrier for desorption from this excited state. The molecule thus remains quasi trapped until a transition to the vibronic ground state occurs, after which the molecule can desorb. Alternatively, the molecule can fully accommodate to the excited vibronic state and get trapped in it, as described by Holloway and collaborators [181,183,184]. In very recent calculations by Kosloff and Citri for the system O_2-Ag(111) it is observed that the molecule spends more than a picosecond on its way to dissociation, because it is trapped in an intermediate negative ion state [109,185].

Summarising, for the Ag surfaces molecular chemisorption states have been reported that desorb above $T_s = 175$ K and a physisorbed state desorbing below $T_s = 50$ K. Here we will show transient trapping of oxygen molecules. The trapped molecules loose their memory and desorb again. The trapping curve as a function of incident energy and angle for this new species coincides with the initial sticking coefficient dependence in the known molecular chemisorption state [124]. We infer that the trapping is due to partial equilibration in the molecular chemisorption state.

4.2 Experimental

The experiments have been performed in a molecular beam scattering machine described before [186,56, chapter 3]. Shortly, it consists of a triply differentially pumped molecular beam line connected to a UHV scattering chamber. The second stage of the beam line contains a double slit (0.5% duty cycle) chopper giving a sufficient time resolution for the time-of-flight (TOF) experiments and a beam flag to switch the beam on and off. The first stage contains the nozzle and the third stage acts as a buffer stage.

The molecular beam is generated by a supersonic expansion of a gas mixture of oxygen and helium from a 80 μm CW quartz nozzle. By changing the oxygen/helium ratio in the gas mixture and heating the nozzle (maximum temperature approximately 1100 K) we can vary the energy of the oxygen molecules to about 1.8 eV. Separate electronic flow controllers control the flows of oxygen and helium.

The sample is mounted in the middle of the scattering chamber on a 3-axes goniometer [125, chapter 2]. A quadrupole mass spectrometer (QMS) can be rotated around the sample to detect the particles leaving the surface in the TOF experiment. Combining the movements of the manipulator and the rotatable QMS gives accurate control (by computer) over the incident and exit angles of particles in the scattering experiment. By moving the sample out of the beam and the QMS in the beam path the TOF of the direct beam can be recorded. Measurements can also be done out of the plane of incidence, defined through the surface normal and the incident beam, and the azimuthal angle over the sample surface can be varied. ℓN_2-cooling allows a minimum sample temperature of about 120 K, which is measured with a thermocoax K-type thermocouple inserted in the side of the sample and is controlled by a commercial controller.

To check the surface quality the system is equipped with LEED and AES. A residual

gas analyser (RGA) is present for monitoring the back ground gas and an ion sputter gun for cleaning the sample.

For the TOF experiments the flight time of the oxygen molecule was measured from the chopper in the beam line to the rotatable QMS. The delay between the time pick off from the chopper blade and passing of the beam is calibrated by varying the chopper rotation speed. Detected particles, marking the end of the TOF, were counted by a home build multichannel scaler in 2 μs bins. In analysing the TOF spectra, the ion flight time through the QMS was subtracted from the TOF time axis.

Parameters describing the distribution of the particles (flux, flow velocity v_β, temperature T_α) in the beam and of the scattered particles were derived by fitting the recorded TOF spectra to shifted Maxwell-Boltzmann (MB) distributions convoluted over the finite chopper opening time or over the spread of arrival times of the impinging molecules on the surface, respectively. From these parameters a mean translational energy per particle can be derived, $<E>=<E(v_\beta, T_\alpha)>$. In the text $<E>$ will be denoted as E. The TOF spectra of the scattered particles can be fitted with up to three of these MB distributions and for one of these a surface residence can be taken into account as is described before [186, chapter 3]. We can also choose to fix parameters to certain values in the fitting process.

4.3 Results

Scattering results of O_2 from a Ag(111) surface will be presented. First results from a clean, $T_s = 150$ K surface are described as a function of incident energy of the oxygen molecules for three different scattering geometries at a scattering angle θ_f as close as possible to the surface normal as our experimental setup allows. Then some angularly resolved results and results obtained at a range of different surface temperatures are described. A measurement on an oxygen covered surface ends the results section.

4.3.1 Incident energy dependence

In figure 4.1 the time-of-flight (TOF) spectra for a fixed scattering geometry and incident energies of molecular oxygen varying from $E_i = 0.10$ eV to 1.48 eV are shown. The intensity axes in figure 4.1 represent the measured number density of oxygen molecules arriving at the QMS. The different TOF distributions are corrected for their different incident fluxes, so their relative intensities can be compared. The angle of incidence was $\theta_i = 50°$, the scattering angle $\theta_f = 10°$, both measured with respect to the surface normal, the out-of-plane angle, the angle beteen the incident and detection plane, $\phi_f = 0°$ and the surface temperature was kept at $T_s = 150$ K, so below the desorption temperature of molecular oxygen. However, a build up of oxygen on the surface is negligible because the sticking probability for dissociative and non-dissociative sticking is very low for our range of energies [124, chapter 5]. This was checked by flashing the sample between the recording of the different TOF spectra and monitoring the O_2 residual gas pressure during the flash. If any, desorption from the molecular and/or dissociated state was very low. Flashing the sample between the TOF recordings prevented oxygen build up during taking multiple TOF spectra.

Three different processes can be seen to play a role in the scattering of molecular oxygen from the Ag(111) surface. At low incident energies oxygen molecules can physisorb (trap)

at the surface and desorb again. The energy distribution of those desorbing molecules is described by a non-shifted Maxwell-Boltzmann distribution [66,186, chapter 3] with a temperature, $T_\alpha \approx 130$ K, below but close to the surface temperature. Such a distribution leads to a slow very broad TOF distribution as is seen in the upper left panel of figure 4.1. With increasing incident energy the trapping probability should decrease as the molecule is less likely to loose enough of its incident translational energy to trap at the surface, which is indeed observed [187].

Increasing the incident energy results in the appearance of two other peaks in the TOF spectra. They show a sharp increase in intensity above $E_\mathrm{i} = 0.36$ eV incident energy and they level off or show a decrease in intensity above 1 eV. The recorded TOF spectra are fitted to different (shifted) Maxwell-Boltzmann distributions as is described elsewhere [186, chapter 3]. Apart from $\theta_\mathrm{i} = 50°$ and $\theta_\mathrm{f} = 10°$, also at $\theta_\mathrm{i} = 40°$ and $\theta_\mathrm{f} = 20°$, and at $\theta_\mathrm{i} = 60°$ and $\theta_\mathrm{f} = 0°$ TOF spectra were recorded. Results of those fits for the two fast contributions in the TOF spectra are shown in figure 4.2. The fitting results are expressed in a measure for the flux, a mean energy per scattered molecule E_f, the flow velocity of the shifted Maxwell-Boltzmann distribution v_β, and the temperature of the energy distribution T_α. This latter parameter is a measure for the width of the energy distribution of the scattered molecules. Results for the trapping-desorption contribution from the physisorption well will be shown later. In those cases where no separate contributions could be distinguished in the TOF spectra, only one Maxwell-Boltzmann distribution was used in the fitting procedure.

As is obvious from figure 4.2, above $E_\mathrm{i} = 0.5$ eV incident energy the fast contribution in the TOF spectra can be separated into two contributions, both showing at first an increase in intensity with increasing incident energy. The fastest contribution shows a subsequent leveling off and the slower one a subsequent decrease in intensity. Both contributions are expressed in the same flux intensity units and are normalised to 1.0 for the largest flux in the fastest TOF contribution. The intensities for the three different scattering geometries are also linked, which means that the intensities for the different scattering geometries can be compared. The energy of the fastest species shows a strong correlation with incident energy; a larger incident energy results in a larger energy of the scattered molecule. However, the energy of the slower contribution hardly shows a dependence on incident energy and is also not dependent on incident angle θ_i or scattering angle θ_f, whereas the faster species is. A slight decrease in energy for the slower species is observed with increasing incident energy. As we do not think the measurement and the fitting procedure to be reliable enough to yield such a small decrease, we will consider the energy of the slower scattering process constant as function of the incident energy, being about 0.14 ± 0.01 eV at a surface temperature of $T_\mathrm{s} = 150$ K.

The independence of the energy of the slower scattering process from the incident energy of the molecular oxygen beam is reason to assign this species to arise from a trapping-desorption process. Later on we will give more evidence and also show it is not compatible with trapping-desorption from neither the physisorption nor the molecular chemisorption state. This means it cannot be assigned to arise from some known (stable) state at the surface. For this reason we will label it as "transient trapping-desorption" (TTD). The faster scattering process is labeled as "direct-inelastic scattering" (DIS), because of its strong dependence on incident energy and its maximum in intensity at about the specular reflection angle [186, chapter 3].

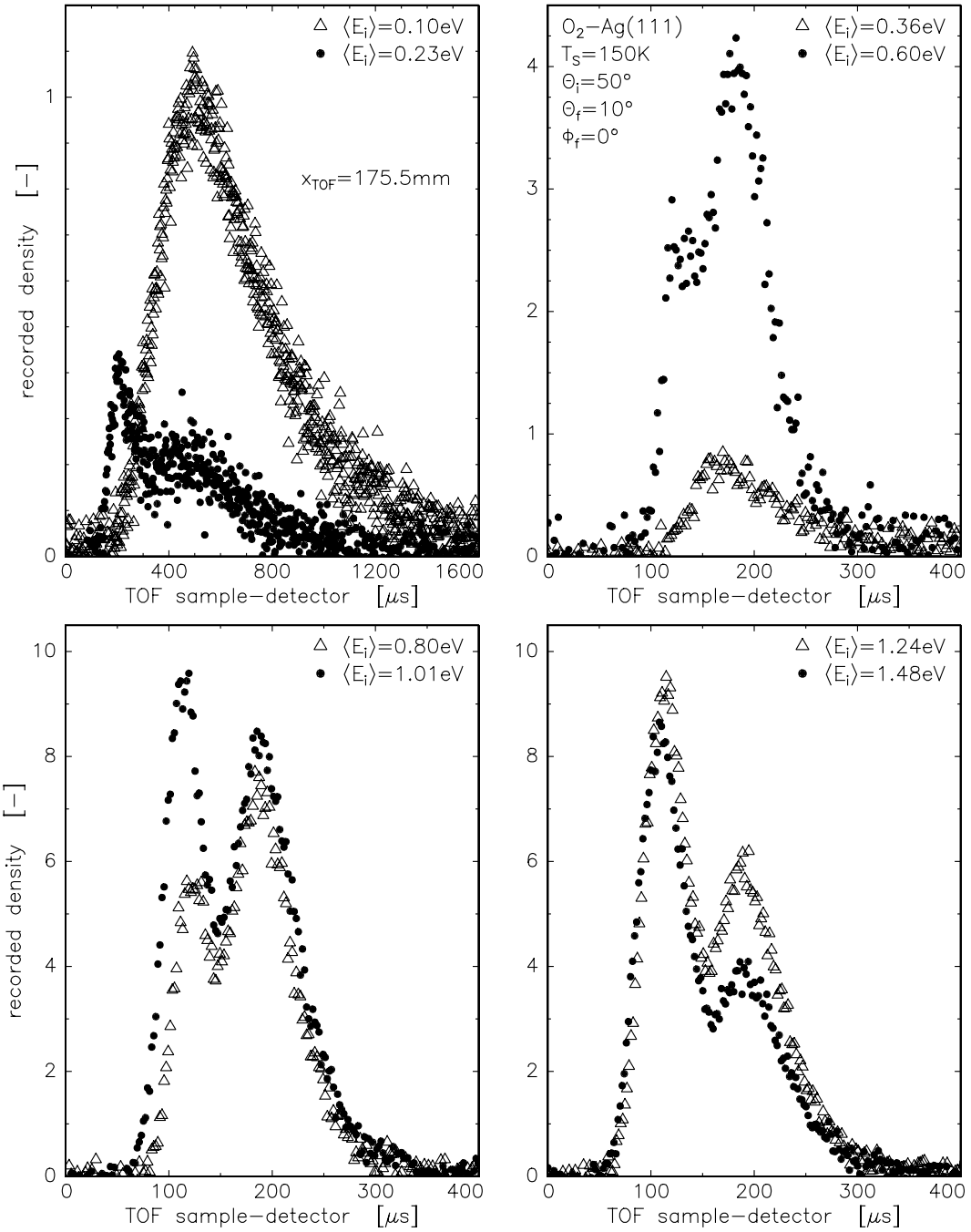

Figure 4.1 *Time-of-flight spectra of scattered oxygen molecules for incident energies of molecular oxygen on the Ag(111) surface in the energy range of $E_i = 0.10$ eV to 1.48 eV, incident at $\theta_i = 50°$ at a surface temperature of $T_s = 150$ K. The scattered molecules are detected in the plane of incidence at $\theta_f = 10°$. The time axes is the measured flight time corrected for the trigger delay, flight time through the detector and the flight time from the chopper to the sample according to the flow velocity of the incident molecules.*

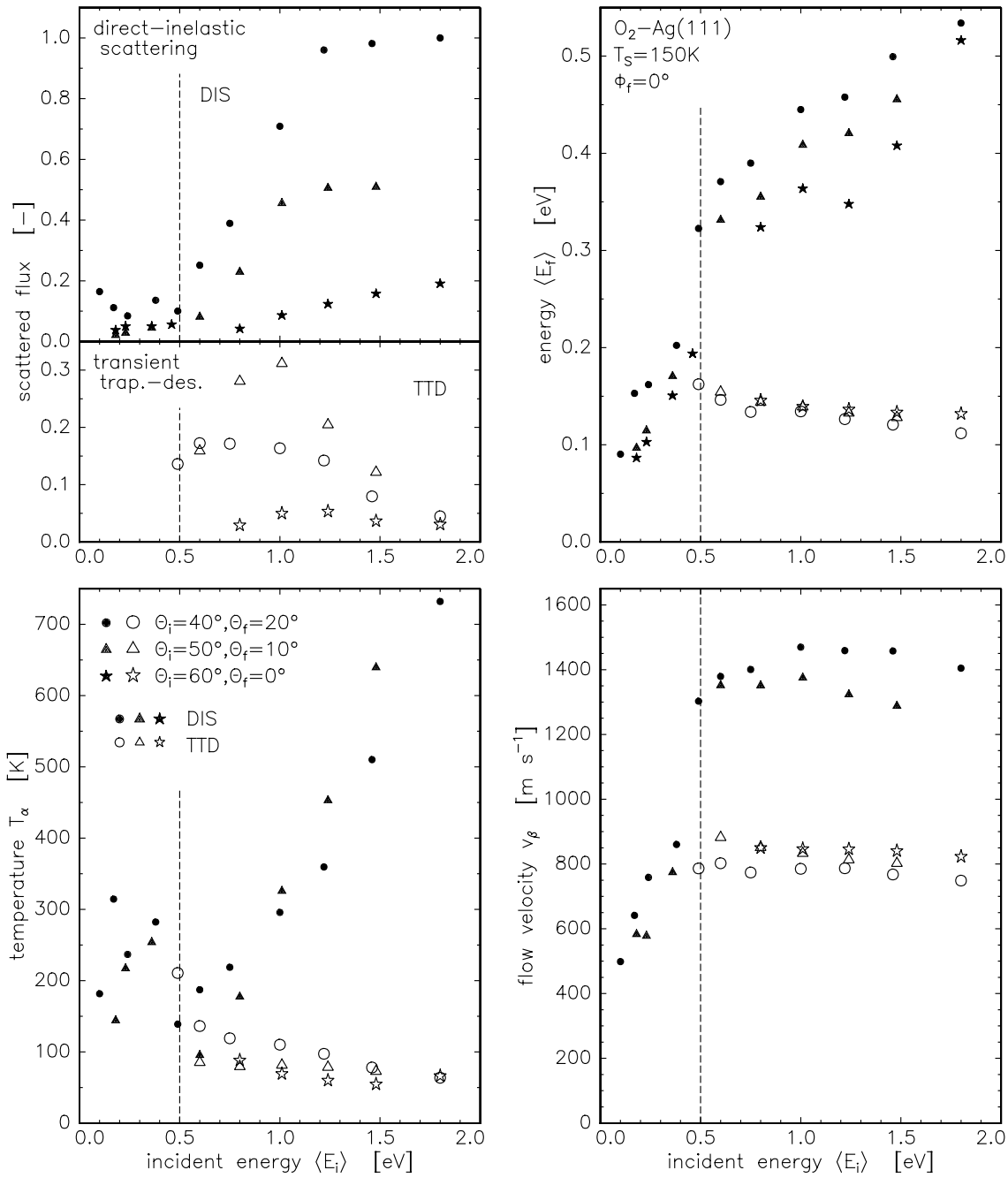

Figure 4.2 *Parameters describing the different contributions in the time-of-flight spectra of oxygen molecules scattered from a $T_s = 150$ K surface for three different scattering geometries. The scattered molecules are detected in the plane of incidence as close to the surface normal as the experimental setup allows.*

The energy distribution of the TTD process is not described by a non-shifted Maxwell-Boltzmann distribution with a surface temperature equal to the surface temperature as can be seen in the lower panels of figure 4.2. Its temperature seems to be below 100 K. Due to a large overlap of the DIS and the TTD contribution for $\theta_i = 40°$, $\theta_f = 20°$ the error in the temperature T_α will be somewhat larger than for the other two scattering geometries. More important is the non-zero flow velocity of about $v_\beta = 800$ m s^{-1} suggesting the desorption to be activated. This large flow velocity is responsible for the energy of the TTD distribution being much larger than the energy associated with a non-shifted Maxwell-Boltzmann distribution with a temperature equal to the surface temperature $E = 2\,k_B T_s \approx$ 0.02 eV. The larger T_α for $\theta_i = 40°$ and $\theta_f = 20°$ is compensated with a somewhat lower flow velocity than for the other two geometries by the fitting procedure, yielding about the same energy as for the other two scattering geometries.

Looking at the T_α and v_β of the DIS contribution it is seen that the strong dependence of the energy of this contribution on the incident energy is determined by the strong dependence of T_α on the incident energy. The incident energy dependence of the flow velocity is rather small. At approximately the onset energy in DIS and TTD scattering, the temperature T_α of both distributions is about equal; at increasing incident energy they diverge with the temperature of the TTD distribution staying essentially constant.

The values for T_α and v_β of the DIS contribution for $\theta_i = 60°$ and $\theta_f = 0°$ are not shown. Letting all the fit parameters of the Maxwell-Boltzmann distributions free did lead to a low and even zero flow velocity v_β for the large incident energies and an extremely large temperature T_α upto a few thousand Kelvin. Keeping the flow velocity fixed to $v_\beta = 1200$ m s^{-1} resulted in a fit of approximately equal quality and a T_α following the ones found for the other two scattering geometries. The values found for the energies as shown in figure 4.2 for the free parameters are almost equal to the values for the energy found when keeping v_β fixed. As the $\theta_i = 60°$ and $\theta_f = 0°$ data is of rather poor quality due to its low intensity, we believe the trends shown in figure 4.2 to be right. All the data shown in the figure is obtained by letting all parameters free during fitting. Keeping the flow velocity fixed to $v_\beta = 1200$ m s^{-1} also resulted in an increase of the TTD flux and a decrease of the DIS flux for $E_i > 1.2$ eV.

Below 0.5 eV incident energy the fast peak in the TOF distributions was fitted with one shifted Maxwell-Boltzmann distribution. Just below 0.5 eV for $\theta_i = 40°$, $\theta_f = 20°$ it is obvious that both the DIS and TTD will contribute to this peak in the TOF spectra. A direct-inelastic scattering process with a different origin than the one observed above 0.5 eV incident energy might also play a role as both the DIS and TTD contribution tend to go to zero intensity below 0.5 eV. For the $E_i = 0.5$ eV, $\theta_i = 40°$, $\theta_f = 20°$ results three, but possibly four different processes contribute to the TOF spectrum.

4.3.2 Angularly resolved intensity distribution

Further evidence for the TTD contribution to arise from trapping-desorption is an intensity distribution which is peaked around the surface normal. The intensity should also not be dependent on the out-of-plane angle ϕ_f, measured with respect to the incident plane, but only on the angle θ_f, measured with respect to the surface normal (see figure 2.4). The top panels in figure 4.3 show the recorded TOF spectra for $E_i = 0.80$ eV incident energy,

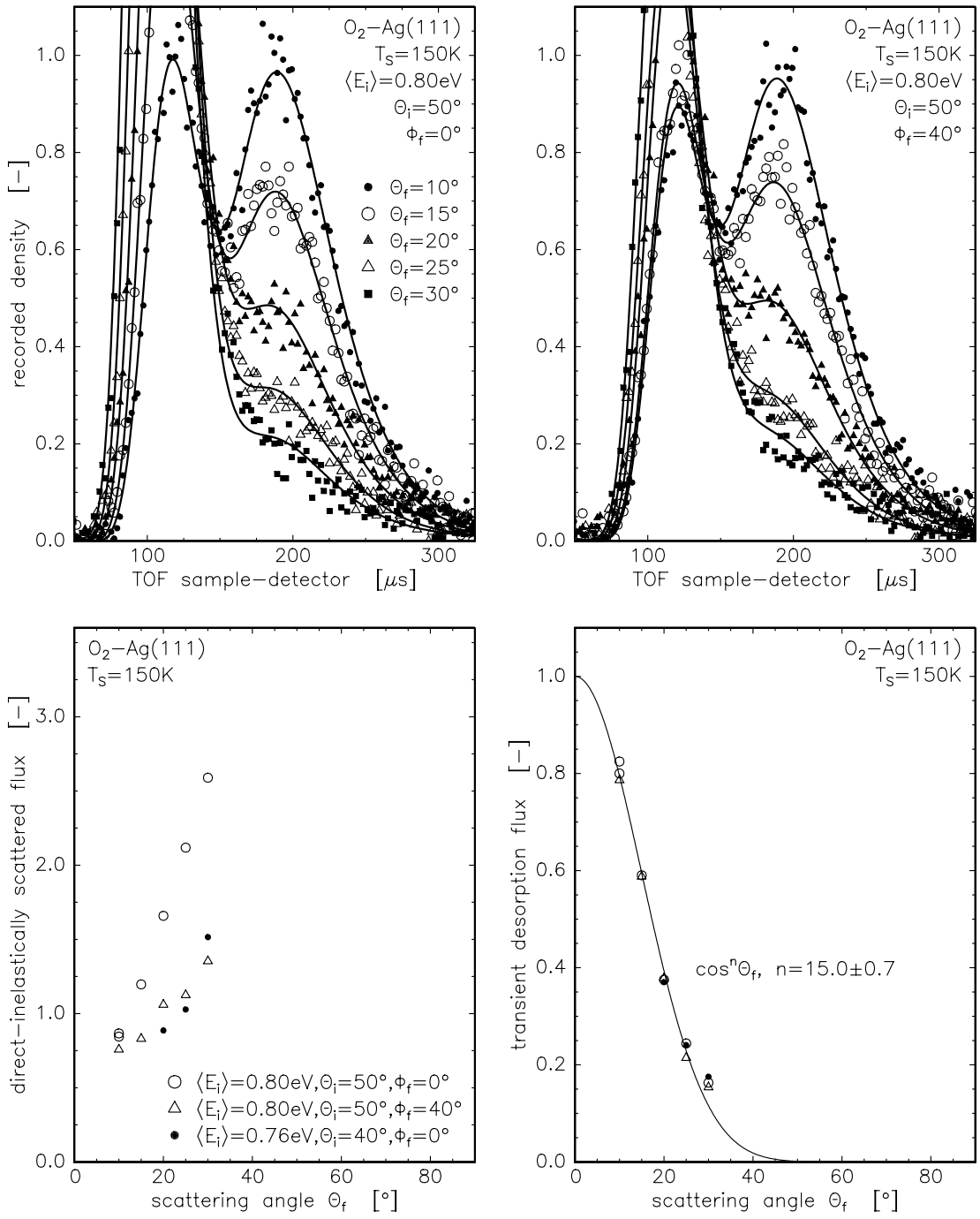

Figure 4.3 *The upper panels display the TOF spectra for $E_i = 0.80$ eV O_2 molecules incident at $\theta_i = 50°$ at $T_s = 150$ K, recorded at different angles θ_f and both in the plane of incidence and for $\phi_f = 40°$ away from the plane of incidence. In the lower panel the (fitted) flux in the DIS and the TTD contribution is shown for the spectra in the upper panels and for another set of scattering parameters. These values are displayed in the same units for both panels, normalised to the extrapolated TTD flux at $\theta_f = 0°$ for both incident angles. The lines in the upper panels are fits to the data, the line in the lower left panel is according to a $\cos^{15}\theta_f$ function.*

$\theta_i = 50°$ angle of incidence and scattering angles θ_f from 10° to 30°. The top left panel shows the spectra measured in the plane of incidence, so for $\phi_f = 0°$, and the top right panel for $\phi_f = 40°$ out of the plane of incidence.

These spectra were again fitted with a double shifted Maxwell-Boltzmann distribution. The results for the flux are shown in the bottom left and right panel for the DIS and TTD contribution, respectively. Their intensity axes are expressed in the same units. It is seen that indeed the intensity of the TTD contribution peaks around the surface normal and can be described quite accurately by a $\cos^n \theta_f$ intensity distribution, with $n = 15.0 \pm 0.7$. Only the points for $\theta_f = 30°$ deviate from this line, but the error bars will be quite large here because of the overlap of a small TTD contribution and a large DIS contribution. Looking at the fit through these two TOF spectra one can see that the flux for the TTD contribution is indeed taken to be somewhat too large. The intensity axes of the bottom panels are scaled so to yield the value 1.0 for the extrapolated TTD contribution at $\theta_f = 0°$. As expected, the DIS flux intensities for $\phi_f = 40°$ out of the scattering plane are smaller than the ones measured in the plane of incidence. The TTD flux intensities in and out of the incident plane are equal.

Angularly resolved measurements done for $E_i = 0.76$ eV and $\theta_i = 40°$ and detected at $\theta_f = 20°$, 25° and 30° are also displayed in the bottom panels. They are in good agreement with the $\cos^n \theta_f$ intensity distribution.

No change in energy of the TTD contribution could be observed as a function of scattering angle θ_f, which is also apparent in figure 4.2. For $\theta_f = 25°$ and 30° the flow velocity v_β and temperature T_α of the TTD contribution were fixed to the values found for the smaller angles θ_f when fitting the TOF spectra.

4.3.3 Surface temperature dependence

The surface temperature has a large influence on the energy of the TTD contribution as can be seen in the TOF spectra displayed in the left panel of figure 4.4. These spectra were taken in the plane of incidence ($\phi_f = 0°$) for $E_i = 0.80$ eV and $\theta_i = 50°$. For $T_s = 150$ K both the DIS and TTD contribution clearly can be distinghuised, but at surface temperatures of $T_s = 350$ K and higher both contributions have merged into one peak in the TOF spectra.

Fitting again a double shifted Maxwell-Boltzmann distribution to the data yields the values for the energy of the TTD contribution at various surface temperatures as displayed in the right panel. The results obtained for $E_i = 0.76$ eV, $\theta_i = 40°$, $\theta_f = 20°$ and $\phi_i = 0°$ are also displayed here. For those surface temperatures where the DIS and TTD contribution cannot clearly be distinguished in the TOF spectra, the values for the flux, v_β and T_α of the DIS distribution were fixed to the values found at lower surface temperatures. No change of these parameters was observed when changing the surface temperature for which both contributions still can be distinguished. Above $T_s = 350$ K the fitting procedure did not yield satisfactory results, because the overlap between the two contributions became too large.

The TTD energy values show to be linearly dependent on the surface temperature. Drawing a straight line through the data points yields an offset of 0.06 eV for $T_s = 0$ K and a slope $\Delta E / \Delta T_s = 6.02 \times k_B / e$ [eV K^{-1}], with k_B Boltzmann's constant and e the unit charge (to express the energy in eV). Both v_β and T_α increase with increasing surface temperature.

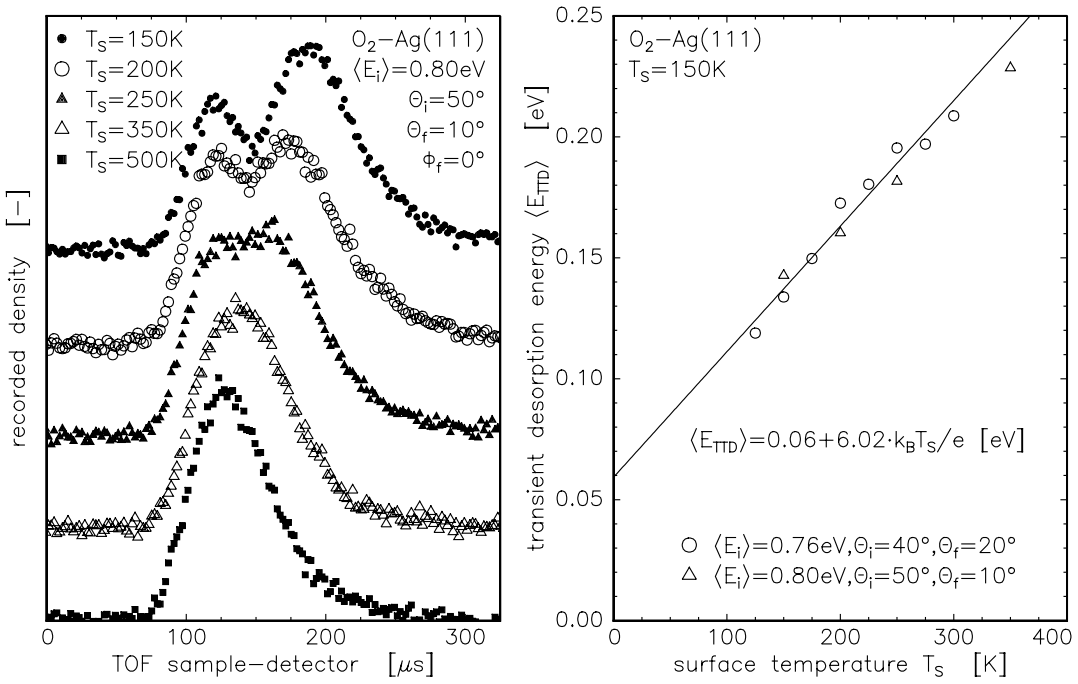

Figure 4.4 *The left panel displays the TOF spectra for $E_i = 0.80$ eV O_2 molecules, incident at $\theta_i = 50°$ and detected in the plane of incidence at $\theta_f = 10°$, for various surface temperatures. In the left panel the energy of the (fitted) TTD contribution is shown for the the scattering parameters of the left panel and another set of scattering parameters. The line is a linear fit to the data and is described by the displayed equation.*

The analysis of the data so far ignored a possible surface residence time of the molecules. This assumption will now be reexamined. We tried to fit the TTD contribution with a Maxwell-Boltzmann distribution also convoluted over a surface residence time, which did not lead to satisfactory results. To fit the TOF spectra taken at the different surface temperatures, we had to assume a desorption energy of $E_{\rm des} = 20$ meV and a prefactor of $\nu_{\rm des} = 6 \times 10^4$ s^{-1}. Assuming a simple Arrhenius behaviour the desorption rate constant $k_{\rm des}$ and the surface residence time $\tau_{\rm des}$ are expected to be given by

$$k_{\rm des} = \frac{1}{\tau_{\rm des}} = \nu \, \exp\left(-\frac{E_{\rm des}}{k_{\rm B}\, T_{\rm s}}\right) \quad . \tag{4.1}$$

These values are quite unphysical and lead to an extremely small change in the residence time from $\tau_{\rm des} \approx 100$ μs at $T_{\rm s} = 125$ K by about a factor 3 to $\tau_{\rm des} \approx 35$ μs at $T_{\rm s} = 300$ K. The flux intensity of the TTD contribution also decreases drastically, according to the fit, with increasing surface temperature when taking these surface residence times into account. Not taking the surface residence time into account results in a flux of the TTD contribution which is not dependent on the surface temperature. It was concluded that a surface residence time of the oxygen molecules does not play a role at the surface temperatures of these experiments. Assuming a residence time of $\tau_{\rm des} < 1$ μs at $T_{\rm s} = 125$ K and $\nu_{\rm des} = 10^{13\pm2}$ s^{-1} leads to an upper limit for the desorption energy of $E_{\rm des} = 0.17 \pm 0.05$ eV.

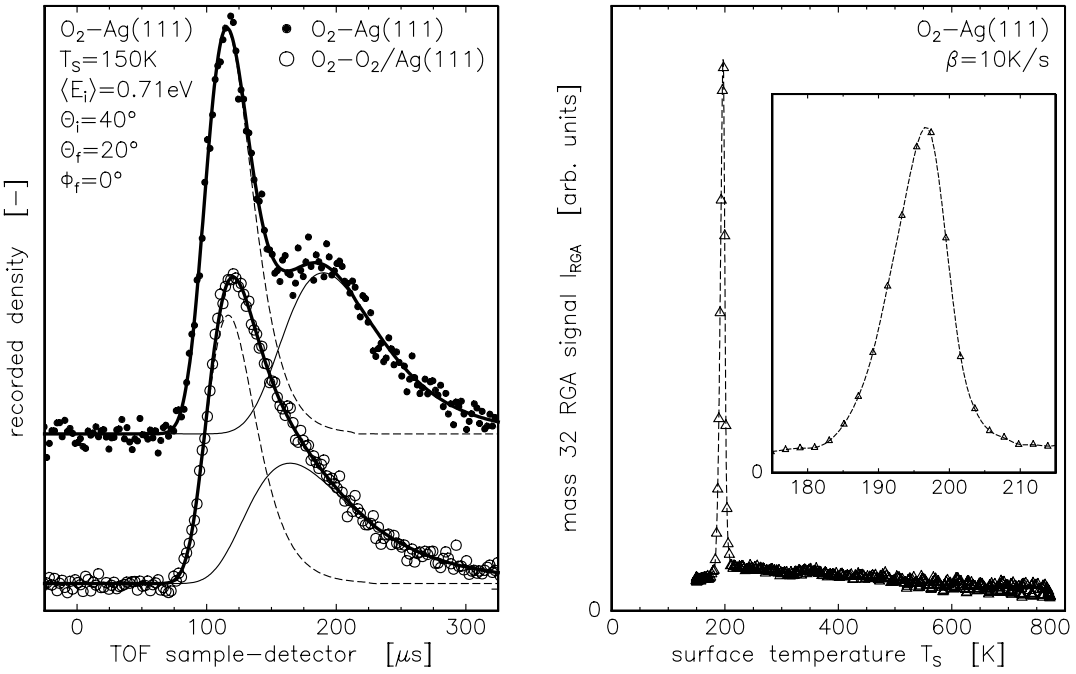

Figure 4.5 *In the left panel the TOF spectra are shown for oxygen molecules scattered from a clean surface and a surface after a large dose of molecular oxygen and are taken for* $\theta_i = 40°$, $\theta_f = 20°$, $\phi_f = 0°$, $T_s = 150$ *K and* $E_i = 0.71$ *eV. The lines are a result of fitting two Maxwell-Boltzmann distributions to the TOF spectra; the dashed line for the DIS, the full line for the TTD contribution and the thick line the sum of both contributions. In the right panel the TPD spectrum after the oxygen dose is shown taken at a linear heating rate of* $\beta \approx 10$ *K* s^{-1}. *The line in this panel is a guide to the eye only.*

4.3.4 Trapping probabilities

Knowing the angular desorption distribution of the TTD contribution we can extract the relative trapping probability by dividing the TTD fluxes shown in figure 4.2 by $\cos^{15}\theta_f$ and normalising the result. The same can be done for the trapping in the physisorption state assuming an angular desorption distribution of $\cos\theta_f$ from this state. Both relative trapping probabilities are linked. If one absolute trapping value is known, the relative trapping probabilities can then be converted into absolute trapping probabilities.

To estimate the magnitude of the trapping probabilities a calculation based on hard cube scattering for trapping in the physisorption well following a procedure as given by Kuipers [153] is carried out. As the O_2 molecule approaches the surface it will be accelerated in the physisorption well (and gain the energy of the well in the translational energy) and then transfer energy to the surface in the collision. After the collision the molecule is decellerated again when leaving the physisorption well. If the translational energy of the molecule now becomes negative it cannot escape the well and will become trapped at the surface. The trapping probability is dependent on surface temperature, well depth and the (effective) cube mass in the collision. The cube mass is in general larger then the mass of one silver atom. Only momentum perpendicular to the surface is exchanged in a

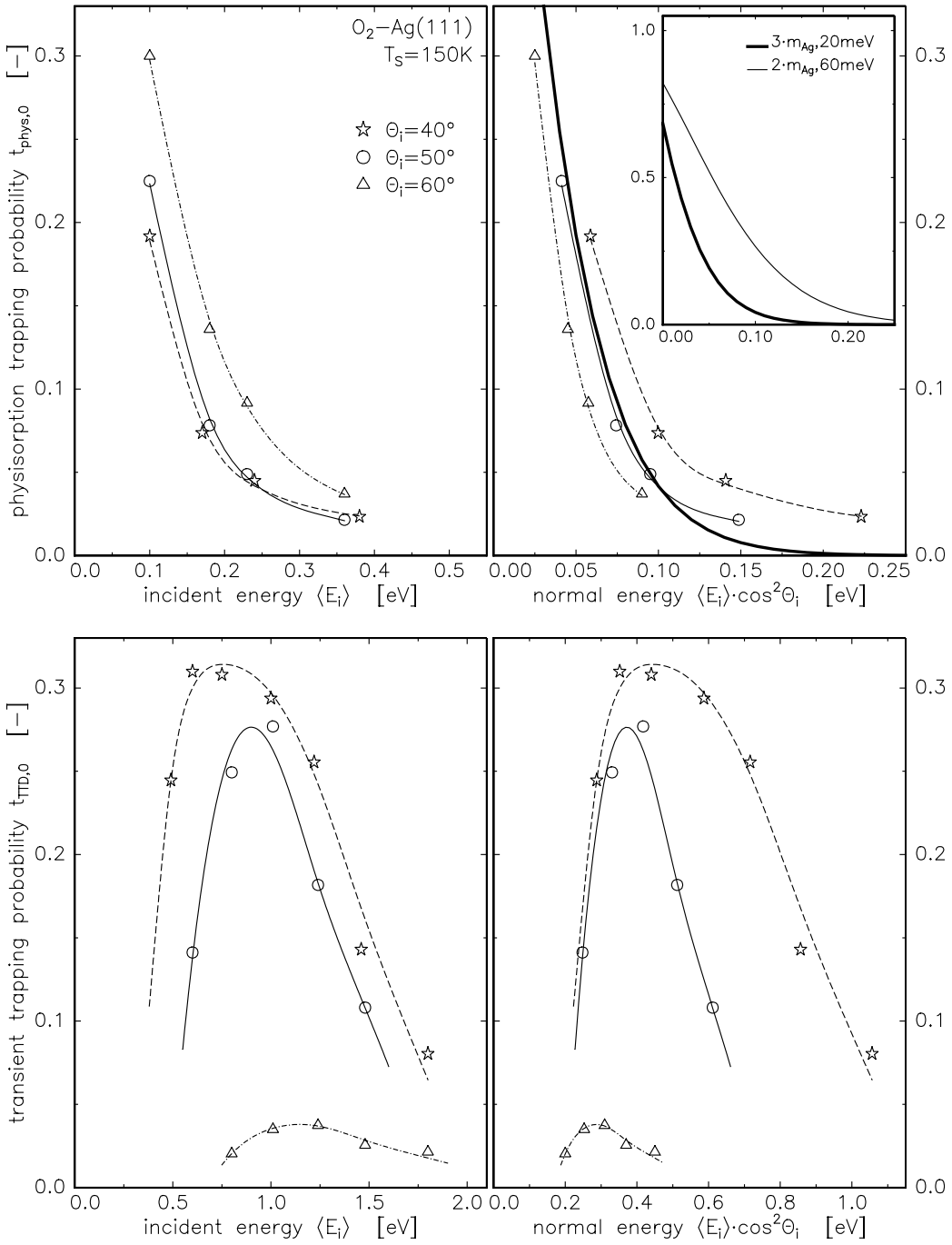

Figure 4.6 *Trapping probabilities in the physisorption (upper panels) and transient* O_2 *state (lower panels) for three different incident angles as function of incident energy (left panels) and normal incident energy (right panels). The lines through the data points are a guide to the eye only. The lines in the inset of the upper right panel and the thick line in the upper right panel are a result of hard cube calculations for the parameters as indicated. The values for the trapping probabilities are a rough estimate only and are based on the hard cube calculations.*

(flat) cube collision, so the trapping can only be calculated as function of normal incident energy. For our estimate we used a well depth of 20 meV and an effective cube mass of three times the mass of one silver atom ($m_{\mathrm{Ag}} = 108$ amu). A calculation with twice the silver mass and a well depth of 60 meV is also carried out, resulting in larger values for the trapping probabilities. Lines according to both calculations together with the (crude) estimate for the trapping probabilities in both the physisorption state and the transient state are shown in figure 4.6. The upper panels show the trapping in the physisorption state and the lower panels the trapping in the transient state both as function of total and normal incident energy, shown in the left and right panels, respectively. It is observed that trapping in the physisorption state decreases with increasing incident energy, as is expected. The energy scaling is intermediate between total energy and normal energy scaling showing that parallel momentum enhances the physisorption trapping probability but that the normal momentum is still the dominant momentum component. Plotting the physisorption trapping as function of $E_{\mathrm{i}} \cos\theta_{\mathrm{i}}$ (not shown) gives a very good overlap of the three trapping curves.

Trapping in the transient state is activated and shows a normal incident energy threshold just below $E_{\mathrm{i}} \cos^2\theta_{\mathrm{i}} = 0.2$ eV. For incident energies exceeding $E_{\mathrm{i}} = 1$ eV the transient trapping decreases again. Plotted as function of incident energy, the transient trapping curves for $\theta_{\mathrm{i}} = 40°$ and $50°$ almost overlap for energies larger than 1 eV. The transient trapping curve for $\theta_{\mathrm{i}} = 60°$ is considerably lower. The maximum transient trapping observed is approximately 30%, which is a quite large.

4.3.5 Azimuthal dependence

For $E_{\mathrm{i}} = 0.76$ eV, $\theta_{\mathrm{i}} = 40°$, $\theta_{\mathrm{f}} = 20°$, $\phi_{\mathrm{f}} = 0°$ and $T_{\mathrm{s}} = 150$ K the azimuthal angle ϕ_{i} was changed over $60°$ in steps of $10°$. The azimuthal angle ϕ_{i} is the angle between the plane of incidence and a defined direction on the sample surface (see figure 2.4). No change in the DIS nor in the TTD was observed and therefore it is concluded that the azimuthal orientation of the crystal is not important in the scattering processes.

4.3.6 Dependence on oxygen coverage

Most of the experiments presented here are carried out below the desorption temperature of molecularly adsorbed oxygen (approximately 200 K) and are thus also below the desorption temperature of atomically adsorbed oxygen (approximately 600 K). Oxygen adsorption is expected to modify the scattering process. Figure 4.5 shows the TOF spectra of oxygen scattering from a clean surface and from a surface partly covered by oxygen for $E_{\mathrm{i}} = 0.76$ eV, $\theta_{\mathrm{i}} = 40°$, $\theta_{\mathrm{f}} = 20°$, $\phi_{\mathrm{f}} = 0°$ and $T_{\mathrm{s}} = 150$ K. The intensities of both spectra are in the same units. It is clearly seen that oxygen adsorption does not only lead to a (slight) decrease in scattered intensity, but also causes the TTD contribution to become much faster.

Again fitting shifted Maxwell-Boltzmann distributions to the TOF spectra shows the energy of the TTD contribution to increase from 0.14 eV for the clean surface to 0.22 ± 0.04 eV for the oxygen covered surface. However, the flow velocity v_β hardly changes and thus does not account for the energy increase. This increase is due to an increase of the width of the energy distribution of the TTD contribution; it increases from $T_\alpha \approx 125$ K to

$T_\alpha = 450 \pm 150$ K. Due to the large overlap of both the DIS and the TTD contribution, the fits are a bit ambiguous. The flux in the DIS contribution has decreased for the oxygen covered surface and the flux in the TTD contribution shows to be equal or even to have increased.

Doing a temperature programmed desorption (TPD) measurement after the scattering experiments shows a clear desorption peak at 200 K and no noticable desorption around 600 K. This implies that the TOF spectrum for the covered surface represents scattering from a Ag(111) surface partly covered by molecular oxygen. The asymmetric shape of the TPD signal as function of surface temperature is a characteristic of first order desorption kinetics.

From the helium reflectivity measurement performed during the dosing of O_2 and comparing it with a helium reflectivity study presented elsewhere [124, chapter 5] we estimate the coverage after dosing about $\psi = 0.03$ ML. One monolayer (ML) is defined as 1 O_2 molecule per Ag surface atom.

4.4 Discussion

From scattering experiments of oxygen from the Ag(111) surface done at $T_s = 600$ K surface temperature it was concluded that for normal incident energies above a threshold the chemisorption part of the potential is probed by (part of) the incident flux [186, chapter 3]. An upper limit for this threshold is $E_i \cos^2 \theta_i = 0.3$ eV. For incident energies exceeding this threshold more of the incident flux probes the chemisorption part of the interaction potential until a saturation is reached. It was concluded that at this incident energy (almost) all the incident flux samples the chemisorption interaction.

This conclusion is supported by the results presented here. It is seen that at low incident energies ($E_i \leq 0.3$ eV) hardly any direct-inelastic scattering is observed for angles θ_f close to the surface normal ($\theta_f \leq 20°$). We do observe desorption in the TOF characterised by a temperature slightly below the surface temperature and a zero flow velocity. Trapping in the state from which this desorption is observed, decreases with increasing incident energy. These observations are compatible with probing the physisorption regime in the O_2-Ag(111) interaction potential as can be concluded by comparing the results with low incident energy scattering results for physisorption systems [187,188].

For higher incident energies a sharp rise in direct-inelastically scattered intensity at $\theta_f \leq 20°$ is observed in the TOF together with a second trapping-desorption contribution. Both show the same energy threshold, which shifts to larger energies for the larger incident angles. The energy threshold can be expressed in a value for the normal incident energy and is about $E_i \cos^2 \theta_i \approx 0.2$ eV. The second trapping-desorption contribution observed is assigned as trapping-desorption because of

- the independence of its final energy on the incident energy,
- its intensity distribution which is peaked around the surface normal,
- its intensity distribution which is not dependent on the angle ϕ_f away from the plane of incidence,

- a strong dependence of its final energy on the surface temperature and
- the decrease in its intensity with increasing incident energy.

The last point is equivalent to a decreasing fraction of the incident flux loosing enough energy with increasing incident energy to be able to trap at the surface.

The question arises in what state does part of the oxygen flux trap above the energy threshold. The assignment of the state from which the TTD occurs cannot be determined from the data presented here in isolation from other results. It is obviously not due to molecular physisorption, because trapping in the physisorption state is observed at low incident energy. It also is not due to molecular chemisorption, because desorption from the molecular chemisorbed state should be observed at or above the desorption temperatures from these state (approximately 200 K). The entrance to this state is activated and the desorption energy from this state should be consideraby smaller than the desorption energy of the known molecular chemisorption state, because desorption without noticable residence time at the surface is observed even for a surface temperature as low as $T_s = 125$ K. Therefore, another unknown state of molecular adsorption of O_2 on Ag(111) has to be invoked. Because the adsorption into this state is activated, it seems reasonable to presume that the unknown state concerns a weakly bound chemisorbed molecule. We note that most clearly on Pd(111), but also on Pt(111) more than one molecular chemisorbed species has been observed. The nature of these species is not fully clear.

More light on the nature of this state could be shed if we new its relation to the well known molecular chemisorbed species, desorbing at $T_s = 200$ K. Therefore, we have carried out a study to characterise the adsorption into this molecularly chemisorbed state. Its results will be presented elsewhere, but we want to show one salient feature here. The initial sticking coefficient $s_{M,0}$ for molecular chemisorption is plotted together with the trapping probability $t_{TTD,0}$ for the TTD in the left panel of figure 4.7. The similarity is very striking and suggests that adsorption into both states is mediated by the same process.

The assumption that in the energy disposal step the same repulsive wall is seen calls for a comparison to direct-inelastic scattering. Therefore, the peak flux (the maximum intensity in the angular flux distribution) for DIS and the width of the DIS angular flux distribution is plotted in the right panel of figure 4.7. These measurements were carried out at a surface temperature of $T_s = 600$ K [186, chapter 3]. It is clear that DIS sets in around the incident energy where the molecular chemisorption and the TTD set in. Where the angular width of the DIS levels off as a function of incident energy, molecular chemisorption and TTD decrease. The DIS signal at this angle is attributed to scattering from the repulsive wall connected to chemisorption. Its onset coincides roughly with that for molecular chemisorption and the TTD, supporting that in all three processes the same wall is probed. The stabilisation of the width is attributed to the fact that all scattering is due to the molecular chemisorption wall. At this energy molecular chemisorption and TTD are less likely because the translational energy has a lower probability to be accommodated in a single collision.

Summarising, the data suggests that molecular chemisorption, TTD and DIS are all mediated by the same process. This makes it less likely that TTD is mediated by a state that is totally different from the molecular chemisorption state, here referred to by $O_2^{\delta-}$. By contrast, a dynamic difference may exist between the TTD and the molecular chemisorption.

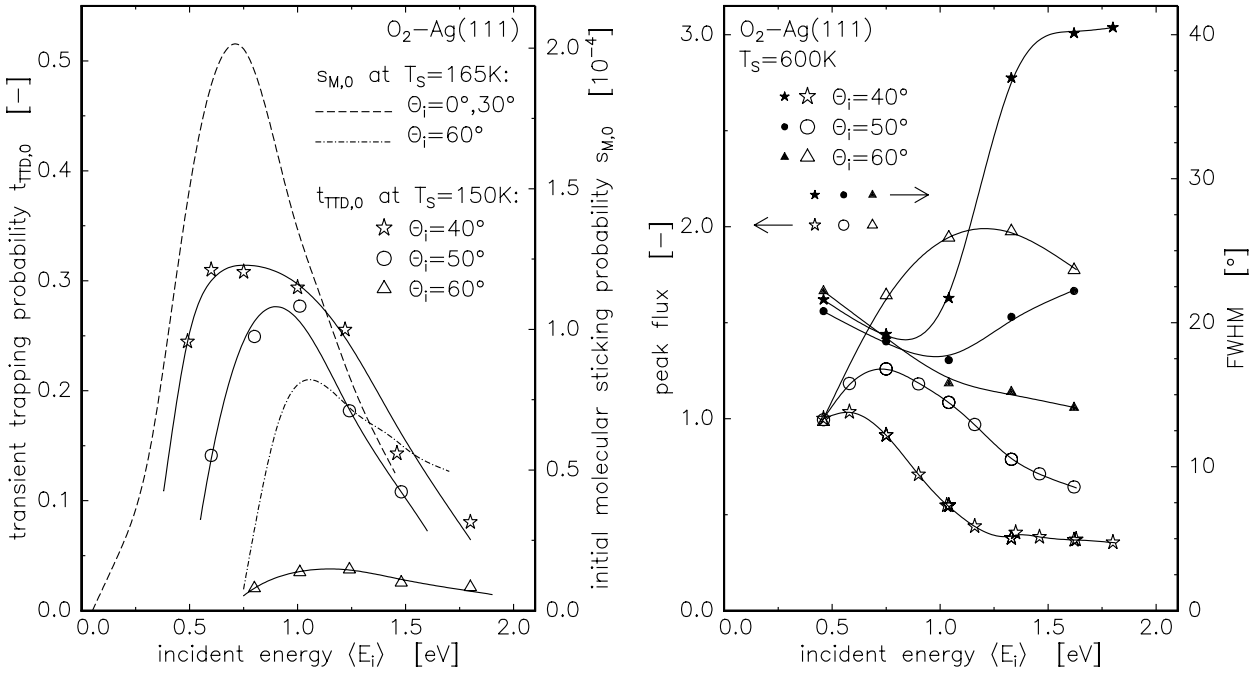

Figure 4.7 *An overlay of the transient trapping probability $t_{\mathrm{TTD},0}$ and the initial molecular sticking coefficient $s_{\mathrm{M},0}$ is shown in the left panel. The peak flux and FWHM of angularly resolved scattered flux distributions taken from O_2-Ag(111) scattering experiments done at $T_s = 600$ K are displayed in the right panel.*

The TTD channel may be due to dynamical, quasi-trapping in the molecular chemisorption well as predicted theoretically by Holloway and Gadzuk [181,183], Luntz [189] and Kosloff and Citri [185,109].

To understand the dynamics of the O_2-Ag interaction knowledge about the relevant potential energy surfaces is required. There are two recent surfaces available, a computed one for the O_2-Ag(110) interaction [71] and two quite similar empirical ones concerning O_2-Ag(111) [60,96,97,109,185]. The surfaces are presented as a function of the intramolecular distance of O_2 and of the O_2-Ag distance. No lateral variation is considered. Both surfaces show three wells for the physisorbed, the molecularly chemisorbed and the dissociated molecule. The molecularly chemisorbed species is separated from the other states by barriers or crossing seams. These barriers are insufficiently high to account for the observed barrier to molecular chemisorption and the surfaces need to be improved on this point. Both surfaces show that the molecularly chemisorbed O_2 in equilibrium is considerably stretched with respect to the free O_2 molecule. In addition, the chemisorbed molecule cannot desorb adiabatically without compression of its bond.

To describe the dynamics it is important to know if the interaction is occurring on the lowest (adiabatic) potential only or on several potential energy surfaces simultaneously, implying electronically non-adiabatic behaviour and a breakdown of the Born-Oppenheimer approximation. The latter point is considered by Kosloff and Citri [185,109]. In view of the rather low velocities involved and for simplicity we will assume that most of the dynamics

can be qualitatively explained using the lowest potential energy surface only. We note that Kosloff and Citri could not get quantitative agreement between theory and earlier experiments with the adiabatic ground state only.

If an O_2 molecule approaches the Ag surface it passes through the physisorption well and reaches the top of the barrier or crossing seam if it has sufficient energy. When it crosses the barrier to the $O_2^{\delta-}$ state the molecule is suddenly vibrationally excited. This vibrational excitation has been seen extensively in gas phase scattering [120,190]. The molecule cannot leave the $O_2^{\delta-}$ well as free O_2^- because it lacks translational energy to overcome the endothermicity of this process (workfunction minus electron affinity). At higher translational energies this is possible and has been observed [161,162,164]. The molecule, when further entering the $O_2^{\delta-}$ well, has three forms of energy: normal translational energy, parallel translational energy and vibrational energy. The equilibration of these forms of energy determines what the ultimate fate of the molecule will be. If the normal translational energy does not accommodate the molecule will recross the barrier and escape into the gas phase, provided it is again vibrationally compressed before it leaves into the gas phase. Trajectories for such situations have been computed by Holloway and Gadzuk [180]. One of their figures is reproduced here as figure 4.8. The frequency of the molecule surface vibration on both Ag(111) and Ag(110) is about 200 cm^{-1} and the intramolecular vibration frequency is about 650 cm^{-1}, resulting in vibrational periods of 160 and 50 femtoseconds, respectively [37,82]. Since the intramolecular vibration is fast an event like given in the trajectory of the left panel is not unlikely. It will result in direct inelastic scattering after a collision with the $O_2^{\delta-}$ repulsive wall. Elsewhere we have shown that this indeed occurs in direct-inelastic scattering [186, chapter 3]. When the molecule is not compressed it cannot escape, even when the molecule-surface separation is large. This is shown in the right panel of figure 4.8. It will be accelerated back to the surface and equilibrate. The trajectory in this figure does not equilibrate and desorbs eventually, because no dissipation of the energy of the molecule is taken into account in the calculation. This is indeed the case for O_2-Ag(111) because the incident conditions for which approximately 30% of the incident molecules transiently trap, yield a molecular sticking probability of about 2×10^{-4}. Other examples of trajectories quasi-trapped in the molecular chemisorption well can be found in figure 5 from a paper by Gadzuk [182].

Trajectory calculations for interactions with Ar atoms with flat Pt (111) and Ag(111) show that the equilibration normal to the surface is rapid: one or two bounces only [191,136,192]. The same studies have shown that the accommodation of the parallel momentum is very slow, exceeding a picosecond, due to the lack of corrugation of the surface. From our present work and earlier work by Spruit et al. on O_2 scattering from Ag(111) at high energies, we know that the Ag surface is very corrugated to the incoming O_2 molecule [65,67]. The same has been concluded for N_2 adsorption on W(110) [193–196]. Therefore we infer that the equilibration of the parallel momentum will occur within a picosecond. The molecule can at most make a few hops over the surface and visit a few sites. Finally, the equilibration of the vibrational motion is important. From direct measurements of the lifetime of vibrationally excited NO and CO on metal surfaces it is known that this time is a few picoseconds [197–200]. Therefore, the vibrational excitation lives longer than the other modes. At any time when the molecule is fully compressed, the barrier in the potential energy surface will be probed again and the molecule may desorb. Upon desorption

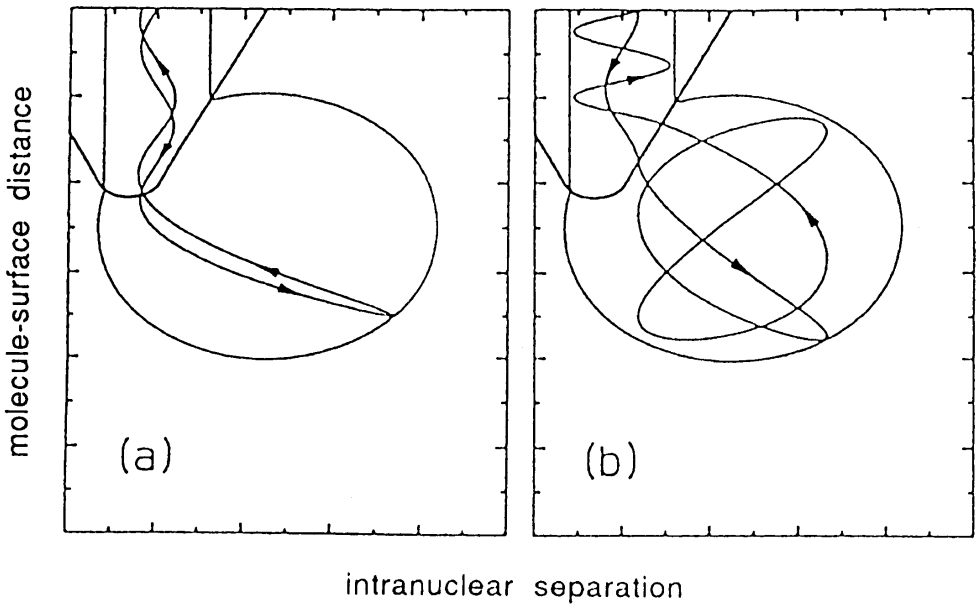

Figure 4.8 *Two types of trajectories sampling the chemisorption part of the molecule-surface interaction. Both trajectories escape again to the gas phase. Trajectory b shows a resonance character. The figure is taken from a paper of Holloway and Gadzuk [180].*

its memory of the initial conditions has been erased and the molecule appears fast, as is expected using a simple Van Willigen picture [201]. Thus we believe the long lived intermediate at the surface is a resonance in which the molecule resides at the surface while vibrationally excited. Upon desorption, the molecule will not be strongly vibrationally excited or not at all.

The final energy E_f measured is about $E_{TTD} \approx 0.14$ eV and more or less independent of incident energy. This and the independence on azimuthal scattering angle demonstrate the equilibration of the parallel and normal momentum of the molecule. At $E_i = 0.5$ eV beam energy the energy difference between TTD and DIS is about equal to one vibrational quantum of O_2. This may point to vibrational excitation of the O_2 after TTD. The strong energy dependence of the final energy difference between TTD and DIS does not support this picture. The final energy for TTD is most likely directly related to the barrier height for molecular chemisorption. For this process we observe a sharp increase above $E_i = 0.2$ eV. The desorption energy for TTD extrapolated to $T_s = 0$ K is about 0.06 eV. For hydrogenic systems these values are observed too and obey detailed balance [202,203]. The difference between the barrier heights determined for the present systems may be due to the fact that there is in fact a distribution of barrier heights [204] and due to recoil effects [24].

The temperature dependence of the final energy of TTD exhibits a $E_{TTD} = D + 6k_B T_s$ dependence, with D the value for E_{TTD} at $T_s = 0$ K and k_B Boltzmann's constant. When the molecule reaches the top of the barrier, it is expected to be about in equilibrium with the surface [205] and leave with an energy of $D + 2k_B T_s$. The factor of 6 observed rather than 2 is most surprising and not understood. It may be related to the fact that for desorption survival of the vibrational excitation of the molecule is required. This survival is expected to increase with increasing temperature of the electron gas of the solid, and therefore with

increasing T_s [206].

4.5 Conclusion

It is shown that that oxygen molecules colliding with a Ag(111) surface can trap in a physisorption state at low incident energy. For normal incident energies exceeding $E_i \cos^2 \theta_i = 0.2$ eV the molecules can dynamically trap in the molecular chemisorption state. This dynamic trapping is explained by vibrational excitation of the O_2 molecule when entering the molecular chemisorption well and an inefficient equilibration of the vibrational excitation. The trapping curve as function of incident energy and angle for the dynamic trapping shows a strong resemblance with the sticking dependence for molecular chemisorption. The peaked angular flux distribution and the translational energy far above thermal of the desorption from this dynamic trapping is explained by crossing a barrier above the vacuum zero level.

Chapter 5

Dissociative and Non-Dissociative Sticking of Oxygen at the Ag(111) Surface

Abstract *A molecular oxygen beam has been used to study the dissociative and molecular sticking probability at the Ag(111) surface as function of incident energy and angle, surface temperature and surface coverage. Two mechanisms are seen to play a role in the dissociative sticking: a direct one, due to thermally assisted tunneling, and a precursor mediated one. Both are strongly activated by incident energy. The molecular chemisorption state is shown to be the precursor to dissociation. Activation energies and frequency factors for desorption and dissociation rates are deduced from the analysis of TPD spectra.*

5.1 Introduction

Studying the adsorption of molecules at surfaces provides information on the potential energy surface of the molecule-surface interaction and thus ultimately on the bond breaking and making processes at surfaces. If a bond in a molecule is broken the dissociation fragments may react with other adsorbates present on the surface or impinging from the gas phase. Understanding the bond breaking mechanism will give greater insight into processes such as surface catalysis, etching and corrosion. The impinging molecule may adsorb in different states at the surface, such as a physisorption, a molecular chemisorption or a dissociated state. Access to the different states may be direct from the gas phase or via another state, which is then assigned as a precursor state.

In the case of H_2 on Cu surfaces it has been shown that the dissociated state can be accessed directly by increasing the translational energy of the impinging H_2 molecule [207–209]. Increasing the vibrational energy of the incident molecule also enhances the sticking probability. These results show that a barrier to dissociation exists at an extended H-H bond length which can be overcome by increasing the translational and/or the vibrational energy.

A system which shows an indirect, precursor mediated, dissociation process is N_2-Fe(111). Initially a molecular chemisorption precursor state is accessed directly. Subse-

quently a thermally activated process acts as the second step to dissociation, revealed in the surface temperature dependence of the dissociative sticking probability. This was shown to increase from 10^{-7} to approximately 0.1 by increasing the incident energy from thermal to over 3.5 eV [210].

The dissociation of O_2 on the Pt(111) surface shows two different channels to dissociative sticking. Below 0.1 eV incident energy the dissociative sticking has been shown to proceed via trapping into the physisorption state followed by a sequence of two thermally activated processes to dissociation. The molecule moves into the molecular chemisorption state and then into the dissociated state. At incident translational energies exceeding 0.1 eV the molecular chemisorption state can be accessed directly. In both energy regimes the dissociative sticking is thus precursor mediated and direct dissociation was not observed [211–214,145].

Gas-surface systems which show a temperature dependence in their dissociative sticking probability, but do not proceed via a precursor intermediate include CH_4-Pt(111) and O_2-Cu(100). Both systems show an increase in sticking with increasing surface temperature and in both cases the behaviour is explained by a coupling of the barrier to dissociation to the crystal lattice and thus the lattice vibrations. In the case of O_2-Cu(100) Hall et al. [24] demonstrated that the incident molecule transfers energy to the surface and the remaining energy is then used to overcome the barrier to dissociation. At a larger surface temperature less energy is transferred to the lattice and thus more translational energy is available for overcoming the barrier and thus sticking. These recoil effects in surface dissociation have been shown theoretically by Hand and Harris [215]. For CH_4-Pt(111) it has been shown that a moving barrier helps to increase the tunneling probability to dissociation, so-called thermally assisted tunneling [25,216,217]. A larger incident energy or a higher surface temperature brings the molecule closer to the top of the barrier and the tunneling probability to dissociation will increase.

The interaction of O_2-Ag has drawn quite some attention over the years and four different states of oxygen at the surface have been identified: a shallow physisorption, a molecular chemisorption, an atomic adsorption and a subsurface state. In the energy range 0–0.6 eV dissociative sticking on Ag(110) is activated and proceeds via the molecular chemisorption state [103]. The molecular chemisorption state is accessed directly from the gas phase and the physisorption state does not act as a precursor for either dissociative or non-dissociative sticking. The dissociative sticking probability increases from approximately 10^{-4} at low incident energy to approximately 0.5 for $E_i = 0.6$ eV at normal incidence to the surface. For the Ag(111) surface the dissociative sticking probability has been shown to be orders of magnitude smaller, even for incident energies as high as $E_i = 1.5$ eV [68]. For ambient oxygen adsorption it is also observed that sticking on Ag(111) shows a much smaller probability than on the Ag(110) surface [46,48].

In this paper we will present results on sticking of oxygen in the molecular and atomic chemisorption state at the Ag(111) surface as function of incident energy and angle of the O_2 molecules and as function of surface temperature. The observed dependencies will reveal the existence of two processes to dissociation. The uptake of molecular and dissociated oxygen and the desorption kinetics are also studied.

5.2 Experimental

The experiments have been performed in a molecular beam scattering machine described before [56,186, chapter 3]. Briefly, it consists of a triply differentially pumped molecular beam line connected to a UHV scattering chamber. The first stage contains the nozzle and the second stage of the beam line contains a chopper. Both a double slit 0.5% duty cycle chopper for time-of-flight (TOF) experiments and a 50% one for adsorption experiments are used. Not spinning the chopper and putting it in the open position results in a continuous molecular beam. A beam flag to switch the beam on and off is also present in the second stage. The third stage acts as a buffer chamber.

The molecular beam is generated by a supersonic expansion of a gas mixture of oxygen and helium from a 80 μm CW quartz nozzle. By changing the oxygen/helium ratio in the gas mixture and heating the nozzle (maximum temperature approximately 1100 K) we can vary the energy of the oxygen molecules to about 1.8 eV. Separate electronic flow controllers control the flows of oxygen and helium.

The sample is mounted in the middle of the scattering chamber on a 3-axis goniometer [125, chapter 2]. A quadrupole mass spectrometer (QMS) can be rotated around the sample to detect the particles leaving the surface. Combining the movements of the manipulator and the rotatable QMS gives accurate control (by computer) over the incident and exit angles of particles in the scattering experiment. By moving the sample out of the beam and the QMS into the beam path the TOF of the direct beam can be recorded. In this way the translational energy of the oxygen molecules is derived for the different nozzle temperatures and flow settings. The azimuthal angle can also be varied. ℓN_2-cooling allows a minimum sample temperature of about $T_s = 160$ K. Due to technical problems in cooling we could not reach a temperature as low as $T_s = 120$ K as was reached before [122,123, chapter 4]. The sample temperature is measured with a thermocoax K-type thermocouple inserted in the side of the sample and is controlled by a commercial controller. The controller also allows linear ramping of the sample temperature employed in this study for the temperature programmed desorption (TPD) measurements

A residual gas analyser (RGA) is present for monitoring the background gas and an ion sputter gun for cleaning the sample. Monitoring the background gas also gives values for incident flux and desorption rates in TPD experiments as will be shown below.

The samples are cut by spark erosion from a single crystal rod of 5N purity and polished by standard polishing techniques. Once in UHV the sample received a treatment of sputtering (500 eV Ar^+ ions) and annealing cycles until the angular width of the specularly reflected He-intensity was approximately 2°, which is the angular resolution of our experiment and determined by the divergence of the incident beam and the entrance aperture of the QMS detector. To further check the surface quality the system is also equipped with LEED and AES.

The RGA has been calibrated for the absolute oxygen partial pressure rise in the system. By letting in different flows of oxygen through a leak valve and reading the RGA signal I_{RGA} for the settings used during the experiments and the pressure given by the ionisation gauge the calibration factor between RGA reading and absolute pressure can be found. However, the ionisation gauge is calibrated for nitrogen. To correct this reading to a pressure for oxygen we took the manufacturer supplied conversion factor for CO (= 0.92). Since the

ionisation probabilities for O_2 and CO are identical as function of electron impact energy the conversion factors will also be equal. Knowing the partial pressure rise Δp due to incoming flux or desorption from the surface in pressure units now we can express it in amount per unit time by taking the ideal gas law and differentiating it with respect to time:

$$n = \frac{\Delta p\, V}{k_{\mathrm{B}}\, T} \quad \Longrightarrow \quad \frac{dn}{dt} = \frac{1}{k_{\mathrm{B}}\, T}\left[\frac{d(\Delta p)}{dt}\, V + \Delta p\, \frac{dV}{dt}\right] = \frac{V}{k_{\mathrm{B}}\, T}\left[\frac{d(\Delta p)}{dt} + \Delta p\, \frac{S}{V}\right] \tag{5.1}$$

$$\approx \frac{\Delta p\, S}{k_{\mathrm{B}}\, T} \qquad \text{if} \quad \frac{d(\Delta p)}{dt} \ll \Delta p\, \frac{S}{V} \ , \tag{5.2}$$

with n the number density, T the temperature of the system, $S = dV/dt$ the pumping speed, V the volume of the system and k_{B} Boltzmann's constant. dn/dt represents the flux in the beam or the desorption rate from the surface per unit time. Equation 5.2 only holds in a steady state equation and is usually also taken to be valid for measured TPD spectra provided the heating rate is not to high. Since the molecular beam diameter is known at the position of the sample the incident flux on the sample can be given in amount per unit surface area per unit time. The cross section of the beam has to be divided by $\cos\theta_{\mathrm{i}}$ to get the beam covered surface area. This covered surface area will yield the desorption in a TPD experiment. Now we are able to express incident flux I_{flux} and desorption rate I_{RGA} in amount per unit area and unit time and to express, after an integration over time, the molecular oxygen dose and desorption yield in amount per unit area. We have taken the pumping speed as given by the manufacturer ($S = 500\ \ell\ \mathrm{s}^{-1}$) of the turbomolecular pump pumping the UHV chamber in equations 5.1 and 5.2. This value of S will represent an upper limit as it will probably be somewhat reduced due to pumping resistances. The error in the cross section of the beam is estimated to be $\pm 10\%$. The surfaces coverages found in this way agree well with LEED observations.

For the TOF experiments the flight time of the oxygen molecule was measured from the 0.5% duty cycle chopper in the beam line to the rotatable QMS. The delay between the time pick off from the chopper blade and passing of the beam is calibrated by varying the chopper rotation speed. Detected particles, marking the end of the TOF, were counted by a home built multichannel scaler in 2 μs bins. In analysing the TOF spectra, the ion flight time through the QMS was subtracted from the TOF time axis. The recorded TOF spectra are fitted to shifted Maxwell-Boltzmann distributions convoluted over the finite chopper opening time yielding the mean energy per particle $<E_{\mathrm{i}}>$ in the beam [186, chapter 3]. In the text $<E_{\mathrm{i}}>$ will be replaced by E_{i}.

5.3 Results and Discussion

Initial sticking probabilities are derived by taking the ratio of the integrated TPD spectrum, the TPD yield Y, and the integrated oxygen partial pressure rise in the scattering chamber during dosing, the oxygen dose D. The integrations were carried out after subtraction of background taken linear in time. The settings of the RGA were identical for all measurements.

First results will be presented on the change of the sticking probabilities with surface coverage. From this a maximum TPD yield can be obtained for which an approximate

linear relation with the oxygen dose exists. If the relation between the sticking probability and the surface coverage is known the initial sticking probability can also be derived after a build up of such a large surface coverage for which the linearity does not hold. This has been carried out for both dissociative and molecular sticking. Helium reflectivity measurements as a function of oxygen coverage will also be presented, giving information on the surface structure during and after oxygen desorption

The initial sticking probabilities s_0 for both molecular and dissociative sticking will then be presented, followed by results concerning desorption, giving information on desorption energies $E_{\rm des}$ and prefactors $\nu_{\rm des}$.

Contrary to the results of the group of Rocca we encounter no problem in measuring dissociative and non-dissociative oxygen uptake at the Ag(111) surface in the incident energy region accessible in their setup ($E_{\rm i} \leq 0.6$ eV, $s < 10^{-4}$) [218]. Oxygen adsorption due to coadsorption with contaminations present in the beam (like H_2O) is very unlikely in our experiments. We monitored the specular He-intensity of a pure helium beam from a cold surface for several hours and could not measure an appreciable loss in He-intensity over that time. H_2O will also desorb from a Ag surface above $T_{\rm s} = 160$ K. The reason for the discrepency between our studies and the Genova group are not clear to us. At first we note that different probe methods are used (EELS versus TPD and He reflection). Secondly it is referred that substantial Ag mass transport occurs upon chemisorption. Therefore, the sticking coefficients may strongly depend on the precise condition of the crystal used.

We have only observed desorption around $T_{\rm s} = 200$ K and 600 K. In some cases desorption around $T_{\rm s} = 380$ K has been observed by others [28,45,83,99,100]. The molecular nature of this desorption feature was concluded from isotopic mixing experiments [45] and can be attributed to defects [99].

5.3.1 Dissociative oxygen uptake studied by TPD

The uptake of molecular and atomic oxygen has been studied as a function of the oxygen dose on the surface. Figure 5.1 shows the results for the dissociative oxygen uptake. For a number of different molecular oxygen doses D the desorption yield around $T_{\rm s} = 600$ K (integration of the desorption rate over time, yielding a number for the amount of desorbed oxygen molecules) is displayed in the top left panel. The uptake experiment was carried out for $E_{\rm i} = 1.54$ eV, $\theta_{\rm i} = 30°$ and a surface temperature of $T_{\rm s} = 400$ K. At these conditions the dissociative sticking probability $s_{\rm D}$ is about the largest attainable for the experimental conditions accessible in our setup, although it is still very small (approximately 10^{-3}). Due to the still very low dissociative sticking probability it took over 75 minutes (50% chopper) to reach the maximum coverage.

In the upper right panel of figure 5.1 TPD spectra for four different oxygen doses at a heating rate of $\beta \approx 10$ K s^{-1} are shown. A constant background has been subtracted from these spectra. It is seen that the spectra consist of two contributions. One populated at the lower coverages, and desorbing at this heating rate just above $T_{\rm s} = 600$ K, and one populated at larger coverages, and desorbing just below $T_{\rm s} = 600$ K. For the largest coverages the contribution at the higher temperature is hardly visible. In deriving the dissociative sticking probability both peaks are integrated. Later on we will discuss the two peaks in the recombinative TPD spectra.

It should be noted that the intensity axis is expressed in desorbing O_2 molecules per unit area per unit time. To be able to integrate it over surface temperature T_s it should first be converted to desorption per unit area per Kelvin:

$$\int_{t_1}^{t_2} I_{\mathrm{RGA}}(t)\,dt = \int_{T_{s,1}}^{T_{s,2}} I_{\mathrm{RGA}}(T_s)\,\frac{dt}{dT_s}\,dT_s = \int_{T_{s,1}}^{Ts,2} \frac{I_{\mathrm{RGA}}(T_s)}{\beta}\,dT_s \tag{5.3}$$

Both the desorption rate and the surface temperature are recorded as function af time, with the surface temperature increasing in a linear fashion β. We have integrated the TPD spectra over time, so a conversion to another integration variable was not needed. The peak desorption temperature for both contributions does not seem to depend on the oxygen coverage, pointing to first order desorption kinetics. However, the peak shape of the TPD spectrum is not in accord with first order desorption kinetics. We will come back to this later on.

The integrated desorption signal, the TPD yield Y, for the different oxygen doses lies quite nicely along a smooth curve, which should reflect the change of the dissociative sticking probability with increasing coverage ψ. The TPD yield is proportional to the surface coverage: $Y \propto \psi$. We have tried to fit these data for two models for the change of the sticking probability with coverage. One shows a change of the sticking probability s linearly dependent on the amount of free surface area (first order Langmuir behaviour)

$$s = s_0\left[1 - \frac{\psi}{\psi_{\max}}\right] = s_0\left[1 - \frac{Y}{Y_{\max}}\right] \tag{5.4}$$

and the other one, the Langmuir expression for dissociative adsorption, shows a quadratic dependence on the amount of free surface area

$$s = s_0\left[1 - \frac{\psi}{\psi_{\max}}\right]^2 = s_0\left[1 - \frac{Y}{Y_{\max}}\right]^2 \quad , \tag{5.5}$$

with s_0 the initial sticking probability, $\psi_{\max}$ the maximum oxygen coverage and $Y_{\max}$ the corresponding maximum TPD yield. According to the first model one available surface site is sufficient for dissociation. In the second model two adjacent free sites are needed for the dissociation as might be expected for the dissociation of a diatomic molecule. However, adsorbate interactions have been neglected in this interpretation. If two empty nearest neighbour sites are needed for dissociation both equation 5.4 and 5.5 can also be derived when assuming no interaction or strong attractive forces between the adsorbates, respectively [219]. The effect of the attractive interaction is the separation of the adsorbed layer in two phases: one corresponding to saturation and one to a bare surface.

The TPD yield differs by a factor 2 from the atomic oxygen coverage ψ_D, when expressed in amount per unit surface area, due to the recombination of two oxygen atoms to one oxygen molecule, which is detected by the RGA, in the desorption process: $Y = 1/2\,\psi_D$. Solving the differential equation

$$s = \frac{dY}{dD} \quad \Longleftrightarrow \quad \frac{dY}{s} = dD \quad , \tag{5.6}$$

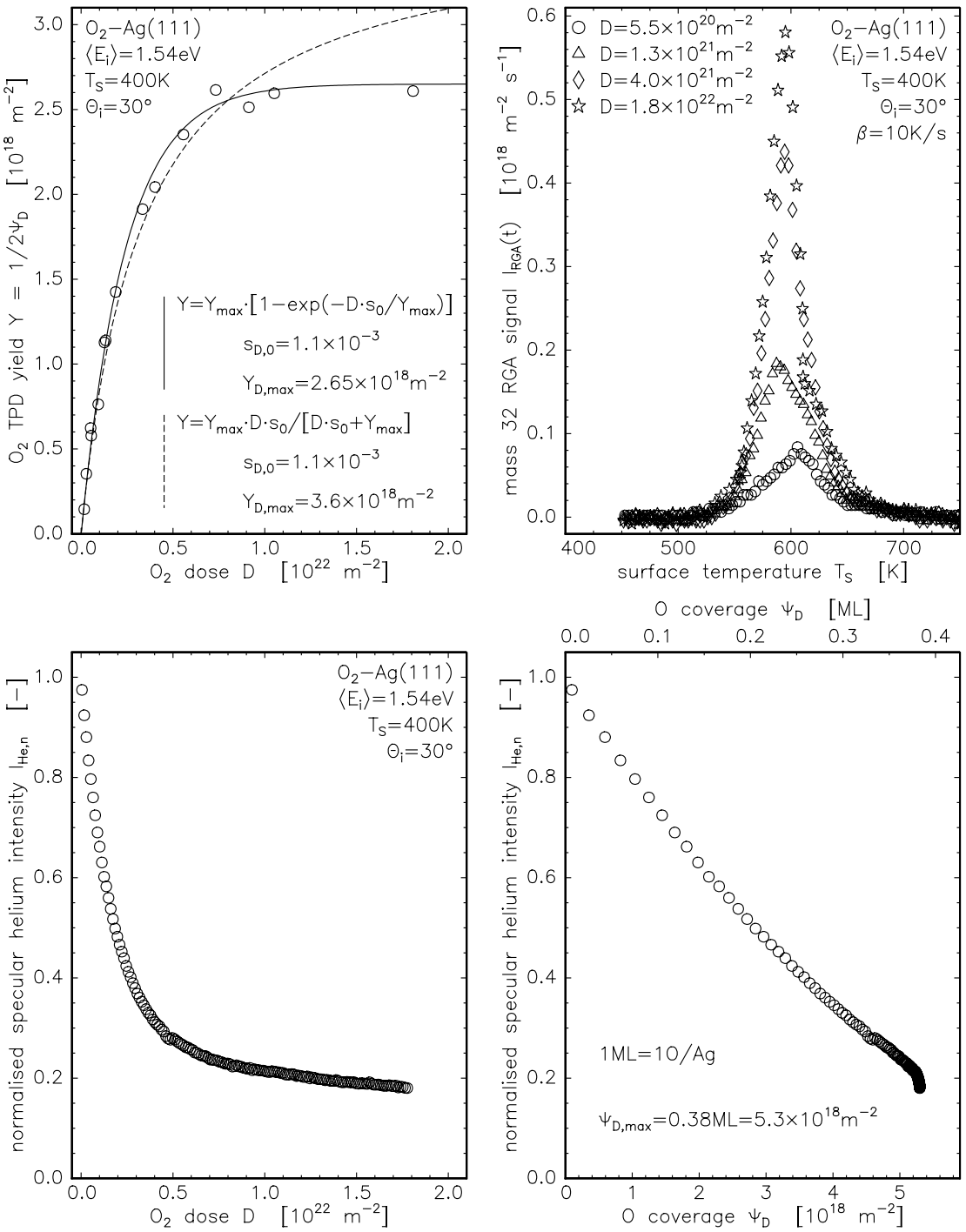

Figure 5.1 *In the upper left panel the integrated TPD peak area at the desorption temperature of 600 K is displayed as function of oxygen dose. A fitted line according to the formula shown is drawn through the data. Some TPD spectra are shown in the upper right panel. The lower left panels show the normalised He-intensity for the same incident parameters as hold for the upper right panel as function of both O_2 dose and atomic oxygen coverage. The lower right panel shows the normalised He-intensity as function of atomic oxygen coverage, derived by using the relation between O_2 dose and TPD yield from the upper left panel.*

with D the molecular oxygen dose, gives the expressions for the TPD yield Y as function of dose D for both models of the sticking probability:

$$Y = Y_{\max}\left[1-\exp\left(-\frac{D\,s_0}{Y_{\max}}\right)\right] \quad \text{and} \tag{5.7}$$

$$Y = \frac{Y_{\max}\,D\,s_0}{D\,s_0+Y_{\max}} \quad , \tag{5.8}$$

respectively. Equations 5.4, 5.5, 5.6, 5.7 and 5.8 are generally applicable and we have not referred to dissociative or molecular sticking. We will refer to quantities dealing with the dissociated state with a subscript $_{\rm D}$ (e.g. $s_{\rm D}$) and to quantities dealing with the molecular state with a subscript $_{\rm M}$ (e.g. $s_{\rm M}$). Lines according to both models are drawn in the upper left panel of figure 5.1 and it is observed that the first one shows the best correspondence with the data. The measured maximum coverage was also found in the measurements displayed in figure 5.6, so only equation 5.4 can describe the dependence of the dissociative sticking on the surface coverage. Apparently, one free available site for adsorption is sufficient for dissociation or strong attractive forces exist between the adsorbed oxygen atoms. The values taken for both $s_{\rm D,0}$ and $Y_{\max}$ in both models are shown in the figure. The maximum coverage is observed to be $\psi_{\rm D,max}=0.38$ ML, with 1 ML defined as 1 O atom per Ag surface atom. Since the distance between the Ag atoms at the Ag(111) surface is 2.89 Å, the area of one surface atom is approximately 7.23 Å^2.

5.3.2 Dissociative oxygen uptake studied by MBTEAS

The bottom left panel of figure 5.1 shows the specular helium intensity of the Ag(111) surface as it becomes covered with atomic oxygen during dosing with molecular oxygen. For this we use the He seeding gas in the beam as a probe for the oxygen surface coverage. Since the He-reflectivity of the surface is very sensitive to adsorbates present (large scattering cross section for He) the specular He-intensity will decrease upon increasing surface coverage. This technique is known as thermal energy atom scattering (TEAS) or helium atom scattering (HAS) and is described very well in a book by Poelsema and Comsa [5]. As we use a mixed beam of probe particles and oxygen molecules we refer to it as mixed beam TEAS (MBTEAS) [68]. The incident conditions are the same as for the uptake experiments in the upper panels. Performing the experiments at $\theta_{\rm i}=30°$ allowed us to monitor the specular He-intensity. For smaller incident angles our detector cannot reach the He-specular and for larger incident angles the sticking coefficient drops sharply.

It is seen that for oxygen doses for which the maximum coverage is reached the surface is still reflective for helium. In the past this asymptotic behaviour was explained by a removal reaction, responsible for removing oxygen from the surface [68]. However, monitoring the reflectivity of the covered surface with a pure helium beam did not show an increase of the reflectivity under normal working pressures. A background pressure of 5×10^{-8} mbar H_2 was needed to see a removal reaction from the surface. Our TPD studies show that the uptake has vanished at high coverage. We conclude therefore that the remaining He-reflectivity was not due to a clean off reaction but a property of the oxide covered surface.

Knowing both the normalised specular He-intensity $I_{\rm He,n}$ and the atomic oxygen surface coverage $\psi_{\rm D}$ as a function of molecular oxygen dose we know the He-reflectivity as a function

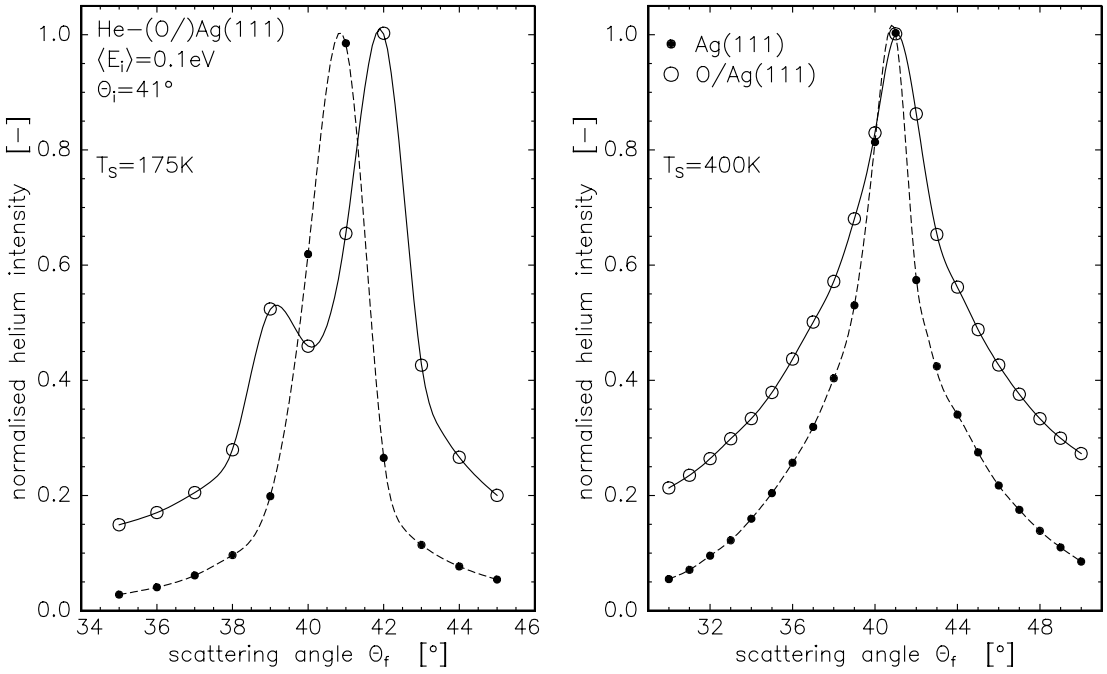

Figure 5.2 *Angular resolved He-intensity for a clean and atomic oxygen covered Ag(111) surface, O/Ag(111)(4×4), for two surface temperatures.*

of oxygen coverage as is shown in the lower right panel of figure 5.1. An almost linear relationship between He-reflectivity and atomic oxygen coverage is observed and now a value for the scattering cross section of atomic oxygen for He, $\Sigma^{\mathrm{He}}_{\mathrm{O/Ag(111)}}$, can be given. The scattering cross section is defined in the limit of zero surface coverage (no overlap of cross sections) as

$$\Sigma^{\mathrm{eff}} = -\left.\frac{dI_{\mathrm{He,n}}}{d\psi}\right|_{\psi=0} \quad . \tag{5.9}$$

The scattering cross section depends on the angle of incidence of the incident helium due to shadowing effects and can approximately be accounted for by

$$\Sigma^{\mathrm{eff}} = \frac{\Sigma}{\cos\theta_{\mathrm{i}}} \quad , \tag{5.10}$$

with Σ the cross section for $\theta_{\mathrm{i}} = 0°$. Applying this to the helium scattering results of figure 5.1 yields a cross section of $\Sigma^{\mathrm{He}}_{\mathrm{O/Ag(111)}} = 18$ Å^2, which is a very small value compared to scattering cross sections found for other adsorbates [5]. For a surface fully covered with diffuse scatterers the He-reflectivity is also expected to drop to extremely small values, which is not observed in this case, which seems to saturate at about 20%. At the maximum coverage the reflectivity is still (slowly) decreasing, showing that some details of the dissociative oxygen uptake are not accounted for.

Figure 5.2 shows the angularly resolved normalised He-intensity for both the clean and atomic oxygen covered Ag(111) surface at a surface temperature $T_{\mathrm{s}} = 400$ K in the right

panel and $T_s = 175$ K in the left panel. A slight peak shift for the covered surface is observed with respect to the clean surface at $T_s = 400$ K. This shift becomes more obvious at the lower surface temperature as the widths of the distributions decrease. For the covered surface $T_s = 175$ K two peaks are observed about 1° shifted towards either side of the specular direction. The intensity in the subspecular peak is less than in the superspecular peak and the subspecular peak also shows a larger shift away from the specular direction. This peak splitting might be explained by a long range reconstruction of the surface upon oxidation, resulting in a long range "triangular" corrugation. He-reflection will in this case occur from two in opposite directions tilted surfaces (with respect to the bare Ag(111) surface). This picture is supported by STM measurements carried out on an oxidised Ag(111) sample (oxidised at $T_s = 900$ K and 1 bar oxygen pressure) by Bao and coworkers [98]. They also observe a long range corrugation with approximately 1 Å amplitude and 80 Å periodicity. As we have carried out the He-intensity measurements of figure 5.1 at $T_s = 400$ K the influence of a peak shift and splitting upon increasing oxygen coverage can be neglected. The asymmetry in the peak splitting can be explained by an asymmetric corrugation: one plane of the triangular corrugation showing showing a larger tilt and thus also occupying less surface area than the other plane. Less surface area will show a lower reflected He-intensity. Both from the clean and oxygen covered Ag(111) surface we did not observe first order He-diffraction peaks. This indicates that the oxidised surface must be smooth on the atomic scale, which is also indicated by the non-vanishing reflectivity of the oxygen covered surface.

A 4×4 LEED pattern is observed after reaching the saturation coverage as has been reported before for this silver surface [29,48] and was explained by the formation of a thin $Ag_2O(111)$ overlayer rotated over 30° into coincidence with the Ag(111) surface [29]. The Ag_2O layer has a cuprite structure consisting of a trilayer repeat unit: a hexagonal Ag layer surrounded by two hexagonal oxygen layers (0.68 Å distance). As the distance between the oxygen atoms in the layers is 6.69 Å and the distance between the Ag atoms of the bare surface is 2.89 Å one derives a coverage of $\psi_D = 0.373$ ML for one trilayer. We measure a maximum coverage of $\psi_{D,max} = 0.38$ ML and Campbell [48] derives a maximum coverage of 0.41 ± 0.04, both in good correspondence with the formation of one Ag_2O trilayer on the silver substrate. The distance between the Ag atoms in the $Ag_2O(111)$ tri-layer is 3.35 Å and 2.89 Å for the Ag(111) surface plane. Accounting for the 30° degrees rotation gives a misfit of approximately 0.4%, with the overlayer in need of more space. If the full misfit should give rise to a long range triangular relaxation then the planes would be tilted by approximately 5°. We find approximately 1° tilting based on the splitting of the specular He-reflectivity, indicating that the overlayer must be almost fully compressed. The formation of this oxide overlayer also explains the He-reflectivity still present after reaching the saturation atomic oxygen coverage and the absence of first and higher order defraction in the He-scattering. The adsorbed dissociated oxygen does not act as a purely diffuse scatterer, but merely as a reflective scatterer as was also observed for the H/Pt(111) system [5]. The difference in reflectivity for the clean and covered surface might also be caused by a large difference in Debye-Waller factor for scattering from the clean or oxidised surface.

5.3.3 Molecular oxygen uptake

Figure 5.4 shows the same information as displayed in figure 5.1, but in this case for the uptake of molecular oxygen. To prevent the oxygen from desorbing on the time scale of the experiment, the surface temperature has to be chosen well below the TPD peak desorption temperature. A surface temperature of $T_s = 165$ K seems low enough and due to technical problems in cooling we also could not go to a lower surface temperature. Dissociation of molecular oxygen in the heating process is absent for the Ag(111) surface as is observed in the TPD spectrum displayed in the upper right panel. This spectrum was measured [122, chapter 4], when cooling the sample posed no problem. Only desorption around $T_s = 200$ K is observed for adsorption at $E_i = 0.76$ eV, $\theta_i = 30°$ and $T_s = 150$ K and no (or negligible) dissociation has occured upon heating the sample. Since the maximum desorption temperature is just below $T_s = 200$ K, which is close to the starting temperature of the temperature ramp (when dosing at $T_s = 165$ K), the heating is not linear with time in the molecular desorption region and there is an overlap in desorption from the filament for heating the sample and the oxygen desorption from the sample surface. Background subtraction before integrating the TPD spectra is in this case more difficult leading to the spread in data points observed in the upper left panel of figure 5.4.

The lower panels of figure 5.4 again show the specular helium intensity upon molecular oxygen adsorption and it is observed that in this case the specular intensity goes to zero. Two inflection points are observed, marking a distinct change in the overlap of the helium scattering cross section of the molecular oxygen. Assuming the molecular oxygen to adsorb in an $n \times n$ overlayer, the inflection points seem to coincide with a 10×10 and a 4×4 overlayer when making a first estimate of the O_2 coverage from the upper left panel. Assuming a sticking probability linearly dependent on the molecular oxygen surface coverage, so according to equation 5.4, and assuming a maximum coverage of $\psi_{M,max} = 0.25$ ML (equivalent to a 2×2 overlayer) leads to the line shown in the upper left panel. Using this relation gives the specular helium intensity as a function of coverage, which is displayed in the lower right panel of figure 5.4. With any other assumption for values n of the $n \times n$ ordered overlayers the data could not be described.

Now an estimate for the value of the helium scattering cross section of the O_2 molecule adsorbed on the Ag(111) surface, $\Sigma^{He}_{O_2/Ag(111)}$, can be made. If the full surface hit by the molecular beam is covered with the 10×10 overlayer at the first inflection point ($I_{He,n} \approx 0.4$ at $T_s = 165$ K), the effective scattering cross section will be (1−0.4) times the surface area taken by $10 \times 10 = 100$ silver surface atoms, which is equivalent to about 723 Å^2. Correcting for the $\cos\theta_i$ dependence of the cross section gives a value of $\Sigma^{He}_{O_2/Ag(111)} \approx (1 - 0.4) \times 700 \times \cos\theta_i = 376$ Å^2. This value is rather large compared to the cross section for CO on the Pt(111) surface of $\Sigma^{He}_{CO/Pt(111)} \approx 125$ Å^2 [5]. However, it is observed that the specular helium intensity at the first inflection point is decreasing with increasing surface temperature at equal O_2 dose, suggesting an increase in the scattering cross section with increasing surface temperature and thus a lower cross section than the value derived at $T_s = 165$ K for lower surface temperatures. For Ag(110) surface disorder was observed in the temperature range beween $T_s \approx 150$ K and 200 K by ESDIAD [47] and EELS [106]. If this also occur for the Ag(111) surface than the change in reflected He-intensity at the first inflection point might be explained by a surface order/disorder transition and the

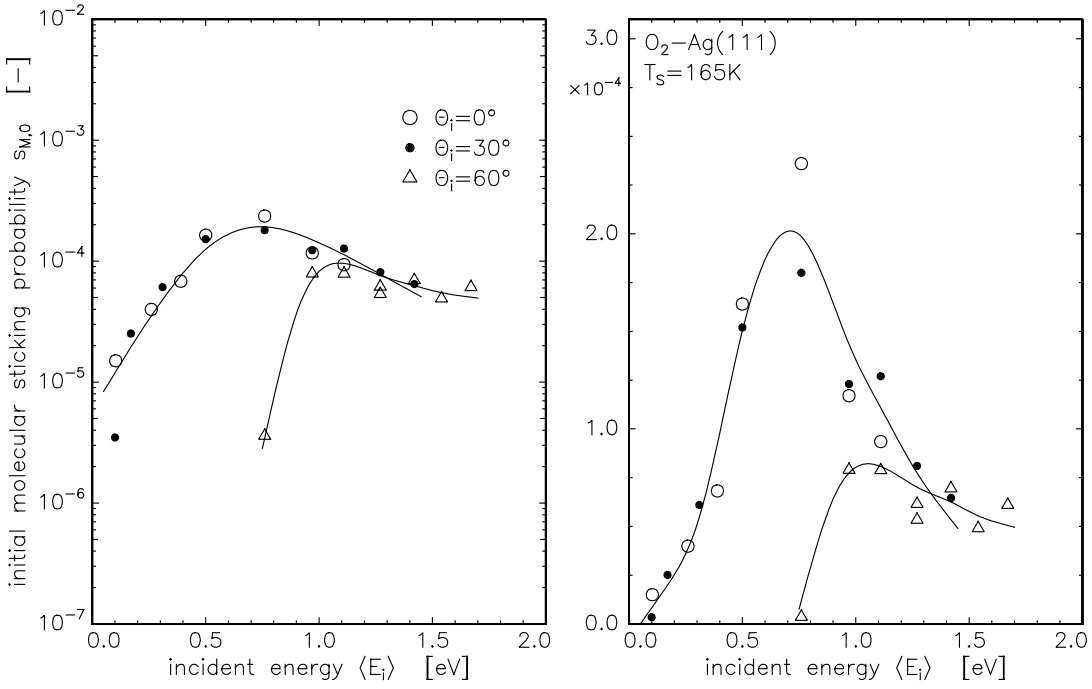

Figure 5.3 *Initial molecular sticking probability as function of incident energy for different angles of incidence. The full lines through the data points are a guide to the eye only and the dashed and dashed-dotted lines show the energy dependence of the transient trapping probability.*

derived value for $\Sigma^{\mathrm{He}}_{\mathrm{O_2/Ag(111)}}$ may not be meaningful. For the two surface temperatures $T_\mathrm{s} = 180$ K and 190 K molecular desorption from the surface is taking place. In the case of the saturated 4×4 overlayer ($4^2 \times 7.23 = 116$ Å^2) the cross sections overlap and the specular He-intensity should be approximately zero as is indeed observed after the second inflection point. Plotting the He-intensity logarithmically shows a still decreasing intensity after this inflection point. This indicates a further adsorption of molecular oxygen, which is compatible with the assumed saturation coverage of $\psi_{\mathrm{M,max}} = 0.25$ ML. We did not check the ordering of the adsorbed overlayer with LEED.

5.3.4 Initial molecular sticking coefficient

The initial molecular sticking probability $s_{\mathrm{M},0}$ measured at a surface temperature $T_\mathrm{s} = 165$ K is very small and never exceeds a value of $s_{\mathrm{M},0} = 3\times10^{-4}$ as is observed in figure 5.3. It was determined by taking the ratio of the time integrated O_2 pressure rise, as measured by the RGA, due to the desorption around $T_\mathrm{s} = 200$ K after dosing the sample with oxygen. Both integrations were carried out after a linear background subtraction. This method yields the molecular sticking probability since molecular dissociation upon heating the surface is negligible. The left panel of figure 5.3 displays the data on a logarithmic axis and the right panel on a linear axis. The sticking appears to be activated and the influence of a physisorption precursor is absent. The influence of a physisorption well would show up as an increase in sticking towards smaller incident energies, which is clearly not observed.

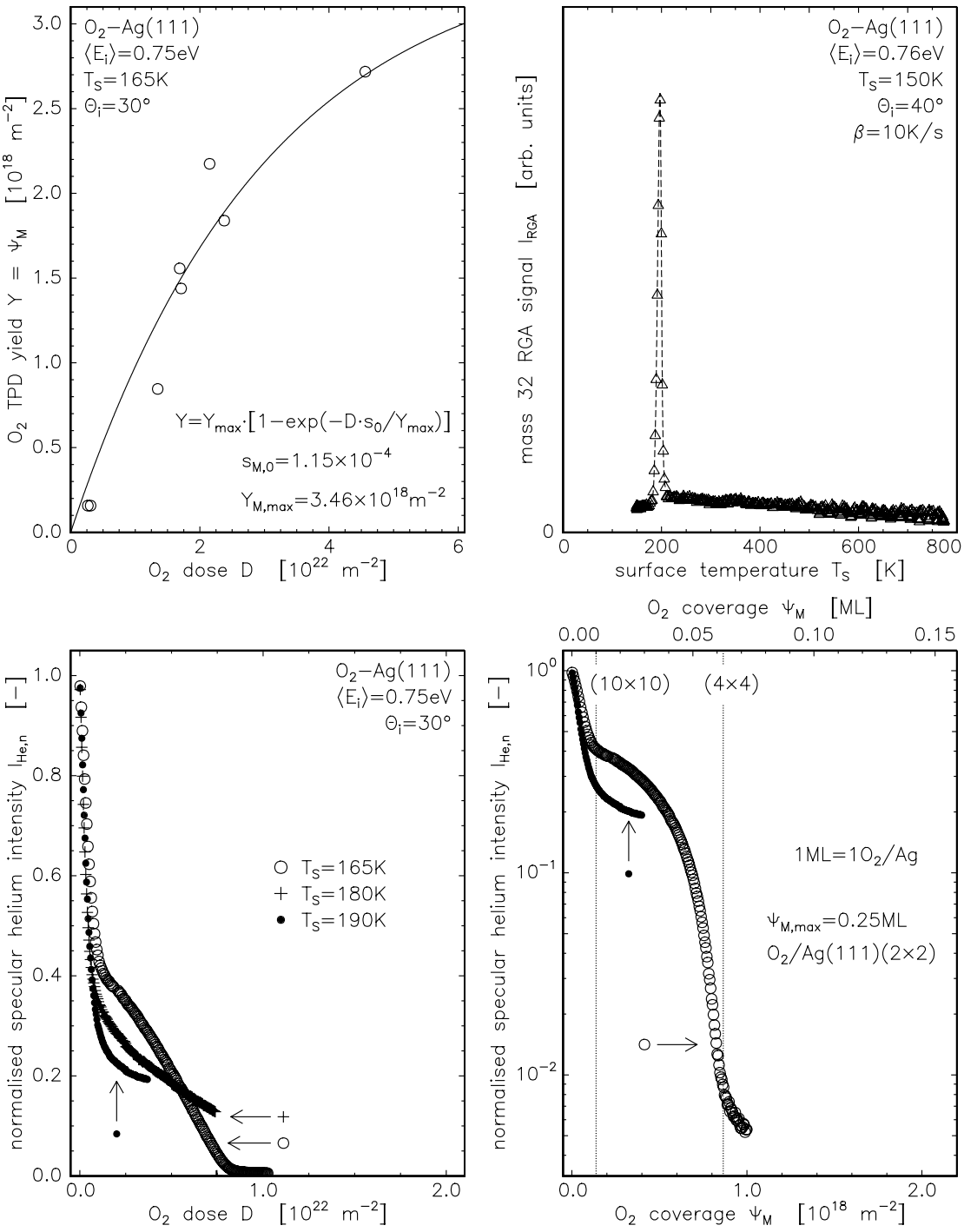

Figure 5.4 *In the upper left panel the integrated TPD peak area at the desorption temperature of 200 K is displayed as function of oxygen dose. A fitted line according to the formula shown is drawn through the data. A TPD spectrum is shown in the upper right panel. The lower panels show the normalised He-intensity, for the same incidence parameters as hold for the upper right panels, for three surface temperatures as function of both oxygen dose (left panel) and molecular oxygen coverage (right panel).*

The decrease in molecular sticking with increasing incident energy seen at larger incident molecular oxygen energies is in a regime where trapping in a physisorption state has reduced to zero [122, chapter 4]. The threshold energy for adsorption is observed to be much larger in the case of an incident angle of $\theta_i = 60°$. Results for $\theta_i = 0°$ and 30° cannot be distinguished.

In the right panel of figure 5.3 the trapping probability curves of a previously found transient oxygen state [122, chapter 4] are also shown. The correspondence between energy and angular dependence of the trapping in this transient state $t_{TTD,0}$ and the initial molecular sticking probability is remarkable, although not perfect.

5.3.5 Initial dissociative sticking coefficient

We have determined the initial dissociative sticking probability $s_{D,0}$ as a function of incident energy E_i, incident angle θ_i and surface temperature T_s as is shown in figure 5.5. All the dissociative sticking probabilities were determined above the desorption temperature from the molecular chemisorption state and well below the peak desorption temperature observed in the TPD experiments. The method employed was the same as for determining the molecular sticking probability except that now the $T_s = 600$ K desorption peak is integrated after a linear background subtraction. The upper left panel of figure 5.5 shows the incident energy dependence for two surface temperatures at $\theta_i = 30°$. Clearly two steps in the increase of the sticking probability are observed with increasing incident energy: at $E_i \approx 0.2$ eV and 1.2 eV for $T_s = 222$ K and at $E_i \approx 0.4$ eV and 0.9 eV for $T_s = 400$ K. Again the influence of the physisorption state is seen to be absent. The two steps in the sticking probability increase show an opposite temperature dependence and they will therefore be attributed to two different mechanisms to dissociation. The mechanism at work above the first step will be referred to as mechanism A. Mechanism B is the one working above the second step in the dissociative sticking increase. Both mechanisms are seen to overlap around $E_i = 1$ eV. At lower and higher incident energies one is dominant over the other. For mechanism A an enhancement of the sticking probability with decreasing surface temperature is seen and for mechanism B an enhancement with increasing surface temperature. Even for an incident energy as high as $E_i = 1.7$ eV the initial sticking probability remains below $s_{D,0} = 2 \times 10^{-3}$, but has not reached a saturation value or a maximum yet. The upper left panel also shows the relative amount of vibrationally excited oxygen molecules in the beam. Generally, it is assumed that rotational excitation cools very efficiently in the supersonic expansion from the nozzle, whereas the vibrational excitation does not [111]. Assuming the vibrational excitation to be given by the nozzle temperature results in the populations as depicted. Below $E_i = 0.5$ eV the nozzle temperature was constant. The population can be read from the vertical axis, but should be multiplied by 100. It is clearly seen that the energy dependence of the sticking does not follow the vibrational excitation in the beam. From this observation it cannot be concluded that vibrational excitation is not important in the dissociative sticking process. Clearly the incident energy is the most important parameter.

The different temperature dependencies are also obvious in the upper right panel showing the surface temperature dependence for a few incident energies at $\theta_i = 30°$. The two incident energies $E_i = 1.27$ eV and 1.54 eV show a monotonic increase of the dissociative sticking with increasing surface temperature T_s. At $E_i = 0.50$ eV a monotonic decrease is seen with increasing T_s and at $E_i = 0.97$ eV both an increase and a decrease in initial

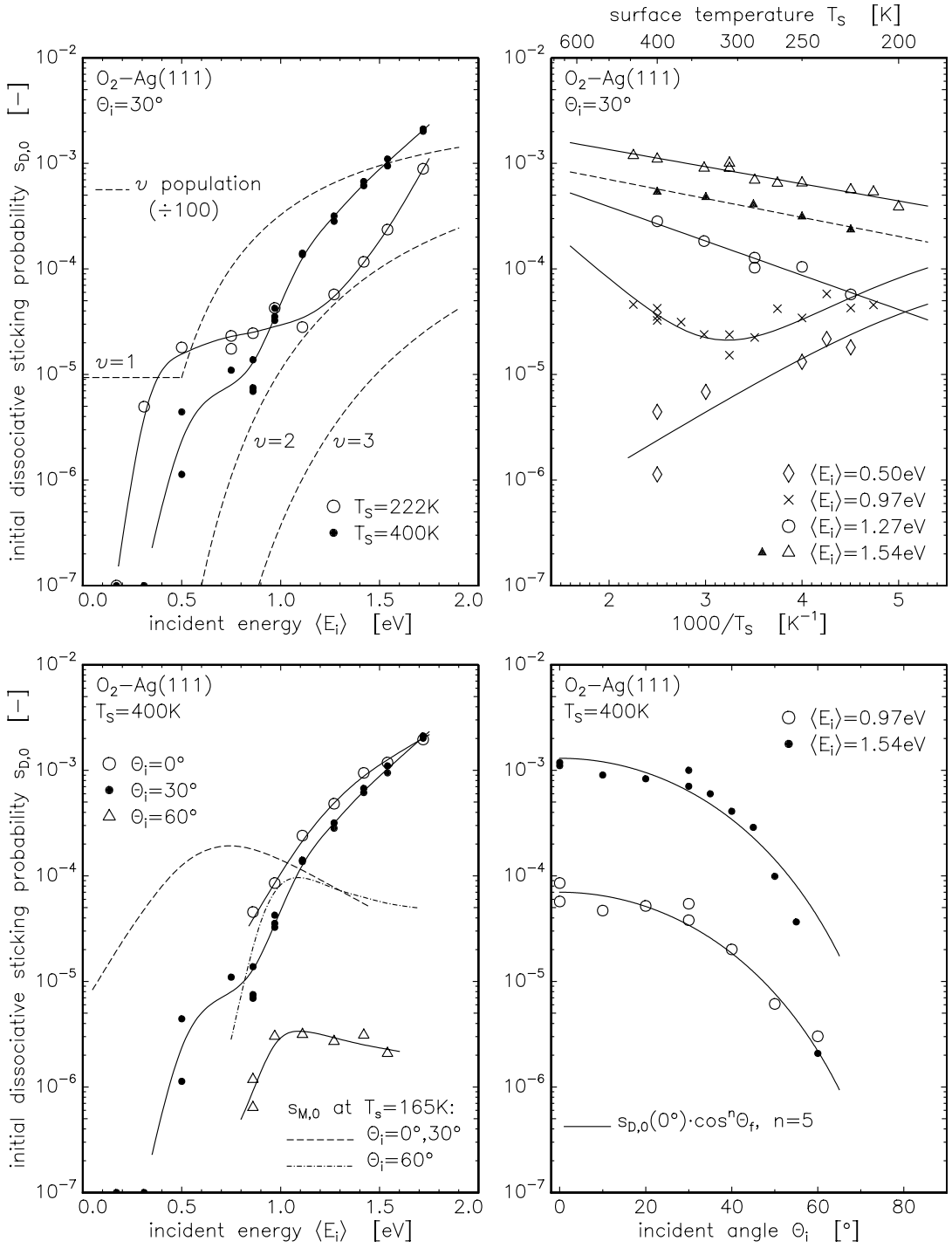

Figure 5.5 *Initial dissociative sticking probability as function of various experimental parameters. The full lines through the data points in the left panels are a guide to the eye only and the lines in the right panels are according to a formalism as described in the text. In the upper left panel the vibrational excitation in the beam is given by the dashed lines. In the lower left panel the energy dependence of the molecular sticking is given by the dashed and dashed-dotted line. The full lines in the lower right panel are according to the angular dependence displayed.*

dissociative sticking is observed in different temperature ranges. These findings clearly demonstrate once more the presence of two distinct mechanisms (denoted as A and B) in the dissociative sticking.

The lower right panel of figure 5.5 shows the incident angle dependence of the dissociative sticking for $E_i = 0.97$ eV and 1.54 eV at a surface temperature of $T_s = 400$ K. On the scale of the figure the sticking probability stays more or less constant up to $\theta_i = 30°$. With increasing incident angle a sharp drop in the dissociative sticking probability is seen. The sticking probabilities for both incident energies drop to about the same value at $\theta_i = 60°$. The lines through the data points are according to a $\cos^n \theta_f$, with $n = 5$. It only describes the $E_i = 0.97$ eV data quite well. In the lower left panel the incident energy dependence of the dissociative sticking is shown for three incident angles. Indeed, for $\theta_i = 0°$ and 30° the sticking probabilities are rather close for incident energies above $E_i = 0.97$ eV and at $\theta_i = 60°$ the sticking probability is greatly reduced. The sharp increase in sticking seen for $\theta_i = 0°$ and 30° above $E_i \approx 1$ eV is absent at $\theta_i = 60°$. It seems that only mechanism A operates for $\theta_i > 60°$ and that mechanism B is inaccessible.

A dependence of the dissociative sticking probability on T_s is anticipated if the dissociation proceeds via another state. First the molecule has to trap in this so called precursor state and then it can either dissociate or desorb. The dissociative sticking is then described by the trapping probability α in the precursor state and the ratio of the rate of dissociation and the sum of the rates of both dissociation and desorption from the precursor state. Assuming the rate constant k is given by an Arrhenius expression

$$k = \frac{1}{\tau} = \nu \exp\left(-\frac{E}{k_B T_s}\right) \quad , \tag{5.11}$$

with τ the characteristic surface residence time, ν the prefactor or frequency factor, E the activation energy for dissociation or desorption and k_B Boltzmann's constant, the temperature dependence of the dissociative sticking probability is described as

$$s_D = \frac{\alpha\, k_{diss}}{k_{diss} + k_{des}} = \alpha \left[1 + \frac{\nu_{des}}{\nu_{diss}} \exp\left(-\frac{E_{des} - E_{diss}}{k_B T_s}\right)\right]^{-1} \quad . \tag{5.12}$$

In the case of the desorption rate constant k_{des} being considerably larger than the dissociation rate constant k_{diss} in a certain surface temperature range the dissociative sticking probability is approximated by

$$s_D \approx \alpha \frac{k_{diss}}{k_{des}} = \alpha \frac{\nu_{diss}}{\nu_{des}} \exp\left(-\frac{E_{diss} - E_{des}}{k_B T_s}\right) \quad , \; k_{des} \gg k_{diss} \quad . \tag{5.13}$$

Obviously, s_D will never exceed α for precursor mediated dissociative sticking.

The lines drawn through the data points in the upper right panel are according to equation 5.12 and 5.13. For $E_i = 0.97$ eV the sum of two of the equations is taken (with different parameters); one dominant in the low surface temperature region and the other dominant in the high surface temperature region. Since the molecular sticking may possibly act as the precursor in the low surface temperature region and also for $E_i = 0.50$ eV in the whole temperature region sampled we took equation 5.12 for those cases (mechanism A) with α set to approximately the value found for $s_{M,0}$ at the same E_i and θ_i as for $s_{D,0}$. The

activation energy difference for desorption and dissociation was taken equal for both incident energies, $E_{\mathrm{M,des}}-E_{\mathrm{M,diss}}=0.11\pm0.04$ eV, just as the ratio for the prefactors, $\nu_{\mathrm{M,des}}/\nu_{\mathrm{M,diss}}=1000\pm750$. The given error bars are an estimate found by varying the parameters. For the trapping probabilities in the precursor state $\alpha=1.0\times10^{-4}$ for $E_{\mathrm{i}}=0.50$ eV and $\alpha=2.2\times10^{-4}$ for $E_{\mathrm{i}}=0.97$ eV are taken. It is assumed that molecular sticking does not occur via another precursor state and thus does not show a surface temperature dependence [220].

The lines in the high surface temperature region of $E_{\mathrm{i}}=0.97$ eV and through the data for $E_{\mathrm{i}}=1.27$ eV and 1.54 eV (mechanism B) are according to equation 5.13. The differences in activation energies found, using the formalism for precursor mediated sticking, are different for the three incident energies: $E_{\mathrm{diss}}-E_{\mathrm{des}}=0.159$ eV, 0.064 eV and 0.034 eV for $E_{\mathrm{i}}=0.97$ eV, 1.27 eV and 1.54 eV, respectively. For the axis intersection at infinate surface temperature an approximately equal value for all three incident energies was found: $\alpha\nu_{\mathrm{diss}}/\nu_{\mathrm{des}}=(2.4\pm0.8)\times10^{-3}$. One should realise that the data following mechanism B is described in terms of a precursor mechanism which is not the case as can be concluded from the different values for $E_{\mathrm{diss}}-E_{\mathrm{des}}$.

It is seen that for $E_{\mathrm{i}}=1.54$ eV two data sets are present for the surface temperature dependence of the initial dissociative sticking coefficient, which represents a sudden drop by a factor of about 2 in the dissociative sticking probabilities measured. However, all the trends in the dissociative sticking observed did not change. The cause for this drop is not known. Throughout all the experiments the surface received an equal treatment in cleaning, desorption, etc.

5.3.6 Recombinative desorption

It was already mentioned above that the TPD maximum did not shift in temperature with changing coverage (figure 5.1). This is a characteristic of first order desorption, although the shape of the TPD spectrum is not compatible with this kind of desorption. The top panels of figure 5.6 show a number of TPD spectra, taken at the same conditions as for figure 5.1 and after saturating the surface, but recorded with different heating rates. One observes that the shape of the spectra is first order-like for heating rates up to $\beta\approx5$ K s^{-1}. For larger heating rates the shape becomes rather symmetric. For heating rates below $\beta\approx5$ K s^{-1} also a peak shift as function of β is observed, which is absent above $\beta\approx5$ K s^{-1}. The symmetric shape for the recombinative desorption of oxygen from silver surfaces is also known from literature [45,48,84,85]. The TPD spectra were in these cases also taken at heating rates larger than 5 K s^{-1}. Again the intensity axes are not converted to desorption per unit area per Kelvin in figure 5.6. However, performing the proper integration of the TPD spectra leads to identical TPD desorption yields as is displayed in the bottom left panel.

One can derive a value for the desorption energy $E_{\mathrm{D,des}}$ by varying the heating rate and measuring the peak desorption temperatures T_{peak} for the different TPD spectra [221]. From the slope of the relation between $\ln(T_{\mathrm{peak}}^2/\beta)$ and $1/T_{\mathrm{peak}}$, as is shown in the bottom right panel of figure 5.6, the value for $E_{\mathrm{D,des}}$ is found. Using this value for $E_{\mathrm{D,des}}$ in the equation for first order desorption yields a value for the prefactor $\nu_{\mathrm{D,des}}$. These values govern the desorption rate of adsorbed atomic oxygen according to equation 5.11, with $k=k_{\mathrm{D,des}}$, $\tau=\tau_{\mathrm{D,des}}$ and $E=E_{\mathrm{D,des}}$. We find values for the desorption energy and prefactor

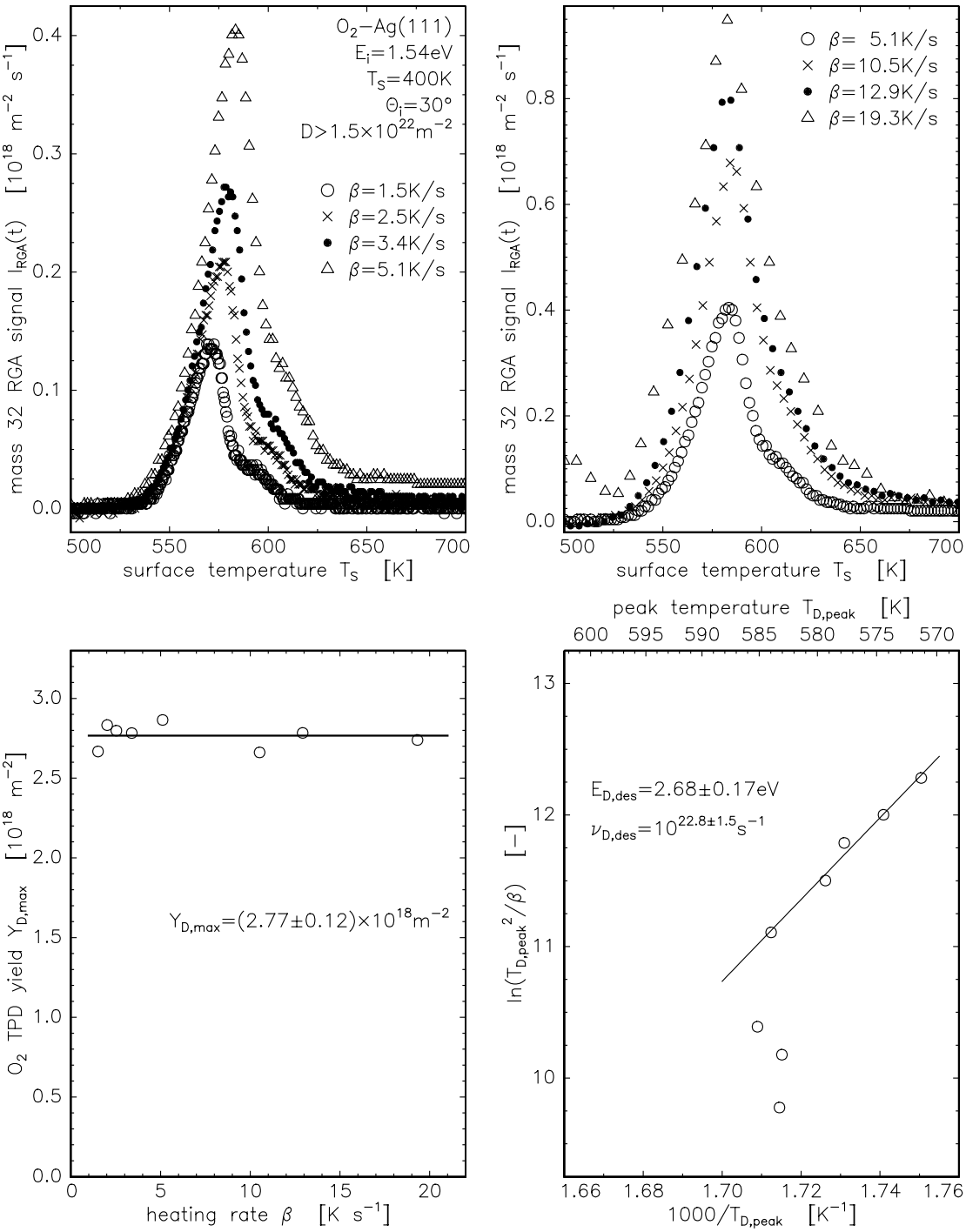

Figure 5.6 *The upper panels show TPD spectra for different ramp rates. Note that the intensity axes are not converted to desorption per Kelvin, but are still in desorption per second. The lower left panel shows the integrated TPD curve values for the different ramp rates and the lower right panel the TPD peak temperature shift for the different ramp rates plotted in such a way that the slope yields the activation energy* $E_{\mathrm{D,des}}$.

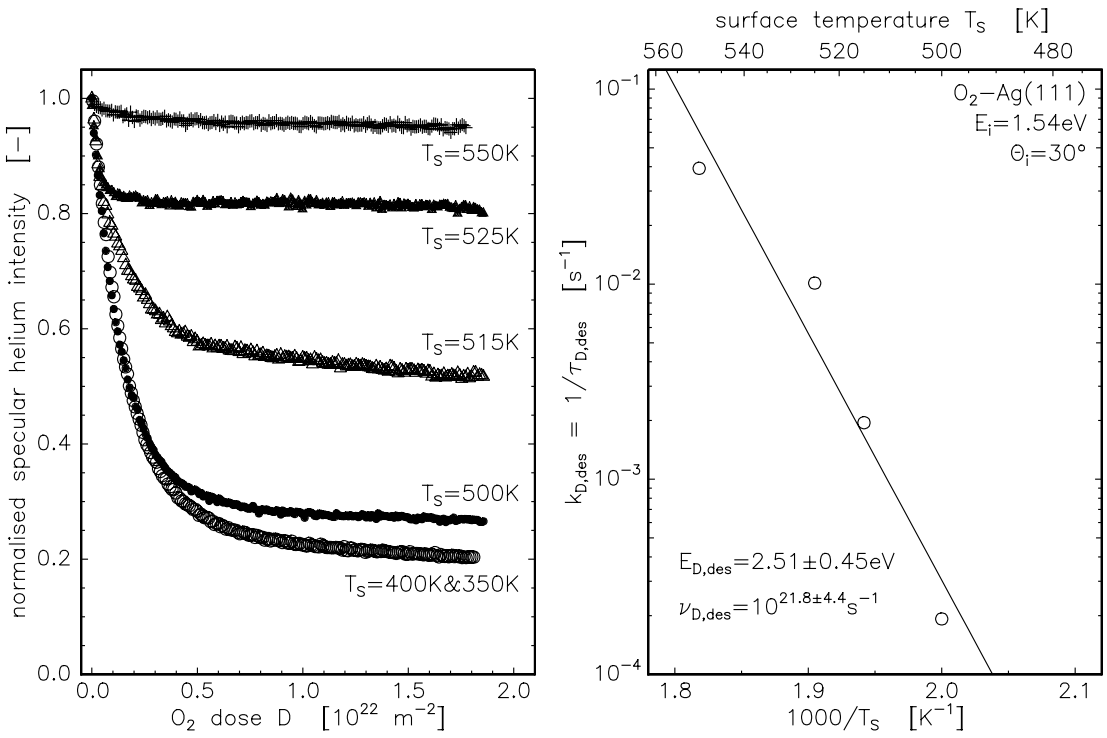

Figure 5.7 *He-reflectivity during dissociative oxygen uptake at surface temperatures for which desorption is significant. The right panel shows an estimate for the surface residence time from the asymptotic value of the helium reflectivity.*

of $E_{\mathrm{D,des}} = 2.68 \pm 0.17$ eV and $\nu_{\mathrm{D,des}} = 10^{22.8\pm1.5}$ s^{-1}. These values are larger than the values found by Campbell for the desorption of O_2 from Ag(111) [48]. However, he made an assumption for the prefactor of $\nu_{\mathrm{D,des}} = 10^{15}$ s^{-1} leading to a considerable lower value for the desorption energy $E_{\mathrm{D,des}}$ using the surface temperature of the peak maximum of a single TPD spectrum taken at $\beta = 14$ K s^{-1}. We note that the only assumption made in our analysis is first order desorption kinetics with constant prefactor and desorption energy.

One should notice that for heating rates $\beta > 5$ K s^{-1} the peak desorption temperature does not shift. This leads to the points, which are not on the line in the lower right panel of figure 5.6. Clearly, the analysis of the TPD spectra by the peak shift with heating rate does not hold for $\beta > 5$ K s^{-1} and may not even hold for the lower heating rates as well.

We also followed another procedure to find valus for $E_{\mathrm{D,des}}$ and $\nu_{\mathrm{D,des}}$ using the specular helium intensity as a probe for the surface coverage. A comparable method was used in the determination of Na ionicity on a partially covered W(110) surface [222]. If an adsorption experiment is carried out at a surface temperature for which desorption becomes important on the time scale of the experiment the coverage will reach an equilibrium given by the rate of dissociative adsorption and the desorption rate. Knowing the surface coverage ψ_{D} from the specular He-intensity the sticking probability $s_{\mathrm{D}}(\psi_{\mathrm{D}})$ is then known through equation 5.4 with the proper value for $\psi_{\mathrm{D,max}}$ and extrapolation of the temperature dependence of the initial sticking probability $s_{\mathrm{D},0}$ to the surface temperatures of the measurements (for the

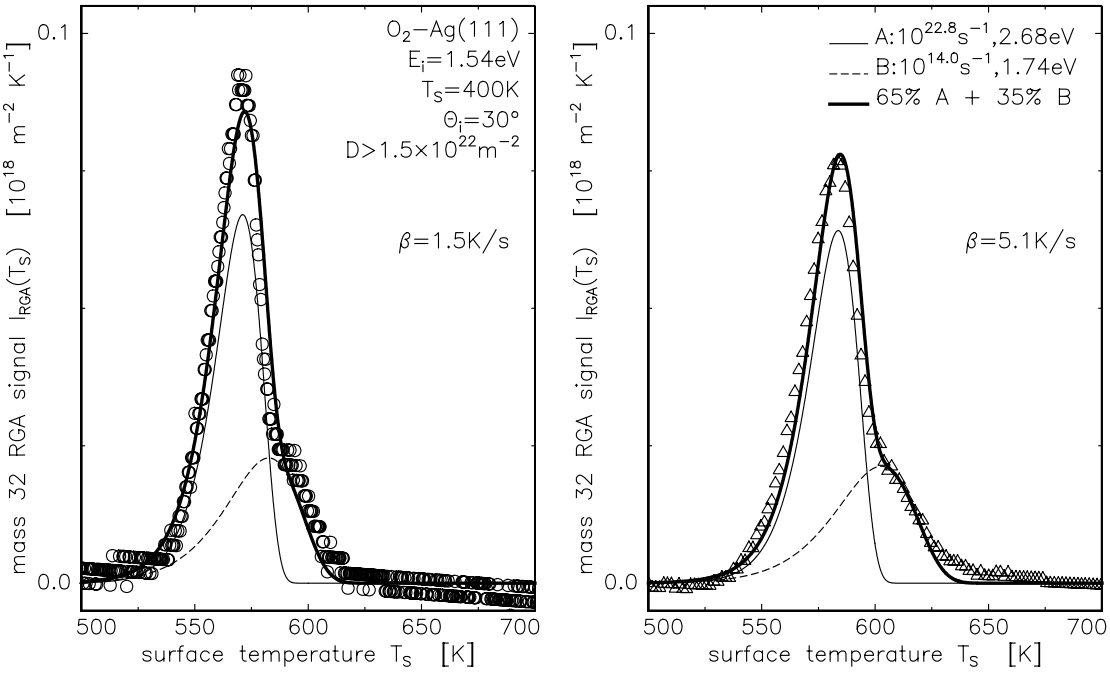

Figure 5.8 *Simulation of two TPD spectra taken at different ramp rates. In the the simulation first order desorption from two states is assumed with the prefactors $\nu_{\mathrm{D,des}}$ and desorption energies $E_{\mathrm{D,des}}$ as indicated. A linear background is subtracted from the data.*

conditions of these experiments $s_{\mathrm{D},0}$ hardly varies). In equilibrium holds

$$I_{\mathrm{flux}}\, s_{\mathrm{D}}(\psi_{\mathrm{D}}) = k_{\mathrm{D,des}}\, \psi_{\mathrm{D}} \quad . \tag{5.14}$$

The found desorption rate constants found in such a way for the different surface temperatures are shown in the right panel of figure 5.7. Fitting a straight line through the data points yields $E_{\mathrm{D,des}} = 2.51 \pm 0.45$ eV and $\nu_{\mathrm{D,des}} = 10^{21.8\pm4.4}$ s^{-1}. These values are in good correspondence with the values found for the TPD analysis.

Having found the values for the frequency factor $\nu_{\mathrm{D,des}}$ and desorption energy $E_{\mathrm{D,des}}$ one can simulate the TPD spectra and check if the values found do hold for the whole desorption spectrum. Still assuming first order desorption results in the desorption rate (desorption per unit time)

$$\frac{dn}{dt} = n\, k_{\mathrm{des}} = n\, \nu_{\mathrm{des}}\, \exp\left(-\frac{E_{\mathrm{des}}}{k_{\mathrm{B}}\, T_{\mathrm{s}}}\right) \quad . \tag{5.15}$$

The equation can be rewritten as a desorption per unit temperature for a linear heating rate β

$$\frac{dn}{dT_{\mathrm{s}}} = \frac{dt}{dT_{\mathrm{s}}}\, n\, \nu_{\mathrm{des}}\, \exp\left(-\frac{E_{\mathrm{des}}}{k_{\mathrm{B}}\, T_{\mathrm{s}}}\right) = \frac{n\, \nu_{\mathrm{des}}}{\beta}\, \exp\left(-\frac{E_{\mathrm{des}}}{k_{\mathrm{B}}\, T_{\mathrm{s}}}\right) \quad . \tag{5.16}$$

A straightforward numerical evaluation of the last equation leads to a simulated TPD spectrum. The results of those simulations in the case of recombinative desorption for two heating rates are shown in figure 5.8. We assumed recombinative desorption from

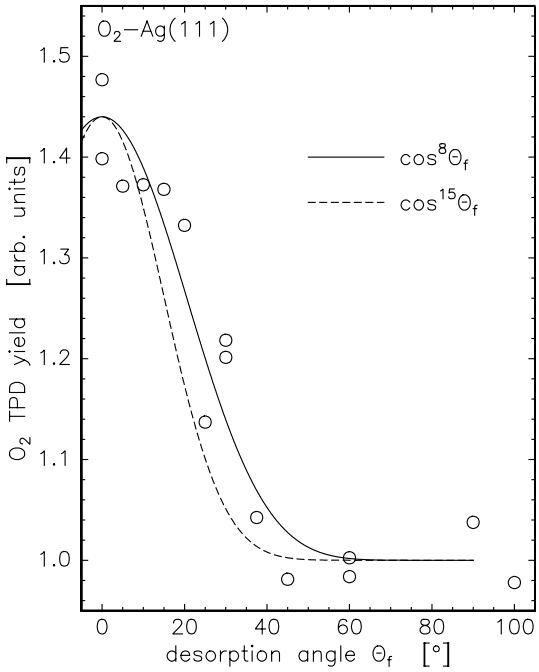

Figure 5.9 *Angular resolved TPD yield of the 600 K desorption peak. The data is normalised to the yield observed behind the sample. The lines hold for a* $\cos^{\mathrm{n}}\theta_{\mathrm{f}}$ *distribution* ($\mathrm{n}=8$ *for the full line and* $\mathrm{n}=15$ *for the dashed line).*

two independent sites (no population of one state from the other) on the surface in the simulation to account for the double peak observed in the spectra. For the main peak the values for $\nu_{\mathrm{D,des}}$ and $E_{\mathrm{D,des}}$ were taken as derived from the analysis described above. The second peak is simulated by taking the values found by us [223, chapter 6] for the recombinative desorption from the Ag(110) surface, which shows a single desorption peak only (in the simulation the value for $E_{\mathrm{D,des}}$ was taken 0.01 eV larger). Desorption from the Ag(110) surface shows much lower values for $\nu_{\mathrm{D,des}}$ and $E_{\mathrm{D,des}}$: $\nu_{\mathrm{D,des}} = 10^{14.0\pm0.5}$ s^{-1} and $E_{\mathrm{D,des}} = 1.73 \pm 0.05$ eV [223, chapter 6]. Setting the prefactor of the smaller peak to the value found for the main peak did lead to a worse fit to the measured TPD spectra. The starting value for the surface coverage in the simulation was the one found for the TPD yield of the measured spectra (approximately 2.77×10^{18} m^{-2}) and 65% was set to desorb in the main peak. The simulations describe the measured data remarkably well. No change of the prefactor $\nu_{\mathrm{D,des}}$ and desorption energy $E_{\mathrm{D,des}}$ are necessary to describe the desorption and although the desorption is recombinative it is of first order in the surface coverage.

The double recombinative desorption peak was not observed before since all reported TPD spectra for O_2/Ag(111) were taken at heating rates over 10 K s^{-1} [45,48,84,85]. It is tempting to assign the low intensity desorption peak to desorption from (110) type defect sites as its desorption parameters are almost identical to the ones we found for recombinative desorption from the Ag(110) surface. The relative number of defect sites would then be 35%. Although we certainly do not think our surface to be defect free, 35% seems an extremely high number. Moreover, if it is true one would expect the values for the sticking

probabilities presented to be about 35% of the values measured for the Ag(110) surface, displaying much larger sticking probabilities. Since this is not observed we suggest the double recombinative desorption peak to be characteristic for the Ag(111) surface.

The structure of the oxide overlayer on Ag(111) is very different from that of the clean surface. Complex mass transport of Ag atoms has to take place during the formation of the overlayer. On the Ag(110) surface it has been demonstrated that -Ag-O-Ag- strings are formed. For oxidation of Cu(111) formation of strings has been proposed as a first step of the reconstruction. The double peak structure may indicate that at first O_2 molecules from a 2-dimensional network from the reconstructed overlayer are desorbing. At higher temperatures the reconstruction has been reduced to Ag-O strings that decompose and lead to O_2 desorption in the same way as for the Ag(110) surface. Therefore, the desorption behaviour at high temperatures may be similar for Ag(111) and Ag(110).

The angular resolved TPD yield has been measured with our rotatable differentially pumped mass spectrometer (QMS). The result is shown in figure 5.9 with the TPD yield normalised to the yield measured when the QMS is not facing the sample surface. Measuring a desorption spectrum for this configuration means that the QMS is also quite sensitive to the pressure rise in the scattering chamber. It is seen that the desorption is strongly peaked around the surface normal and can be described by a $\cos^8\theta_f$ angular intensity distribution. Previously a $\cos^{15}\theta_f$ angular desorption distribution was found for the already mentioned transient oxygen state observed at the Ag(111) surface plane [122, chapter 4]. A line according to such an angular intensity distribution is also drawn in the figure.

5.3.7 Molecular desorption and dissociation

To analyse the molecular desorption the TPD spectrum measured after adsorption at $T_s =$ 150 K [122, chapter 4] was taken because the present molecular TPD spectra, measured after adsorption at $T_s = 165$ K, were troubled by a non-linear heating rate and an overlap with desorption from the filament. Since only one spectrum is available we tried to fit it using again the above described first order desorption kinetics. The results for several combinations of $\nu_{M,des}$ and $E_{M,des}$, keeping the maximum desorption at an equal surface temperature, are shown in the left panel of figure 5.10, together with the data from which a linear background is subtracted. The data is also shown in the upper right panel of figure 5.4 without background subtraction. Studying the simulations it is observed that molecular desorption is also best described by a very large prefactor in the desorption rate constant $k_{M,des}$. Of the four simulations shown the best fit to the data is given by $\nu_{M,des} = 10^{22}$ s^{-1} and $E_{M,des} = 0.84$ eV. Smaller prefactors lead to broader spectra and smaller values for $E_{M,des}$ and larger prefactors to larger values for $E_{M,des}$.

Assuming molecular chemisorption as a precursor to dissociation then dissociation of the molecule should be a possibility in the TPD run if it is a simple consecutive process. For this to be the case recombinative desorption should be seen around $T_s = 600$ K, which is not observed as is obvious from the TPD spectrum shown in the upper right panel of figure 5.4. So, if dissociation from the molecular state is an option for the molecularly adsorbed molecule it should only be possible, on the time scale of the TPD experiment, when all molecules have already desorbed from the molecular state. Dissociation from the molecular state can also be described by equation 5.16, with the desorption parameters

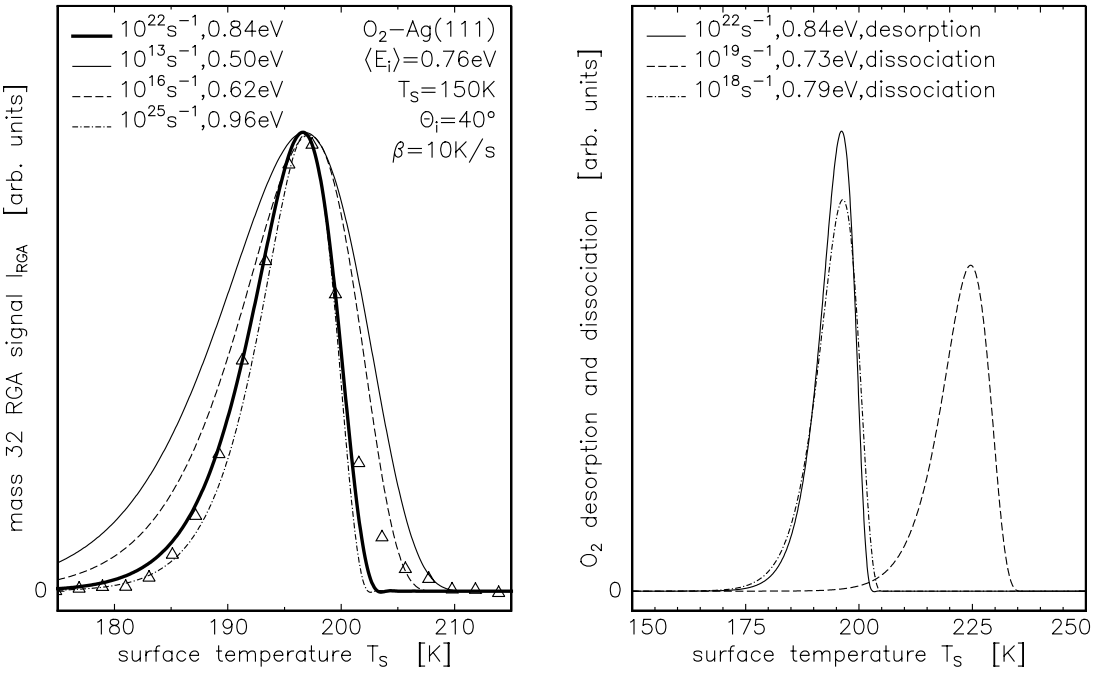

Figure 5.10 *Simulation of molecular desorption and possible dissociation. The left panel shows the measured and simulated TPD spectra for different combinations of prefactor and desorption energy. The right panel shows the simulated TPD spectrum giving the best correspondence to the measured one and simulated "dissociation spectra" for two combinations of prefactor and dissociation energy.*

replaced by the dissociation parameters $\nu_{\mathrm{M,diss}}$ and $E_{\mathrm{M,diss}}$. These parameters are known from the analysis of the surface temperature dependence of the initial dissociative sticking coefficient, in the regime for which the molecular chemisorption state is thought to act as a precursor (mechanism A), and the molecular desorption parameters. The surface temperature dependence of the dissociative sticking did yield a ratio for the prefactors and an energy difference for the desorption energies. From this analysis $\nu_{\mathrm{M,diss}} = 10^{19}$ s^{-1} and $E_{\mathrm{M,diss}} = 0.73$ eV are derived. In the right panel of figure 5.10 the resulting "temperature programmed dissociation spectrum" is shown when desorption is switched off and it is observed that desorption and dissociation almost perfectly overlap. For this to be true about half of the molecular oxygen surface coverage should dissociate, which is not observed. For the dissociation spectrum to shift to such surface temperatures that there is a negligable overlap with the desorption spectrum a ratio of the prefactors $\nu_{\mathrm{M,des}}/\nu_{\mathrm{M,diss}} = 10^4$ and an energy difference $E_{\mathrm{M,des}} - E_{\mathrm{M,diss}} = 0.05$ eV had to be assumed, which cannot describe the observed temperature dependence of the dissociative sticking following mechanism A. The resulting dissociation spectrum is also shown in the right panel of figure 5.10.

Clearly the dissociation mechanism is more complex than just a simple choice between two barriers for the molecularly adsorbed molecule. It is very well possible that dissociation can only occur if enough free Ag atoms are present at the surface. This will influence the kinetics of the desorption and dissociation.

In a very limited number of TPD spectra for which only molecular desorption should be observed we also detected small amount of recombinative desorption. If this dissociation was a result of direct dissociation or dissociation from the molecular state is not known.

5.3.8 Extended desorption analysis

We have taken simple first order desorption kinetics to explain our desorption data. By varying the sample heating rate for desorption values for the desorption energy $E_{\mathrm{D,des}}$ and frequency factor $\nu_{\mathrm{D,des}}$ were found. Since the commonly applied TPD analysis procedures have their limitations [224] the measured TPD spectra were also simulated using the found values for $E_{\mathrm{D,des}}$ and $\nu_{\mathrm{D,des}}$. Although the correspondence with the measured TPD spectra for heating rates $\beta \leq 5.1$ K s^{-1} is remarkable, the fixed surface temperature of the TPD maximum and rather symmetric shape of the TPD spectrum for larger heating rates is not explained by the assumed first order desorption kinetics and by taking $E_{\mathrm{D,des}}$ and $\nu_{\mathrm{D,des}}$ not dependent on the surface coverage.

Applying the heating rate variation method to recombinative oxygen desorption from the Ag(110) surface does also show a very good correspondence with first order desorption kinetics [35,223, chapter 6]. However, recording desorption traces for different initial coverages but equal heating rates showed a TPD peak shift to larger surface temperatures, which is in contradiction with first order desorption kinetics [35]. Bowker [34] could explain these TPD spectra by taking the effect of lateral interactions [219,225,226] (attractive forces beteen the adsorbates in this case) into account. The desorption rate is in this case dependent on the occupation of nearest neighbour pair sites and has a coverage dependent activation energy, but a coverage independent frequency factor of 4×10^{14} s^{-1}. A lower value for the desorption energy in the limit of zero surface coverage and for the frequency factor with respect to the first order rate analysis were found. Also Zhdanov did a simulation of these spectra taking lateral interactions but also a surface reconstruction into account [227,94]. He took a fixed value for the frequency factor of 10^{15} s^{-1}. In the case of the O_2 desorption from Ag(111) lateral interactions are also expected to play a role in the desorption process. For this system the number of nearest neighbours is larger and the formation of the oxide tri-layer (a reconstruction) may complicate the desorption.

Another phenomenon complicating the matter is the possible influence of precursor intermediates. Rate expressions for desorption can become quite extensive and also dependent on surface coverage [226,228–230]. Values found for the frequency factor and desorption energy taking precursor intermediates into consideration can differ considerably from the values found using simple first or second order desorption kinetics [228].

We have made no attempt to perform simulations of our TPD spectra taking adsorbate interactions, surface reconstructions or precursor intermediates into account. It is only pointed out that the values found for the desorption energy and frequency factor have to be treated with considerable care. The fact that the desorption temperatures found for both molecular and recombinative desorption are so close for the Ag(110) and Ag(111) surface must mean that the desorption energies and prefactors cannot differ too much for both surface planes.

The reason for having found an about identical unrealistically large frequency factor ν_{des} in the case of molecular and recombinative desorption from the Ag(111) surface possibly in-

dicates a common precursor intermediate. Lateral interactions and surface reconstructions will be different for both adsorptions and thus affect the real value in a different way.

5.3.9 Sticking mechanisms

We have already distinguished two mechanisms, A and B, for the dissociative sticking probability. The mechanisms display a different dependence on incident energy and angle and on surface temperature. Mechanism A shows a decrease in dissociative sticking with increasing surface temperature and mechanism B an increase. For $\theta_i \geq 60°$ mechanism B does not work and only mechanism A remains acting. The dependence of mechanism A on incident energy shows an almost exact resemblance to the dependence of the initial molecular sticking coefficient on the incident energy, except for the more than one order of magnitude difference. This correspondence in behaviour suggests that for mechanism A molecular chemisorption acts as a precursor to dissociation. The surface temperature dependence of mechanism A is also in accord with this precursor mechanism and explains the large difference in magnitude between molecular sticking and dissociative sticking according to mechanism A. The dissociative sticking was measured at $T_s = 400$ K and molecular sticking at $T_s = 165$ K. Using a formalism based on precursor mediated dissociative sticking we could fit the dissociation data. The value for molecular sticking was taken for the trapping probability in the precursor. However, the dissociation during a TPD from the molecular state is far overestimated if the activation energy and frequency factor, that follow from the precursor formalism and the value found for the activation energy and frequency factor for the desorption from the molecular state as found from the TPD analysis, are used for dissociation from the precursor. This observation is as yet without explanation. It may very well be that the dissociation step requires mass transport, which may be prohibited if the surface is covered by molecularly adsorbed O_2. In this case it will be possible that dissociation does not occur during a TPD.

The dependence of the molecular sticking on the incident energy also shows a good correspondence with the trapping curves of previously observed transiently trapped oxygen [122,123, chapter 4] as is displayed in figure 5.3. There is a large difference in magnitude (approximately three orders). The good correspondence in incident energy behaviour can be explained by the entering of both the transient trapping and the molecular state via an equal process, although with different barriers in between, or by the transient state acting as a precursor to molecular chemisorption. It is hard to visualise yet another state acting as a precursor to both the transient trapping and molecular chemisorption and we favour therefore the transient trapping to act as a precursor to molecular chemisorption. As the transient species is in a non-equilibrated state, it is possible that the coupling to molecular chemisorption is dependent on the angle of incidence. We thus suggest that the transient oxygen state is a precursor to molecular sticking and that the molecular state acts as a precursor to dissociation. Since the transient state was explained by the vibrational excitation of the oxygen molecule on entering the molecular chemisorption region of the interaction potential an isotope effect can be expected in molecular and dissociative sticking. An isotope effect was indeed observed in our group employing adsorption of the two isotopically labelled oxygen molecules $^{16}O_2$ and $^{18}O_2$ in a high pressure cell [84,85]. The observed isotope effect was observed to be close to the one expected by the Franck-Condon

factors for the $O_2(\nu{=}0)$ to the $O_2^-(\nu{=}0)$ transition for both isotopes. The formation of O_2^- has been observed directly in scattering experiments at high energies [161,162].

For mechanism B of the dissociative sticking it was already concluded that it cannot be due to precursor mediated dissociation, because a different slope of $s_{D,0}$ as function of $1/T_s$ is observed for different incident energies. For the dissociation of O_2 on Cu(100) [24], the dissociation of CH_4 on Pt(111) [25,216] and the dissociation of O_2 on Si(100) [231] a similar surface temperature dependence was observed. For the latter case it was argued that electron transfer to the incident molecule is enhanced by increasing the surface temperature. An identical mechanism was put forward for the vibrational excitation of NO in collision with the Ag(111) surface [17]. However, if an identical mechanism plays a role in the dissociative sticking of O_2 at Ag(111) also an enhanced molecular sticking with increasing surface temperature is expected. Since this is not observed we reject this mechanism for the observed sticking behaviour.

The first two cases, O_2-Cu(100) and CH_4-Pt(111), were explained by a coupling of the barrier to dissociation to the lattice. Increasing the surface temperature in the case of O_2-Cu(100) gave less energy transfer of the molecule in the recoil from the lattice and thus more translational energy available for crossing the barrier to dissociation. Thermally assisted tunneling has been used to explain the CH_4-Pt(111) results. In this case the translational energy in the center of mass frame (c.m.) of barrier and incident particle can be increased by an outward moving barrier. The energy difference between the top of the barrier and the translational energy in the c.m. frame will in this case be decreased and in this way enhance the tunneling probability. An exponential increase of the sticking is in this case observed in experiment and theory [216], whereas it is not in the case of O_2-Cu(100). Our results for the dissociation of O_2 on Ag(111) also show an exponential increase with surface temperature and we therefore also infer thermally assisted tunneling to dissociation for mechanism B.

5.4 Conclusion

Upon dissociative O_2 adsorption the Ag(111) surface is shown to reconstruct and form an Ag_2O overlayer and a slight long range relaxation of the surface is observed. Two mechanisms are observed for dissociative sticking: a precursor mediated one, with the molecular chemisorption state acting as a precursor and a direct one, which is due to tunneling of the molecule and is thermally assisted. For molecular sticking an earlier observed transient oxygen state is suggested to act as a precursor. A simple analysis of the measured TPD spectra shows that adsorbate interactions, surface reconstructions and a precursor intermediate to desorption can be of importance in the desorption process.

Chapter 6

The Interaction of Oxygen with the Ag(110) Surface

Abstract *Results on the scattering and dissociative sticking of O_2 molecules on the Ag(110) surface are presented. By employing a molecular beam both the dependence on incident energy and angle of the molecules is probed. The dependence on the azimuthal orientation of the surface is also investigated. The two main azimuths display a different corrugation as observed by the incident molecule in the scattering experiment. Dissociative sticking is observed to proceed via the molecular chemisorption state and is strongly enhanced by the incident energy. An azimuthal dependence in sticking is observed. The uptake of oxygen is observed to display two surface coverage regimes. Dissociative sticking in the low coverage regime is relatively high as compared to sticking at coverages exceeding 0.08 ML. The high coverage regime may be governed by surface diffusion. Results on desorption of O_2 from the Ag(110) surface are also presented.*

6.1 Introduction

By studying the fundamental properties of gas-surface reactions on well defined surfaces one tries to gain more insight into the mechanism of chemical reactions taking place at technologically important surfaces, for instance in catalysis. In such a practical situation the surface will not be well-defined, whereas in most fundamental studies a well-characterised single crystal is taken. Studying the gas-surface interaction of one gas with the different surface planes of one solid material may lead to more insight into the fundamental properties of the interaction. Changing the surface plane alters the geometric and electronic properties presented to the molecule: hence their role in the interaction can addressed. The interaction of oxygen with the different surface planes of silver is a good candidate for such a comparative study.

The Ag(111) and Ag(110) surface have almost identical binding states for oxygen: a shallow physisorption state, a stronger molecular chemisorption state, an atomically adsorbed state and a subsurface one as has been recently reviewed by Besenbacher & Nørskov [115]. The charge transfer to the oxygen molecule in the molecular chemisorption state may be somewhat different for both surfaces. Desorption measurements reveal almost identical

desorption temperatures from these different adsorption states and an equal behaviour for oxygen adsorption may be expected. However, this is not the case. Adsorption measurements from an ambient gas show a difference of at least two orders in magnitude in both the molecular and dissociative sticking probability with the sticking for the Ag(111) having the lowest probability in the order of 10^{-7}–10^{-6} [46,48,84]. These measurements show a different reactivity with oxygen for the two surfaces and the question arises if oxygen adsorption occurs via a similar process on both surfaces or not.

We have already carried out a number of experiments addressing the interaction of O_2 with the Ag(111) surface using a supersonic molecular beam. Both sticking and scattering experiments were done. The scattering experiments did show a large increase in surface corrugation for incident energies exceeding a threshold energy of 0.2 eV [186, chapter 3]. Above the same threshold energy transient trapping-desorption of oxygen at the Ag(111) surface was observed. It was concluded that this involved the trapping of vibrationally excited oxygen molecules into the molecular chemisorption state, without equilibration of the excited molecules [122,123, chapter 4]. Trapping into this transient state shows a maximum probability of approximately 30%. The incident energy and angular dependence of the molecular chemisorption coefficient followed the transient trapping probability, but with a probability approximately three orders of magnitude lower. Dissociative sticking was seen to proceed via the molecular chemisorption state in a thermalising process [124, chapter 5]. A direct process to dissociation was also observed overtaking the precursor process at incident energies exceeding aproximately 1 eV and for incident angles towards the surface normal. The energy threshold observed for the population of the transient and molecular chemisorption state is identical to the one found for the increased surface corrugation. It was suggested that molecular chemisorption was due to leaking of flux from the transient state and thermalising in the molecular chemisorption well.

The Ag(111) surface is a relatively smooth surface with a hexagonal close packed structure. The Ag(110) surface consists of rows of close packed surface atoms in the $<1\bar{1}0>$ direction. This results in a strong surface corrugation in the <001> direction and is due to bulk termination.

Molecular and dissociative sticking at the Ag(110) surface has been measured using a molecular beam by Vattuone et al. [103–106] and Rocca et al. [108]. For this surface the dissociative sticking was also observed to proceed via the molecular chemisorption state. However, the population of the molecular chemisorption state occured with a probability three orders of magnitude larger than on the Ag(111) surface. The incident energy and angular dependence seems almost identical for the two surfaces. Unfortunately Vattuone et al. could not reach incident energies over $E_i = 0.6$ eV and were therefore only able to observe an increase in the sticking of O_2 at the Ag(110) surface with increasing incident energy. A saturation of the sticking coefficient with further increasing incident energy or even a decrease after reaching a maximum value, as we observed for the O_2-Ag(111) system, could not be reported. More information on the incident energy and angular dependence will certainly help in deriving a better physical picture on the adsorption process. The transient trapping of oxygen found at the Ag(111) surface may also play a role at the Ag(110) surface. Experiments on this matter are presented here.

Scattering experiments will also be discussed. From these measurements one obtains information on the energy transfer in the scattering process and the degree of surface

corrugation as experienced by the incident O_2 molecule. The existence of the transient state may also be visible in the time-of-flight (TOF) spectra recorded for the scattering experiments. Desorption from the molecular or atomic chemisorption state may also be apparent in the TOF data because the sticking coefficient is quite large at most incident energies and angles [103].

6.2 Experimental

The experiments have been performed in a molecular beam scattering machine described before [56,186, chapter 3]. Briefly, it consists of a triply differentially pumped molecular beam line connected to a UHV scattering chamber. The first stage contains the nozzle and the second stage of the beam line contains a chopper. Both a double slit 0.5% duty cycle chopper and a 50% one are used. A beam flag to switch the beam on and off is also present in the second stage. The third stage acts as a buffer chamber.

The molecular beam is generated by a supersonic expansion of a gas mixture of oxygen and helium from a 80 μm CW quartz nozzle. By changing the oxygen/helium ratio in the gas mixture and heating the nozzle (maximum temperature approximately 1100 K) we can vary the energy of the oxygen molecules to about 1.8 eV. Separate electronic flow controllers control the flows of oxygen and helium.

The sample is mounted in the middle of the scattering chamber on a 3-axis goniometer [125, chapter 2]. A quadrupole mass spectrometer (QMS) can be rotated around the sample to detect the particles leaving the surface after desorption or direct scattering. Combining the movements of the manipulator and the rotatable QMS gives accurate control (by computer) over the incident and exit angles of particles in the scattering experiment [125, chapter 2]. By moving the sample out of the beam and the QMS into the beam path the TOF of the direct beam can be recorded. In this way the translational energy of the oxygen molecules is derived for the different nozzle temperatures and flow settings. The azimuthal angle can also be varied. ℓN_2-cooling allows a minimum sample temperature of about $T_s = 160$ K. The sample temperature is measured with a thermocoax K-type thermocouple inserted in the side of the sample and is controlled by a commercial controller. The controller allows for linear ramping of the sample temperature employed in this study for the temperature programmed desorption (TPD) measurements

A residual gas analyser (RGA) is present for monitoring the background gas and an ion sputter gun for cleaning the sample. The RGA has been calibrated for the absolute oxygen partial pressure rise in the system [124, chapter 5]. Monitoring the background pressure gives values for incident flux and desorption rates in TPD experiments. Surface coverages can be given since the surface area as covered by the molecular beam is known.

The samples are cut by spark erosion from a single crystal rod of 5N purity to within 0.1° of the (110) plane and polished by standard polishing techniques. Once in UHV the sample received a treatment of sputtering (500 eV Ar^+ ions) and annealing cycles until the angular width of the specularly reflected He-intensity was approximately 2°, which is the angular resolution of our experiment and determined by the divergence of the incident beam and the entrance aperture of the QMS detector. For He scattering along the <001> azimuth of the surface, the corrugated direction, we could measure the second order diffraction peak

and at least 25% of the incident He-flux could be accounted for in the detected scattered flux. To further check the surface quality the system is also equipped with LEED and AES.

Sticking probabilities above 0.05 are measured with the method of King & Wells [219]. In this method the partial pressure of the reactive gas is monitored in time. A partial pressure trace for O_2 is shown in figure 6.1. Before t_1 the beam is prevented from entering the UHV chamber by closing the beam flag in the beam line (see figure 1.2) The partial pressure measured is the residual oxygen pressure of the system. Then the beam is allowed to enter the UHV chamber at time t_1 by opening the flag in the beam line, but it is not allowed to hit the sample by keeping the flag in the UHV chamber closed. The observed pressure rise is proportional to the incident flux of O_2 molecules. Upon opening the UHV beam flag at time t_2 the partial pressure will drop due to oxygen sticking to the surface and the partial pressure decrease is proportional to the number of molecules that stick to the surface. Taking the ratio of pressure drop and pressure rise, denoted as a and b, respectively, in figure 6.1, yields the initial sticking probability. The pressure increase after the sharp drop reflects a decrease in sticking with increasing surface coverage. By integrating the pressure drop one can obtain the sticking coefficient as function of surface coverage. At time t_3 and t_4 the UHV flag and the flag in the beam line are closed, respectively. The left axis of figure 6.1 is the partial oxygen pressure expressed in mbar. It shows that the pressure increase in the system due to the oxygen in the beam (0.5% chopper) is in the 10^{-12} mbar range. The right axis shows the number of oxygen molecules that scatter from a surface and thus contribute to the partial pressure rise in the system. It is expressed in the number of molecules hitting an area as taken by one Ag-atom at the Ag(110) surface per second. The surface may in this case be either the UHV flag or the sample surface. We employed the 0.5% duty cycly chopper for these measurements to reduce the average flux entering the UHV chamber and incident on the surface, because of the vacuum time constant of the UHV system. The measured pressure drop due to oxygen sticking is too low if the uptake of oxygen at the surface is faster than this time constant.

Sticking probabilities below 0.5% were measured using the 50% chopper and determining the ratio of molecules that have stuck to the surface and the oxygen dose at the surface. The oxygen dose is derived by integrating the partial pressure rise in the system during dosing and the number of molecules that have stuck by measuring and integrating a TPD (temperature programmed desorption) spectrum after adsorption [124, chpater 5].

For the TOF experiments the flight time of the oxygen molecule was measured from the 0.5% duty cycle chopper in the beam line to the rotatable QMS. The delay between the time pick off from the chopper blade and passing of the beam is calibrated by varying the chopper rotation speed. Detected particles, marking the end of the TOF, were counted by a home built multichannel scaler in 2 μs bins. In analysing the TOF spectra, the ion flight time through the QMS was subtracted from the TOF time axis. The recorded TOF spectra are fitted to shifted Maxwell-Boltzmann distributions convoluted over the finite chopper opening time yielding the mean energy per particle $<E_i>$ in the beam [186, chapter 3]. From these distributions of both the incident and scattered particles a relative value for incident and scattered flux can be found and also the mean values for the energy $<E>$ of the incident and scattered or desorbing particles. The scattered flux is normalised to the incident flux. In the text $<E>$ will be replaced by E.

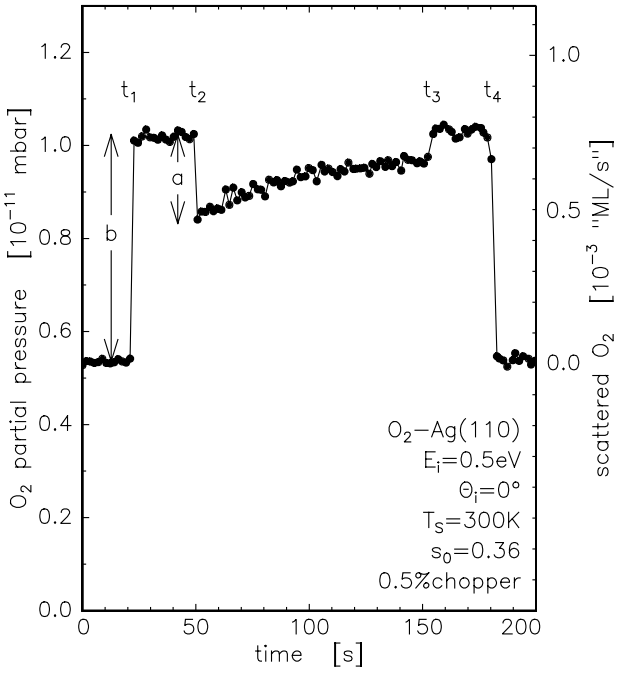

Figure 6.1 *Oxygen partial pressure trace displaying the method of King & Wells for measuring the sticking probability. The left axis shows the oxygen partial pressure in the systyem and the right axis the number of reflected molecules from the incident molecular beam.*

6.3 Results and Discussion

Results on scattering, sticking, uptake and desorption of oxygen for the Ag(110) surface will be presented. Scattering and sticking has been done along both the <1$\bar{1}$0> and the <001> azimuths. Sticking, uptake and desorption measurements are done only for the dissociated state since we could not reach a low enough surface temperature to isolate the molecular chemisorption state at the surface.

6.3.1 Oxygen scattering

Angular resolved scattering results expressed in scattered flux and in the energy ratio of energy of the molecule after the collision E_f over the incident energy E_i are shown in figure 6.2 and 6.3 for different incident energies at a fixed surface temperature and for different surface temperatures at a fixed incident energy, respectively. All scattering measurements are carried out in the plane of incidence ($\phi_f = 0°$) and for $\theta_i = 40°$. The left panels show the results for scattering along the <1$\bar{1}$0> azimuth and the right panels for scattering along the <001> azimuth. To prevent the uptake of dissociated oxygen at surface temperatures below the recombinative desorption temperature of $T_s \approx 600$ K we increased the CO partial pressure to 2×10^{-7} mbar during the scattering experiments to react the adsorbed oxygen off forming CO_2. Below $T_s = 300$ K the silver surface becomes covered with a carbonate species, as has been observed before [44,48], preventing scattering

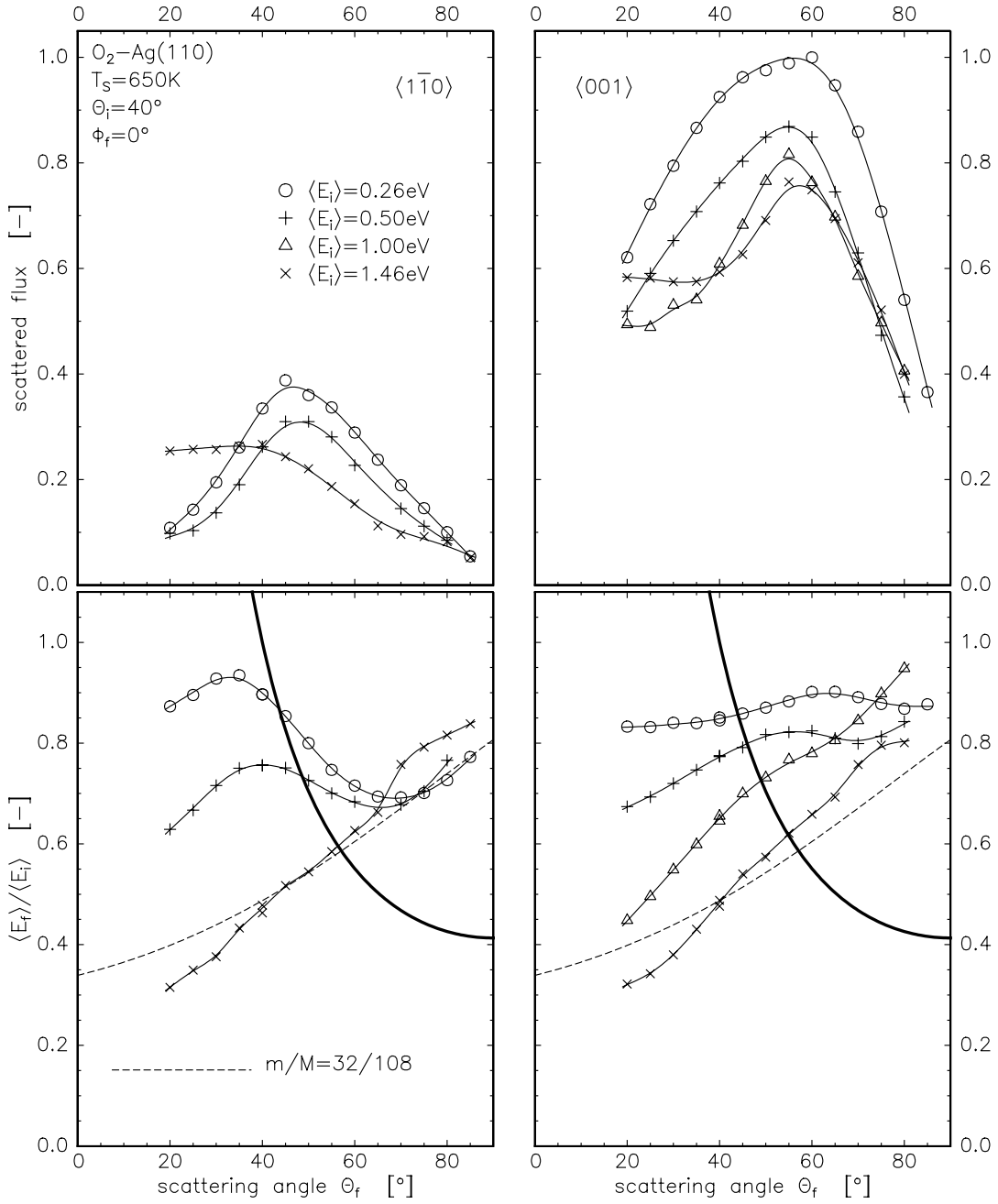

Figure 6.2 *Angular resolved energy and flux distributions of O_2 molecules scattered from a Ag(110) surface for $\theta_i = 40°$, $T_s = 650$ K and several incident energies. The lines through the data points are a guide to the eye only. The thick line in the lower panels holds for parallel momentum conservation and the dashed line for hard sphere scattering.*

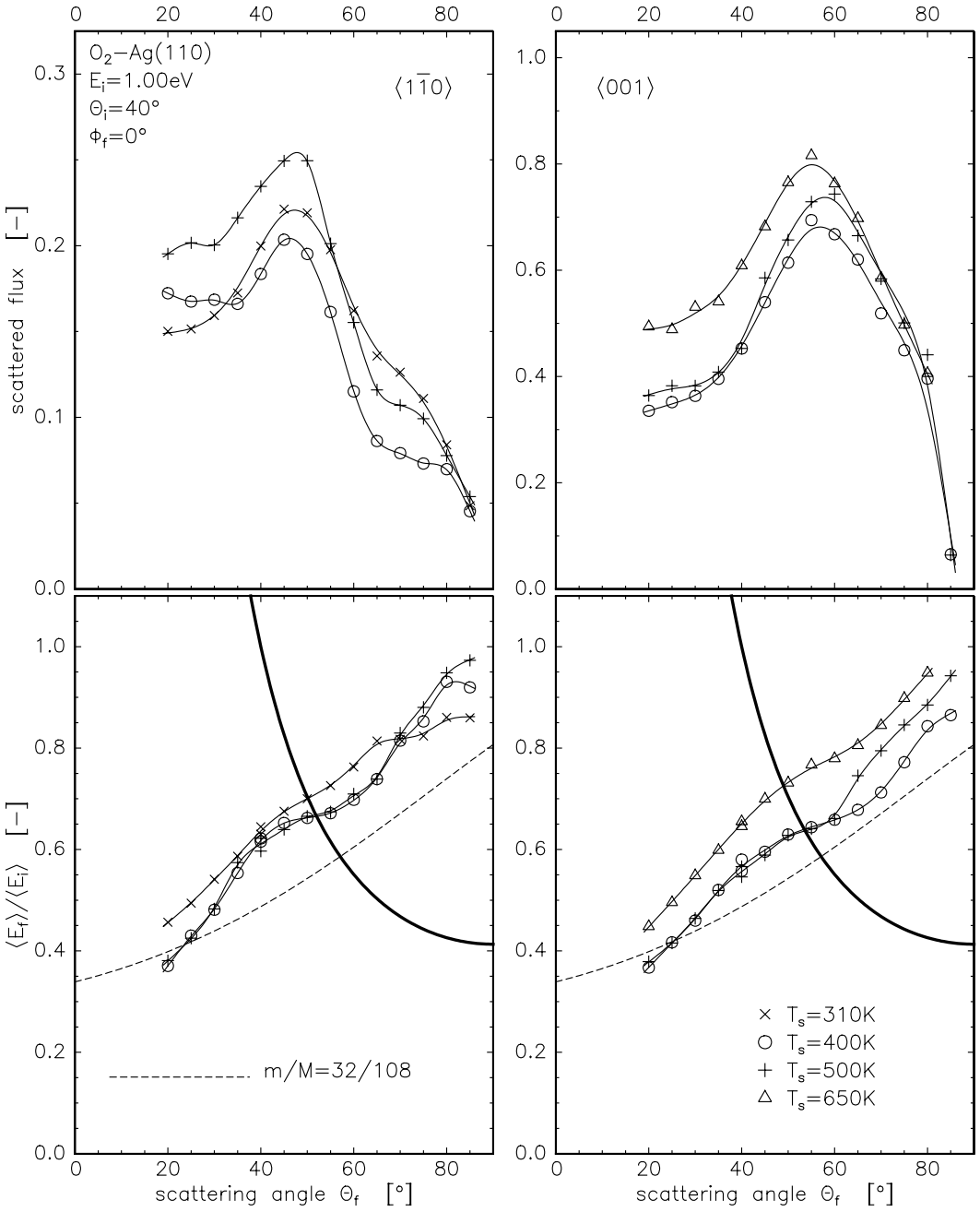

Figure 6.3 *Angular resolved energy and flux distributions of O_2 molecules scattered from a Ag(110) surface for $\theta_i = 40°$, $E_i = 1.00$ eV and several surface temperatures. The lines through the data points are a guide to the eye only. The thick line in the lower panels holds for parallel momentum conservation and the dashed line for hard sphere scattering.*

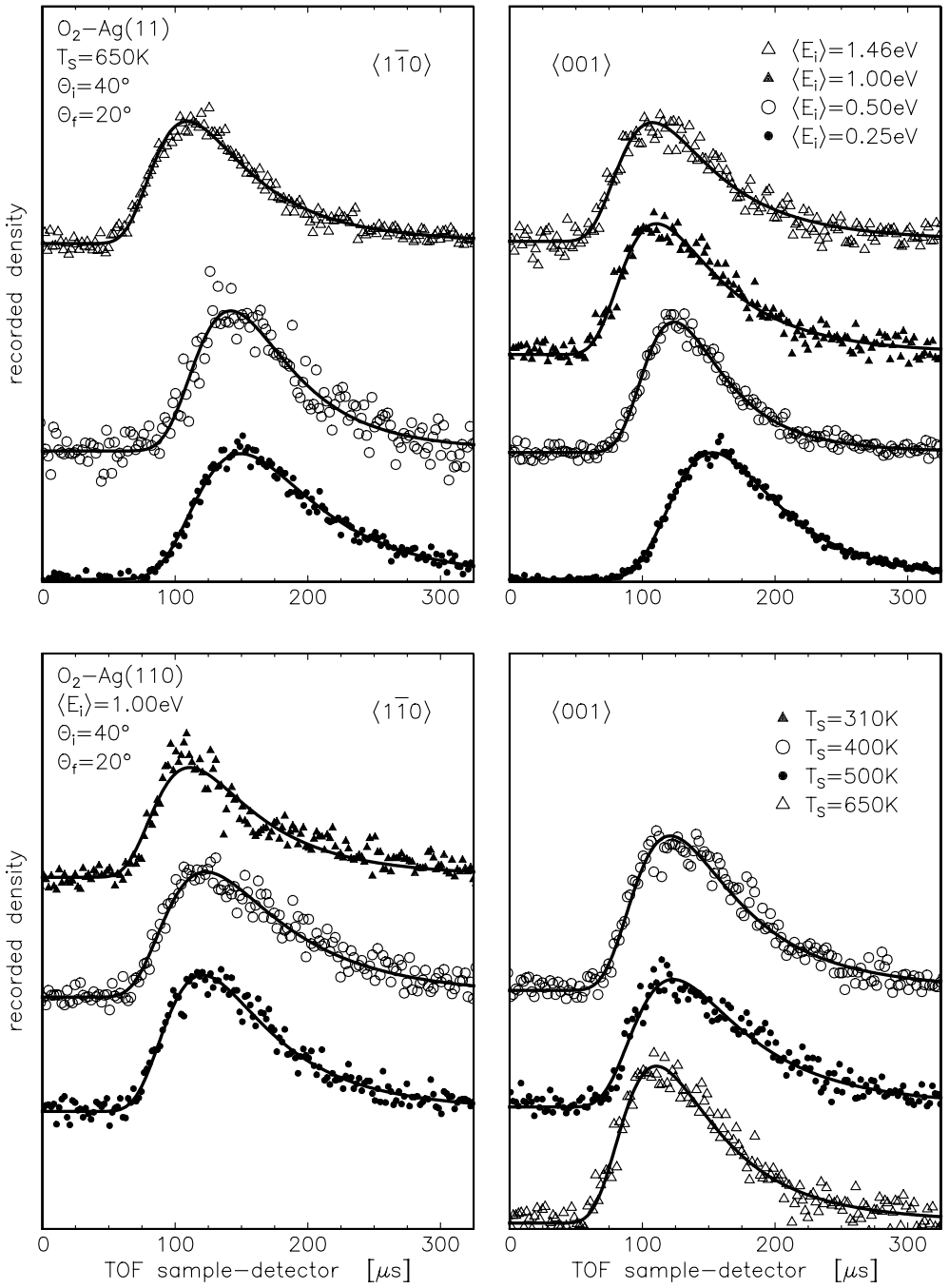

Figure 6.4 *Time-of-flight spectra for fixed surface temperature of $T_s = 650$ K are shown in the upper panels and for a fixed incident energy $E_i = 1.00$ eV in the lower panels. The left panels are for scattering along the <1$\bar{1}$0> azimuth and the right panels for scattering along the <001> azimuth. These spectra are taken for $\theta_i = 40°$ and $\theta_f = 20°$. Lines resulting from fitting a single Maxwell-Boltzman distribution to the data are drawn trough the data points.*

experiments below this surface temperature. The top panels of both figures show the scattered relative flux normalised to the maximum scattered relative flux value found, which is for $E_i = 0.26$ eV along the <001> azimuth. It is observed that the scattered flux detected along the $<1\bar{1}0>$ azimuth is considerably lower than detected along the <001> azimuth. The bottom panels of both figures show the energy ratios for the scattered molecules. The thick line is according to parallel momentum conservation in the collision and the dashed line according to a binary collision ("hard sphere scattering") of a mass 32 (O_2) with a mass 108 (Ag) [186, chapter 3].

Turning our attention first to figure 6.2 one observes that scattering along the <001> azimuth results in a broader angular flux distribution for the different incident energies, especially true for low E_i. The maximum in the distribution has also shifted further away from the specular direction towards the surface. Scattering along this azimuth means scattering across the rows on the Ag(110) surface and thus along the most corrugated direction on this surface. However, it does not lead to less detected scattered flux than for scattering along the rows (the $<1\bar{1}0>$ azimuth). We attribute the observed difference in scattered flux intensity along the azimuths to a defocussing of the flux for scattering along the $<1\bar{1}0>$ azimuth. This defocussing has been observed for ion scattering along this orientation [232,233], when the ion is incident 'on-top' of the rows. A weak focusing was observed for ions incident in the grooves. An O_2 molecule is easily scattered away from the plane of incidence if it is incident along the rows of the surface corrugation and a broader out-of-plane intensity distribution should be the case than for the <001> azimuth. We have not carried out such an out-of-plane measurement. A difference in sticking probabilities cannot account for the difference in the intensities of observed scattered flux since they differ only by approximately 16% and sticking is even larger for the <001> azimuth as will be shown in section 6.3.2. The broader intensity distributions should also lead to a decrease of the maximum intensity. For the largest incident energy the scattered flux is observed to have increased for subspecular scattering angles.

The shape of the angular distributions along the <001> and $<1\bar{1}0>$ azimuths is very different. This is due to the different corrugation. Helium scattering shows only specular scattering along the $<1\bar{1}0>$ azimuth [234,235]. Scattering along this azimuth is quite similar for both He and O_2 to scattering from the Ag(111) crystal [186, chapter 3]. A peak around specular is observed and a shoulder towards smaller scattering angles. The specular peak may be due mostly to scattering from the bottom of the flat $<1\bar{1}0>$ grooves (from the second layer atoms). The shoulder may be due to enhanced corrugation as seen for Ag(111) and due to zig-zag multiple collisions in the grooves. Along the <001> azimuth He scattering shows three diffraction peaks [234]. This indicates corrugation of the surface. It should be noted that no rainbow scattering is observed and the corrugation is not very strong [135,236]. The O_2 scattering shows a pronounced broadening and a shift of the peak position towards the surface. This is indicative for a much stronger corrugation. Such an effect has been observed for Cl_2 scattering from Ag(111) [237], NO scattering from Pt(111) [138,14] and O_2 scattering from W(110) [204]. The shift in the present case is stronger. Kara and DePristo performed calculations of the angular distributions for N_2 from W(110) and a similar shift as in the present work was found [238]. The potential energy surface used in these calculations shows a strong corrugation of the surface and was designed to explain the scaling of the sticking probability of N_2 on W(110) with total rather than normal energy. The resemblance

clearly indicates that the potential along the <001> direction is corrugated.

The energy transfer is also quite different along both azimuths except at the highest incident energy of $E_i = 1.46$ eV. For this incident energy the energy ratio curve follows the hard sphere scattering line quite closely and the scattered molecules must have experienced a very corrugated surface in both cases. At the lower incident energies the energy ratio curves for the $<1\bar{1}0>$ azimuth show some resemblance around the specular direction to the curve for parallel momentum conservation. As we also observed for scattering from the Ag(111) surface some of the incident flux experiences a rather flat surface and another part a more corrugated surface. This is not the case for the <001> azimuth. No indication for parallel momentum conservation is observed. The energy ratio curves are observed to shift upwards and to run horizontal for decreasing incident energy. For $E_i = 0.26$ eV the energy ratio curve is almost constant and displays that approximately 85% of the translational energy is conserved in the collision. This is a larger value than the one found for the scattered flux along the other azimuth or for O_2 scattering from the Ag(111) surface. It shows that for the two lowest incident energies for scattering along the <001> azimuth the scattering process is remarkably different from both parallel momentum conservation and the binary collision model.

Changing the surface temperature for both azimuths and for $E_i = 1.00$ eV does not have a drastic effect on the energy transfer as can be seen in figure 6.3. For the <001> azimuth the scattered flux increases for subspecular angle and for the $<1\bar{1}0>$ azimuth a slight overall change is observed. The most striking observation in the scattered flux distributions is the sharp drop in intensity at $\theta_f = 80°$. It is observed for both azimuths, but is most pronounced for the $<1\bar{1}0>$ azimuth. The feature at $\theta_f = 80°$ along the $<1\bar{1}0>$ azimuth may be due to the preferential focusing of molecules along the grooves discussed above.

Sticking of O_2 in the molecular chemisorption state can reach a probability up to 50%, exceeding the probability for dissociative chemisorption at these surface temperatures, and desorption from this state should be visible in the measured TOF spectra. At $T_s = 650$ K desorption from the dissociated state can also occur. However, the maximum dissociation probability of 5% and the long surface residence time compared to the time scale of the TOF at this surface temperature will make it invisible in the TOF spectra. For scattering of O_2 from the Ag(111) surface we did not observe desorption from the molecular chemisorbed state because the corresponding sticking probability is too low $< 10^{-3}$. Instead, we observed transient trapping-desorption of O_2 molecules, with a sharply peaked desorption distribution around the surface normal. This might also occur at the Ag(110) surface.

The occurence of these two desorption features is not obvious from the TOF spectra as shown in figure 6.4. These TOF spectra are taken for $\theta_i = 40°$, $\theta_f = 20°$ and $\phi_f = 0°$. The top panels show spectra for fixed surface temperature and several incident energies and the bottom panels for a fixed incident energy and several surface temperatures corresponding to figure 6.2 and 6.3, respectively. The left panels again hold for the $<1\bar{1}0>$ azimuth and the right panels for the <001> azimuth. A single shifted Maxwell-Boltzmann distribution seems sufficient to make a good fit to the displayed TOF spectra. However, the TOF spectrum taken along the $<1\bar{1}0>$ azimuth for $E_i = 1.00$ eV at $T_s = 310$ K suggests that two Maxwell-Boltzmann distributions should be taken to fit the data. Clearly, no desorption of molecules according to a non-shifted Maxwell-Boltzmann distribution with a temperature close to the surface temperature is observed. Such a distribution would lead to flight times longer than

350 μs and are not observed. Still, adsorption-desorption from the molecular state should have a large probability. It may be that the desorbing molecules have superthermal energies due to a barrier in the desorption path above the vacuum zero level or that the molecules have not completely thermalised in the molecular well. The transient species observed on Ag(111) [122,123, chapter 4] displayed a strong dependence on surface temperature (figure 4.4) and was only well resolved below $T_s = 300$ K, not possible in this case because of carbonate formation. The results shown in figure 6.2 and 6.3 are obtained by fitting one shifted Maxwell-Boltzmann distribution to the measured TOF spectra.

6.3.2 Oxygen sticking

Figure 6.6 shows the dissociative sticking probabilities measured as a function of incident energy, incident angle, surface temperature and azimuthal orientation. The dissociative sticking probability shows an increase in sticking with increasing incident energy up to $E_i \approx 0.75$ eV, which agrees very well with the measurements of Vattuone et al. [103]. We observe a maximum in the sticking and a subsequent decrease wich was not observed by Vattuone et al. since they could not reach incident energies above $E_i = 0.6$ eV.

The dissociative sticking probability s_D is observed to increase with decreasing surface temperature as was also observed by Vattuone et al. This surface temperature dependence is explained by first sticking into the molecular chemisorption state followed by dissociation via a thermal process. With a subscript $_D$ we will refer to the dissociated state and with a subscript $_M$ to the molecular state. Since the dissociation probability is governed by the competition between desorption and dissociation from the molecular state, it is given by the ratio of the rate constant for dissociation and the sum of rate constants for dissociation and desorption and can be written as

$$s_D = \frac{s_{M,0}\, k_{M,diss}}{k_{M,diss} + k_{M,des}} = s_{M,0} \left[1 + \frac{\nu_{M,des}}{\nu_{M,diss}} \exp\left(-\frac{E_{M,des} - E_{M,diss}}{k_B\, T_s} \right) \right]^{-1} \quad . \tag{6.1}$$

with the rate constant given by

$$k = \frac{1}{\tau} = \nu \exp\left(-\frac{E}{k_B\, T_s} \right) \quad , \tag{6.2}$$

where $\nu_{M,des}$ and $\nu_{M,diss}$ are the prefactors for desorption and dissociation, respectively, $E_{M,des}$ and $E_{M,des}$ the desorption energies from the molecular chemisorption state for desorption and dissociation, respectively, $s_{M,0}$ the initial molecular sticking probability into the molecular chemisorption state and k_B Boltzmann's constant. The full line shown in the upper right panel of figure 6.6 is a fit to the data according to this model. All values except sticking into the molecular chemisorption state are expected to be equal for the data of both incident energies shown. It is a pure coincidence that the data for the two incident energies shown exactly overlaps, meaning that the sticking probabilities into the molecular state are also equal for both incident energies. The value found for $s_{M,0}$ for $E_i = 0.49$ eV is equal to the one reported by Vattuone et al. The values for the difference in desorption energies and the ratio of prefactors differ slightly from the ones found by Vattuone et al.: $\nu_{M,des}/\nu_{M,diss} = 107 \pm 28$ opposed to 40 and $E_{M,des} - E_{M,diss} = 0.14 \pm 0.01$ eV opposed to 0.112 eV for our results and

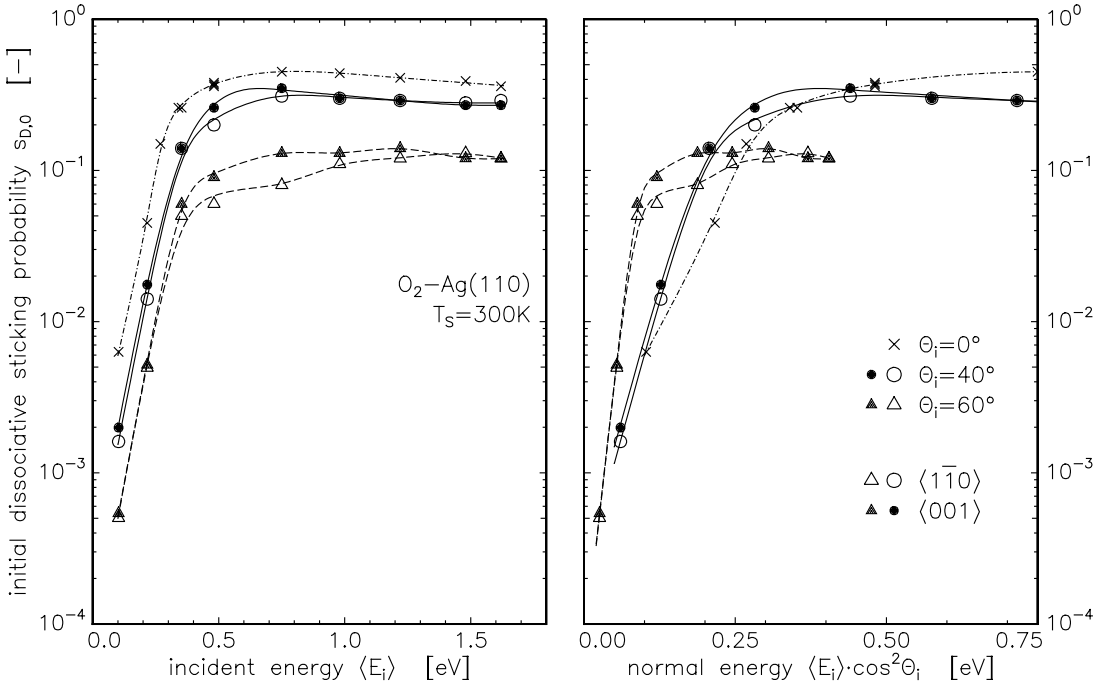

Figure 6.5 *Dissociative sticking probability as function of both total and normal incident energy for different incident angles along both the <1$\bar{1}$0> and <001> azimuth.*

the results of Vattuone et al., respectively. The dashed line in the upper right panel of figure 6.6 is according to their results.

The bottom panels of figure 6.6 show the dissociative sticking probability for different angles of incidence along different azimuthal directions. It is clearly observed that an azimuthal dependence is present in the sticking as was first reported by Vattuone et al. [104]. The largest difference between the <1$\bar{1}$0> and the <001> azimuth observed is approximately 0.05. A variation of the dissociative sticking probability with the azimuth varied in small steps is shown in the inset of the lower right panel. The dissociative sticking probability for the different incident angles and both azimuths is also shown in figure 6.5 on a logarithmic scale and as a function of both total incident and normal incident energy. It is observed that the azimuthal dependence is most pronounced between $E_i = 0.5$ eV and the energy for which the maximum in the sticking probability is reached. Above and below this energy interval the probabilities for both azimuths are almost identical. From the figure 6.5 it is obvious that the energy scaling of the dissociative sticking is between total energy and normal energy scaling. From the plot of the sticking probabilities on a linear scale as function of total energy (bottom left panel of figure 6.6) an energy threshold of approximately 0.2 eV is observed. For the Ag(111) surface a value of 0.2 eV was found as a threshold in the normal incident energy ($E_i \cos^2 \theta_i$) for an increase in surface corrugation and for transient trapping and molecular and dissociative sticking to occur [186,122–124, chapter 3, 4 and 5].

For the O_2-Ag(111) system a second process for the dissociative sticking probability above $E_i \approx 1$ eV and $\theta_i < 60°$ was found [124, chapter 5]. However, even the increase in

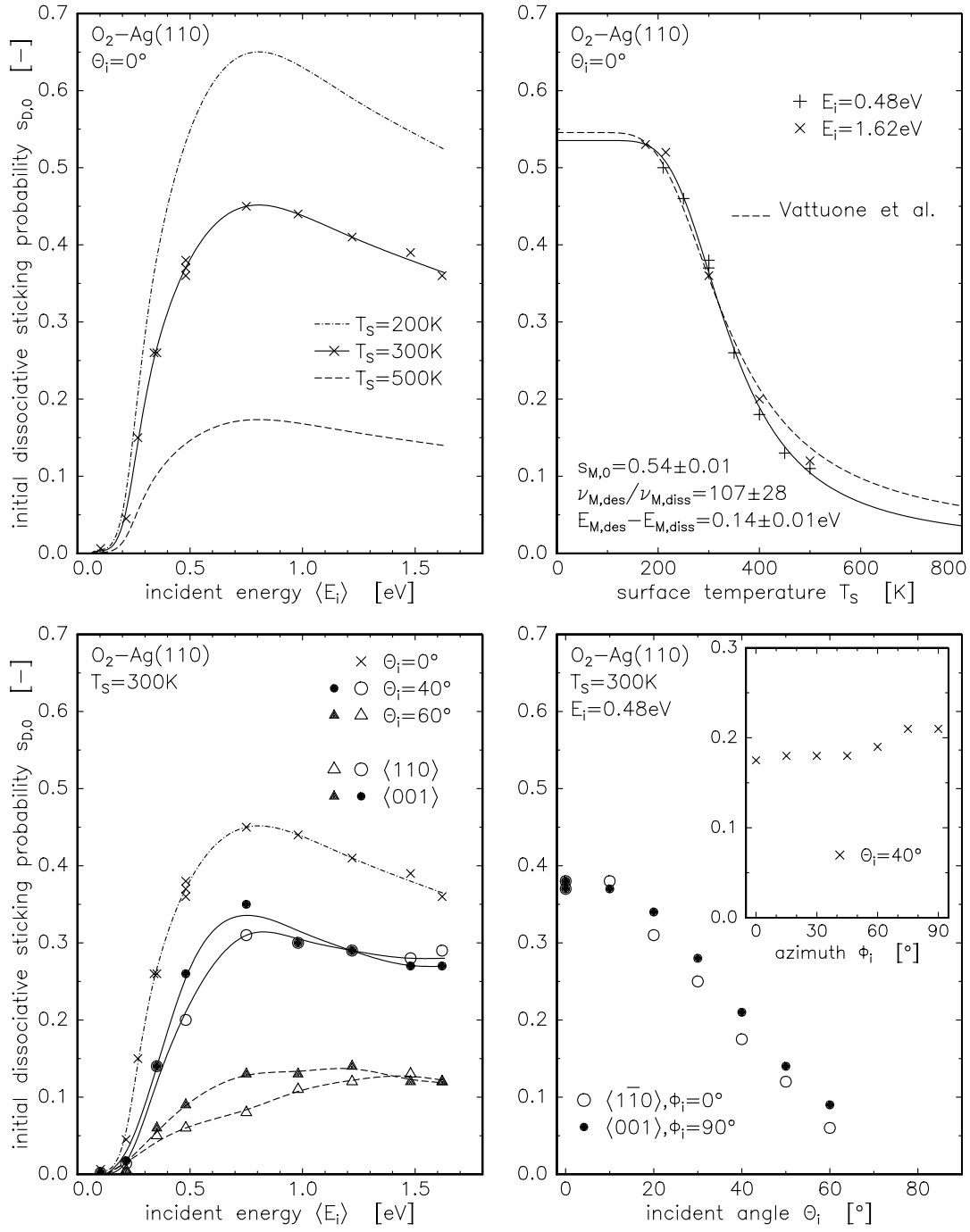

Figure 6.6 *The dissociative sticking probability as function of surface temperature for two incident energies is displayed in the upper right panel. In the lower left panel it is shown for different angles of incidence along the <1$\bar{1}$0> and <001> azimuth as function of incident energy. The lower right panel shows the incident angle dependence for both azimuths and the inset the the dissociative sticking probability while varying the azimuthal angle.*

sticking due to this process resulted only in a maximum sticking probability of 2×10^{-3}. This process, which was attributed to a direct dissociation channel, may also be present for the O_2-Ag(110) but is not visible because the observed indirect dissociation process is three orders of magnitude larger than for the Ag(111) surface.

6.3.3 Dissociative oxygen uptake

The uptake of atomic oxygen has been studied as a function of the oxygen dose on the surface and is shown for two incident beam conditions in the left and right panel of figure 6.7. The initial sticking probabilities at $E_i = 0.1$ eV, $T_s = 400$ K and $E_i = 0.49$ eV, $T_s = 300$ K represent the two extremes of low and high dissociation probabilities on this surface. The insets in the panels show the initial dissociative uptake of oxygen at the surface.

It is observed that the oxygen uptake is initially rapid followed by a slower uptake for atomic oxygen coverages ψ_D above approximately 0.1 ML. The sticking probabilities reported above were the initial sticking probabilities and hold for this 'fast' uptake regime. For the left panel the initial sticking probability is 3.0×10^{-3} and for the right panel it is approximately 30%. After this first uptake regime the sticking probability drops to approximately 5×10^{-4} in both cases for the second uptake regime. Since the probabilities for the first and second regime differ most for the conditions of the right panel the oxygen coverage found marking the change between the regimes is probably most accurate. It is seen to be approximately 0.08 ML. The overall uptake in both regimes can be described by a sticking probability linearly dependent on the atomic oxygen coverage, as we have found for the Ag(111) surface (equation 5.4) [124, chapter 5] and we find final saturation coverages of $\psi_D = 0.86$ ML and 1.14 ML for the incident beam conditions of the left and right panel of figure 6.7, respectively.

The rapid initial decrease in s_D with surface oxygen coverage is in good agreement with the observations of Vattuone et al. [105] who also found a linear dependence on coverage, which varied strongly with surface temperature. They attributed this behaviour to a large increase in the work function of the surface at small oxygen coverages. An alternative explanation originates from STM studies on this system where Ag-O added row structures have been observed to initially form in a (1×13) pattern [239]. This corresponds to an oxygen coverage of $\psi_D = 0.076$ ML, very close to the change in uptake regimes reported here. In that work and also in STM studies on the similar oxygen-Cu(110) system [240] a model has been proposed for the uptake kinetics based upon the diffusion of silver (copper) atoms over the surface. It is suggested that at low oxygen coverages ($\psi_D < 0.08$ ML) the rate of oxygen adsorption is limited by the sticking probability of oxygen on the surface. These molecules are able to locate and dissociate at silver atoms which diffuse readily from step edges at room temperature. Above $\psi_D = 0.08$ ML, however, the formation of Ag-O added rows along the <001> direction effectively blocks the diffusion of silver atoms along the favourable $<1\bar{1}0>$ direction. This produces a coverage regime in which the rate of silver atom diffusion and not oxygen adsorption is rate limiting. Oxygen molecules which do not locate a silver atom within their lifetime on the surface will desorb. This appears to be a more likely explanation than that of Vattuone et al. since the effect of adsorbates on work function is believed to be a very localised one, and should not cause such a significant change at such low coverage [241].

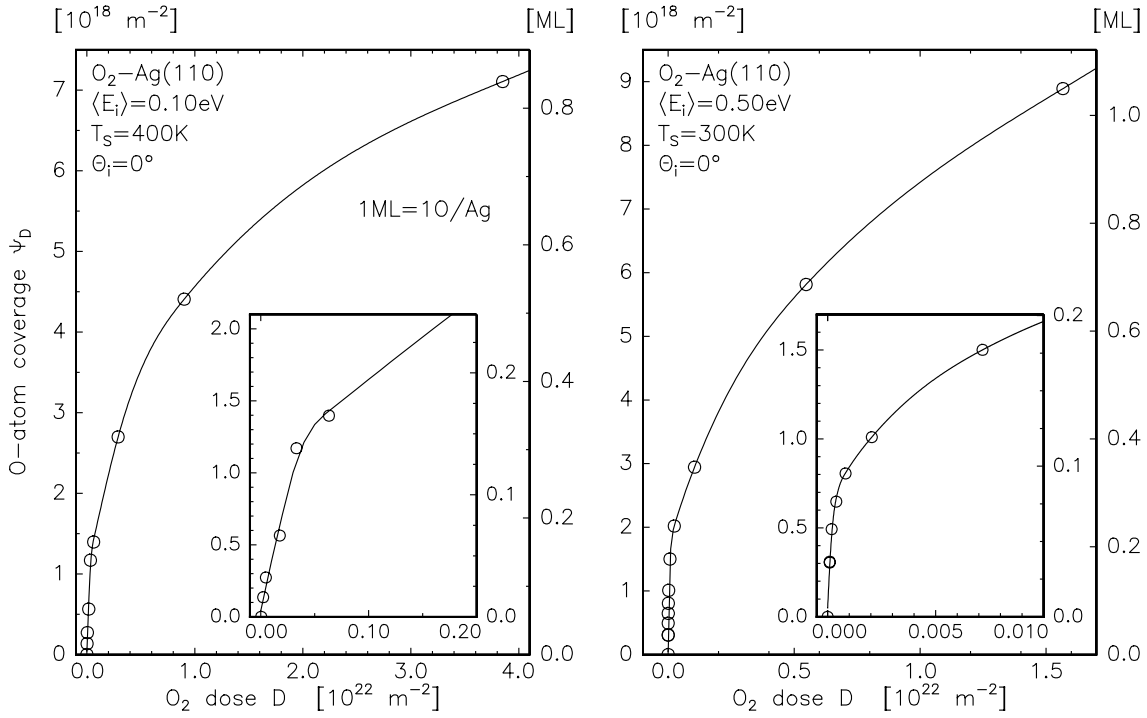

Figure 6.7 *Dissociative oxygen uptake curves for dosing the sample for two different energies of the incident oxygen molecules. The insets show the initial uptake. The O-atom coverage is both given in a number of O-atoms* m^{-2} *and in ML (1 O-atom per Ag surface atom).*

The final saturation coverage appears to increase with the incident beam energy from $\psi_{\rm D} = 0.86$ ML at $E_{\rm i} = 0.1$ eV to $\psi_{\rm D} = 1.14$ ML at $E_{\rm i} = 0.5$ eV. Even higher coverages of $\psi_{\rm D} = 1.30$ ML were observed following dosing with a $E_{\rm i} = 1.42$ eV beam. The saturation coverage observed with thermal energy doses is $\psi_{\rm D} = 0.66$ ML [46], corresponding to the transition from the added row structure to the growth of a silver oxide thin film. Such an increase in the apparent saturation coverage with incident energy has been observed previously for oxygen [204] and nitrogen [194] adsorption on W(110).

6.3.4 Recombinative oxygen desorption

The asymmetric shape of the TPD spectra suggests that the desorption is first order in surface coverage. If this is the case than the maximum desorption temperature should not shift with different initial surface coverages. Figure 6.8 shows different TPD spectra taken at equal heating rate β and different initial coverages. A dramatic positive shift in the peak desorption temperature of 15 K is observed with increasing surface coverage and reaches a saturation at $T_{\rm s} \approx 587$ K for initial coverages above $\psi_{\rm D} = 0.25$ ML. This surface coverage corresponds to (1×4) structure. This similar peak shift was also observed by Bowker [35]. However, they did not observe a saturation because they did measure the shift for $\psi_{\rm D} < 0.33$ ML. The shift could be reproduced in simulations by Bowker [34] and Zhdanov [94] taking adsorbate interactions and a surface reconstruction into account.

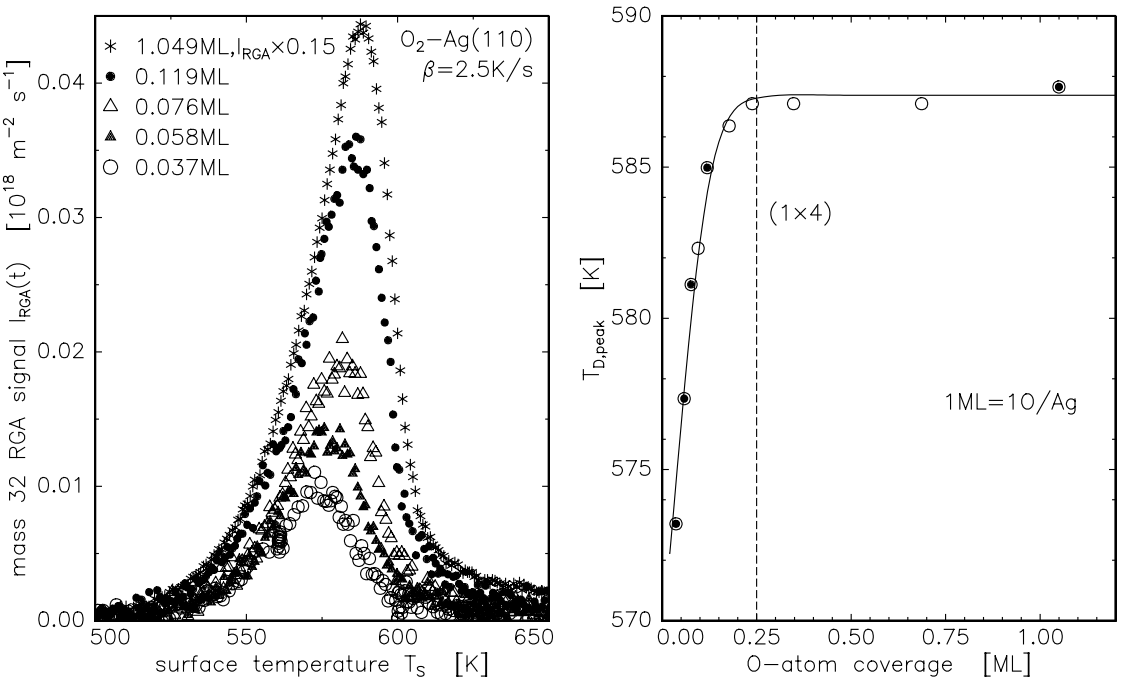

Figure 6.8 *The right panel displays the peak desorption temperature of TPD spectra as a function of atomic oxygen coverage. TPD spectra are shown for the filled symbols in the left panel. The 1.049 ML TPD spectrum is scaled by the indicated factor before plotting.*

The top left panel of figure 6.9 shows TPD spectra taken at different heating rates β. Assuming first order desorption then from the slope of $\ln(T_{\rm peak}^2/\beta)$ versus $1/T_{\rm peak}$, as is shown in the top right panel, a value for the desorption energy $E_{\rm D,des}$ is found. The peak desorption temperature $T_{\rm peak}$ varies over a larger range than for recombinative O_2 desorption from the Ag(111) surface [124, chapter 5]. Using the found value for $E_{\rm D,des}$ in the proper equation for first order desorption yields a value for the prefactor $\nu_{\rm D,des}$. The values found from this analysis are $E_{\rm D,des} = 1.73 \pm 0.05$ eV and $\nu_{\rm D,des} = 10^{14.0\pm0.4}$ s^{-1}. Simulating the TPD spectra for first order desorption for the lowest and highest heating rate applied, using

$$\frac{dn}{dT_{\rm s}} = \frac{dt}{dT_{\rm s}}\, n\, \nu_{\rm des}\, \exp\left(-\frac{E_{\rm des}}{k_{\rm B}\, T_{\rm s}}\right) = \frac{n\, \nu_{\rm des}}{\beta}\, \exp\left(-\frac{E_{\rm des}}{k_{\rm B}\, T_{\rm s}}\right) \quad , \tag{6.3}$$

yields the full lines in the lower panels of figure 6.9. It is observed that the simulation gives only a moderate correspondence to the measured data, as can be expected since the desorption is not of genuine first order. The width of the simulated spectra is too large. However, we find almost identical values for the desorption energy and prefactor as Bowker [34], Zhdanov [94] and Campbell [46]. It shows that the influence of the adsorbate interactions and the surface reconstruction are not of great influence on deriving these paramters in this way. This is in contrast to the results for the desorption of O_2 from the Ag(111) surface [124, chapter 5]. Applying the same formalism does for this system lead to a considerable overestimation of the parameters for the desorption rate.

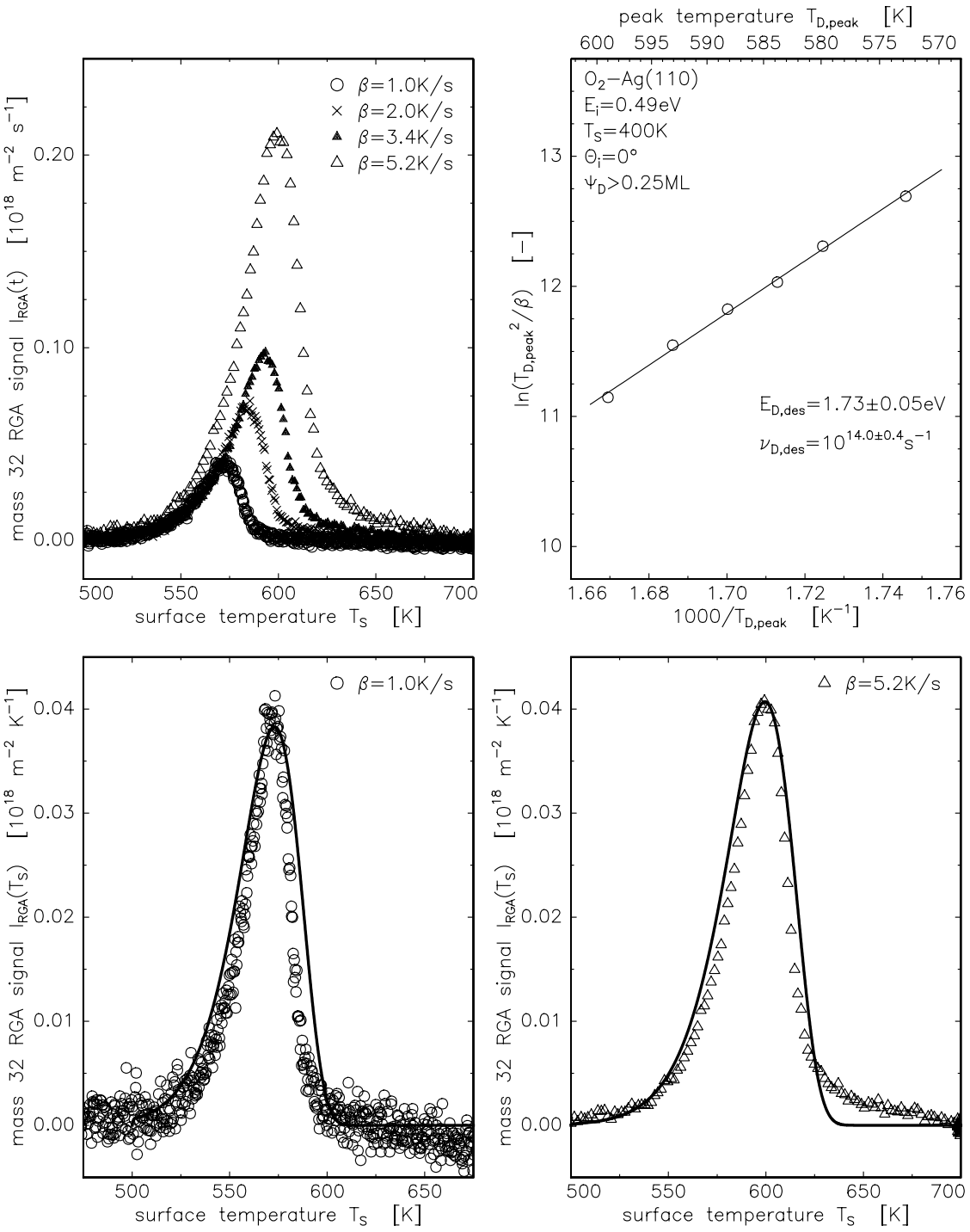

Figure 6.9 *The upper panels show TPD spectra for different ramp rates and from the slope of the linear dependence shown in the upper right panel a value for $E_{\mathrm{D,des}}$ can be found. The bottom panels show two TPD spectra at different ramp rates together with a simulation of these spectra assuming first order desorption and values for the prefactor $\nu_{\mathrm{D,des}}$ and desorption energy $E_{\mathrm{D,des}}$ as given in the upper right panel. Note that the intensity axis of the upper left panel is in amount per second and in the bottom panels in amount per Kelvin.*

6.4 Sticking mechanisms

Comparing the results for the dissociative and molecular sticking of O_2 on Ag(111) with those on Ag(110) one observes that both surfaces show an increase in both sticking probabilities with increasing incident energy and with about equal activation energy. A maximum and subsequent decrease in dissociative sticking is also observed for both the Ag(110) and Ag(111) surface planes. However, over two orders of magnitude difference in sticking probabilities is observed. For Ag(111) a large transient trapping is observed with only a small probability of sticking from this state, which is suggested to act as a precursor. If the transient state also exists and acts as a precursor for the Ag(110) surface, the probability of chemisorption from the transient should be much higher. For the Ag(111) surface the transient has been connected to an vibrationally excited state of the $O_2^{\delta-}$ molecular precursor. The lifetime of this state was sufficiently long, that it decays primarily through desorption, not through equilibration and molecular chemisorption. Due to the strong similarity of the probability for molecular and dissociative chemisorption (vide figures 6.6 and 6.5 and work by Vattuone et al. [103]) it is clear that molecular chemisorption acts as a precursor to dissociative adsorption. Therefore, we infer that at the Ag(110) surface transient trapping occurs, which is followed by rapid molecular chemisorption. The transfer occurs so rapidly that even at high energies (> 1 eV) molecular chemisorption occurs. The difference between the (111) and (110) faces may be due to the fact that at (110) the electron density in the grooves may be higher, enhancing charge transfer to $O_2^{\delta-}$ and so bonding of $O_2^{\delta-}$ in the grooves occurs readily. By contrast, on the (111) face bonding of $O_2^{\delta-}$ may be more difficult and involve defect sites. The subsequent dissociation step is also more probable on the (110) face. This could be due to the fact that ad-atom diffusion occurs more readily on this face than on the (111). We note that in the calculations by Van den Hoek and Baerends for O_2 dissociation on a Ag(110) like cluster, the binding energy of the dissociated molecule (having an internuclear distance of 6 Å) is much less than the binding energy of two O-ad atoms as follows from TPD. This might be due to the fact that strong bonding is only obtained after formation of the Ag-O add-rows. Formation of such reconstructed surfaces may be much more easy on the (110) than on the (111) face. STM studies of the oxidation of the Ag(111) face, preferably carried out using fast molecular beams can shed more light on this matter. It is clear from our work and the present STM studies that oxidation of Ag(110) and Ag(111) is a complex process involving both complex adsorption dynamics through the formation of $O_2^{\delta-}$ species and their subsequent dissociation involving imperfections at the surface.

Just as for the O_2-Ag(111) systen also for O_2-Ag(110) an influence of a physisorption well on the dissociative sticking is not observed. Such an influence would show up as an increase in sticking for decreasing incident energies.

6.5 Conclusion

It has been shown that the Ag(110) surface shows a different scattering behaviour for O_2 scattering along the <001> and the <1$\bar{1}$0> azimuths. The <001> azimuth has been shown to be much more corrugated. According to the energy transfer of the scattered molecules the corrugation is equal for both azimuths for incident energies of $E_i = 1.00$ eV

at $\theta_i = 40°$. Dissociative sticking probabilities are smaller along the $<1\bar{1}0>$ azimuth for energies between $E_i = 0.5$ eV and the incident energy for which a maximum in the sticking is observed. Hence a larger corrugation observed by the incident molecule leads to a larger sticking probability. A threshold of $E_i \approx 0.2$ eV total energy is observed for the increase in the dissociative sticking. It is seen to proceed via the molecular chemisorption state and is likely to first trap into a transient O_2 also observed for the Ag(111) surface. Thermalising to the bottom of the molecular chemisorption well must in this case be a much more likely process. Desorption from the molecular state could not be distinguished in the TOF spectra. This may be due to a barrier in the desorption channel or to the influence of the transient O_2 state. An influence of the physisorption state on the dissociative sticking is not observed.

The dissociative uptake of O_2 is shown to display a low coverage regime upto 0.08 ML, with a relatively high sticking probability as compared to the uptake above this value. Surface diffusion may limit the sticking in the high coverage regime. The maximum uptake can exceed 1 ML and is dependent on the incident energy of the O_2 molecule.

TPD spectra taken are analysed using a first order desorption model and give values for the desorption energy and prefactor close the ones found by taking adsorbate interactions and a surface reconstruction into account. The shape of the TPD spectra is in accordance with first order desorption, but the peak shift with different initial coverages with second order desorption.

References

1. R A van Santen and H P C E Kuipers, *The mechanism of ethylene epoxidation*, Advances in Catalysis 35 (1987), pages 265–321.
2. G A Somorjai, *Introduction to surface chemistry and catalysis*, John Wiley & Sons, New York, 1994.
3. J A Barker and D J Auerbach, *Gas-surface interactions and dynamics; thermal energy atomic and molecular beam studies*, Surface Science Reports 4 (1984), pages 1–99.
4. C T Rettner and M N R Ashfold, editors, *Dynamics of gas-surface interactions*, The Royal Society of Chemistry, 1991.
5. B Poelsema and G Comsa, *Scattering of thermal energy atoms*, volume 115 of Springer tracts in modern physics, Springer-Verlag, 1989.
6. E K Schweizer and C T Rettner, *Quantum effects in the scattering of argon from 2H-W(100)*, Physical Review Letters 62 (1989), pages 3085–3088.
7. S Yamamoto and R E Stickney, *Molecular beam study of the scattering of rare gases from the (110) face of a tungsten crystal*, Journal of Chemical Physics 53 (1970), page 1594.
8. F O Goodman and H Y Wachman, *Dynamics of gas-surface scattering*, Academic press, 1976.
9. C Steinbrüchel, *The hard-spheroid model for gas-surface interactions*, Chemical Physics Letters 76 (1980), pages 58–61.
10. C Steinbrüchel, *Gas-surface scattering distributions according to the hard-spheroid model*, Surface Science 115 (1982), pages 247–258.
11. G O Sitz, A C Kummel and R N Zare, *Direct inelastic scattering of N_2 from Ag(111). I. Rotational populations and alignment*, Journal of Chemical Physics 89 (1988), pages 2558–2571.
12. A C Kummel, G O Sitz and R N Zare, *Direct inelastic scattering of N_2 from Ag(111). III. Normal incident N_2*, Journal of Chemical Physics 89 (1988), pages 6947–6955.
13. F H Geuzebroek, A E Wiskerke, M G Tenner, A W Kleyn, S Stolte and A Namiki, *Rotational excitation of oriented molecules as a probe of molecule-surface interaction*, Journal of Chemical Physics 95 (1991), pages 8409–8421.
14. A E Wiskerke, C A Taatjes, A W Kleyn, R J W E Lahaye, S Stolte, D K Bronnikov and B E Hayden, *Survival mechanism for rotational rainbows in highly attractive molecule-surface systems: NO scattering from Pt(111)*, Chemical Physics Letters 216 (1993), pages 93–99.
15. T F Hanisco, Chun Yan and A C Kummel, *Energy and momentum distributions and projections in the scattering of CO from Ag(111)*, Journal of Chemical Physics 97 (1992), pages 1484–1497.
16. C T Rettner, F Fabre, J Kimman and D J Auerbach, *Observation of direct vibrational excitation in gas-surface collisions - NO on Ag(111)*, Physical Review Letters 55 (1985), pages 1904–1907.
17. C T Rettner, J Kimman, F Fabre, D J Auerbach and H Morawitz, *Direct vibrational excitation in gas-surface collisions of NO with Ag(111)*, Surface Science 192 (1987), pages 107–130.
18. E W Kuipers, M G Tenner, A W Kleyn and S Stolte, *Observation of steric effects in gas-surface scattering*, Nature 334 (1988), pages 420–422.
19. M G Tenner, E W Kuipers, A W Kleyn and S Stolte, *Steric effects in molecular adsorption*, Journal of Chemical Physics 89 (1988), pages 6552–6553.
20. E W Kuipers, M G Tenner, A W Kleyn and S Stolte, *Steric effects in molecular adsorption due to an anisotropic repulsion*, Surface Science 211 (1989), pages 819–828.

21. E W Kuipers, M G Tenner, A W Kleyn and S Stolte, *Steric effects for NO/Pt(111) adsorption and scattering*, Physical Review Letters 62 (1989), pages 2152–2155.
22. E W Kuipers, M G Tenner, A W Kleyn and S Stolte, *Dependance of the NO/Ag(111) trapping probability on molecular orientation*, Chemical Physics 138 (1989), pages 451–460.
23. M G Tenner, F H Geuzebroek, E W Kuipers, A E Wiskerke, A W Kleyn, S Stolte and A Namiki, *Orientation dependence of rotational excitation in NO scattering from Ag(111)*, Chemical Physics Letters 168 (1990), pages 45–50.
24. J Hall, O Saksager and I Chorkendorff, *Dissociative chemisorption of O_2 on Cu(100). Effects of mechanical energy transfer and recoil*, Chemical Physics Letters 216 (1993), pages 413–417.
25. J Harris, J Simon, A C Luntz, C B Mullins and C T Rettner, *Thermally assisted tunneling: CH_4 dissociation on Pt(111)*, Physical Review Letters 67 (1991), pages 652–655.
26. G Rovida, F Pratesi, M Maglietta and E Ferroni, *Effects of oxygen on silver surface structure*, Journal of Vacuum Science and Technology 9 (1972), pages 796–799.
27. H A Engelhardt, A M Bradshaw and D Menzel, *The co-adsorption of oxygen and carbon monoxide on silver*, Surface Science 40 (1973), pages 410–413.
28. P A Kilty, N C Rol and W H M Sachtler, in proceedings of the 5th International Congress on Catalysis, edited by J W Hightower, 1973, page 929.
29. G Rovida, F Pratesi, M Maglietta and E Ferroni, *Chemisorption of oxygen on the silver(111) surface*, Surface Science 43 (1974), pages 230–256.
30. G Rovida and F Pratesi, *Chemisorption of oxygen on the silver (110) surface*, Surface Science 52 (1975), pages 542–555.
31. W Heiland, F Iberl and E Taglauer, *Oxygen adsorption on (110) silver*, Surface Science 53 (1975), pages 383–392.
32. H A Engelhardt and D Menzel, *Adsorption of oxygen on silver single crystal surfaces*, Surface Science 57 (1976), pages 591–618.
33. M A Barteau and R J Madix, *The adsorption of molecular oxygen species on Ag(110)*, Surface Science 97 (1980), pages 101–110.
34. M Bowker, *The effect of lateral interactions on the desorption of oxygen from Ag(110)*, Surface Science 100 (1980), pages L472–L474.
35. M Bowker, M A Barteau and R J Madix, *Oxygen induced adsorption and reaction of H_2, H_2O, CO and CO_2 on single crystal Ag(110)*, Surface Science 92 (1980), pages 528–548.
36. B A Sexton and R J Madix, *Vibrational spectra of molecular and atomic oxygen on Ag(110)*, Chemical Physics Letters 76 (1980), pages 294–297.
37. C Backx, C P M de Groot and P Biloen, *Adsorption of oxygen on Ag(110) studied by high resolution ELS and TPD*, Surface Science 104 (1981), pages 300–317.
38. M A Barteau and R J Madix, *Lateral interaction effects on the reaction of CO_2 and oxygen adsorbed on Ag(110)*, Journal of Chemical Physics 74 (1981), pages 4144–4149.
39. M Kitson and R M Lambert, *Basic studies of the oxygen chemistry of silver: oxygen, dioxygen and superoxide on potassium-dosed Ag(100)*, Surface Science 109 (1981), pages 60–74.
40. M Kitson and R M Lambert, *The properties of binary and ternary mixed adsorption layers: potassium, chlorine and oxygen on silver(100)*, Surface Science 110 (1981), pages 205–216.
41. D Schmeisser, J E Demuth and Ph Avouris, *Electron-energy-loss studies of physisorbed O_2 and N_2 on Ag and Cu surfaces*, Physical Review B 26 (1982), pages 4857–4863.
42. C Benndorff, M Franck and F Thieme, *Oxygen adsorption on Ag(111) in the temperature range from 100–500 K: UPS, XPS and EELS investigations*, Surface Science 128 (1983), pages 417–423.
43. K C Prince and A M Bradshaw, *Valence level photoelectron spectroscopy of the oxygen and carbonate species on silver(110)*, Surface Science 126 (1983), pages 49–57.
44. C Backx, C P M de Groot, P Biloen and W M H Sachtler, *Interaction of O_2, CO_2, CO, C_2H_4 and C_2H_4O with Ag(110)*, Surface Science 128 (1983), pages 81–103.
45. R B Grant and R M Lambert, *Basic studies of the oxygen surface chemistry of silver: chemisorbed*

atomic and molecular species on pure Ag(111), Surface Science 146 (1984), pages 256–268.

46. C T Campbell and M T Paffett, *The interactions of O_2, CO and CO_2 with Ag(110)*, Surface Science 143 (1984), pages 517–535.
47. K Bange, T E Madey and J K Sass, *The adsorption of oxygen on Ag(110): a new view of structure and bonding*, Chemical Physics Letters 113 (1985), pages 56–62.
48. C T Campbell, *Atomic and molecular oxygen adsorption on Ag(111)*, Surface Science 157 (1985), pages 43–60.
49. R Sporken, P A Thiry, J J Pireaux, R Caudano and A Adnot, *Work function measurements with a high resolution electron energy loss spectrometer: application to the interaction of oxygen with Ag(110)*, Surface Science 160 (1985), pages 443–450.
50. A Selmani, J M Sichel and D R Salahub, *Chemisorption of O_2 on Ag(110): a molecular orbital cluster study*, Surface Science 157 (1985), pages 208–232.
51. E L Garfunkel, X Ding, G Dong, S Yang, X Hou and X Wang, *The coadsorption of sodium and oxygen on Ag(100): an XPS, UPS and HREELS study*, Surface Science 164 (1985), pages 511–525.
52. D Schmeisser and K Jacobi, *The interaction of oxygen with silver clusters and surfaces*, Surface Science 156 (1985), pages 911–919.
53. C T Campbell, *An XPS study of molecular chemisorbed oxygen on Ag(111)*, Surface Science 173 (1986), pages L641–L646.
54. K C Prince, G Paolucci and A M Bradshaw, *Oxygen adsorption on silver(110): dispersion, bonding and precursor state*, Surface Science 175 (1986), pages 101–122.
55. A Selmani, J Andzelm and D R Salahub, *Chemisorption of O and O_2 on Ag(110): an LCGTO-LSD cluster study*, International Journal of Quantum Chemistry 24 (1986), pages 829–842.
56. M E M Spruit, E W Kuipers, M G Tenner, J Kimman and A W Kleyn, *Molecular-beam scattering of O_2 and Ar from Ag(111)*, Journal of Vacuum Science and Technology A 5 (1987), pages 496–500.
57. K Prabhakaran and C N R Rao, *A combined EELS-XPS study of molecularly chemisorbed oxygen on silver surfaces: evidence for superoxo and peroxo species*, Surface Science 186 (1987), pages L575–L580.
58. J Stöhr and D A Outka, *Determination of molecular orientations on surfaces from the angular dependance of near-edge X-ray-absorption fine-structure spectra*, Physical Review B 36 (1987), pages 7891–7905.
59. D A Outka, J Stöhr, W Jark, P Stevens, J Solomon and R J Madix, *Orientation and bond length of molecular oxygen on Ag(110) and Pt(111): a near edge x-ray-absorption fine-structure study*, Physical Review B 35 (1987), pages 4119–4122.
60. M E M Spruit, *Probing gas-surface interactions with a molecular beam*, PhD thesis, University of Amsterdam, June 1988.
61. X Bao, S Dong and J Deng, *Adsorption of oxygen on electrolytic silver by UPS and work function measurements*, Surface Science 199 (1988), pages 493–506.
62. M Dean and M Bowker, *Adsorption studies on catalysts under UHV/HV conditions. I. oxygen adsorption on alumina supported silver*, Applied Surface Science 35 (1988/89), pages 27–40.
63. W Segeth, J H Wijngaard and G A Sawatsky, *The electronic structure of a new $c(2 \times 2)$ oxygen phase on Ag(110)*, Surface Science 194 (1988), pages 615–625.
64. P J van den Hoek and A W Kleyn, *Calculations of 1 eV–3 keV oxygen scattering from Ag(111) using ab initio pair potentials*, Journal of Chemical Physics 91 (1989), pages 4318–4329.
65. M E M Spruit, P J van den Hoek, E W Kuipers, F H Geuzebroek and A W Kleyn, *Direct inelastic scattering of superthermal Ar, CO, NO and O_2 from Ag(111)*, Surface Science 214 (1989), pages 591–615.
66. M E M Spruit, E W Kuipers, F H Geuzebroek and A W Kleyn, *Trapping-desorption of O_2 from Ag(111)*, Surface Science 215 (1989), pages 421–436.
67. M E M Spruit, P J van den Hoek, E W Kuipers, F H Geuzebroek and A W Kleyn, *Onset of surface corrugation in molecular scattering from Ag(111)*, Physical Review B 39 (1989), pages 3915–3918.

68. M E M Spruit and A W Kleyn, *Dissociative adsorption of O_2 on Ag(111)*, Chemical Physics Letters 159 (1989), pages 342–348.
69. K Broomfield and R M Lambert, *Model studies of oxygen chemisorption on silver surfaces using an AgO_2 cluster*, Molecular Physics 66 (1989), pages 421–427.
70. M C Zonnevylle, R Hoffmann, P J van den Hoek and R A van Santen, *Covalent effects in molecule-surface charge exchange: O_2 on Ag(111)*, Surface Science 223 (1989), pages 233–257.
71. P J van den Hoek and E J Baerends, *Chemisorption and dissociation of O_2 on Ag(110)*, Surface Science 221 (1989), pages L791–L799.
72. E A Carter and W A Goddard III, *Chemisorption of oxygen, chlorine, hydrogen, hydroxide, and ethylene on silver clusters: a model for the olefin epoxidation reaction*, Surface Science 209 (1989), pages 243–289.
73. Y E Sung, W Y Lee, H K Rhee and H I Lee, *The effect of oxygen on the chemisorption on polycrystalline silver surface*, Korean Journal of Chemistry (English) 6 (1989), pages 300–305.
74. C S Ares Fang, *Surface structural transition of adsorption of oxygen on Ag(100)*, Surface Science 235 (1990), pages L291–L294.
75. H Nakatsuji and H Nakai, *Theoretical study on molecular and dissociative chemisorptions of an O_2 molecule on an Ag surface: dipped adcluster model combined with symmetry-adapted cluster-confirmation interaction method*, Chemical Physics Letters 174 (1990), pages 283–286.
76. M K Rajumon, K Prabhakaran and C N R Rao, *Adsorption of oxygen on (100), (110) and (111) surfaces of Ag, Cu and Ni: An electron spectroscopic study*, Surface Science 233 (1990), pages L237–L242.
77. M Rocca, P Traversaro and U Valbusa, *Initial sticking coefficient of O_2 on Ag(001)*, Journal of Electron Spectroscopy and Related Phenomena 54/55 (1990), pages 131–141.
78. G Bracco, E Massetti and R Tatarek, *Phonon spectrum of $p(3\times1)$O-Ag(110) along <110>*, Journal of Electron Spectroscopy and Related Phenomena 54/55 (1990), pages 317–324.
79. G Bracco, R Tatarek and G Vandoni, *Oxygen effectiveness in restructuring the silver(110) surface: the $p(3\times1)$ oxygen chemisorbed phase*, Physical Review B 42 (1990), pages 1852–1855.
80. L Li, Y Liu, G Weng, W Wang and Z Zhang, *Optical SHG study on oxygen absorption on silver surface*, Zhongguo Jiguang 17 (1990), pages 665–668.
81. K Fan, X Bao and J Deng, *Theoretical analysis of molecular state adsorption on silver surface*, Huaxue Xuebao 48 (1990), pages 330–336.
82. A F Carley, P R Davies, M W Roberts and K K Thomas, *Hydroxylation of molecularly adsorbed water at Ag(111) and Cu(100) surfaces by dioxygen: photoelectron and vibrational spectroscopic studies*, Surface Science 238 (1990), pages L467–L472.
83. X Bao, J Deng, R Zhai, D Wang and X Guo, *HREELS of methanol oxidation on polycrystalline silver - spectroscopic evidence for adsorbed intermediates in the conversion of methoxide to formaldehyde and water*, Catalysis Letters 4 (1990), pages 25–36.
84. P H F Reijnen, A Raukema, U van Slooten and A W Kleyn, *Isotope effect in dissociative adsorption of O_2 on Ag(111)*, Surface Science 253 (1991), pages 24–32.
85. P H F Reijnen, A Raukema, U van Slooten and A W Kleyn, *Isotope effect in dissociative chemisorption of O_2 on Ag(111)*, Journal of Chemical Physics 94 (1991), pages 2368–2369.
86. X Y Shen, K Q Zhang and Y L Tan, *Scattering of O_2 from an Ag(110) surface*, in Springer series in surface science 24, The structure of surfaces III, edited by S Y Tong, M A van Hove, K Takayanagi and X D Xie, Springer-Verlag Berlin, Heidelberg, 1991, pages 197–203.
87. M Rocca, U Valbusa, A Gussoni, G Maloberti and L Racca, *Apparatus for adsorption studies*, Review of Scientific Instruments 62 (1991), pages 2172–2176.
88. T Sakurai, T Hashizume and S Hyodo, *Field ion scanning tunneling microscopy and its application to oxygen adsorption on the Ag(100)(1×1) surface*, Progress of Theoretical Physics Supplement 106 (1991), pages 387–395.
89. M Canepa, C Guarnaschelli, L Mattera, M Polese, S Terreni and D Truffelli, *An experimental apparatus to study chemisorption at surfaces by He diffractive scattering, ultraviolet photoemission, and metastable deexcitation spectroscopies*, Review of Scientific Instruments 62 (1991), pages 1431–1437.

90. L Becker, S Aminipirooz, A Schmalz, B Hillert, M Pedio and J Haase, *Missing-row reconstruction in the system (2×1)O/Ag(110): a surface extended X-ray-absorption fine-structure study*, Physical Review B 44 (1991), pages 13655–13659.
91. C Rehren, M Muhler, X Bao, R Schloegl and G Ertl, *The interaction of silver with oxygen: an investigation with thermal desorption and photoelectron spectroscopy*, Zeitschrift fur Physikalische Chemie 174 (1991), pages 11–52.
92. X D Wang, W T Tysoe, R G Greenler and K. Truszkowska, *A reflection-absorption infrared spectroscopy study of the adsorption of dioxygen species on a silver surface*, Surface Science 258 (1991), pages 335–345.
93. M Taniguchi, K Tanaka, T Hashizume and T Sakurai, *Ordering of Ag-O chains on the Ag(110) surface*, Surface Science 262 (1992), pages L123–L128.
94. V P Zhdanov, *Surface reconstruction and thermal desorption: the missing row model for H/Cu(110) and O/Ag(110)*, Surface Science 277 (1992), pages 155–163.
95. R J Guest, B Hernnäs, P Bennich, O Björneholm, A Nilsson and R E Palmer, *Orientation of a molecular precursor: a NEXAFS study of O_2/Ag(110)*, Surface Science 278 (1992), pages 239–245.
96. H Nakatsuji and H Nakai, *dipped adcluster model study for the end-on chemisorption of O_2 on an Ag surface*, Canadian Journal of Chemistry 70 (1992), pages 404–408.
97. H Nakatsuji and H Nakai, *Potential-energy curves of dioxygen anion species, O_2^- and O_2^{2-}*, Chemical Physics Letters 197 (1992), pages 339–345.
98. X Bao, J V Barth, G Lehmpfuhl, R Schuster, Y Uchida, R Schlögl and G Ertl, *Oxygen-induced restructuring of Ag(111)*, Surface Science 284 (1993), pages 14–22.
99. K Wu, D Wang, X Wei, Y Cao and X Gao, *The role of chlorine in oxygen adsorption on Ag(111)*, Journal of Catalysis 140 (1993), pages 370–383.
100. K Wu, D Wang, X Wei, Y Cao and X Guo, *The role of dioxygen in methanol oxidation on Ag*, Surface Science 304 (1994), pages L475–L480.
101. M K Bhan, P K Nag, G P Miller and J C Gregory, *Chemical and morphological changes on silver surfaces produced by microwave generated atomic oxygen*, Journal of Vacuum Science and Technology A 12 (1994), pages 699–706.
102. B Pettinger, X Bao, I C Wilcock, M Muhler and G Ertl, *Surface-enhanced Raman scattering from surface and subsurface oxygen species at microscopically well-defined Ag surfaces*, Physical Review Letters 72 (1994), pages 1561–1564.
103. L Vattuone, M Rocca, C Boragno and U Valbusa, *Initial sticking coefficient of O_2 on Ag(110)*, Journal of Chemical Physics 101 (1994), pages 713–725.
104. L Vattuone, C Boragno, M Pupo, P Restelli, M Rocca and U Valbusa, *Azimuthal dependance of sticking probability of O_2 on Ag(110)*, Physical Review Letters 72 (1994), pages 510–513.
105. L Vattuone, M Rocca, C Boragno and U Valbusa, *Coverage dependance of sticking coefficient of O_2 on Ag(110)*, Journal of Chemical Physics 101 (1994), pages 726–730.
106. L Vattuone, M Rocca, P Restelli, M Pupo, C Boragno and U Valbusa, *Low temperature dissociation of O_2 on Ag(110): surface disorder and reconstruction*, Physical Review B 49 (1994), pages 5113–5116.
107. L Vattuone, M Rocca and U Valbusa, *Anharmonic shift in the stretching frequency of O_2 chemisorbed on Ag(110)*, Surface Science 314 (1994), pages L904–L908.
108. M Rocca, L Vattuone, C Boragno and U Valbusa, *Adsorption of molecular oxygen on Ag(110)*, Journal of Electron Spectroscopy and Related Phenomena 64/65 (1994), pages 577–581.
109. O Citri and R Kosloff, *The role of non-adiabatic mechanisms in the dissociation dynamics of O_2 on silver surfaces*, To be published.
110. J M Horne and D R Miller, *Diffraction of He and H_2 from Ag(111)*, Surface Science 66 (1977), pages 365–368.
111. G Scoles, editor, *Atomic and molecular beam methods*, volume 1, Oxford university press, 1988.
112. A E DePristo and A Kara, *Molecule-surface scattering and reaction dynamics*, Advances in Chemical Physics 77 (1990), pages 163–253.

113. J Harris, *Mechanical energy transfer in particle-surface collisions*, in Dynamics of gas-surface interactions, edited by C T Rettner and M N R Ashfold, The Royal Society of Chemistry, 1991, chapter 1.
114. S Holloway, *Quantum effects in gas-solid interactions*, in Dynamics of gas-surface interactions, edited by C T Rettner and M N R Ashfold, The Royal Society of Chemistry, 1991, chapter 3.
115. F Besenbacher and J K Nørskov, *Oxygen chemisorption on metal surfaces: general trends for Cu, Ni and Ag*, Progress in Surface Science 44 (1993), pages 5–66.
116. M Karikorpi, S Holloway, N Henriksen and J K Nørskov, *Dynamics of molecule-surface interactions*, Surface Science 179 (1987), pages L41–L48.
117. D Halstead and S Holloway, *Quantum mechanical scattering of H_2 from metal surfaces: diffraction and dissociative adsorption*, Journal of Chemical Physics 88 (1988), pages 7197–7208.
118. C W A Evers, A E de Vries and J Los, *Nonreactive scattering of K by Br_2 in the energy range of 1–10 eV*, Chemical Physics 29 (1978), page 388.
119. A W Kleyn, V N Khromov and J Los, *Vibrational effects in K,Cs+O_2 collisions*, Chemical Physics 52 (1980), pages 65–79.
120. A W Kleyn, E A Gislason and J Los, *Vibronic excitation in K+O_2 collisions*, Chemical Physics 52 (1980), pages 81–95.
121. A W Kleyn, E A Gislason and J Los, *Neutral scattering and vibrational excitation in K+Br_2 collisions*, Chemical Physics 60 (1981), pages 11–22.
122. A Raukema and A W Kleyn, *O_2 transient trapping-desorption at the Ag(111) surface*, To be published.
123. A Raukema and A W Kleyn, *Transient trapping-desorption of molecules at surfaces*, submitted to Physical Review Letters.
124. A Raukema, D A Butler, F M A Box and A W Kleyn, *Dissociative and non-dissociative sticking of O_2 at the Ag(111) surface*, To be published.
125. A Raukema, A P de Jongh, H P Alberda, R Boddenberg, F G Giskes, E de Haas, A W Kleyn, H Neerings, R Schaafsma and H Veerman, *An UHV compatible 3-axis goniometer in a molecular beam scattering apparatus*, To be published.
126. A Albers, J M M Droog and G A Bootsma, *Ellipsometry study of the effect of argon bombardment on the structure and reactivity of Ag(111)*, Surface Science 64 (1977), pages 1–22.
127. C T Rettner, J A Barker and D S Bethune, *Angular and velocity distributions characteristic of the transition between the thermal and structure regimes of gas-surface scattering*, Physical Review Letters 67 (1991), pages 2183–2186.
128. R J W E Lahaye, S Stolte, A W Kleyn, R J Smith and S Holloway, *Site dependent energy loss in Ar scattering from Pt(111)*, Surface Science 307–309 (1993), pages 187–192.
129. S M Liu, W E Rodgers and E L Knuth, in 'Rarified gas dynamics', edited by M Becker and M Fiebig, DFVLR-Press, Porz-Wahn, Germany, 1974.
130. F O Goodman and H Y Wachman, *Dynamics of gas-surface scattering*, Academic press, 1976, chapter 7.
131. J A Barker, C T Rettner and D S Bethune, *The interaction of Xe with the Pt(111) surface*, Chemical Physics Letters 188 (1992), pages 471–476.
132. J A Barker and C T Rettner, *Accurate potential energy surface for Xe/Pt(111): a benchmark gas/surface interaction potential*, Journal of Chemical Physics 97 (1992), pages 5844–5850. See also [133].
133. J A Barker and C T Rettner, *Erratum: Accurate potential energy surface for Xe/Pt(111): a benchmark gas/surface interaction potential*, Journal of Chemical Physics 101 (1994), page 9202.
134. J C Tully, *Washboard model of gas-surface scattering*, Journal of Chemical Physics 92 (1990), pages 680–686.
135. A W Kleyn and T C M Horn, *Rainbow scattering from solid surfaces*, Physics Reports 199 (1991), pages 191–230.
136. R J W E Lahaye, A W Kleyn, S Stolte and S Holloway, *Scattering of Ar from Ag(111)*, To be published.
137. E J J Kirchner, A W Kleyn and E J Baerends, *A comparative study of Ar/Ag(111) potentials*, Journal of Chemical Physics 101 (1994), pages 9155–9163.

138. A E Wiskerke and A W Kleyn, *Angular and translational energy distributions of NO scattered from Pt(111)*, submitted to Journal of Physics - Condensed Matter.
139. G O Sitz, A C Kummel and R N Zare, *Alignment and orientation of N_2 scattered from Ag(111)*, Journal of Chemical Physics 87 (1987), pages 3247–3249.
140. G O Sitz, A C Kummel, R N Zare and J C Tully, *Direct inelastic scattering of N_2 from Ag(111). II. Orientation*, Journal of Chemical Physics 89 (1988), pages 2572–2582.
141. A C Kummel, G O Sitz and R N Zare, *Determination of orientation of the ground state using 2-photon nonresonant excitation*, Journal of Chemical Physics 88 (1988), pages 6707–6732.
142. A C Kummel, G O Sitz, R N Zare and J C Tully, *Direct inelastic scattering of N_2 from Ag(111). IV. Scattering from a high-temperature surface*, Journal of Chemical Physics 91 (1989), pages 5793–5801.
143. A E Wiskerke, C A Taatjes, A W Kleyn, R J W E Lahaye, S Stolte, D K Bronnikov and B E Hayden, *Rotational excitation in scattering of hyperthermal NO from Pt(111)*, Journal of Chemical Physics 102 (1995).
144. A E Wiskerke, F H Geuzebroek, A W Kleyn and B E Hayden, *A molecular beam study of the O_2-Pt(111) interaction*, Surface Science 272 (1992), pages 256–263.
145. C T Rettner and C B Mullins, *Dynamics of the chemisorption of O_2 on Pt(111): dissociation via direct population of a molecularly chemisorbed precursor at high incidence kinetic energy*, Journal of Chemical Physics 94 (1991), pages 1626–1635.
146. J P Anderson, in 'Gas dynamics 4. Molecular beam and low density gas dynamics', edited by P P Wegener, 1974.
147. K C Janda, J E Hurst, C A Becker, J P Cowin, D J Auerbach and L Wharton Jr, *Direct measurements of velocity distributions in argon beam-tungsten surface scattering*, Journal of Chemical Physics 72 (1980), pages 2403–2410.
148. H Haberland, U Buck and M Tolle, *Velocity distribution of supersonic nozzle beams*, Review of Scientific Instruments 56 (1985), pages 1712–1716.
149. D J Auerbach, *Multiple-phonon inelastic scattering*, in 'Atomic and molecular beam methods', Volume 2, edited by G Scoles, Oxford university press, 1992, chapter 15.
150. P R Bevington, *Data reduction and error analysis for the physical sciences*, McGraw-Hill, 1969.
151. W H Press, B P Flannery, S A Teukolsky and W T Vetterling, *Numerical recipes, the art of scientific computing*, Cambridge university press, 1986.
152. J C Tully, *Dynamics of gas-surface interactions: thermal desorption of Ar and Xe from platinum*, Surface Science 111 (1981), pages 461–478.
153. E W Kuipers, M G Tenner, M E M Spruit and A W Kleyn, *Differential trapping probabilities and desorption of physisorbed molecules: application to NO/Ag(111)*, Surface Science 205 (1988), pages 241–268.
154. R P H Gasser, *An introduction to chemisorption and catalysis by metals*, Oxford university press, 1987.
155. E W Kuipers, A Vardi, A Danon and A Amirav, *Surface-molecule proton transfer: a demonstration of the Eley-Rideal mechanism*, Physical Review Letters 66 (1991), pages 116–119.
156. E W Kuipers, A Vardi, A Danon and A Amirav, *Surface molecule proton transfer in the scattering of hyperthermal DABCO from H/Pt(111)*, Surface Science 261 (1992), pages 299–312.
157. C T Rettner and D J Auerbach, *Distinguishing the direct and indirect products of a gas-surface reaction*, Science 263 (1994), pages 365–367.
158. J Harris and B Kasemo, *On precursor mechanisms for surface reactions*, Surface Science 105 (1981), pages L281–L287.
159. M W Roberts, *Evidence for the role of surface transients and precursor states in determining molecular pathways in surface reactions*, Applied Surface Science 52 (1991), pages 133–140.
160. J W Gadzuk, *Surface harpooning*, Comments on Atomic and Molecular Physics 16 (1985), pages 219–240.
161. P Haochang, T C M Horn and A W Kleyn, *Harpooning in surface scattering: O_2^- formation in collisions*

of O_2^+ from Ag(111), Physical Review Letters 57 (1986), pages 3035–3038.

162. P H F Reijnen, P J van den Hoek, A W Kleyn, U Imke and K J Snowdon, *The O_2-Ag(111) interaction studied by 100–1000 eV glancing incidence O_2^+ scattering*, Surface Science 221 (1989), pages 427–453.
163. A W Kleyn, *Harpooning and chemistry at surfaces*, in 'Invited papers of the 16$^{\text{th}}$ International Conference on the Physics of Electronic and Atomic Collisions', edited by A Dalgarno, R S Freund, P M Koch, M S Lubell and T B Lucatorto, American Institute of Physics Conference Proceedings, New York, 1990, pages 451–457.
164. P H F Reijnen, U van Slooten and A W Kleyn, *Negative ion formation and dissociation in scattering of fast O_2 and NO from Ag(111) and Pt(111)*, Journal of Chemical Physics 94 (1991), pages 695–703.
165. T Matsushima, *Dissociation of oxygen admolecules on Rh(111), Pt(111) and Pd(111) surfaces at low temperatures*, Surface Science 157 (1985), pages 297–318.
166. X Guo, A Hoffman and J T Yates Jr, *Adsorption kinetics and isotope equilibration of oxygen adsorbed on the Pd(111)*, Journal of Chemical Physics 90 (1989), pages 5787–5792.
167. R Imbihl and J E Demuth, *Adsorption of oxygen on a Pd(111) surface studied by high resolution electron energy loss spectroscopy*, Surface Science 173 (1986), pages 395–410.
168. K W Kolasinski, F Cemic and E Hasselbrink, *O_2/Pd(111) - Clarification of the correspondence between thermal desorption features and chemisorption states*, Chemical Physics Letters 219 (1994), pages 113–117.
169. J L Gland, B A Sexton and G B Fisher, *Oxygen interactions with the Pt(111) surface*, Surface Science 95 (1980), pages 587–602.
170. H Steininger, S Lehwald and H Ibach, *Adsorption of oxygen on Pt(111)*, Surface Science 123 (1982), pages 1–17.
171. N R Avery, *An EELS and TDS study of molecular oxygen desorption and decomposition on Pt(111)*, Chemical Physics Letters 96 (1983), pages 371–373.
172. S Daiser and K Wandelt, *The short-ranging catalytic activity of surface defects: two forms of adsorbed oxygen on a stepped Pt(111) surface at 100 K*, Surface Science 128 (1983), pages L213–L222.
173. A Cudok, H Froitzheim and G Hess, *Kinetics of the dissociative adsorption of O_2 on Pt(111): a TREELS study*, Surface Science 307–309 (1994), pages 761–767.
174. H R Siddiqui, A Winkler, X Guo, P Hagans and J T Yates Jr, *Chemisorption site retention during thermal desorption - a study of O_2 chemisorption on Pt(112)*, Surface Science 193 (1988), pages L17–L23.
175. J Fusy and R Ducros, *Oxygen adsorption on Pt(110)(1×2) at 100 K*, Surface Science 214 (1989), pages 337–346.
176. J Schmidt, Ch Stuhlmann and H Ibach, *Oxygen adsorption on the Pt(110)(1×2) surface studied with EELS*, Surface Science 284 (1990), pages 121–128.
177. Y Ohno, T Matsushima, S Tanaka, E Yagasaki and M Kamada, *Orientation of oxygen admolecules on a reconstructed platinum(110)(1×2) surface: a near-edge X-ray-absorption fine-structure study*, Surface Science 271 (1992), pages 281–289.
178. J C Lin, N Shamir, Y B Shao and R Gomer, *Adsorption, desorption and dissociation of N_2 on W(110)*, Surface Science 231 (1990), pages 333–343.
179. Q J Zhang, J C Lin, N Shamir and R Gomer, *Electron stimulated desorption and conversion of N_2 adsorbed on a tungsten (110) plane*, Surface Science 231 (1990), pages 344–355.
180. S Holloway and J W Gadzuk, *Charge transfer, vibrational excitation, and dissociative adsorption in molecule-surface collisions: classical trajectory theory*, Journal of Chemical Physics 82 (1985), pages 5203–5215.
181. J W Gadzuk and S Holloway, *Charge transfer and vibrational excitation in molecule-surface collisions: trajectorized quantum theory*, Physica Scripta 32 (1985), pages 413–422.
182. J W Gadzuk, *Vibrational excitation in molecule-surface collisions. Analytical modelling versus classical trajectories*, Journal of Chemical Physics 86 (1987), pages 5196–5209.
183. S Holloway, M Karikorpi and J W Gadzuk, *Dynamics of molecular collisions with surfaces: excitation, dissociation and diffraction*, Nuclear Instruments and Methods in Physics Research B 27 (1987),

pages 37–54.

184. D Halstead and S Holloway, *The influence of the potential energy surface topologies on the dissociation of H_2*, Journal of Chemical Physics 93 (1990), pages 2859–2870.

185. R Kosloff and O Citri, *Non-adiabatic transitions on metal surfaces as a mechanism of dissociation of adsorbed molecules*, Faraday Discussions 96 (1993), pages 175–187.

186. A Raukema, R J Dirksen and A W Kleyn, *Probing the (dual) repulsive wall in the interaction of O_2, N_2 and Ar with the Ag(111) surface*, To be published.

187. C B Mullins, C T Rettner and D J Auerbach, *Variation of the trapping probability of Ar on Pt(111) with kinetic energy and angle of incidence: the changing role of parallel momentum with surface temperature*, Chemical Physics Letters 163 (1989), pages 111–115.

188. C T Rettner, D S Bethune and E K Schweizer, *Measurements of Xe desorption rates from Pt(111): rates for an ideal surface and in the defect-dominated regime*, Journal of Chemical Physics 92 (1990), pages 1442–1457.

189. A C Luntz, private communication.

190. A W Kleyn, J Los and E A Gislason, *Vibronic coupling at intersections of covalent and ionic sites*, Physics Reports 90 (1982), pages 1–71.

191. M Head-Gordon, C T Rettner, C B Mullins, D J Auerbach and J C Tully, *On the nature of trapping and desorption at high surface temperatures. Theory and experiments for the Ar-Pt(111) system*, Journal of Chemical Physics 94 (1991), pages 1516–1527.

192. R J Smith, A Kara and S Holloway, *A molecular dynamics study for the trapping and scattering of Ar/Pt(111)*, Surface Science 281 (1993), pages 296–308.

193. D J Auerbach, H E Pfnür, C T Rettner, J E Schlaegel, J Lee and R J Madix, *Kinetic energy and angular dependance of activated dissociative adsorption of N_2 on W(110): observed insensitivity to incidence angle*, Journal of Chemical Physics 81 (1984), pages 2515–2516.

194. H E Pfnür, C T Rettner, J Lee, R J Madix and D J Auerbach, *Dynamics of the activated dissociative chemisorption of N_2 on W(110): a molecular beam study*, Journal of Chemical Physics 85 (1986), pages 7452–7466.

195. A Kara and A E DePristo, *Dissociative chemisorption in the N_2/W(110) system: rotational state and angular momentum polarization dependence*, Journal of Chemical Physics 88 (1988), pages 5240–5242.

196. A Kara and A E DePristo, *On the concept and distribution of reactive sites in dissociative chemisorption*, Journal of Chemical Physics 92 (1990), pages 5653–5660.

197. M Morin, N J Levinos and A L Harris, *Vibrational energy transfer of CO/Cu(100): nonadiabatic vibration/electron coupling*, Journal of Chemical Physics 96 (1992), pages 3950–3956.

198. T A Germer, J C Stephenson, E J Heilweil and R R Cavanagh, *Hot carrier excitation of adlayers - time-resolved measurements of adsorbate-lattice coupling*, Physical Review Letters 71 (1993), pages 3327–3330.

199. T A Germer, J C Stephenson, E J Heilweil and R R Cavanagh, *Picosecond measurements of substrate-to-adsorbate energy transfer - the frustrated translation of CO/Pt(111)*, Journal of Chemical Physics 98 (1993), pages 9986–9994.

200. R R Cavanagh, E J Heilweil and J C Stephenson, *Time-resolved measurements of energy transfer at surfaces*, Surface Science 300 (1994), pages 643–655.

201. W van Willigen, *Angular distribution of hydrogen molecules desorbed from metal surfaces*, Physics Letters 28A (1968), pages 80–81.

202. H A Michelsen and D J Auerbach, *A critical examination of data on the dissociative adsorption and associative desorption of hydrogen at copper surfaces*, Journal of Chemical Physics 94 (1991), pages 7502–7520.

203. C T Rettner, H A Michelsen and D J Auerbach, *From quantum-state-specific dynamics to reaction rates - the dominant role of translational energy in promoting the dissociation of D_2 on Cu(111) under equilibrium conditions*, Faraday Discussions 96 (1993), pages 17–31.

204. C T Rettner, L A DeLouise and D J Auerbach, *Effect of incidence kinetic energy and surface coverage*

on the dissociative chemisorption of oxygen on W(110), Journal of Chemical Physics 85 (1986), pages 1131–1149.

205. J Harris, S Holloway, T S Rahman and K Yang, *On the dynamics of the associative desorption of H_2*, Journal of Chemical Physics 89 (1988), pages 4427–4439.
206. J A Misewich, A Kalamarides, T F Heinz, U Hofer and M M T Loy, *Vibrationally assisted electronic desorption - femtosecond surface chemistry of O_2/Pd(111)*, Journal of Chemical Physics 100 (1994), pages 736–739.
207. B E Hayden and C L A Lamont, *Coupled translational-vibrational activation in dissociative hydrogen acsorption on Cu(110)*, Physical Review Letters 63 (1989), pages 1823–1825.
208. G Anger, A Winkler and K D Rendulic, *Adsorption and desorption-kinetics in the systems H_2/Cu(111), H_2/Cu(110) and H_2/Cu(100)*, Surface Science 220 (1989), pages 1–17.
209. C T Rettner, D J Auerbach and H A Michelsen, *Role of vibrational and translational energy in the activated dissociative adsorption of D_2 on Cu(111)*, Physical Review Letters 68 (1992), pages 1164–1167.
210. C T Rettner and H Stein, *Effect of translational energy on the chemisorption of N_2 on Fe(111): activated dissociation via a precursor state*, Physical Review Letters 59 (1987), pages 2768–2771.
211. M D Williams, D S Bethune and A C Luntz, *Coexistence of precursor and direct dynamics: the sticking of O_2 on a Pt(111) surface*, Journal of Chemical Physics 88 (1988), pages 2843–2845.
212. A C Luntz, M D Williams and D S Bethune, *The sticking of O_2 on a Pt(111) surface*, Journal of Chemical Physics 89 (1989), pages 4381–4395.
213. A C Luntz, J Grimblot and D E Fowler, *Sequential precursors in dissociative chemisorption: O_2 on Pt(111)*, Physical Review B 39 (1989), pages 12903–12906.
214. J Grimblot, A C Luntz and D E Fowler, *Low temperature adsorption of O_2 on Pt(111)*, Journal of Electron Spectroscopy and Related Phenomena 52 (1990), pages 161–174.
215. H Hand and J Harris, *Recoil effects in surface dissociation*, Journal of Chemical Physics 92 (1990), pages 7610–7617.
216. A C Luntz and J Harris, *CH_4 dissociation on metals: a quantum dynamics model*, Surface Science 258 (1991), pages 397–426.
217. A C Luntz and J Harris, *The role of tunneling in precursor mediated dissociation: alkanes on metal surfaces*, Journal of Chemical Physics 96 (1992), pages 7054–7063.
218. M Rocca, private communication.
219. D A King and M G Wells, *Reaction mechanism in desorption kinetics: nitrogen on the {100} plane of tungsten*, Proceedings of the Royal Society (London) A 339 (1974), pages 245–269.
220. C T Rettner, H Stein and E K Schweizer, *Effect of collision energy and incidence angle on the precursor-mediated dissociative chemisorption of N_2 on W(100)*, Journal of Chemical Physics 89 (1988), pages 3337–3341.
221. D P Woodruff and T A Delchar, *Modern techniques in surface science*, Cambridge solid state science series, Cambridge university press, 1986.
222. E G Overbosch, S Tomoda and J Los, *How ionic is Na at a partially covered W(110) surface*, in proceedings of the 7^{th} International Vacuum Congress & 3^{rd} International Conference on Solid Surfaces, 1977, pages 1345–1347.
223. A Raukema, D A Butler and A W Kleyn, *The interaction of O_2 with the Ag(110) surface*, To be published.
224. A M de Jong and J W Niemantsverdriet, *Thermal desorption analysis: comparative test of ten commonly applied procedures*, Surface Science 233 (1990), pages 355–365.
225. D A King, *Thermal desorption from metal surfaces: a review*, Surface Science 47 (1975), pages 384–402.
226. D A King, *Kinetics of adsorption, desorption, and migration at single-crystal metal surfaces*, CRC Critical Review in Solid State and Material Sciences 7 (1978), pages 167–208.
227. V P Zhdanov, *Elementary physicochemical processes on solid surfaces*, Plenum, New York, 1991.

228. D A King, *The influence of weakly bound intermediate states on thermal desorption kinetics*, Surface Science 64 (1977), pages 43–51.

229. R Gorte and L D Schmidt, *Desorption kinetics with precursor intermediates*, Surface Science 76 (1978), pages 559–573.

230. A Cassuto and D A King, *Rate expressions for adsorption and desorption kinetics with precursor states and lateral interactions*, Surface Science 102 (1981), pages 388–404.

231. T Miyake, S Soeki, H Kato, T Nakamura, A Namiki, H Kamba and T Suzaki, *Molecular-beam study of oxygen on Si(100)*, Physical Review B 42 (1990), pages 11801–11807.

232. R L McEachern, D M Goodstein and B H Cooper, *Trajectory analysis of low-energy and hyperthermal ions scattered from Cu(110)*, Physical Review B 39 (1989), pages 10503–10513.

233. D L Adler and B H Cooper, *Energy and angular distributions 100 to 400 eV Na^+ scattering from Cu(110)*, Physical Review B 43 (1991), pages 3876–3892.

234. R Schinke and A C Luntz, *Experimental He-Ag(110) interaction potential*, Surface Science 124 (1983), pages L60–L66.

235. A C Luntz, L Mattera, M Rocca, S Terreni, F Tommasini and U Valbusa, *Study of the Ag(110) surface by He diffraction*, Surface Science 126 (1983), pages 695–701.

236. K H Rieder, *Surface structural research with atom beams diffraction: helium versus neon*, Surface Review Letters 1 (1994), pages 51–65.

237. F H Geuzebroek, M E M Spruit and A W Kleyn, *Scattering of Cl_2 from clean and Cl covered Ag(111)*, Surface Science 271 (1992), pages 207–216.

238. A Kara and A E DePristo, *Dynamics of dissociative chemisorption: N_2/W(110)*, Surface Science 193 (1988), pages 437–454.

239. T Hashizume, J E Rowe, R A Malic, K Motai, K Cho, J Kishimoto and T Sakurai, *Vibrational and structural studies of oxygen adsorption on the Ag(110) surface*, Journal of Vacuum Science and Technology B 12 (1994), pages 1809–1812.

240. Y Kuk, F M Chua, P J Silverman and J A Meyer, *O chemisorption on Cu(110) by scanning tunneling microscopy*, Physical Review B 41 (1990), pages 12393–12402.

241. N D Lang, S Holloway and J K Nørskov, *Electrostatic adsorbate-adsorbate interactions: the poisoning and promotion of the molecular adsorption reaction*, Surface Science 150 (1985), pages 24–38.

Summary

The interaction between oxygen and silver surfaces is studied with the aid of a molecular oxygen beam. Both scattering and sticking experiments from the Ag(111) and the Ag(110) surface are described. Scattering experiments give information on the energy exchange between the incident molecule and the surface. The energy exchange as a function of incident energy and angle is measured as a function of exit angle and will reveal details of the potential energy hypersurface governing the interaction between the incident molecule and the surface. Trapping of molecules at the surface followed by desorption can also be traced in scattering experiments. The scattering experiments are performed by measuring the time-of-flight of molecules from a high speed chopper mounted in the beam line to a rotatable detector mounted in the scattering chamber. Sticking of oxygen molecules in the limit of zero surface coverage is also studied as a function of incident energy and angle and will give complementary information on the interaction potential. Results on the uptake of oxygen at increasing surface coverage and on the controlled desorption after uptake are also presented.

The silver sample is mounted in an UHV chamber to which a molecular beam line is connected. To allow for different angles of incidence, both with respect to the surface normal and to a reference direction on the surface (azimuthal angle), and for different exit angles of the scattered or desorbing particles the sample is mounted on a sample manipulator. In **chapter 2** a newly designed sample manipulator with six degrees of freedom is described. It allows for cooling of the sample with ℓN_2 and heating by radiation or electron bombardment from a filament behind the sample. By moving both the sample manipulator and the rotatable detector the incident angles and exit angles can be set. The mathematics describing the relation between these four angles and the detector and manipulator position is also presented in this chapter.

Scattering results for O_2 from Ag(111) are given in **chapter 3**. For comparison also Ar and N_2 are scattered from this surface. Of these three gases only O_2 is known to be chemically reactive with silver. If the normal incident energy of O_2 exceeds a threshold energy, part of the O_2 flux is observed to enter the chemisorption part of the interaction. An upper limit for this threshold, as deduced from the scattering experiments, is $E_i \cos^2 \theta_i =$ 0.3 eV. From this value upwards the specularly reflected flux decreases and the angular resolved flux distribution broadens towards the surface normal. The energy transfer is seen to change from scattering from a rather flat surface to scattering from individual surface atoms with increasing incident energy. These experiments are mainly carried out at a surface temperature of $T_s = 600$ K, the desorption temperature for recombinative desorption of dissociated oxygen.

Scattering experiments carried out at $T_s = 150$ K, below the desorption temperature

from the molecular chemisorption state (approximately 200 K) and above the desorption temperature from the physisorption state (below 50 K) are presented in **chapter 4**. The results show trapping-desorption from the physisorption state at low incident O_2 energy. The physisorption trapping probability decreases with increasing incident energy as should be the case. Above the threshold energy of $E_i \cos^2 \theta_i = 0.2$ eV , as observed in this case, another trapping-desorption channel is observed. Trapping in the physisorption state is already seen to have vanished and at $T_s = 150$ K the molecular chemisorption state should be stable at the surface. But the trapping as a function of incident energy and angle shows a strong resemblance with the sticking in the molecular chemisorption state as will be presented in chapter 5. The second trapping-desorption channel is refered to as transient trapping-desorption and is explained as quasi-trapping in the molecular chemisorption state, without equilibration leading to molecular chemisorption. The molecules that overcome the barrier to molecular chemisorpion become strongly vibrationally excited and will show a complicated motion in the molecular chemisorption well. Entering and leaving this well may be an almost vibrationally adiabatic process. Transient trapping shows a maximum of approximately 30% of the incident flux and a subsequent decrease.

Results on both sticking in the molecular chemisorption and dissociated oxygen state are presented in **chapter 5**. Both again show the $E_i \cos^2 \theta_i = 0.2$ eV threshold. The incident energy and angle dependence are similar to that of transient trapping. Molecular chemisorption is probably due to equilibration of a very small amount of transiently trapped molecules. From dissociative sticking masurements as a function of surface temperature it is concluded that dissociation of the O_2 molecule occurs via the molecular chemisorption state; a precursor mechanism for dissociation. But for incident angles $\theta_i \leq 30°$ and incident energies exceeding approximately 1 eV another direct route to dissociation is observed. This mechanism shows a strong decrease with increasing incident angle above 30° and is overtaken by the precursor mechanism at $\theta_i = 60°$. A tunneling mechanism to dissociation seems most likely. The precursor mechanism shows a maximum as afunction of incident energy and a subsequent decrease and peaks at a probability of 2×10^{-4}. The other mechanism shows a monotonic increase with increasing incident energy and is approximately 2×10^{-3} for $E_i = 1.7$ eV.

The dissociative oxygen uptake leads to the formation of an Ag_2O overlayer as is concluded from LEED and the maximum oxygen uptake. A simple analysis of TPD traces gives extraordinary large values for the prefactor and desorption energy in the desorption rate constant. A more detailed analysis should account for adsorbate interactions and a surface reconstruction. The simple first order desorption analysis of the TPD traces from the molecular chemisorption state also gives too large values for both parameters of the rate constant.

The final chapter, **chapter 6**, deals with the O_2-Ag(110) interaction. Both scattering and dissociative sticking measurements are done along both the $<1\bar{1}0>$ and the <001> azimuthal direction. The widths of the angularly resolved scattered flux distribution have strongly increased with respect to the ones taken at the Ag(111) surface and the energy transfer of the O_2 molecules shows a stronger resemblance to scattering from individual surface atoms. These effects are most pronounced for the <001> azimuth.

Dissociative sticking shows along both azimuths a threshold in the total incident energy of $E_i = 0.2$ eV. The sticking probability also shows a maximum and a subsequent decrease

and the molecular chemisorption state acts as a precursor to dissociation. A direct dissociation mechanism as in the case of Ag(111) is not observed. Contrary to the Ag(111) surface the sticking probability can reach a maximum value of approximately 50%. The time-of-flight data do show an indication of transient trapping-desorption. For the Ag(110) surface the probability for equilibration to the bottom of the molecular chemisorption well must have a considerably larger probability but the mechanism is presumably identical.

Analysis of TPD traces for the Ag(110) surface gives more reliable values for the prefactor and desorption energy of O_2 from the dissociated state: $\nu_{\mathrm{des}} \approx 10^{14}\ \mathrm{s}^{-1}$ and $E_{\mathrm{des}} \approx 1.7\ \mathrm{eV}$. Since the desorption temperature for the dissociated state are almost equal for both the Ag(110) and Ag(111) surface the values found for the Ag(110) surface are also expected to hold for the Ag(111) surface.

Dynamica van Chemisorptie; een uitgebreide samenvatting

Wij worden omgeven door een gas, namelijk lucht. Lucht is een mengsel van voornamelijk stikstof ($\pm 80\%$) en zuurstof ($\pm 20\%$). Een gas bestaat uit deeltjes, moleculen genaamd, die op relatief grote onderlinge afstand door elkaar bewegen en ook met elkaar kunnen botsen. Een molecuul is opgebouwd uit atomen. Deze atomen zitten aan elkaar vast in het molecuul. Een edelgas (helium (He), neon (Ne), argon (Ar), etc.) komt voor als atomen, "moleculen" die uit één atoom bestaan. Een zuurstof-molecuul (O_2) bestaat uit twee zuurstof-atomen (O), een stikstof-molecuul (N_2) uit twee stikstof-atomen (N), maar een stikstofmonoxide-molecuul (NO) bestaat uit een stikstof-atoom en een zuurstofatoom. Stikstofmonoxide is geen gasmengsel maar een gas dat bestaat uit NO-moleculen. Stikstofdioxide is een gas dat bestaat uit NO_2-moleculen. Lucht is een mengsel dat voornamelijk uit O_2 en N_2-moleculen bestaat.

In een gas bewegen de moleculen, zoals al genoemd, door elkaar. De temperatuur van het gas is een maat voor de gemiddelde snelheid van de moleculen in het gas. Hoe hoger de temperatuur, hoe hoger de gemiddelde snelheid. De druk neemt toe in een afgesloten vat als de temperatuur hoger wordt en het aantal moleculen constant blijft. De druk neemt ook toe als bij gelijk blijvende temperatuur het aantal gas-moleculen groter wordt. Druk is een maat voor aantal en gemiddelde snelheid van de gas-moleculen. Bij een hogere druk zijn er óf meer gas-deeltjes óf ze bewegen met een hogere gemiddelde snelheid óf een combinatie van beide.

De druk kan gemeten worden omdat de gas-moleculen botsen met een wand. Daardoor wordt een kracht uitgeoefend op deze wand en die kan gemeten worden. Deze kracht is vergelijkbaar met het meten van een gewicht op een weegschaal. Dit gewicht oefent een kracht uit op de weegschaal.

Als de moleculen botsen met een wand (het oppervlak) kunnen ze er ook aan blijven "plakken" en eventueel een chemische reactie met dat oppervlak aangaan. De reactie van zuurstof-moleculen met ijzer bijvoorbeeld noemen we roesten; er wordt een ijxeroxide gemaakt aan de buitenkant van het ijzer. De algemene naam voor een reactie met zuurstof-moleculen is oxideren. Het ene metaal oxideert gemakkelijk, zoals ijzer, het andere metaal niet, zoals bijvoorbeeld zilver of goud. De oxidatie-reactie vindt plaats aan de buitenkant van het metaal; aan het oppervlak. Aan het metaaloppervlak kan ook een chemische reaktie optreden tussen gas-moleculen die aan het oppervlak zijn blijven plakken. Een reactie tussen gas-moleculen die niet of nauwelijks mogelijk is als de gas-moleculen elkaar in een gasmengsel tegenkomen kan soms wel mogelijk worden als ze elkaar op een oppervlak tegenkomen. Niet op elk (metaal-)oppervlak zal deze chemische reactie tussen de gead-

sorbeerde (= geplakte) gas-moleculen mogelijk zijn. De reactie tussen NO-moleculen en O_2-moleculen is bijvoorbeeld mogelijk op een rhodium-oppervlak. Het schadelijke stikstofmonoxide (NO), dat in uitlaatgassen van een automotor voorkomt, wordt in deze reaktie omgezet in stikstof (N_2). Deze reaktie vindt plaats in de katalysator in de uitlaat van een auto. Hiermee is direkt de naam gegeven aan het (metaal-)oppervlak dat een chemische reaktie tussen verschillende gas-moleculen bevordert, namelijk "katalysator". Als er verschillende reacties mogelijk zijn tussen twee verschillende gas-moleculen, dan kan een goed gekozen katalysator de reactie tot het gewenste reactie-product bevorderen. Het gas etheen (C_2H_4) kan met zuurstof (O_2) reageren en verbranden tot kooldioxide (CO_2) en water (H_2O) of een oxide vormen; een zogenaamd epoxide (C_2H_4O). Dit epoxide is een tussenproduct in de chemische industrie. Het verbranden van etheen is een reactie die normaal in de gasfase kan voorkomen. De reaktie tot het epoxide gebeurt bijna uitsluitend en met een hoge specificiteit ten opzichte van de verbrandingsreactie op een zilver-oppervlak. Op dit zilver-oppervlak moeten het etheen en het zuurstof in een dusdanige toestand voorkomen dat een reactie tot het epoxide mogelijk is.

Het onderwerp van dit proefschrift is "de reactie" van het zuurstof-molecuul met een zilver-oppervlak. Het is van praktisch belang om de katalysator-werking van het zilver-oppervlak voor de epoxide reactie (beter) te begrijpen, en van fundamenteel belang om in het algemeen meer te weten te komen over hoe reacties tussen gas-moleculen en metaal-oppervlakken verlopen. In dit proefschrift wordt niet gekeken naar reacties tussen gas-moleculen aan het metaal-oppervlak, maar naar de chemische reactie tussen een gas-molecuul (zuurstof: O_2) en een metaal-oppervlak (zilver: Ag). We laten de O_2-moleculen botsen met het metaal-oppervlak en kijken dan wat er gebeurt. Het molecuul kan blijven plakken (adsorberen) en een chemische reactie met het zilver-oppervlak aangaan (chemisorptie), maar het kan ook reflecteren van het zilver-oppervlak. Wij kunnen de reactie bestuderen op een tijdschaal die overeenkomt met de tijdschaal van de botsing van het gas-molecuul met het oppervlak: dynamica van chemisorptie.

We willen de wisselwerking tussen het gas-molecuul met een schoon "ideaal" metaal-oppervlak bestuderen. Omdat in de open lucht altijd een dun laagje gas-moleculen op een oppervlak aanwezig is, hebben wij ons zilver-preparaat in een vacuum-opstelling gemonteerd. Dit is een ultra-hoog vacuum (UHV) opstelling, wat wil zeggen dat de druk in de opstelling lager dan een miljoenste van een miljoenste van de omgevingsdruk (10^{-12} bar= 10^{-9} mbar = 0.000000000001 bar) is. Over een langere tijd kunnen wij ons preparaat "schoon" houden. Met langere tijd wordt lang ten opzichte van de meettijd voor een experiment bedoeld; tijdens een meting moet het zilver-preparaat schoon blijven. Een schematische weergave van het apparaat is te zien in figuur 1.2 van hoofdstuk 1. Het preparaat is gemonteerd in een manipulator die is aangegeven met een S in de figuur. De verschillende vacuum-pompen aan de opstelling zijn aangegeven met een P.

We laten voor een experiment niet zomaar een zuiver gas binnen in de opstelling, maar maken eerst een bundel van de gas-moleculen: een moleculaire bundel. Deze bundel maken we door een gasleiding te nemen waarin aan het uiteinde een gaatje van ongeveer 0.1 mm doorsnede zit. In de gasleiding heerst een druk van een paar bar, maar aan de andere kant van het gaatje heerst vacuum. Door dit drukverschil wordt het gas door het gaatje geperst en wel zodanig dat de snelheid van het (expanderende) gas de lokale geluidssnelheid overschrijdt: een supersone expansie van het gas. Het gevolg is dat de gas-moleculen in één

richting bewegen en dat alle gas-moleculen bijna dezelfde snelheid hebben. De snelheid van de gas-moleculen kunnen we variëren door het uiteinde van de gas-leiding te verhitten en gebruik te maken van een gas-mengsel. In een omgevingsgas zijn een heleboel snelheden van de gas-moleculen aanwezig volgens een verdeling die afhangt van de temperatuur. Wij zijn in staat om een bepaalde snelheid van de gas-moleculen te selecteren in ons experiment. Het uiteinde van de gas-leiding dat verhit kan worden noemen we een nozzle en is aangegeven met een N in figuur 1.2. Tussen de nozzle en het zilver-preparaat bevinden zich nog een paar gaatjes, diafragma's, om een (bijna) evenwijdige bundel te maken. Deze diafragma's zitten in verschillende wanden die de vacuum-kamer waar het gas uit de nozzle komt en de experimenteer-kamer waar het preparaat zich bevindt van elkaar scheiden. Tussen deze wanden zitten ruimtes (kamers) die weer apart worden afgepompt, zogenaamd differentieel pompen

In de experimenteer-kamer kan het preparaat in een dusdanige stand worden gezet dat verschillende invalshoeken van de gas-moleculen in de moleculaire bundel op het preparaat ingesteld kunnen worden. De van het preparaat gereflecteerde gas-moleculen worden gemeten met een detector die, in een vlak, rond het preparaat kan bewegen. Omdat we de gereflecteerde gas-moleculen in alle richtingen willen kunnen detecteren moeten het preparaat en de detector in een zodanige positie worden gezet dat dit mogelijk is. De manipulator waarin het preparaat is gemonteerd, kan in verschillende vrijheidsgraden bewegen (3 rechtlijnige bewegingen (translaties) en 3 ronddraaiende bewegingen (rotaties)) en is speciaal door ons ontwikkeld en gebouwd voor de experimentele opstelling. Een beschrijving van de manipulator is gegeven in **hoofdstuk 2**. Een manipulator die al deze bewegingen over een groot bereik kan uitvoeren is uniek en was niet commercieel beschikbaar. Verder biedt deze manipulator de mogelijkheid om de temperatuur van het preparaat over een groot bereik te varieren. Er kan gekoeld worden met behulp van vloeibaar stikstof tot ongeveer $-150°$ C en verhit tot boven een temperatuur waar zilver smelt (ongeveer 1200° C).

In hoofdstuk 3 tot en met 6 staan de verschillende experimenten, resultaten en interpretatie beschreven. Voordat deze in het kort worden beschreven moet er iets meer worden gezegd over het oppervlak van het zilver-preparaat. Er zijn namelijk verschillende zilver-oppervlakken. Zoals al genoemd, zijn gas-moleculen opgebouwd uit atomen. Een vaste stof is ook opgebouwd uit atomen, die netjes opeengestapeld zijn in de vaste stof. Vaak wordt deze nette opeenstapeling in de vaste stof doorbroken door fouten in de rangschikking; breukvlakken en verontreinigingen in de vaste stof. Wij maken gebruik van hele zuivere (99.999% zuiver) zilver-preparaten, waarin de atomen allemaal netjes zijn opeengestapeld (zogenaamde éénkristallen). Een oppervlak van de vaste stof betekent dat deze opeenstapeling ophoudt en deze kan in verschillende richtingen van de opeenstapeling worden afgebroken. Dit levert verschillende soorten oppervlakken op. Zilver kent drie soorten basis-oppervlakken en met twee hiervan heb ik experimenten gedaan. Deze oppervlakken worden het (111)- en het (110)-oppervlak genoemd: het Ag(111)-oppervlak en het Ag(110)-oppervlak. De eigenschappen van beide soorten oppervlakken verschillen van elkaar. In hoodstuk 3, 4 en 5 zijn experimenten met het Ag(111)-oppervlak besproken en in hoofdstuk 6 met het Ag(110)-oppervlak.

Met behulp van verstrooiingsexperimenten zoals die in **hoofdstuk 3** zijn besproken kan worden bekeken hoe de botsende zuurstof-moleculen het Ag(111)-oppervlak "zien". Zijn dit afzonderlijke atomen of is dit een glad oppervlak? Dit kunnen we bepalen door de

snelheid van het botsende gas-molecuul voor en na de botsing te vergelijken. De snelheid kunnen we bepalen door de tijd te meten die het gas-molecuul er over doet om van een positie in de bundellijn naar de detector te komen. De positie in de bundellijn is een snel ronddraaiiende schijf met twee smalle openingen, die de gas-moleculen in de bundel kunnen doorlaten. Deze schijf (chopper) is aangegeven met een C in figuur 1.2. De vluchtafstand van de schijf naar de detector is bekend en dus kan de snelheid, en dus de bewegingsenergie, van het gas-molecuul worden bepaald en wel in verschillende verstrooingsrichtingen. Ook de in deze richtingen verstrooide intensiteit kan gemeten worden. Een dergelijk resultaat is te zien in figuur 3.2. De twee bovenste plaatjes laten de gereflecteerde intensiteit zien. Een hoek van 0° betekent loodrecht op het oppervlak, een hoek van 90° betekent evenwijdig aan het oppervlak. Een schematische weergave van de verstrooing is te zien rechts onder in figuur 3.3. Voor lage snelheid en dus lage energie van het botsende gas-molecuul (E_i) geldt redelijk goed dat de hoek van inval gelijk is aan de hoek van uitval. Dit is te vergelijken met een biljartbal die tegen de rand van de biljarttafel botst. De rand van de biljarttafel geeft alleen niet mee, het zilver-oppervlak zal dit wel een beetje doen en is te vergelijken met het springen op het matras van een bed. Als het oppervlak mooi glad is voor het botsende gas-molecuul dan zou de energie van het gas-molecuul na de botsing de dikke lijn in de onderste twee plaatjes van figuur 3.2 moeten volgen. Voor de laagste energie klopt dit weer redelijk goed. Voor de hoogste energie van het botsende deeltje absoluut niet. Deze volgt de streep-lijn beter. Deze streep-lijn geeft de energie na botsing van afzonderlijke zilver-atomen in het oppervlak en is te vergelijken met het botsen van twee biljartballen. De botsende biljartbal heeft alleen een lagere massa dan de biljartbal waarop gebotst wordt. De snelheid van de botsende biljartbal zal anders zijn als de andere biljartbal vol of "dun" geraakt wordt. Voor lage snelheden (energieën) van het botsende zuurstof-molecuul ziet het oppervlak er vlak uit, maar voor hoge snelheden ziet het zuurstof-molecuul de afzonderlijke zilver-atomen in het oppervlak. Bij een botsing van de zuurstof-moleculen met het zilver-oppervlak moet niet aan echt raken worden gedacht, maar meer met krachten zoals die tussen gelijke polen van magneten worden uitgeoefend. Deze krachten zijn "op afstand". De botsingsmetingen van de zuurstof-moleculen met het Ag(111)-oppervlak zijn in hoofdstuk 3 vergeleken met botsingen van argon-atomen en stikstof-moleculen met dit zilver-oppervlak. Het gedrag van het zuurstof-molecuul is duidelijk anders en geeft al informatie over de chemie die optreedt tussen het zuurstof-molecuul en dit zilver-oppervlak.

Figuur 3.6 laat twee gemeten vluchttijd-spectra van zuurstof-moleculen zien. Behalve de temperatuur van het zilver zijn de omstandigheden voor beide metingen dezelfde. In het plaatje links boven is de meting te zien voor een temperatuur van 600 K = 327° C en in het rechter plaatje voor 150 K = −123° C. Het is duidelijk zichtbaar dat er bij de lagere oppervlakte temperatuur onder deze omstandigheden twee dingen met de zuurstof-moleculen kunnen gebeuren in de botsing want er zijn twee pieken te zien in het rechter plaatje. De zuurstof-moleculen kunnen op twee verschillende tijden bij de detector aankomen. Dit verschijnsel is nader bestudeerd in **hoofdstuk 4**. Het blijkt dat de zuurstof-moleculen tijdelijk aan het oppervlak gevangen kunnen worden en er dan weer van af komen. Ze doen er in dit geval langer over om bij de detector te komen. Dit veroorzaakt de dubbele piek in het rechter plaatje van de figuur. Bij de hogere temperatuur komen ze sneller van het zilver-oppervlak af en de twee pieken vallen samen. Het is vaker gezien dat moleculen ingevangen kunnen worden aan het oppervlak, maar ze komen daarna in evenwicht met

het oppervlak en dampen er eventueel vanaf als de temperatuur hoog genoeg is. Dit zien wij ook, maar dan bij hele lage snelheden van de zuurstof-moleculen en is te zien in het linker boven plaatje van figuur 4.1. Dit verdwijnt bij hogere inkomende snelheid van de zuurstof-moleculen en dan komt de volgende dubbele piek tevoorschijn die we al hadden gezien in figuur 3.6 en ook in de andere plaatjes van figuur 4.1 duidelijk zichtbaar is. Het zuurstof-molecuul wordt bij hogere inkomende snelheden gevangen in een toestand die niet stabiel aan het zilver-oppervlak kan zijn en komt daarna weer van het oppervlak af. Iets dergelijks is nog niet eerder waargenomen. Het zou best algemeen kunnen gelden, maar niet zichtbaar kunnen zijn, en ook zou het van belang kunnen zijn in het optreden van bepaalde chemische reacties tussen gas-moleculen aan de oppervlakken van vaste stoffen (zoals metalen). Voor het Ag(111)-oppervlak is de kans dat een zuurstof-molecuul in deze nieuwe toestand aan het oppervlak wordt gevangen maximaal 30%, dus behoorlijk groot.

De kans daarentegen dat het zuurstof-molecuul blijft plakken aan het Ag(111)-oppervlak is ontzettend klein. Dit is besproken in **hoofdstuk 5**. Hier is de plakkans van het zuurstof-molecuul in twee verschillende toestanden onderzocht. Een toestand van een molecuul aan een oppervlak kan voorgesteld worden als een put waar het molecuul in kan vallen. Soms moet het molecuul over een muurtje heen geholpen worden om in de put te vallen. Aan het oppervlak kunnen meerdere van deze putten, met een verschillende diepte, zijn. Eén put representeert het plakken van het molecuul als een molecuul met chemische krachten aan het oppervlak. Een veel minder diepe put is het plakken als molecuul aan het oppervlak met hele zwakke, zogenaamde physische krachten. Een derde put is het plakken als afzonderlijke atomen aan het oppervlak. Het molecuul is in dit geval uit elkaar gevallen en de afzonderlijke atomen zijn ook met chemische krachten aan het oppervlak gebonden. Wij hebben de plakkans in de putten van de chemische krachten bestudeerd. Er blijkt een overeenkomst te zijn met het niet-stabiele zuurstof, zoals die in hoofdstuk 4 is aangetoond. Alleen zijn de gemeten plakkansen een factor 1000 kleiner. Blijkbaar sijpelt er een klein deel van het niet-stabiele zuurstof naar een stabiele toestand van het zuurstof aan het Ag(111) oppervlak. Er blijkt ook dat de put die overeenkomt met de afzonderlijke zuurstof-atomen aan het oppervlak (dissociatie) bevolkt wordt via de put waarin het molecuul chemisch aan het oppervlak gebonden is. De waarschijnlijkheid van dit laatste proces is afhankelijk van de temperatuur van het zilver. Om in de dissociatieve put te vallen wordt bij hoge snelheid van het botsende deeltje ook een tweede soort proces mogelijk. Dit is ook een nieuwe waarneming voor moleculen die uit twee atomen bestaan. Het molecuul valt hierbij hoogst waarschijnlijk direct uit elkaar als het met het oppervlak botst. De hoogste plakkans die we gemeten hebben is ongeveer 0.2%

Als het molecuul of atoom in de put is gevallen kan het erbij een bepaalde temperatuur van het zilver ook als het ware weer worden uitgeschopt (desorptie). Naarmate de put dieper is zal dit bij een hogere temperatuur van het preparaat gebeuren. Dit is ook bestudeerd in hoofdstuk 5 en kan informatie geven over de diepte van de put. Eerst laten we zuurstof-moleculen in een bepaalde toestand (put) plakken, verhogen daarna geleidelijk de temperatuur en meten bij welke temperatuur de zuurstof-moleculen weer van het oppervlak afdampen.

Het laatste hoofdstuk, **hoofdstuk 6**, behandelt de wisselwerking tussen het zuurstof-molecuul en dat andere zilver-oppervlak; het Ag(110)-oppervlak. Hier blijken de afzonderlijke oppervlakte-atomen veel beter zichtbaar voor de botsende zuurstof-moleculen dan voor

het Ag(111)-oppervlak. Ook is de plakkans voor de zuurstof-moleculen aan het Ag(110)-oppervlak veel hoger. We hebben plakkansen van ruim 50% gemeten. Dit staat in schril contrast tot de heel lage plakkansen die voor het andere zilver oppervlak zijn bepaald. Het laat zien dat de chemie tussen een gas-molecuul en een metaal duidelijk kan afhangen van de rangschikking van de metaal-atomen aan het oppervlak.

Nawoord

Op de voorkant van dit proefschrift staat de naam van maar één persoon. Dit betekent niet dat dit proefschrift door alleen de bijdrage van deze ene persoon tot stand is gekomen. Integendeel, de resultaten die in dit proefschrift staan beschreven konden slechts tot stand komen dankzij de inspanning van een groot aantal personen. Iedereen die een bijdrage heeft geleverd wil ik hierbij bedanken.

Mijn promoter, Aart Kleyn, heeft met zijn enthousiaste begeleiding een grote invloed gehad op het verloop van mijn onderzoek. Gelukkig heeft hij mij wel altijd de vrijheid gegeven om mijn eigen weg te zoeken. Met Arjan Wiskerke, Rob Lahaye en in het begin van mijn promotie ook met Frank Geuzebroek heb ik het experiment 'Harpoen' gedeeld en we hebben samen vele problemen opgelost. Frieke Box en Ruud Dirksen hebben in het kader van hun doctoraalscriptie ook een bijdrage geleverd aan het verkrijgen en uitwerken van een deel van de resultaten. The last year David Butler has been of great help. It was a real pleasure and very stimulating to work with him. Joop Los heeft alle resultaten erg kritisch bestudeerd en zijn visie heeft voor een belangrijk deel bijgedragen aan de interpretatie.

Het opzetten en onderhouden van wetenschappelijke apparatuur vergt ook de inzet van de ondersteunende groepen. Een aantal ontwerpen en vele tekeningen, waaronder de nieuwe manipulator voor de opstelling, zijn gemaakt door Paul de Jongh, Herman Ficke, Evert de Haas en Joop van Dorsselaer. Stonden de ontwerpen eenmaal op papier dan was daarna het fabriceren in de vakkundige handen van Henk Neerings, Ed Neugebauer, Wim Brouwer, Piet Kea, Ruud Boddenberg, Wim Barsinghorn en Hildebrand Voort. Ook voor een klusje 'even' tussendoor werd een oplossing gevonden. Electronica, automatisering, computers en het schrijven van de benodigde software, onder andere voor de vernieuwde automatisering voor 'Harpoen', was in vertrouwde handen bij Hans Alberda, Henk Veerman, Cees van Doornik, Henk Dekker, Idsard Attema, Paul van Deenen, Marco Wijnberg, Jan van Elst, Ben Okhuysen, Guus Ruwiel, Hans ter Horst en Ronald Grosman. De in de experimenten gebruikte samples zijn gezaagd en gepolijst door René Koper. Een speciale collega is natuurlijk Frans Vitalis, bij wie je met de meest onmogelijke wiskundige en numerieke problemen kunt aankloppen. Dit lijstje met namen zal niet volledig zijn. Veel meer mensen hebben een bijdrage geleverd in vorm van het uitvoeren van reparaties en het geven van de nodige adviezen.

In de groep moleculaire bundels was ik in de afgelopen jaren in prettig gezelschap. Er was altijd de technische hulp van Frans Giskes, Richard Schaafsma en in het begin ook van Jasper Kuijper. Met Udo van Slooten, Wim Koppers, Arjen Bot, Manfred Tenner en Bart Berenbak heb ik in wisselende samenstelling en met veel plezier een kamer op 'Amolf' mogen delen. Ook de andere leden van de groep, Hans Jenniskens, Malcolm Kadodwala, Katsuyoshi Tsumori, Craig Taatjes, Ron Heeren, Paul Dorlandt, Eric Kirchner, Paul Reij-

nen en Dag Anderson, hebben een plezierige bijdrage geleverd aan de wetenschappelijke en meer wereldse discussies.

Nicole heeft verschillende originele ideeën voor de omslag aangedragen. Mijn ouders bedank ik omdat ze mij altijd gestimuleerd hebben om te studeren. Marita neemt een bijzondere plaats in. Haar steun en vertrouwen hebben mij enorm geholpen.

Age Raukema

februari 1995